UNIVERSITY OF SOUTHAMPTON

FACULTY OF ENGINEERING AND PHYSICAL SCIENCES

Institute of Sound and Vibration Research

Vibration measurement and control of planetary gears

by

Kolade Abiola Olanipekun

Thesis for the degree of Doctor of Philosophy

June 2019

UNIVERSITY OF SOUTHAMPTON

ABSTRACT

FACULTY OF ENGINEERING AND PHYSICAL SCIENCES

Institute of Sound Vibration Research

Thesis for the degree of Doctor of Philosophy

Vibration measurement and control of planetary gears

by Kolade Abiola Olanipekun

Planetary gears are widely used in many applications such as power transmission in automotive vehicles, aircraft, turbines, power screws etc. They are different from parallel shafts gears because of their compactness, better load-carrying capacity etc. These advantages do not restrict them from vibrating during operation. This research work focuses on their mathematical modelling, vibration measurement and control.

Mathematical modelling was done in order to predict the free and forced vibration responses of a planetary gear comprising different numbers of up to six planet gears. Two coordinate systems were used namely fixed and rotating frames of reference. It is shown that the same natural frequencies can be obtained using either a fixed or rotating frame of reference, but on the condition that the carrier speed is set to zero when using a rotating frame of reference. Furthermore, the effect of the carrier speed on the natural frequencies were investigated using a rotating frame of reference on a four-planet model. It shows that only the natural frequencies of the translational modes are either increasing or decreasing, the natural frequencies of the rotational and planet modes remain significantly unchanged. Both the predicted and experimental results were compared, there is a certain level of agreement.

Spinning vibration experiments were conducted in order to determine the effect of various loads at a constant speed, and various speeds at a constant load on the natural and mesh frequencies of a planetary gear. This was achieved with the use of MEMs accelerometers which were mounted and rotate with the system to measure the vibration of a carrier, sun and planets. A further investigation identified the principal source of vibration in the planetary gear train during operation considering different loads and speeds. A Principal component analysis (PCA) was employed to identify the principal vibration sources.

Finally, a method of active vibration control called pole placement was used to shift the poles of the system theoretically in order to mitigate vibration. This was done to prevent resonances which may occur if the frequency of the synchronous vibration or mesh frequency coincides with any of the system natural frequencies. Poles were assigned to the carrier and sun gear for different scenarios and subsequently assigned simultaneously to them. Some of the poles of the translational modes whose

vibration can be very severe were shifted, the poles corresponding to the rotational modes remain unchanged.

Table of Contents

List of Figures

List of tables

Academic Thesis: Declaration of Authorship

I, Kolade Abiola Olanipekun declare that this thesis entitled “Vibration measurement and control of planetary gears” and the work presented in it are my own and has been generated by me as the result of my own original research.

I confirm that:

1. This work was done wholly or mainly while in candidature for a research degree at this University;
2. Where any part of this thesis has previously been submitted for a degree or any other qualification at this University or any other institution, this has been clearly stated;
3. Where I have consulted the published work of others, this is always clearly attributed;
4. Where I have quoted from the work of others, the source is always given. With the exception of such quotations, this thesis is entirely my own work;
5. I have acknowledged all main sources of help;
6. Where the thesis is based on work done by myself jointly with others, I have made clear exactly what was done by others and what I have contributed myself;
7. Either none of this work has been published before submission, or parts of this work have been published as:

   Active vibration control of planetary gears by pole placement. RASD Conference 2019. Proceedings, Journal of Physics, Conference Series.

Signed: ……

Date: ……

Acknowledgements

I thank God Almighty for His love and goodness to me. He has made it possible for me to complete this thesis. I will continue to praise Him forever.

I would like to thank my supervisors Dr N.S. Ferguson and Dr E. Rustighi for their guidance, patience, support and encouragement throughout the work. I also appreciate the Faculty of Engineering and Physical Science (formerly Faculty of Engineering and the Environment) for their financial assistance when I was in a very serious financial hardship. Also, my sincere gratitude goes to Institution of Mechanical Engineers (IMechE), UK for their support during my third year.

I would like to thank my siblings and in-laws. Special thanks go to my wife, Abimbola, for her prayers, constant support, encouragement and understanding throughout the programme. Also, I want to thank my lovely dad Mr N.K. Olanipekun for his prayers, constant support and encouragement throughout the period of study. I cannot but thank my darling son, Eriifeoluwa for his understanding since the beginning of the programme.

Finally, I want to thank my friends in Nigeria and Southampton especially my colleagues in ISVR for the 4-year experience in such a nice environment.

Nomenclature

Ω_c	Rotational speed of the carrier
Ω_s	Rotational speed of the sun gear
Ω_p	Rotational speed of the planet gear
e_{sn}	Transmission error between sun and planet gear
c	Carrier
r	Ring
s	Sun
p	Planet
N	Number of planet
Ψ_{sn}	Mesh angle between sun and planet
Ψ_{rn}	Mesh angle between planet and ring
Ψ_n	Planet position
x_c	Translational coordinate of the carrier in the x direction
y_c	Translational coordinate of the carrier in the y direction
u_c	Rotational coordinate of the carrier
x_r	Translational coordinate of the ring in the x direction
y_r	Translational coordinate of the ring gear in the y direction
u_r	Rotational coordinate of the ring
x_s	Translational coordinate of the sun gear in the y direction
y_s	Translational coordinate of the sun gear in the y direction
u_s	Rotational coordinate of the sun gear
ζ_n	Radial coordinate of *nth* planet gear
η_n	Tangential coordinate of the nth planet gear
u_n	Rotational coordinate of the planet
α_s	Pressure angle in the sun-planet mesh
α_r	Pressure angle in the ring planet-planet mesh
$\mathbf{M}$	Global mass matrix using a fixed frame of reference
$\mathbf{C}$	Global damping matrix using a fixed frame of reference

$\mathbf{K_b}$	Global bearing stiffness matrix using a fixed frame of reference
$\mathbf{K}_m$	Global contact stiffness matrix using a fixed frame of reference
δ_{sn}	Sun-planet mesh deflection
δ_{sn}	Planet-ring mesh deflection
$\bar{\mathbf{M}}$	Global mass matrix using a rotating frame of reference
$\bar{\mathbf{C}}$	Global damping matrix using a rotating frame of reference
$\bar{\mathbf{G}}_{\boldsymbol{y}}$	Global Coriolis matrix using a rotating frame of reference
$\bar{\mathbf{K}}_{\boldsymbol{b}}$	Global bearing stiffness matrix using a rotating frame of reference
$\bar{\mathbf{C}}_{\boldsymbol{b}}$	Global bearing damping matrix using a rotating frame of reference
$\bar{\mathbf{K}}_{\boldsymbol{m}}$	Global contact stiffness matrix using a rotating frame of reference
f_m	Mesh stiffness
M	Module
T_s	Torque applied on the sun gear
T_c	Torque applied on the carrier
P_s	Power on the sun gear
P_c	Power on the carrier
ζ	Damping ratio
σ	Real part of eigenvalue
ω_d	Damped natural frequency
v	Voltage
R	Electrical resistance
U	Conjugate of eigenvector coefficient
Λ	Eigenvalue of the principal component
G	Feedback gain matrix proportional to stiffness
F	Feedback gain proportional to damping
λ	Closed loop eigenvalues

H	Inverse dynamic stiffness matrix
Z_r	Number of teeth on the ring gear
Z_s	Number of teeth on the run gear
Z_p	Number of teeth on the planet gear

Abbreviations

PSD	Power Spectral Density
TSA	Time Synchronous Averaging
PCA	Principal Component Analysis

Chapter 1 Introduction

Planetary gears are widely used in many applications such as power transmission in automotive vehicles, helicopters, turbines, aircraft engines, tractors etc. A typical planetary gear train comprises a carrier, ring, sun and planet gears. The carrier, ring and sun gears are referred to as the central members and any of them can be made an input or output member. This is one of the advantages over a parallel shaft gear because different speed ratios can be obtained by simply changing the input and the output member while the remaining central member is kept stationary [1]. Another better comparative advantage over a parallel shaft gear train is that the load is transmitted by several contacts of the tooth surfaces (i.e. a good load distribution). Also, the arrangement of the shaft leads to a compact layout. These features bring about versatility in their applications, especially in the transmission system of an automobile. In most cases, the planetary gear system may be either spur or helical gear. Spur planetary gears are frequently used in heavy machines, while the helical planetary gear (which is relatively quieter and more durable because of gradual engagement of the teeth) are used in automatic transmission systems.

However, in planetary gears there can still be vibration and noise due to dynamic overload, backlash, fluid entrainment, friction, gravity as in the planetary gear of a wind turbine [2], variation in the stiffness of teeth contact surface [3], as well as transmission error. Many research studies have been carried out on vibrations of gears [4], because of the wide applications, which includes torque and power transmission in numerous machines as mentioned earlier.

In most cases, the vibration of parallel axis and planetary gears are measured on the casing because typical available accelerometers cannot rotate with the system. A filtered response of the original vibration signal with a significant noise contamination is measured by an accelerometer externally mounted on the casing [5]. Therefore, fault detection in the system may not be easy especially in the time domain. In this case, signal separation techniques like time synchronous averaging (TSA) may be employed to identify the fault in the components. TSA makes it possible to isolate a component signal from noise or any unwanted signal [6] measured from the gearbox. (Abhinav et al [5] stated that although fault can be identified from TSA signal but such a fault must be associated with gear teeth). If there is a crack on the carrier, TSA will not work well according to Abhinav et al. [5]. This is because there is the possibility that the resonance frequency that will show the fault due to the crack has been isolated because it is not synchronised with the carrier speed. Therefore, they proposed a method known as Complex Morlet Wavelet to extract a useful signal from the raw signal. Some researchers like Jong et al. [6] used a method known as Autocorrelation-based TSA to solve the

problem associated with the conventional TSA used in condition monitoring of planetary gearboxes of wind turbine.

1.1 Description of an epicyclic gear and types

For a proper understanding it is essential to describe an epicyclic gear and discuss the three possible types. Planetary gear train, which is also known as epicyclic gear, comprises a sun gear which rotates about a fixed axis, planet gears which rotate about their axis and revolve around the sun gear like the planets orbit around the sun in solar system. A carrier serves as a link between two or more planet gears with revolute joints at the centre of the planets and there is a ring gear, which has internal teeth arrangement, which meshes with the planet gears.

The various types of planetary gears depend on which member is fixed and this in turn determines their speed ratios considering the input and the output member. The three configurations or naming descriptions are: planetary type, solar type and star type.

(1) In the planetary type, the input gear may be the carrier while the output is the sun gear or vice versa. The ring gear, which has internal teeth, is stationary and meshed with the planet gears which are also moving in an epicyclic motion around the sun gear (Figure 1-1).

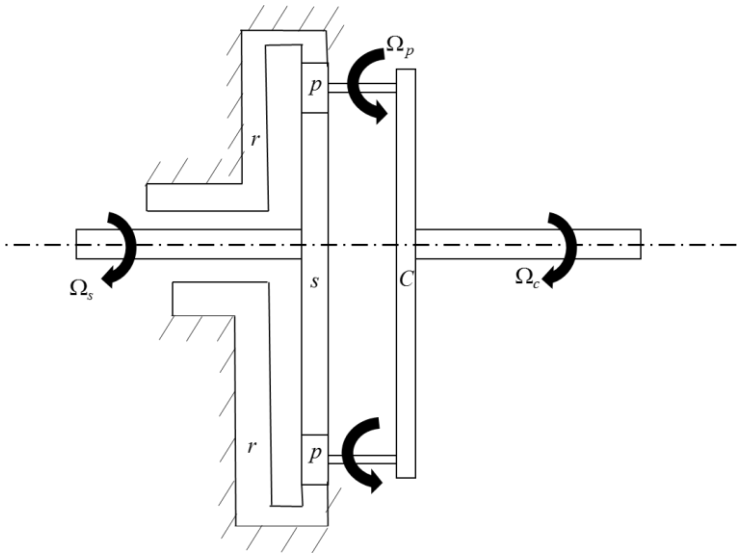

Figure 1-1 Schematic diagram of planetary type of epicyclic gear with a stationary ring gear. The carrier, ring, sun and planet gears are denoted by *c*, *r*, *s* and p respectively.

(2) In the solar type, the sun is fixed, the input gear may be either the ring or the carrier, and the same thing is applicable for the output (Figure1-2).

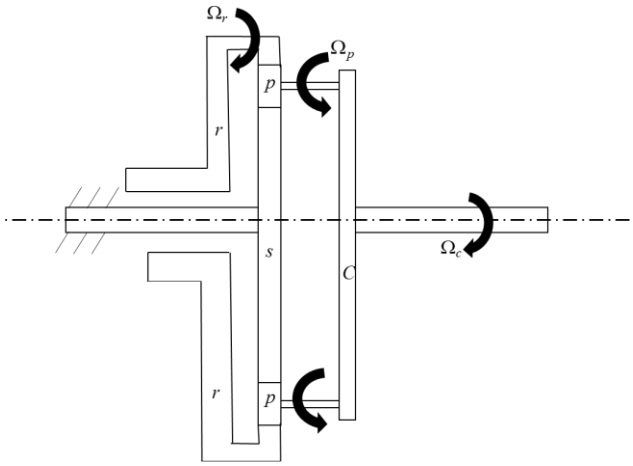

Figure 1-2 Schematic diagram of solar type of epicyclic gear with a stationary sun gear. The carrier, ring, sun and planet gears are denoted by *c, r, s* and p respectively.

(3) In the star type, the sun and the ring are moving while the carrier is fixed. In this latter case, the planets gears rotate about a fixed position without revolving around the sun gear. This makes the gear system behave like an ordinary gear train, thereby the planet gears act like idlers (Figure 1-3).

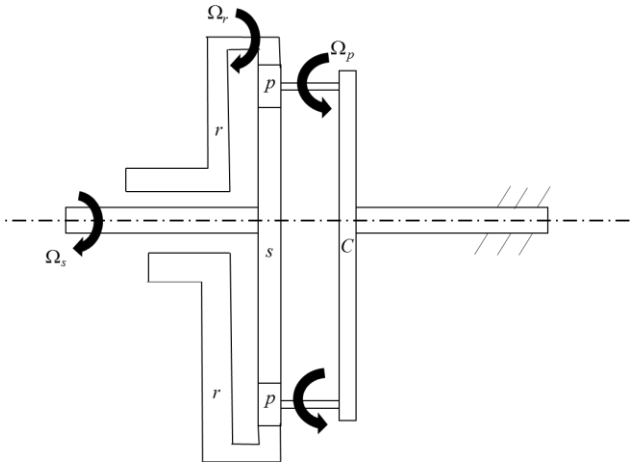

Figure 1-3 . Schematic diagram of star type of epicyclic gear with a stationary carrier. The carrier, ring, sun and planet gears are denoted by *c, r, s* and p respectively.

The carrier, ring and sun gears share the same axis as shown in Figures 1-1, 1-2 and 1-3**.** The configuration is more flexible than that of a parallel shaft gear. The CAD model of a typical planetary gear test rig for this research is as shown in Figure 1.4 where the main components are the carrier, sun

gear, two planet gears, sun shaft, carrier shaft, the frame, the bearing supports and the fasteners. The particular detailed CAD model for the study was developed for manufacturing some required parts of the test rig for the purpose of vibration experiment and control.

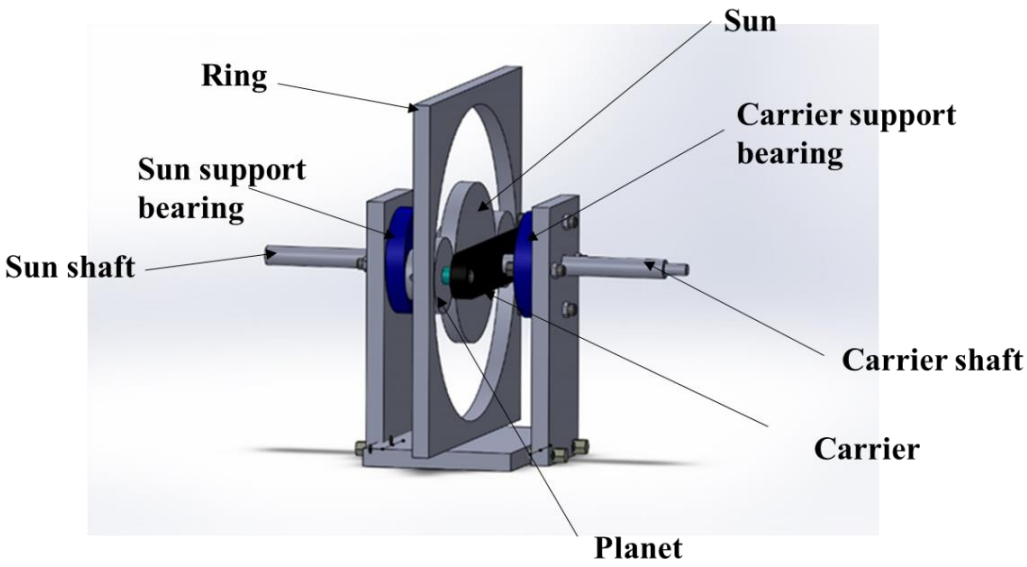

Figure 1-4 CAD model of a planetary gear test rig.

1.2 Transmission error

Transmission error is the main source of excitation [7] which was considered in this study as the external excitation. It is defined *as the distance between the actual position of the output gear and the position it would occupy if the gear drive were perfect*. This implies that for no transmission error, the speed ratio of the mating gears remain constant throughout the cycle of meshing i.e. from approach to recess [8].

Transmission error may also be expressed as the angular or linear displacement that occurs at the pitch point of meshing gear teeth [9]. The phenomenon of transmission error is caused by gear eccentricity, geometrical errors in the tooth profile, wrong positioning of the bearing in the housing, misalignment of shafts, deflection (e.g. contact deformation at the mesh region, deflection due to bending of the gear teeth, shaft deflection) and geometrical modification (such as tip and root relief) in the tooth profile [9].

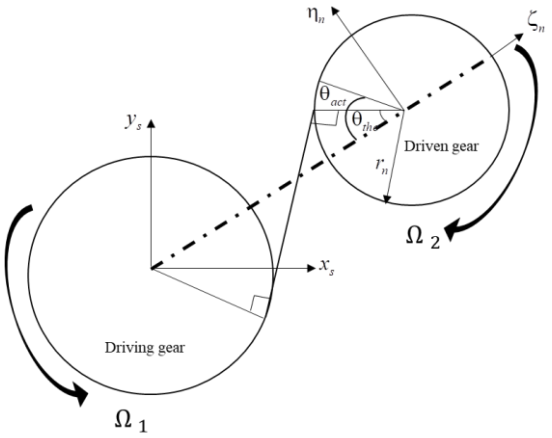

Figure 1-5 Transmission error in gears.

In Figure 1-5, the driving gear is assumed to be rotating at constant angular velocity Ω_1 while the angular velocity of the driven gear is Ω_2. Therefore, the transmission error, e_{sn} in terms of angular displacement is:

$$\delta\theta = \theta_{act} - \theta_{th} \tag{1.1}$$

where, θ_{act} and θ_{th} are the actual and theoretical rotational displacements of the driven gear respectively. Therefore,

$$\delta\theta = \theta_{act} - \Omega_2 t \tag{1.2}$$

In terms of linear displacement at the line of contact or pressure line;

$$e_{sn} = r\delta\theta \tag{1.3}$$

Where t is the time taken from the initial position of the driven gear to the current position and $\delta\theta$ is the angular transmission error. Transmission error can also be determined in terms of linear displacement by multiplying the above terms with radius, r of the base circle of the output gear as written in equation (1.3).

1.3 Methods for controlling gear and rotor vibration

Vibration in planetary gears hinder their performance in assembled machines, so there is a need to suppress vibration because of the adverse effect. There are two main methods of vibration control for gears and rotors namely; passive vibration control and active vibration control.

Passive vibration control involves changing the physical properties of the planetary gear system, typically by design in order to reduce vibration. There are many methods of controlling the vibration of planetary gear using passive modification methods. Tooth profile modification is an example but it is not guaranteed that vibration will be controlled as desired [10]. Other ways of reducing gear vibration passively can be achieved by introducing damping elements, mesh phasing and increasing the contact ratio by reducing the pressure angle or increasing the height of the tooth. Also, some researchers in their work [4] and [11] have shown that some particular instabilities due to parametric excitation (which is another major causes of instabilities in gear train) can be reduced by certain conditions of the mesh phasing, which involves a proper selection of design parameters (like contact ratio) and teeth configuration so that there would be a balancing of the net forces on the meshing teeth. Passive vibration control techniques according to Fuller et al. [12] are mainly effective at high frequencies.

Active control involves changing the dynamics of the system by the application of typically control forces using actuators at some positions to counterbalance the effect of the excitation force (or external disturbance causing the vibration). Active vibration control for rotating systems are of two categories: direct active vibration control technique in which a control force is applied to the rotor directly and active mass balancing technique in which the mass distribution is adjusted by a mass redistribution actuator which is mounted on the rotor [13]. There are some studies where a feedforward control strategy was used to control vibration in a single stage spur gear. Dogruer and Abbas proposed a nonlinear controller with feedforward loop such that the input torque acting on the driving gear can be adjusted. Thus the periodic change in mesh stiffness can be cancelled by a feedforward loop.

1.4 Scope of the research and questions

The scope of this research is to advance the vibration control of a planetary gear based on the dynamic modelling and analysis carried out by Parker et al [14]. First and foremost the dynamic modelling using a fixed and rotating coordinate system were used to analyse a planetary gear system. The results were then compared considering both frames of reference. Modal analysis was carried out to determine the natural frequencies of the system which helps to identify the modes excited in the spinning test. Vibration source identification was carried out using the signal acquired from the spinning test.

In this study, active control by pole placement method was used considering numerical demonstrations to shift the pole of the planetary gear system to avoid resonance which may lead to damage of the system. A feedback loop was typically considered because its signal can be adjusted to

achieve desired result. To achieve this, the models in both frames of reference were subsequently extended to derive a vibration control law developed by Mottershead et al. [15] using pole placement in order to analyse and numerically predict the modified response of planetary gear system.

The research questions are:

- What is the difference between the results of analyzing a planetary gear model using a fixed and rotating frame of reference? The frequency response and modal damping were considered at different rotational speed of the rotating frame of reference.
- What are the effects of loads and rotational speed on the dynamic response of a planetary gear system?
- Would there be the sidebands in the frequency spectrum of a planetary gear measured by a rotating accelerometers like the stationary accelerometers?
- Can the principal source of vibrations in a planetary gear system be obtained from the synchronized vibration signal measured from the individual component?
- Assuming the control force required to achieve vibration control was predicted using a rotating frame of reference what will be the equivalent force using a fixed frame of reference?
- Where is the optimal location to apply a control force in a planetary gear train?

1.5 Aim and objectives of the research

The aim of this research is to model, measure and control the vibration of a planetary gear system. The main objectives are:

- To model a planetary gear system analytically, in order to determine its natural frequencies and mode shapes in the free vibration case using both fixed and rotating coordinate systems.
- To compare the natural frequencies obtained using a fixed coordinate system with those of rotating coordinate systems especially at high rotational speeds.
- To predict the effect of the speed on the resonance frequencies and modal damping ratios of the system using a rotating coordinate reference system.
- To design and develop a suitable experimentally based physical model of a planetary gear system test rig for the purpose of measuring the vibration of carrier, sun and planet gears during operation individually. In this case, there is no need to use a slip ring with instrumentation to measure the vibration of the components. Also, there is no need to use any complicated signal separation techniques to know which component is faulty in the system.

- To perform modal testing on the physical model developed in order to compare the results obtained with predictions from the analytical model.
- To determine the effect of the load and rotational speed on the dynamic response at the mesh and natural frequencies of the system.
- To identify the principal source of vibration in a planetary gear using a method known as Principal Component Analysis (PCA). The relationship between the physical sources would be considered.
- To numerically implement the methods of active vibration control by pole placement in order to mitigate the vibration of a planetary gear.
- To determine the optimal place to put a control force in a planetary gear by comparing the control efforts obtained when a control force is applied either on the carrier or on the sun gear.

1.6 Outline of the thesis

Chapter 1 of this thesis gives a brief introduction covering the areas of applications of planetary gears and its advantages over parallel shaft gears. Despite the advantages, some causes of vibrations in planetary gear system were mentioned with most emphasis on transmission error which is one of the main causes of vibration. The methods of vibration control of rotors and gears are briefly discussed. Also included in this chapter are the aim and objectives of the study, significance, scope and the outline of the thesis. Lastly, the contributions of the study to knowledge were highlighted.

Chapter 2 focuses on the review of recent relevant and applicable literature associated with dynamic and finite element modelling and analysis of gears especially planetary gears. Also, some literature is reviewed for theoretical modelling and vibration experiments of planetary gear, vibration spectra analysis, vibration control of gears and vibration source identification. Finally in this chapter, the workdone in this thesis is briefly discussed.

Chapter 3 involves the dynamic modelling and analysis of planetary gear models comprising from two up to six planet gears. The results of the analysis were compared in each case using both fixed and rotating frames of reference. Parker's parameters are used for simulations in this chapter to see that the analysis is correct, by comparing with the results in his published paper. The results are compared and a few differences identified were discussed.

Chapter 4 deals with the design and construction of a test rig, estimation of planetary gear system parameters required for subsequent natural frequency and frequency response predictions using a rotating frame of reference.

Chapter 5 focuses on the comparison of the predicted and measured behaviours of an experimental planetary gear when it is nonrotating. The measured behaviour is achieved using modal testing and analysis. Also, the mesh force is predicted at the mesh frequency using the dynamic model of the planetary gear.

Chapter 6 focuses on the spinning or rotating test, where the effect of different loads and rotational speeds on the dynamic response of the system at natural and mesh frequencies are investigated. Also investigated is the vibration source in the system over a particular frequency range.

Chapter 7 focuses on the modelling and numerical analysis using active control by a pole placement method. This is done using both a fixed and rotating frame of reference. The optimal location to apply the control force was also determined, by comparing the control effort when control forces are applied on the carrier and sun in the translational directions.

Chapter 8 deals with the general conclusions and suggestions for future work.

1.7 Contributions to knowledge

1. The study has extended an already existing theoretical model using a fixed and rotating coordinate system to analyse and predict the dynamic response of planetary gears. The effect of a high rotational speed on the results predicted using a rotating frame of reference was investigated on the frequency response and modal damping.
2. Design and construction of a suitable planetary gear vibration test rig, which can accommodate wireless MEMS accelerometers that can rotate with the system. This makes the measurement of the carrier, sun and planet gears possible without using any signal separation technique.
3. Estimation of sun-planet and planet-ring mesh stiffnesses dynamically using error minimisation method which is simpler than the existing methods.
4. Investigation into the effect of load and rotational speed on the dynamic response of the carrier, sun and planet gears during operation. The natural and mesh frequencies are the frequencies of interest.
5. Identification of the vibration sources over a particular frequency range in a planetary gear system.
6. The theory of active vibration control by pole placement was extended to formulate a control law using both fixed and rotating frames of reference. The control force required using a rotating frame of reference was determined, and its equivalence was evaluated using the fixed frame of reference for numerical implementation.

7. The optimal location to apply control forces was investigated by comparing the control effort required when a control force was applied to the carrier and sun in the two orthogonal directions.

1.8 Significance of the research

The significant results or potential applications of this research amongst others are as follows:

- The vibration level of each component can be measured individually, hence there is no need for any signal separation techniques like when measured on the casing.
- Reduction of vibration induced failure and noise in planetary gears.
- Increment in life span for planetary gears.
- Ensuring safe, smooth running and productive operation of the mechanical systems where planetary gears are components e.g. wind turbine, automobile systems, helicopters etc.
- Prevention of breakdown due to planetary gear vibration in mechanical systems where the planetary gear train is one of the components and reduction in maintenance cost of the system.
- If vibration is reduced to a certain acceptable limit, noise which can cause passengers' discomfort (for example in a vehicle or aircraft) would also be reduced.

The next chapter will focus on review of relevant and applicable literature to gather more useful information for the study. This will also help to identify knowledge gaps.

Chapter 2 Literature Review

There are some existing analytical models for planetary gears, where for vibration control only passive modification was considered after determining the natural frequencies and mode shapes. Publications covering active methods of control for these systems are scarce. This literature review mainly covers the dynamic modelling, vibration measurement, principal component analysis and vibration control of planetary gear system.

2.1 Dynamic modelling using linear models

The reason for dynamic modelling of planetary gear system depends on whether the aim of modelling would be noise reduction or vibration control. In the 1920s and early 1930s, effort was made to determine the dynamic load on gear teeth by both dynamic analysis (i.e. mathematical modelling) and experiments [16]. Lumped parameter systems were adopted for most of the dynamic models at the time. The meshing gear teeth have stiffness without mass, while the masses i.e. the gears are considered to be rigid.

Kahraman [17] proposed a simplified purely torsional model of a single stage planetary gear system where he derived closed form expressions for the torsional natural frequencies. He stated that the expression may be a useful tool in designing planetary gear systems. The natural modes from the simplified torsional model were compared with predictions from a more complicated transverse-torsional model. He stated that a pure torsional model can be used in many practical situations to predict the natural frequencies of a planetary gear train as required by gear designers. In the case of a transverse- torsional model, he stated that a more general and accurate means of modelling gear sets can be achieved.

Kharaman [18] also developed a three dimensional model of a single-stage planetary gear train with helical gears. The dynamic model takes into consideration the six rigid body motions of the ring, sun, planet gears and the carrier. The generic nature of the formulation permits any number of planet gears to be analysed such that they can be equally or unequally spaced around the sun gear. The natural modes are obtained by solving a derived linear time-invariant equation of motion. The model was also used to determine the forced vibration response, considering a static transmission error as external disturbance. The effect of planet mesh phasing on the dynamic behaviour of a four-planet model was described using such a model.

Analytical models of planetary gear with equally spaced planets were developed and used to determine the eigensolutions, which characterise the unique behaviour of the system for the linear

time-invariant case [14]. Three degrees of freedom (radial, tangential and rotational co-ordinates) rigid body models were adopted in the two dimensional plane. A rotating coordinate system attached to the centre of the carrier was used for the analysis with an assumption that the bearing stiffnesses are isotropic. The model includes some key factors (i.e. time-varying stiffness and Coriolis terms) which may affect the vibration of the planetary gears. Free vibration was considered neglecting the Coriolis terms and the vibration modes were classified into translational, rotational and planet modes (where for the latter only the planets are moving) [14]. The free vibration response obtained was as a result of the equal spaces between the planet gears. In this case, six natural frequencies have a multiplicity of one for the rotational mode in which there is no translation of the centre members (carrier, ring and sun gears). There are another six natural frequencies with multiplicity of two for the translational mode, where there is no rotation of the centre members while the natural frequencies with multiplicity of three were associated with planet mode, where only the planet gears are moving.

Removing the restriction of equal spaces between the planets, the dynamic response of planetary gears with unequal spaces were investigated by Lin and Parker [19].They discovered that the response of the planetary gear system with equally spaced planet gears was different from that of unequally spaced planet gears because of the loss in the cyclic symmetry. In this case, the planet mode, as described earlier, does not change as a result of the change of location of the planet gears. In the case of rotational modes, there is a coupling between the rotational and translational modes; therefore, the unique properties of the mode cannot be identified. The translational mode lost its degenerate form because of the loss of cyclic symmetry in the system.

The simple and single stage model used by Lin and Parker in [14] was extended to a compound and multi-stage planetary gear model. The natural frequencies and the normal modes obtained in this extended model show that the structure of the vibration modes are the same as in the previous model, which has equally spaced planets, and it also retains this well-defined structure for diametrically opposed planets [20].

Lin and Parker [21] investigated the parametric instability in planetary gears where the mesh stiffness of the teeth varies with time. The model used for this investigation is the same as the one used in [14] only that the translational coordinates were ignored. The analysis revealed that parametric instabilities occur as a result of the closeness in the values of the harmonics of the mesh frequency and particular combination of natural frequencies of the planetary gear. General expressions were derived, which permit the reduction of particular parametric instabilities by careful selection of design parameters like the gear ratio and mesh phasing.

The sensitivities of the planetary gear natural frequencies and modes of vibration to some design parameters (like component masses, mesh stiffnesses, operating speed and second moment of masses) were studied by Lin and Parker [22]. Their research considered both the planetary gears that are symmetrical (i.e. cyclically tuned) and unsymmetrical (which are not tuned). Considering the tuned planet arrangements, the sensitivity of the natural frequency to the operating speed was determined in order to know the contribution of Gyroscopic effect. It was discovered that the natural frequencies of the rotational and planet modes are not sensitive to the operating speed, while the sensitivity of the natural frequency of the translational mode to the operating speed increases with the inertia of the component and decreases with the stiffness of the system. Also, rotational modes do not depend on the transverse support stiffnesses and masses of the centre gears and carrier. Translational modes likewise do not depend on the torsional support stiffnesses and inertia of the centre gears and the carrier.

Chaari et al. [23] developed a mathematical model using a fixed frame of reference which took into account the driving unit (torque of the motor), transmission and load. They were included in the model because of some applications like wind turbines where variable loads leads to variations in the transmission speed and eventually the mesh frequency. The dynamic response was computed and it shows a relationship between the level of the vibration amplitude and load magnitude; as the load increases, the level of vibration increases. The study is mainly applicable in modelling of wind turbines which operates under a highly non-stationary condition.

An additional feature present in planetary gears can be due to friction effects in the teeth meshing or indexing errors. These have been considered previously for spur gears. Howard et al. [24] presented a method by which a sliding frictional force can be incorporated in between the meshing teeth of a dynamic model of a meshing spur gear and this was reflected in the equation of motion. The aim was to determine the effect of friction on the resultant vibration of the gear case. It was shown in the study that the inclusion of frictional forces in the model resulted in additional six degrees of freedom which are perpendicular to the pressure line. They also used Finite Element Analysis (FEA) to model the tooth stiffness in order to determine the variation of the mesh stiffness to tooth crack. It was stated that a crack decreases the stiffness of the tooth, therefore the speed of the input shaft fluctuates (i.e. increasing and decreasing) because the other teeth have not experienced cracking.

Inapolat et al. used a transverse-torsional model to investigate the effect of indexing errors (i.e. deviation of any tooth flank from its theoretical position with respect to reference tooth flank) on the dynamic response of spur gear [25]. In this case, a long-period quasi-static transmission error caused by indexing error was considered to be the source of primary excitation. Two cases were investigated

for gears having deterministic and stochastic indexing errors. The dynamic responses of the gear pair for the two cases were compared thereafter to that of spur gear pair with negligible indexing errors. It was concluded that the deterministic indexing errors increase the dynamic response of a gear during a limited number of mesh cycles while the stochastic indexing errors show a larger broadband response.

2.2 Dynamic modelling using nonlinear models

Modelling and analysis was carried out by Parker and Guo [26] for a planetary gear set with tooth wedging (also known as tight meshing of the teeth mainly caused by gravity and bearing clearance nonlinearity) in order to determine its response. The planet bearing forces in relation with the nonlinear behaviour of tooth wedging were analysed. It was concluded that tooth wedging, which can cause bearing failure, increases the bearing forces in the planetary gears and also destroys the load sharing characteristics among the planets. It was also concluded that the phenomenon of tooth wedging may be likely to occur in planetary gears which have heavy elements.

Nonlinear dynamic response of a planetary gear was investigated by Guo and Parker [27] with a lumped parameter model which was developed considering bearing clearance, variation in the gear mesh stiffness and teeth separation. The forced dynamic response was determined by a harmonic balance method with arc length continuation and the stability was analysed by Floquent theory. It was concluded that the input torque can be used to reduce partially some of the nonlinear occurrences, such as jumps which are nonlinear, hardening effect arising from changes from bearing non-contact to contact and softening effect due to teeth separation as a result of the bearing clearance.

Farshad et al., [28] present a brute-force optimization method on the tip relief, which is a tooth profile modification in order to reduce vibration of the planetary gear. A nonlinear dynamic model was used for the investigation and optimal radius and amplitude were determined after determining a number of possible solutions. The method presented was said to be useful in reducing chaotic vibration in planetary gear systems.

Bahk et al. [29] investigated the nonlinear dynamic behaviour of planetary gears with equally spaced planets, using analytical and numerical methods over a range of frequency. Perturbation analysis was used to determine the closed-form approximate solution of the dynamic response. The analytical solution revealed that the tooth separation, which causes nonlinear occurrences such as jump phenomena and subharmonic resonance, occurs even when the torque is large. The solution obtained from the perturbation analysis were confirmed by the harmonic balance method with arc-length continuation, while the finite element and numerical integration simulations were used to validate the results obtained from the perturbation analysis and harmonic balance method.

Kharaman [30] investigated load sharing characteristics of planetary gear transmission using a nonlinear-time varying lumped parameter model, which can incorporate an arbitrary number of planets. The model developed can accommodate problems like manufacturing errors and parametric excitation due to multiple variations in the mesh stiffness. The dynamic load sharing factor (which is the ratio of the actual dynamic load to the ideal static load) was predicted using the model and the effect of manufacturing error like pinion run-out error on the dynamic load sharing factor was identified.

2.3 Finite Element Modelling

The effectiveness of planet phasing on vibration reduction at some harmonics of the tooth mesh frequency was examined by Parker et al. [11]. For this method a dynamic finite element and contact mechanics simulation model was used to demonstrate the phasing phenomena considering the systems with equally spaced planets and unequally spaced planets as well as diametrically opposed planets. It was concluded that there were reductions in some particular resonances due to a coincidence between the natural frequency and some harmonics of the mesh frequency.

The vibration behaviour of a high-speed planetary gear system was studied by Zhaoxia et al. [31].The study considered the parameters like bearing support stiffness and mesh stiffness as well as the effect of mass eccentricity on the planetary gear system. Also, they derived formulae to determine the modal kinetic and strain energies for different modes of vibration at their corresponding frequencies. The kinetic energy calculated was a parameter used to determine the effect of the mass properties on different frequencies. It was concluded that for the rotational mode, the bearing support stiffness has a negligible effect on the centre gears (i.e. carrier, ring and sun gears) and their masses do not have an effect on the mode shapes. For the translational mode, the moment of inertia of the centre gear is insignificant.

The nonlinear dynamic behaviour of a pair of spur gears was obtained by a combination of finite element and contact mechanics analyses over a wide range of operating speed and torque [32]. The mesh forces were calculated by contact analysis at each step of time when the meshing gears are rotating. In this case it is no longer necessary to assume that the sources of external excitation may be parametric excitation and static transmission error or one of them. Two models each comprising a single degree of freedom were studied, the results obtained from one of the models show good agreement with the results obtained from the finite element analysis while the other does not show a good comparison with the experiments. The source of the nonlinear behaviour was stated to be a loss of contact of the meshing teeth.

The effect of errors due to manufacturing of planetary gears was characterised by Cheon and Parker by performing a dynamic analysis using a hybrid finite element method [33]. Errors in the centre gears and carrier were considered as well as their effects on the critical stress on the tooth, bearing forces and load sharing ability. The parameters considered are tooth thickness, run-out error and position error, because they are very common in the manufacturing of gear systems with respect to tolerance control. The most important error that affects the dynamic characteristics like critical stress on the tooth, bearing forces and load sharing capability were discovered to be the indexing error for the planet assembly and run-out error for the planets.

2.4 Theoretical and experimental planetary gear vibration frequency analysis

An understanding of planetary gear vibration spectra is very important and useful to detect any fault in the system. The measured vibration spectra from a planetary gearbox is more complicated than that of a parallel axis gear box [34] . For instance, a symmetric or asymmetric modulation sideband can be seen in the vibration spectra of a planetary gear due to the carrier rotation but it is not common in the measured response of a parallel axis gear [35].

The explanation of the cause of the asymmetry in the modulation sidebands for planetary gear mesh vibrations was given by McFadden and Smith [36]. Sidebands are seen in the planetary gear vibration spectra because of the movement of planet gears and it occurs at the mesh frequency plus or minus the planet pass frequency. The planet pass frequency is the product of the rotational speed of the carrier and the number of planet gears in the system. In their study, they proposed a model to explain the asymmetry in the sideband with respect to the relationship between the vibrations produced by each planet gear as they move relative to the location of the accelerometer. They showed that the motion of a single planet gear past an accelerometer on a gear casing or a stationary ring gear produces a symmetrical sideband about the mesh frequency. They concluded that asymmetry in the sidebands are caused by different phases produced by different planets, because they have different phase angles relative to the first planet. They compared the predictions with measured spectra for three different epicyclic gearboxes and correct spectra were obtained.

Mosher [34] developed a planetary gear vibration model in order to explain some characteristics of the vibration spectra. The model predicts vibration at frequencies that are integer multiples of the planet spacing repetition frequency at gear mesh harmonic frequencies and their sidebands. The predictions by the model were compared to the measurements from a real helicopter transmission during flight. It shows, from the vibration measurements, that the model predicts the frequencies of

large amplitude components to the tenth gear mesh harmonic. However, the frequencies do not match around the higher gear mesh harmonics.

A wavelet transform based methodology for extracting and analysing useful features of planetary gear vibration data was suggested by Abhinav et al. [5]. The vibration data was measured from a planetary gear system present in military helicopters. They used a wavelet transform method because the common technique being used for analysis is time synchronous averaging (TSA). TSA technique is sufficient to identify faults in a fixed axis gear teeth, but will not work efficiently in identification of faults due to a cracked carrier plate. This is because TSA can average out an external disturbance, which can excite a resonance frequency, because they are not in sync with the carrier rotation. Therefore, a wavelet transform based method which can detect the transient response due to a cracked carrier plate was developed.

Inapolat and Kahraman [35] developed a mathematical model that can be used to describe the amplitude modulation (AM) vibration time history of planetary gear sets, which leads to modulation sidebands in the frequency domain. Included in the model are key parameters like the number of planet gears, planet position angle, planet phasing relationship (defined by the position angle) and the number of teeth. A wide range of planetary gear set were considered and classified into five distinct groups according to the amplitudes and frequencies of their sidebands. The five groups are equally spaced planets and in-phase gear meshes, equally spaced planets and sequentially phased gear meshes, unequally spaced planets and in-phase gear meshes, unequally spaced planets and sequentially phased gear meshes and unequally spaced planets and arbitrarily phased gear meshes. To validate the predictions, an experimental planetary gear set-up was developed and three planetary sets out of the five groups earlier described were procured. Measurements were taken from the radial acceleration of the stationary ring gear for a different rotational speeds and torque conditions. A methodology was developed to demonstrate a modulation sideband from the measured signal. There is agreement between the predicted and measured results. They concluded that sidebands are always asymmetrically distributed about the mesh orders in a sequentially phased planetary gear set. They mentioned that a maximum mesh harmonic amplitude can be seen when the planet meshes are in phase, i.e. when the ratio of the number of teeth on the ring to number of planet is equal to an integer. Also, the conclusion shows it is possible to have a symmetric sideband if the gear set is in-phase and equally spaced.

Cooley and Parker [37] investigated the geometry and frequency content of single-mode vibration of planetary gear using both a fixed and rotating frame of reference. A stationary observer measures the gear vibration by fixed displacement probes and lasers. For response seen by a rotating observer,

accelerometers or strain gauges were mounted on individual gear bodies. They showed in their conclusion that the frequency content and phase relationship of the motion in both frames of reference differ. They said there would be sideband frequencies about the natural frequencies for a stationary sensor.

Ayoub et al [38] investigated the effect of varying load and mesh stiffness on the modal properties of planetary gears. The test bench comprised identical planetary reaction gears with a free ring and a planetary test gear with a fixed ring which are driven by an electric motor. The two gear sets are connected back to back by two rigid shafts, this permits power recirculation through the transmission which improves energy efficiency. Hammer impact test were carried out and the vibrations were measured on the fixed and free ring gear at different level of loads. The external loads were applied by adding masses to the reaction gear set. The vibration signals acquired were processed with the software "LMS Test Lab signature acquisition". The natural frequencies were identified from the frequency response functions (FRF) obtained. They concluded that the natural frequencies are increasing with an increase in load. For variation in mesh stiffness, they carried out a parametric test and stated that the natural frequencies vary with mesh position.

2.5 Vibration control of planetary gears

There are some methods of vibration control that have been utilized to mitigate gear vibration. A passive method involves changing the physical properties of the system, like mesh phasing or tip relief on the teeth which have been implemented by some researchers. Seager [39] shows that some difficult harmonic component can be neutralized by suitably choosing the number of teeth. He concluded that the conditions to neutralize the mesh frequency components acting on the central members are if the ratio of the number of teeth of the sun gear to the number on the planet gear is not equal to an integer. Secondly, the source is reduced if the number of teeth on the planet gear plus or minus one divided by the number of planet gears is not an integer. The effectiveness of phasing the planet gear to reduce vibration of planetary gear was studied by Parker [11]. Planet phasing involves configuration of the planet gears, as well as choosing the number of teeth such that self-equilibration of the mesh forces lead to a reduction in the net forces and torques acting on the carrier, ring and sun gears. Phasing reduces the vibration due to some harmonics of the mesh frequency. Richards and Pines [40], presented a passive method to mitigate transmitted vibration generated by gear mesh. A periodic shaft comprising identical elements connected together was designed so as to create stop and pass band regions in the frequency spectra. Transmitted vibrations from the gear mesh to the bearing support were mitigated at various operating speeds. The effect planet mesh phasing on the overall dynamic behaviour of a four-planet model of planetary gear train was studied by Kharaman [18]. He

concluded that transmission error cannot be completely cancelled under static or dynamic conditions considering the higher harmonics excitations. Tharmakulasingam et al. [41] simulated how the transmission error will be affected by modifying the tooth profile. The result of this showed that there is a significant reduction in the transmission error in the spur gear with tooth profile modification (tip relief) compared to the spur gear without tooth profile modification. Gwande and Shaikh [4] carried out an experimental investigation in order to study the effect of planet phasing (which involved unequal spacing of the planets) of a Nylon-6 planetary gear drive on its dynamic response. The experiments were conducted on two planetary gears in configurations with and without phasing. The results shows that the dynamic response of the planetary gear with phasing was minimized compared to the one without phasing.

However, active vibration control method is more versatile than passive methods because the control force can be adjusted based on the vibration characteristics during operation. In addition, passive methods have limitations when several modes are excited. Montague et al. [42] presented a means of reducing mesh vibration in a parallel axis gear by feedforward control using piezoelectric actuators. They presented the principle of the method by an analysis of a vibrating linear system being excited by a harmonic force. The result shows a 70% reduction in the gear mesh vibration at 4500 Hz. Active vibration control method was used by Rebbechi et al. [43] to reduce gear mesh vibration using magnetostrictive actuators inside the gearbox. An adaptive feedforward controller was used to determine the required amplitude and phase of the control force applied to the shaft to reduce vibration at the feet of gearbox housing. The housing vibration was reduced at the first three harmonics of the gear mesh frequency.

2.6 Vibration source identification in gear boxes

There are few research works on vibration source identification of parallel axis and planetary gears. Among the few, there are none where the accelerometers are rotating with the gears. Vibroacoustic source identification of a parallel axis gear has been carried out by Abbassia et al [44], where they quantified the contributions from the principal sources using principal component analysis. The acceleration was measured from the casing and the principal components were analysed. They reported that the virtual coherence is a robust virtual indicator.

Radoslaw and Anna [45] investigated the spectral structure of a gearbox vibration signals using a PCA technique. The purpose of the study is to monitor the condition of the gearbox through the information obtained from the data and make decisions. For the case studies, a good and bad planetary gear were used. They found out that the two sets of data obtained using four stationary accelerometers

have different spectral structures. A correlation matrix was formed and a spectral decomposition was done to prove that the gathered data are different in their internal structure. They show that the signal with many harmonics are generated by the bad gear box with relatively high signal to noise ratio (SNR). In the case of good gearbox, they have smaller number of harmonics with suitable SNR and less sensitive to load variation. They also found out that the data set for a bad gearbox are highly correlated while the one for a good gearbox have a smaller correlation.

Qingbo et al [46] used low-dimensional principal components (PC) representations from the statistical features of the measured signals to characterize and monitor machine conditions. The PCA technique was used to extract PC representations from time and frequency domain measured signals. The capability of each PCs were evaluated using a method known as mean correlation rule (MCR). This enables selection of the PCs whose mean correlation values are larger than the pre-set threshold. The selected PC representation captures the variation of the machine health condition. Vibration signals from experiments conducted on an internal combustion engine sound and automobile gearbox were used to validate the proposed method which they claimed to be effective.

2.7 Current research study

This research focuses on dynamic modelling, analysis and comparison of a planetary gear, analysed using both fixed and rotating frames of reference. The dynamic response of planetary will be predicted and compared to the result from modal test.

2.8 Conclusions

From the past research work, it is evident that the effect of high speed of rotating frame reference attached to the carrier on the modal damping and the frequency response has not been studied numerically. Therefore, this study will consider the effect of high speed of the carrier on the modal damping and frequency response of the system.

It is also evident that vibration measurement of planetary gear components with accelerometers that can rotate with them is very rare. Therefore, it is very possible that the true vibration of this components have not been measured. A spinning test will be conducted on a customised planetary gear vibration test rig which was specially designed and constructed to accommodate wireless MEM accelerometers. The effect of load and rotational speed on the response at the natural and mesh frequencies will be considered. The PCA technique has not been used to identify the source of vibration in a planetary gear system considering the synchronised signals measured with accelerometers rotating with the system. This will be done in this study.

This research study will present the theory for pole placement applied to a planetary gear using both fixed and rotating frames of reference. The method of pole placement has not been used to control the vibration of planetary gear. This method will be employed and the optimal place to apply control force using this method is determined. The theory is an extension of that developed by Mottershead et al. [15] and the model is an extended model developed by Parker [14]. The method is based on output feedback control strategy, where the sensor and actuator can be collocated. The purpose of the pole placement is to shift the natural frequencies of the planetary gear in order to avoid resonance through displacement feedback. Active damping will also be added through velocity feedback.

Chapter 3 Dynamic modelling and analysis of a planetary gear

In order to predict the dynamic response of the planetary gear, accurate dynamic modelling and analysis must be done. This chapter focuses on the theoretical modelling and analysis of a simple planetary gear system using a model (Figure (3-1)) developed by Lin and Parker [14] as a starting point . A rotating frame of reference was originally used by Lin and Parker to develop the equation of motion of Parker's model [14]. This dynamic model can be used to investigate the dynamic behaviour of epicyclic gears in general [47].

The planetary gear model shown in Figure 3.2 will be considered for this study. Like Parker's model, this is assumed to be linear and time invariant when determining the natural frequencies and eigenvectors. Two coordinate systems, namely fixed and rotating frames of reference, will be used in the analysis. According to Friswell et al.[48] , it is easier to use a coordinate system that is not rotating, i.e. fixed frame of reference when modelling a rotor which is axisymmetric and the bearing may either be isotropic or anisotropic. In a situation where the rotor is asymmetric and the bearings are isotropic, a rotating frame of reference is more appropriate. Furthermore, if the rotor is asymmetric and the bearings are anisotropic, a standard eigenvalue problem cannot be used to determine the stability. Therefore, Floquet theory is used to determine the stability. This is because of the time varying coefficients in the equation of motion in both fixed and rotating frames of reference. This leads to parametric excitation of the system.

The mathematical model here will be developed using a fixed frame of reference first and subsequently using a rotating frame of reference attached to the centre of the carrier. The stiffness of the bearing will be assumed to be isotropic when using a rotating frame of reference and the rotating frame will be attached to the centre of the carrier. The reason for using a rotating frame of reference is to establish the effect of the carrier speed on the dynamics of the system especially at a high speed range. This should be sufficient in predicting the dynamic behaviour of the system considering free and forced responses. First and foremost after modelling, a numerical analysis will be done using parameters from Lin and Parker. To be assured that the model is working, the results obtained must be the same with their results. The natural frequencies and the vibration modes is determined considering planetary gear models with different numbers of planet gears. An investigation will be undertaken on free vibration response of a planet gear comprising two planet gears as this has not been reported in any publication. Also, the Coriolis effect on the natural frequencies of the system, because of the rotating reference frame attached to the carrier at its centre, will be shown using a Campbell diagram.

An investigation will also be done to find out if there is any difference in the natural frequencies using either a fixed or rotating frames of reference.

Subsequently, the parameters from the real physical model will be used in Chapter 5 in order to validate the results from the lumped parameter model. Free vibration response will be considered first to determine the natural frequencies and the natural vibration modes of the planetary gear train. Subsequently the model will be extended to incorporate an excitation mechanism and active vibration control strategies in Chapters 5 and 7 respectively.

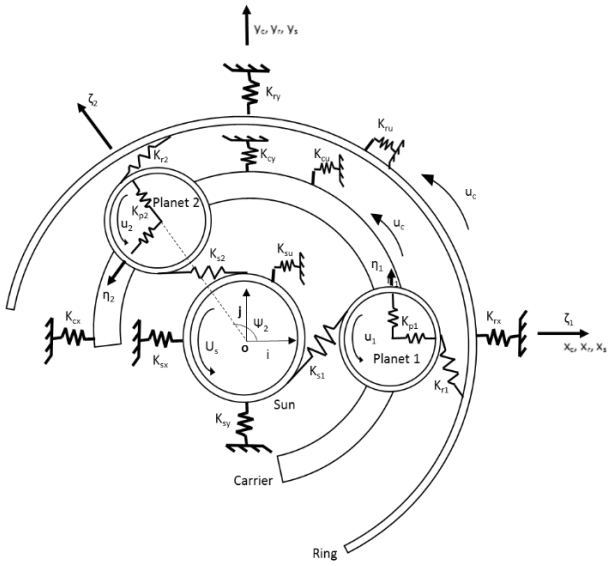

Figure 3-1 Lumped parameter model of planetary gear system and coordinates [14]

3.1 General assumptions for fixed and rotating frames of reference

The analysis focuses on vibration of planetary gear in planar motion only, i.e. in two translational coordinates as well as the rotational coordinate.

The following assumptions hold in formulating the model comprising two planet gears:

a) The main components (i.e. the carrier, ring, sun and planets) are all assumed to be rigid bodies while the connections (i.e. meshing) between sun-planet and ring-planet are represented by linear springs acting along the pressure line which is tangential to the base circle. Time-varying mesh stiffness due to the fluctuation of the number of tooth pairs in contact are ignored.
b) The bearings are assumed to be represented by two perpendicular linear springs for each gear component. They are also assumed to be isotropic when using both frames of reference.

c) The frictional forces between the meshing teeth are neglected, because the system is assumed to be well lubricated.

d) The gear is free of manufacturing, profile and other form of errors; therefore, there is no transmission error for the case of free vibration analysis.

e) The gyroscopic effect is not considered in the model, even though there is a Coriolis effect due to the carrier speed when using a rotating frame of reference.

f) The gears are rotationally symmetric about their centerline, i.e. they look the same after any angular rotation.

g) The carrier is moving at constant angular velocity for the case where a rotating frame of reference was used.

h) The two planet gears are identical and the angle between them is 180^{o}. For cases where they are more than two, they are equally spaced.

i) The natural frequencies are determined for a linear time-invariant case.

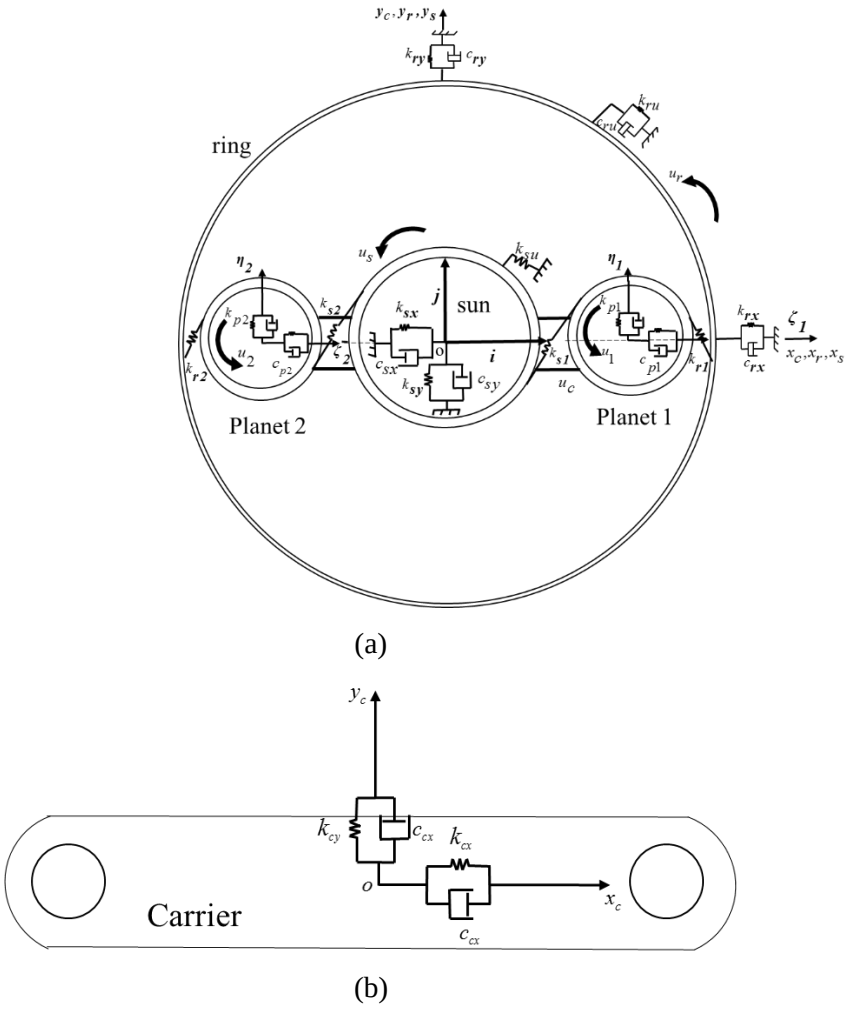

(a)

(b)

Figure 3-2 Dynamic model of planetary gears. The carrier is shown in (b) for clarity.

The extended dynamic model of the planetary gear for this study is shown in Figure 3-2. The carrier, ring, sun and planet gears coordinates x_h, y_h, $h=c,r,s$ and ζ_n, η_n, $n=1$, ….., N are with respect to the frame i,j and k, index n refers to the nth planet and N is the number of planet gears. The rotational coordinates are $u_j = r_j\theta_j$, $h=c,r,s$, 1 …, N. The stiffnesses k_{cx}, k_{rx}, k_{sx} and k_{cy}, k_{ry}, k_{sy} represent the bearing stiffnesses of the carrier, ring gear and sun gear in x and y coordinates, k_{rn} and k_{sn} are the ring-planet and sun-planet mesh stiffnesses respectively. The bearing stiffness of the planet gear is denoted by k_p . The torsional stiffness of the carrier, ring, sun and planets are denoted by k_{cu}, k_{ru}, k_{su} and k_{pu} respectively. The ring gear is assumed to be stationary, therefore its torsional stiffness is very high. The torsional stiffness of the carrier, sun and planet gears are set to zero.

3.1.1 Degrees of freedom

The degrees of freedom are defined as the number of independent generalized coordinates required to specify the configuration of a system. In this research, each component of the planetary gear has three degrees of freedom; one rotational and two translational degrees of freedom. This implies that for a carrier, ring, sun gear and three planets, the number of degrees of freedom would be eighteen.

The degrees of freedom (if one of the centre members is not absent) can be determined using the following equation [14] and [23]:

$$\text{Number of degrees of freedom} = 3(N + 3) \tag{3.1}$$

where N, is the number of planets and 3 in the brackets represent the number of central members (carrier, ring and sun) present. The figure 3 outside the bracket represents the horizontal, vertical and rotational coordinates of each component in the system.

For the model in Figures 3-2a and 3-2b, where there are 2 planets and 3 central members (carrier, ring and sun gears), the number of degrees of freedom is $3(N + 3) = 15$,

3.2 Dynamic model using a fixed frame of reference

It is very important to formulate the governing equations of motion for the planetary gear system in order to accurately predict its dynamic response. In case of linear time invariant (LTI) system like this, the natural frequencies and vibration modes of the gear in different configurations were determined using state space equations.. The dynamic equations of motion were determined using Newton's second law of motion.

3.2.1 Sun-Planet mesh model and equation of motion for the sun gear

The sun-planet mesh which was modelled by a linear spring is shown in Figure 3-3. The subscript *n* refers to the n^{th} planet. It shows the sun-planet mesh model which shows the pressure angle, α_S, (which is the angle between the pressure line AC and the common normal EF to the two gear teeth at the point of contact).

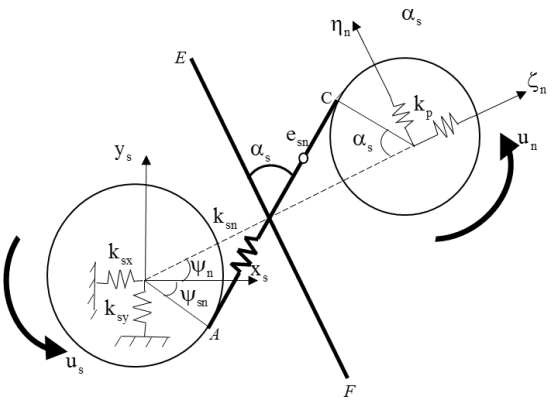

Figure 3-3 Sun and planet mesh model showing the mesh stiffness along the pressure line AC, bearing support stiffness of the sun gear and of the planet .

ψ_n is the angle showing the position of the *nth* planet gear at any point, with respect to the starting point such that $\psi_1 = 0$.

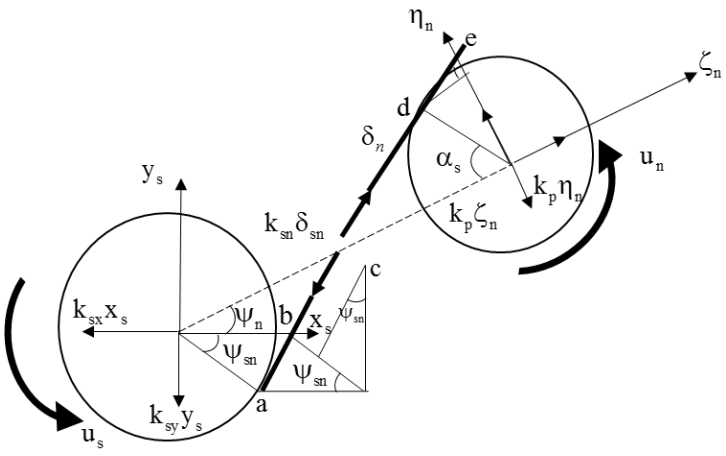

Figure 3-4 Free-body diagram of the sun-planet mesh model showing the mesh force between the sun and planet.

The free-body diagram of the sun-planet mesh model is shown in Figure 3-4, the diagram was considered in deriving the sun-planet mesh deflection δ_{sn}. From Figure 3-4, the relationship between

the position of the *nth* planet (ψ_n), sun-planet mesh angle (ψ_{sn}), and the pressure angle (α_s) can be expressed as

$\psi_n + (-\psi_{sn}) = \alpha_s$; hence

$$\psi_n - \alpha_s = \psi_{sn} \tag{3.2}$$

The deflection of the sun-planet along the pressure line is given by:

$$\delta_{sn} = y_s cos\psi_{sn} - x_s sin\psi_{sn} + u_s - \eta_n cos\alpha_s - \zeta_n sin\alpha_s + u_n + e_{sn} \tag{3.3}$$

For free vibration analysis, e_{sn} which is the transmission error between the sun-planet mesh is set to zero. The forces acting on the sun gear along the pressure line is shown in Figure 3-5.

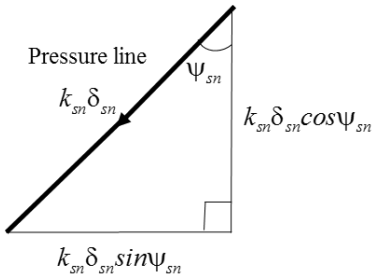

Figure 3-5 Forces acting in the sun-planet mesh which is along the pressure line.

The dynamic equations of motion for the sun gear derived from Figures 3.4 and 3.5 are

$$m_s\ddot{x}_s + c_{sx}\dot{x}_s + k_{sx}x_s - \Sigma k_{sn}\delta_{sn}sin\psi_{sn} = 0 \tag{3.4}$$

$$m_s\ddot{y}_s + c_{sy}\dot{y}_s + k_{sy}y_s + \Sigma k_{sn}\delta_{sn}cos\psi_{sn} = 0 \tag{3.5}$$

$$\frac{I_s}{r_s}\ddot{u}_s + \Sigma k_{sn}\delta_{sn} = 0 \tag{3.6}$$

The matrix form for the equations (3.4, 3.5 and 3.6) is in Appendix A.

3.2.2 Ring-planet mesh model and equation of motion for the ring gear

The planet-ring mesh can be analysed considering Figure 3-6 (a) which was magnified in Figure 3-6 (b)

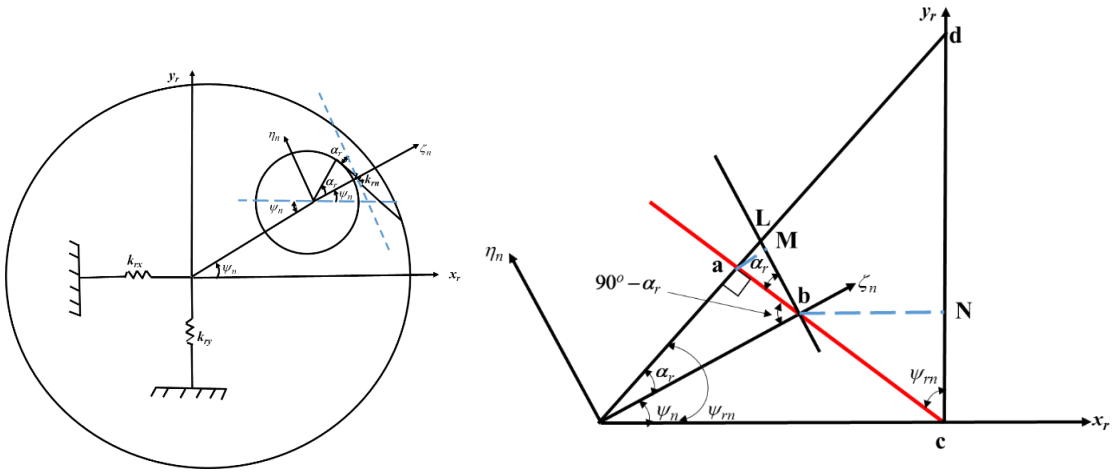

Figure 3-6 Planet and ring deflection model with the pressure line in red.

From Figure 3-6, the relationship between the position of the *nth* planet (ψ_n), ring-planet mesh angle (ψ_{rn}), and the pressure angle of the ring gear (α_r) can be expressed as

$$\psi_{rn} = \psi_n + \alpha_r \tag{3.7}$$

The mesh deflection of the planet-ring can be determined from Figures 3-6. The mesh deflection is written as:

$$\delta_{rn} = y_r cos\psi_{rn} - x_r sin\psi_{rn} + u_r - \eta_n cos\alpha_r + \zeta_n sin\alpha_r - u_n + e_{rn} \tag{3.8}$$

For free vibration analysis, e_{rn} which is the transmission error between the ring-planet mesh is set to zero. The forces acting along the pressure line as resolved are shown in Figure 3-7.

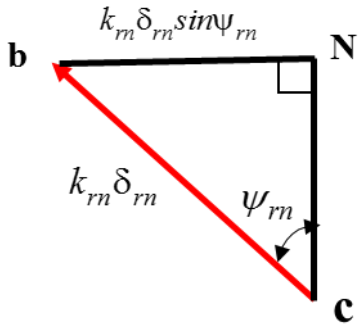

Figure 3-7 Forces acting in the planet-ring mesh along the pressure line.

The dynamic equations of motion of the ring gear are

$$m_r\ddot{x}_r + c_{rx}\dot{x}_r + k_{rx}x_r - \Sigma k_{rn}\delta_{rn}sin\psi_{rn} = 0 \tag{3.9}$$

$$m_r\ddot{y}_r + c_{ry}\dot{y}_r + k_{ry}y_r - \Sigma k_{rn}\delta_{rn}\cos\psi_{rn} = 0 \tag{3.10}$$

$$\frac{I_r}{r_r^2}\ddot{u}_r + c_{ru}\dot{u}_r + k_{ru}u_r + \Sigma k_{rn}\delta_{rn} = 0 \tag{3.11}$$

The matrix form of Equations (3.9, 3.10 and 3.11) is in Appendix A.

3.2.3 Carrier-planet bearing connection and equation of motion of the carrier

In this sub-section, a carrier will be modelled using a fixed frame of reference with translational coordinates x_c and y_c.

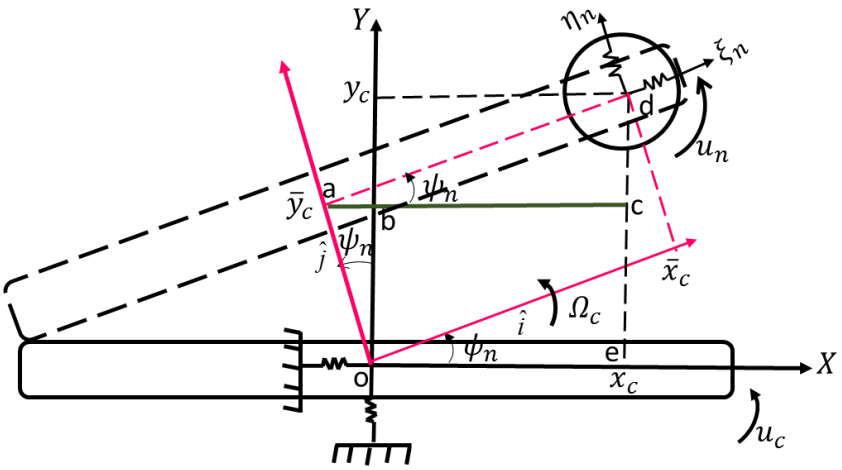

Figure 3-8 Carrier and planet bearing deflection model. The coordinates x_c and y_c are in a fixed frame of reference. The carrier is shown in dotted lines after it has moved in x, y and u coordinates.

Considering Figure 3-8, x_c and y_c are the translational coordinates of the carrier in the horizontal and vertical directions respectively. These two coordinates in a fixed frame of reference can be written in terms of rotating frame of reference as

$$x_c = ac - ab = \bar{x}_c \cos\psi_n - \bar{y}_c \sin\psi_n \tag{3.12}$$

$$y_c = ob + cd = \bar{y}_c \cos\psi_n + \bar{x}_c \sin\psi_n \tag{3.13}$$

Equations (3.12 and 3.13) can be written in matrix form as

$$\begin{Bmatrix} x_c \\ y_c \end{Bmatrix} = \begin{bmatrix} \cos\psi_n & -\sin\psi_n \\ \sin\psi_n & \cos\psi_n \end{bmatrix} \begin{Bmatrix} \bar{x}_c \\ \bar{y}_c \end{Bmatrix} \tag{3.14}$$

The matrix in Equation (3.14) is known as a transformation matrix **T.** It is orthogonal i.e. the inverse of matrix **T** is equal to its transpose. Therefore, the translational coordinates $\bar{x}_c$ and $\bar{y}_c$ (which are in rotating frame of reference) can be determined by pre-multiplying the transpose of matrix **T** with the vector on the left hand side of Equation (3.14).

The radial and tangential deflections of planet bearing can be deduced by considering Figure 3-8 and using Equations (3.12 and 3.13),

Planet bearing radial deflection: $\delta_{nr} = (\bar{x}_c \cos\psi_n - \bar{y}_c \sin\psi_n) - \zeta_n$ (3.15)

Planet bearing tangential deflection: $\delta_{nt} = (\bar{x}_c \sin\psi_n + \bar{y}_c \cos\psi_n) - \eta_n + u_c$ (3.16)

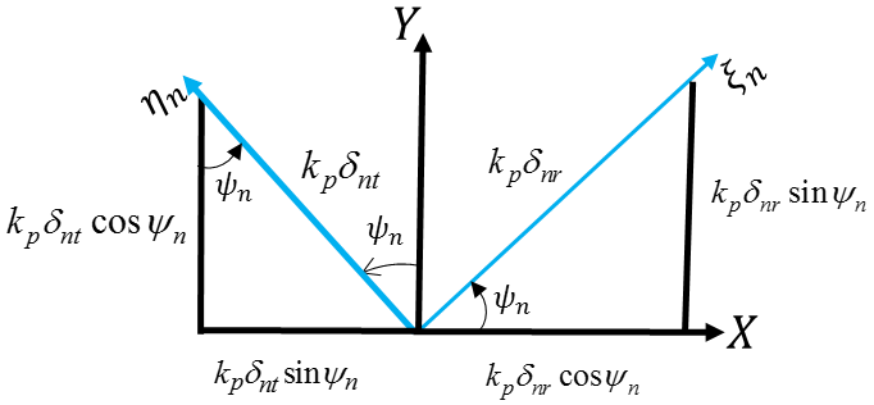

Figure 3-9 Forces acting in the carrier-planet bearing contact.

The dynamic equations of motion of the carrier considering Figures 3-8 and 3.9 is

$$m_c\ddot{x}_c + c_{cx}\dot{x}_c + k_{cx}x_c + \Sigma k_p\delta_{nr}\cos\psi_n + \Sigma k_p\delta_{nt}\sin\psi_n = 0 \tag{3.17}$$

$$m_c\ddot{y}_c + c_{cy}\dot{y}_c + k_{cy}y_c - \Sigma k_p\delta_{nr}\sin\psi_n + \Sigma k_p\delta_{nt}\cos\psi_n = 0 \tag{3.18}$$

$$\frac{I_c}{r_c^2}\ddot{u}_c + k_p\delta_{nt} = 0 \tag{3.19}$$

The matrix form of equations (3.17, 3.18 and 3.19) is in Appendix A.

3.2.4 Equation of motion for the planet gear

Considering Figures 3-8 and 3-9 which show the connection between the carrier and planet bearing as well as Figure 3-10 which shows sun-planet and planet ring meshes, the dynamic equation of motion can be formulated.

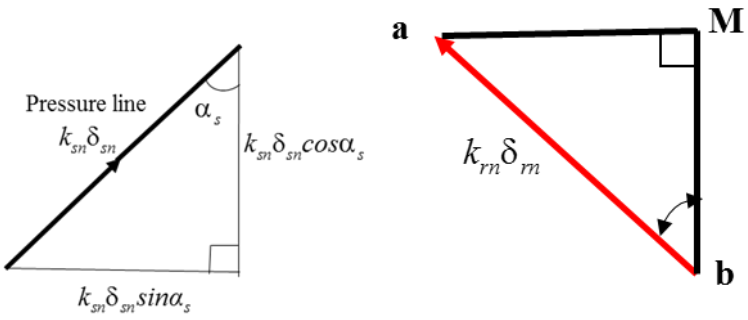

Figure 3-10 Forces acting in the sun-planet and planet-ring mesh along the pressure line.

The dynamic equation of motion of the planetary gear is

$$m_p\ddot{\zeta}_n - k_p\delta_{nr} - \Sigma k_{sn}\delta_{sn}\sin\alpha_s + \Sigma k_{rn}\delta_{rn}\sin\alpha_r = 0 \tag{3.20}$$

$$m_p\ddot{\eta}_n - k_p\delta_{nt} - \Sigma k_{sn}\delta_{sn}\cos\alpha_s - \Sigma k_{rn}\delta_{rn}\cos\alpha_r = 0 \tag{3.21}$$

$$\frac{I_p}{r_p^2}\ddot{u}_n + \Sigma k_{sn}\delta_{sn} - \Sigma k_{rn}\delta_{rn} = 0 \tag{3.22}$$

The matrix form of equations (3.20, 3.21 and 3.22) can be found in Appendix A.

3.2.5 General form of equation of motion using a fixed frame of reference

The equation of motion for the carrier, ring, sun and planet gears have been obtained using a fixed frame of reference. The general form of the equation in matrix form can be written as

$$[\mathbf{M}]\{\ddot{\mathbf{q}}\} + [\mathbf{C}_b]\{\dot{\mathbf{q}}\} + ([\mathbf{K}_b] + [\mathbf{K}_m])\{\mathbf{q}\} = \{\mathbf{0}\} \tag{3.23}$$

where, $\mathbf{M}, \mathbf{C}_b, \mathbf{K}_b \in \Re^{n\times n}$; $\mathbf{M} = \mathbf{M}^T, \mathbf{C}_b = \mathbf{C}_b^T, \mathbf{K}_b = \mathbf{K}_b^T, \mathbf{K}_m = \mathbf{K}_m^T$ are the mass, damping, bearing and mesh stiffnesses respectively. Although two planet gears are shown in Figure 3-2, the equation of motion can be used for a planetary gear with more than two planet gears. In practice, using a fixed frame of reference implies that the accelerometers are not rotating with the components when measuring their vibrations. The next section focuses on the analysis and derivation of the equation of motion using a rotating frame of reference.

3.3 Dynamic model using a rotating frame of reference

In this section, the modelling will be done using a rotating frame of reference and carrier will be the reference. This implies that in practice, the carrier and the accelerometer will be rotating together at the same speed when taking the vibration measurement. Experiment on this rotating frame of reference will be discussed extensively in Chapter 6. The equation of motion in this case will be different from that of fixed frame of reference because of Coriolis and centripetal accelerations terms that are added. The Coriolis effect is defined as the deviation from the actual path as seen by the accelerometer fixed at the centre of the rotating carrier as shown in Figure 3-11. It shows a rotating system which is rotating in a counter clockwise direction, the path of motion seen by a rotating accelerometer on a rotating frame of reference (red line) is the green line in a clockwise direction.

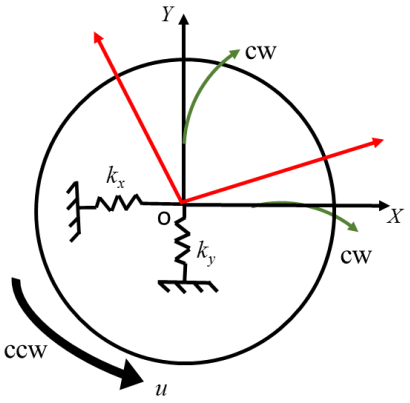

Figure 3-11 Coriolis effect on a rotating system.

3.3.1 Relative motion of components using a rotating frame of reference

In order to analyse dynamics of the gears, the effect of using a rotating frame of reference will be considered. The position of points A and B are defined by the position vectors $\vec{r}_A$ and $\vec{r}_B$ measured with respect to the fixed ***X, Y, Z*** coordinate system shown in Figure 3-12. The origin of the translating and rotating ***x, y, z*** coordinate system is the point A. The relative position of B with respect to A is defined by the vector $\vec{r}_{B/A}$.

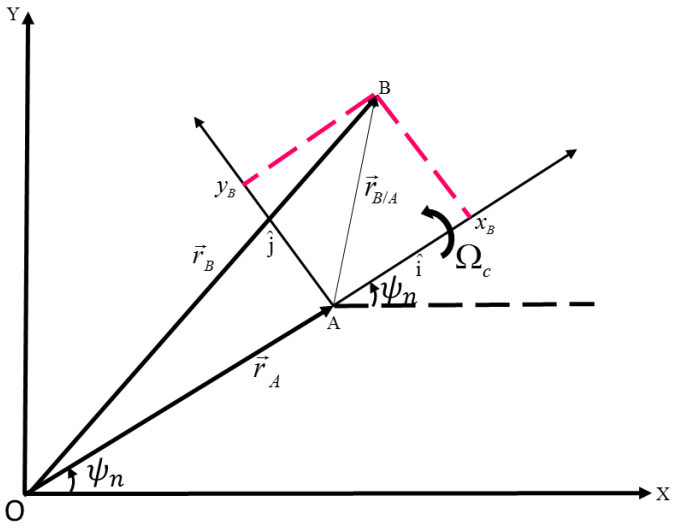

Figure 3-12 Kinematic diagram for rotating frame, Ωc denotes the angular speed of the frame.

Consider Figure 3-12, OA rotates with constant angular speed of Ω_c and it is translating and rotating with respect to fixed XYZ coordinate system with origin O. From Figure 3-12,

$$\vec{r}_B = \vec{r}_A + \vec{r}_{B/A} \tag{3.24}$$

$$\vec{r}_B = \vec{r}_A + x_B\hat{i} + y_B\hat{j} \tag{3.25}$$

For the case of planetary gear modelling and mathematical analysis, the features in Figure 3-12 changes to Figure 3-13. In this case, the position of point A, i.e. the position of the carrier is at the origin O, hence $\vec{r}_A$ becomes zero. This is equivalent to using the centre of mass of the carrier as the origin. The carrier serves as an observer (or a reference) and the translational coordinates x_h and y_h of the carrier, ring, sun and planet gears can be measured with respect to a rotating frame of reference attached to the centre of the carrier.

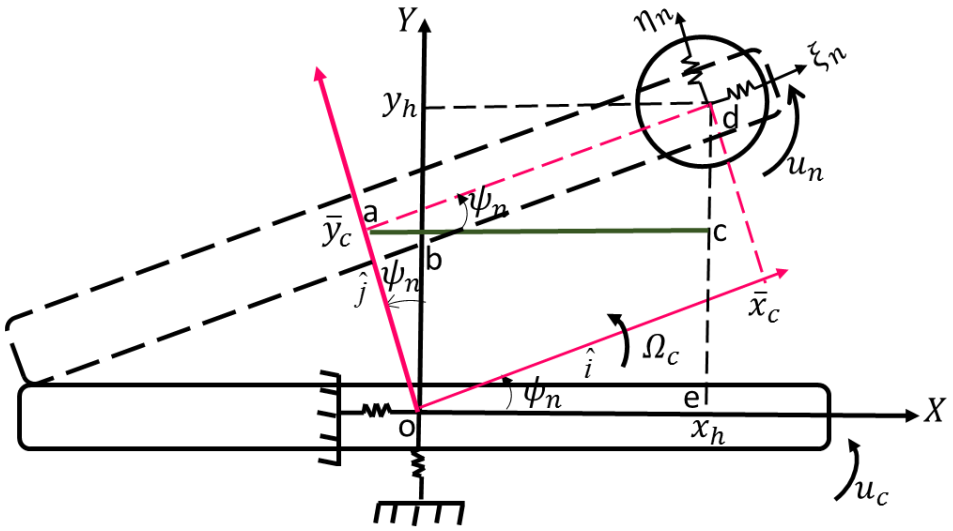

Figure 3-13 Kinematic diagram showing the rotating frame of reference (in pink) fixed to the centre of mass of the carrier at origin O. The carrier is shown in dotted lines after it has moved in x, y and u coordinates.

In Figure 3-13, it is shown that point A in Figure 3-12 is now at the origin O which is the centre of the rotating frame of reference. In this case,

$\vec{r}_A = 0$, therefore Equation (3.25) becomes

$$\vec{r}_B = x_B\hat{i} + y_B\hat{j} \tag{3.26}$$

Then, $\vec{r}_h = x_h\hat{i} + y_h\hat{j}$ (3.27)

where $h = c, r, s$ while $\hat{i}$ and $\hat{j}$ are the unit vectors in x and y directions respectively. It is very important to show the time derivative of the unit vectors before determining the relative velocity and acceleration vectors in rotating frame of reference using Figure 3-14.

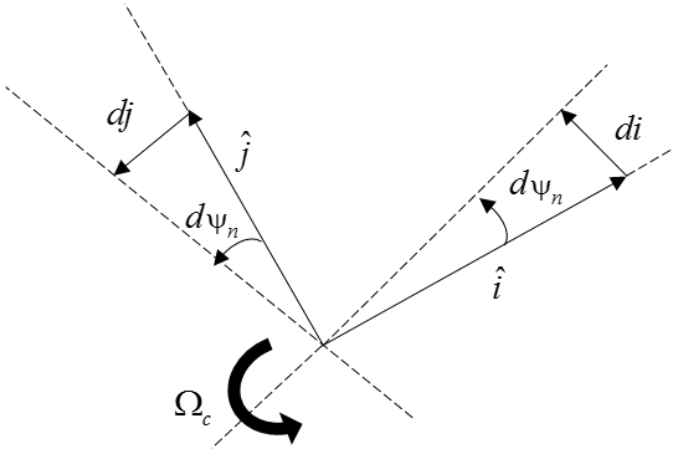

Figure 3-14 Rate of change of unit vectors with respect to time.

$$d\hat{i} = d\psi_n \hat{j} \tag{3.28}$$

$$\frac{d\hat{i}}{dt} = \frac{d\psi_n}{dt}\hat{j} = \Omega_c \hat{j} \tag{3.29}$$

$$d\hat{j} = -d\psi_n \hat{i} \tag{3.30}$$

$$\frac{d\hat{j}}{dt} = -\frac{d\psi_n}{dt}\hat{i} = -\Omega_c \hat{i} \tag{3.31}$$

Differentiating equations (3.27), we obtain equations (3.32)

$$\dot{\bar{r}}_h = \frac{d}{dt}(x_h \hat{i} + y_h \hat{j}) = (\dot{\bar{x}}_h - \Omega_c \bar{y}_h)\hat{i} + (\dot{\bar{y}}_h + \Omega_c \bar{x}_h)\hat{j} \tag{3.32}$$

Differentiating Equation. 3.32, we obtain the acceleration vector using a rotating frames of reference as follows:

$$\ddot{\bar{r}}_h = \frac{d}{dt}[(\dot{\bar{x}}_h - \Omega_c \bar{y}_h)\hat{i} + (\dot{\bar{y}}_h + \Omega_c \bar{x}_h)\hat{j}] = (\ddot{x}_h - 2\Omega_c \dot{y}_h - \Omega_c^2 x_h)\hat{i} + (\ddot{y}_h + 2\Omega_c \dot{x}_h - \Omega_c^2 y_h)\hat{j} \tag{3.33}$$

Equations (3.27), (3.32) and (3.33) show that the position, velocity and acceleration vectors using a rotating frames of reference respectively. They will be included in the equation of motion of the carrier, ring, sun and planet gears using a rotating frame of reference. The terms $(\dot{\Omega}_c x_h)\hat{i}$ and $(\dot{\Omega}_c y_h)\hat{j}$ which are not shown in Equation (3.33) because they are equal to zero, because it was assumed that the carrier is moving at a constant angular velocity. This is equivalent to having the tangential angular acceleration $\dot{\Omega}_c$ of the carrier equal to zero. The terms $(2\Omega_c \dot{y}_h)\hat{i}$ and $(2\Omega_c \dot{x}_h)\hat{j}$ in equation (3.33) are the Coriolis accelerations at the horizontal and vertical directions respectively due to the rotating frame of reference. The terms $(\Omega_c^2 x)\hat{i}$ and $(\Omega_c^2 y)\hat{j}$ are the centripetal accelerations at the horizontal and vertical directions respectively.

3.3.2 Dynamic equation of motion of sun gear using a rotating frame of reference

The dynamic equation of a sun gear using a rotating frame of reference is

$$\bar{m}_s(\ddot{\bar{x}}_s - 2\Omega_c \dot{\bar{y}}_s - \Omega_c^2 \bar{x}_s) + \bar{c}_{sx}(\dot{\bar{x}}_s - \Omega_c \bar{y}_s) + \bar{k}_{sx}\bar{x}_s - \Sigma k_{sn}\delta_{sn}\sin\psi_{sn} = 0 \quad (3.34)$$

$$\bar{m}_s(\ddot{\bar{y}}_s + 2\Omega_c \dot{\bar{x}}_s - \Omega_c^2 \bar{y}_s) + \bar{c}_{sy}(\dot{\bar{y}}_s + \Omega_c \bar{x}_s) + \bar{k}_{sy}\bar{y}_s + \Sigma k_{sn}\delta_{sn}\cos\psi_{sn} = 0 \quad (3.35)$$

$$\frac{I_s}{r_s^2}\ddot{\bar{u}}_s + \Sigma k_{sn}\delta_{sn} = 0 \quad (3.36)$$

The matrix form of equations (3.34, 3.35 and 3.36) for the sun gear using a rotating frame of reference is in Appendix A.

3.3.3 Dynamic equation of motion of ring gear using a rotating frame of reference

The dynamic equation of a ring gear using a rotating frame of reference is

$$\bar{m}_r(\ddot{\bar{x}}_r - 2\Omega_c \dot{\bar{y}}_r - \Omega_c^2 \bar{x}_r) + \bar{c}_{rx}(\dot{\bar{x}}_r - \Omega_c \bar{y}_r) + \bar{k}_{rx}\bar{x}_r - \Sigma k_{rn}\delta_{rn}\sin\psi_{rn} = 0 \quad (3.37)$$

$$\bar{m}_r(\ddot{\bar{y}}_r + 2\Omega_c \dot{\bar{x}}_r - \Omega_c^2 \bar{y}_r) + \bar{c}_{ry}(\dot{\bar{y}}_r + \Omega_c \bar{x}_r) + \bar{k}_{ry}\bar{y}_r - \Sigma k_{rn}\delta_{rn}\cos\psi_{rn} = 0 \quad (3.38)$$

$$\frac{I_r}{r_r^2}\ddot{\bar{u}}_r + \bar{c}_{ru}\dot{\bar{u}}_r + \bar{k}_{ru}\bar{u}_r + \Sigma k_{rn}\delta_{rn} = 0 \quad (3.39)$$

The matrix form of Equations (3.37, 3.38, and 3.39) for the ring gear using a rotating frame of reference is in Appendix A.

3.3.4 Dynamic equation of motion of carrier using a rotating frame of reference

Consider Figure 3-13, which shows a carrier and planet bearing deflection model. The translational coordinates $\bar{x}_c$ and $\bar{y}_c$ are in rotating frame of reference rotating at the carrier speed Ω_c because a rotating frame of reference rotating at the carrier speed was fixed to the carrier at its origin O. The two translational coordinates using a rotating frame of reference can be written as

$$\bar{x}_c = x_c \cos\psi_n + y_c \sin\psi_n \tag{3.40}$$

$$\bar{y}_c = -x_c \sin\psi_n + y_c \cos\psi_n \tag{3.41}$$

The combination of equations (3.40) and (3.41) in matrix form is the inverse of equation (3.14). Hence the radial and tangential deflection of the bearing can be written as

$$\bar{\delta}_{nr} = (x_c \cos\psi_n + y_c \sin\psi_n) - \zeta_n \tag{3.42}$$

$$\bar{\delta}_{nt} = (-x_c \sin\psi_n + y_c \cos\psi_n) - \eta_n + u_c \tag{3.43}$$

where $\bar{\delta}_{nr}$ and $\bar{\delta}_{nt}$ are the planet bearing radial and tangential deflections respectively.

The dynamic equation of carrier using a rotating frame of reference is then

$$\bar{m}_c(\ddot{\bar{x}}_c - 2\Omega_c\dot{\bar{y}}_c - \Omega_c^2\bar{x}_c) + \bar{c}_{cx}(\dot{\bar{x}}_c - \Omega_c\bar{y}_c) + \bar{k}_{cx}\bar{x}_c - \Sigma k_p\delta_{nr}\cos\psi_n + \Sigma k_p\delta_{nt}\sin\psi_n = 0 \tag{3.44}$$

$$\bar{m}_c(\ddot{\bar{y}}_c + 2\Omega_c\dot{\bar{x}}_c - \Omega_c^2\bar{y}_c) + \bar{c}_{cy}(\dot{\bar{y}}_c + \Omega_c\bar{x}_c) + \bar{k}_{cy}\bar{y}_c + \Sigma k_p\delta_{nr}\sin\psi_n + \Sigma k_p\delta_{nt}\cos\psi_n = 0 \tag{3.45}$$

$$\frac{I_c}{r_c^2}\ddot{\bar{u}}_c + k_p\delta_{nt} = 0 \tag{3.46}$$

The matrix form of Equations (3.44, 3.45, and 3.46) for the carrier using a rotating frame of reference is in Appendix A.

3.3.5 Dynamic equation of motion of planet gear using a rotating frame of reference

The dynamic equation of planet gear using a rotating frame of reference is

$$\bar{m}_p(\ddot{\bar{\zeta}}_n - 2\Omega_c\dot{\bar{\eta}}_n - \Omega_c^2\bar{\zeta}_n) - k_p\delta_{nr} - \Sigma k_{sn}\delta_{sn}\sin\alpha_s + \Sigma k_{rn}\delta_{rn}\sin\alpha_r = 0 \tag{3.47}$$

$$\bar{m}_p(\ddot{\bar{\eta}}_n + 2\Omega_c\dot{\bar{\zeta}}_n - \Omega_c^2\bar{\eta}_n) - k_p\delta_{nt} - \Sigma k_{sn}\delta_{sn}\cos\alpha_s - \Sigma k_{rn}\delta_{rn}\cos\alpha_r = 0 \tag{3.48}$$

$$\frac{I_p}{r_p^2}\ddot{\bar{u}}_n + \Sigma k_{sn}\delta_{sn} - \Sigma k_{rn}\delta_{rn} = 0 \qquad (3.49)$$

The matrix form of equatons (3.47, 3.48 and 3.49) for the planet gear using a rotating frame of reference is in Appendix A.

3.3.6 General form of equation of motion using a rotating frame of reference

The combined equation of motion for the carrier, ring, sun and planet gears is thus obtained using a rotating frame of reference. The general form of the equation in matrix form can be written as

$$\left[\bar{\mathbf{M}}\right]\{\ddot{\bar{\mathbf{q}}}\} + \left(\Omega_c\left[\mathbf{G}_y\right] + \left[\bar{\mathbf{C}}_b\right]\right)\{\dot{\bar{\mathbf{q}}}\} + \left(\left[\bar{\mathbf{K}}_b\right] + \left[\mathbf{K}_m\right] + \Omega_c\left[\mathbf{K}_d\right] - \Omega_c^2\left[\mathbf{K}_\Omega\right]\right)\{\bar{\mathbf{q}}\} = \{\mathbf{0}\} \qquad (3.50)$$

where, $\bar{\mathbf{M}}, \bar{\mathbf{C}}_b, \bar{\mathbf{K}}_b, \bar{\mathbf{K}}_m \in \Re^{n\times n}$; $\bar{\mathbf{M}} = \bar{\mathbf{M}}^T, \bar{\mathbf{C}}_b = \bar{\mathbf{C}}_b^T, \bar{\mathbf{K}}_b = \mathbf{K}_b^T, \bar{\mathbf{K}}_m = \mathbf{K}_m^T$, are the mass, damping, bearing and mesh stiffnesses respectively. Also, some terms are introduced in this frame of reference and their matrices due to Coriolis effect of the carrier and these are the $\mathbf{G}_y$, $\mathbf{K}_d$ and $\mathbf{K}_\Omega$; $\mathbf{G_y}$ and $\mathbf{K_d}$ matrices are skew-symmetric while $\mathbf{K}_\Omega = \mathbf{K}_\Omega^T$. In practice, using a rotating frame of reference implies that the practical vibration measurements, such as using surface mounted accelerometers, are rotating with the components.

3.4 Numerical study using the analytical model

3.4.1 Natural frequencies in a rotating frame of reference and their relationship with the fixed frame of reference characteristics

For simplicity, the natural frequencies of a sun gear using a rotating frame of reference and their relationship with the fixed frame of reference was investigated. The axisymmetric sun gear of mass m_s only shown in Figure 3-15 will be used as a case study. It is assumed that the sun gear with isotropic support stiffness (i.e. $k_{sx} = k_{sy} = k_s$) has two degrees of freedom namely in the *x* and *y* directions. This is a case whereby a single mass has two degrees of freedom. The rotating frame is attached to the centre of the sun gear rotating at a constant speed Ω_s as shown in Figure 3-15.

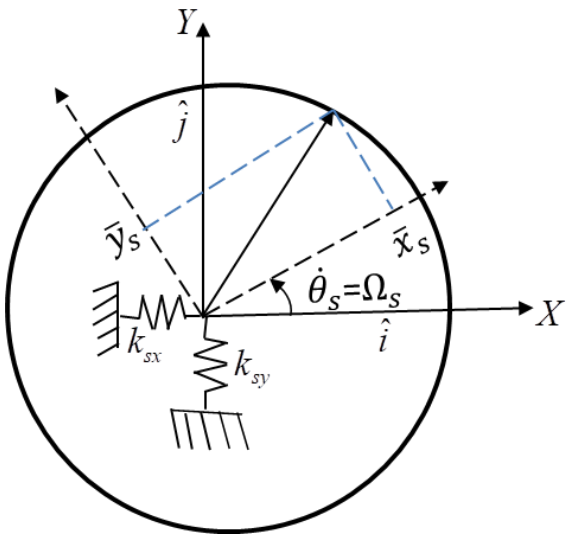

Figure 3-15 Sun gear modelling using a rotating frame of reference

The equations of motion for the undamped and free vibration case in the rotating frame of reference is written as

$$m_s(\ddot{\bar{x}}_s - 2\Omega_s\dot{\bar{y}}_s - \Omega_s^2\bar{x}_s) + k_s\bar{x}_s = 0 \tag{3.51}$$

$$m_s(\ddot{\bar{y}}_s + 2\Omega_s\dot{\bar{x}}_s - \Omega_s^2\bar{y}_s) + k_s\bar{y}_s = 0 \tag{3.52}$$

The overbar relates to the rotating coordinate displacement of the mass centre. The uncoupled equations in the fixed frame of reference with the (x, y) displacements are transformed into a rotating frame of reference with the ($\bar{x}_s, \bar{y}_s$) displacements.

In general, equations (3.51 and 3.52) can be written as

$$\mathbf{M}_s\ddot{\bar{\boldsymbol{q}}}_s + \Omega_s 2\mathbf{M}_s\dot{\bar{\boldsymbol{q}}}_s + (\mathbf{K}_s - \Omega_s^2\mathbf{M}_s)\bar{\boldsymbol{q}}_s = \mathbf{0} \tag{3.53}$$

The $\Omega_s 2\mathbf{M}_s$ and $-\Omega_s^2\mathbf{M}_s$ terms in equation (3.53) are the Coriolis and centripetal accelerations terms respectively.

From equations (3.51) and (3.52)

$$\begin{bmatrix} m_s & 0 \\ 0 & m_s \end{bmatrix}\begin{pmatrix} \ddot{\bar{x}}_s \\ \ddot{\bar{y}}_s \end{pmatrix} + \Omega_s \begin{bmatrix} 0 & -2m_s \\ 2m_s & 0 \end{bmatrix}\begin{pmatrix} \dot{\bar{x}}_s \\ \dot{\bar{y}}_s \end{pmatrix} + \begin{bmatrix} k_s - \Omega_s^2 m_s & 0 \\ 0 & k_s - \Omega_s^2 m_s \end{bmatrix}\begin{pmatrix} \bar{x}_s \\ \bar{y}_s \end{pmatrix} = \begin{pmatrix} 0 \\ 0 \end{pmatrix} \tag{3.54}$$

Let the matrices of the first, second and the third term be **M**, **G** and **K** respectively. **M** is the mass matrix, **G** is the matrix due to Coriolis effect while **K** is the overall stiffness matrix.

The characteristic equation, using $\begin{pmatrix} \bar{x}_s \\ \bar{y}_s \end{pmatrix} = \begin{pmatrix} \bar{X}_s \\ \bar{Y}_s \end{pmatrix} e^{st}$ is given by

$$|\mathbf{K} + s^2\mathbf{M} + s\Omega_s\mathbf{G}| = 0 \tag{3.55}$$

i.e. $$\begin{vmatrix} (k_s - \Omega_s^2 m_s) + s^2 m & -\Omega_s 2m_s \\ \Omega_s 2m_s & (k_s - \Omega_s^2 m_s) + s^2 m \end{vmatrix} = 0 \tag{3.56}$$

$$[(k_s - \Omega_s^2 m_s + s^2 m_s)]^2 + 4\Omega_s^2 m_s^2 s^2 = 0 \tag{3.57}$$

Solving the quadratic equation (3.57) in s^2

$$s^2 = \frac{-2m_s(k_s + \Omega_s^2) \pm \sqrt{(2m_s(k_s + \Omega_s^2 m_s))^2 - 4m_s^2(k_s - \Omega_s^2 m_s)^2}}{2m_s^2} \tag{3.58}$$

The term under the square root:

$$(2m_s^2)(k_s + \Omega_s^2 m_s^2)^2 - 4m_s^2(k_s - \Omega_s^2 m_s)^2 = 4m_s^2[(k_s + \Omega_s^2 m_s)^2 - (k_s - \Omega_s^2 m_s)^2] \tag{3.59}$$

$$= 4m_s^2[(k_s + \Omega_s^2 m_s^2)^2 - (k_s - \Omega_s^2 m_s^2)^2] \tag{3.60}$$

Using the difference of two squares in the form $a^2 - b^2 = (a + b)(a - b)$

$$= 4m_s^2[(k_s + \Omega_s^2 m_s + k_s - \Omega_s^2 m_s)(k_s + \Omega_s^2 m_s - k_s + \Omega_s^2 m_s)] \tag{3.61}$$

$$= 4m_s^2(2k_s)(2\Omega_s^2 m_s) = 16m_s^3 k_s \Omega_s^2 \tag{3.62}$$

Therefore,

$$s^2 = \frac{-2m_s(k_s + \Omega_s^2 m_s) \pm \sqrt{16m_s^3 k_s \Omega_s^2}}{2m_s^2} \tag{3.63}$$

$$= \frac{-(k_s + \Omega_s^2 m_s) \pm 2\sqrt{\Omega_s^2 k_s m_s}}{m_s} \tag{3.64}$$

Let $\omega_s^2 = \frac{k_s}{m_s}$ be the natural frequency in the nonrotating frame of reference.

So $$s^2 = -(\omega_s^2 + \Omega_s^2) \pm 2\sqrt{\omega_s^2 \Omega_s^2} \tag{3.65}$$

$$= -(\omega_s^2 + \Omega_s^2) \pm 2\omega_s \Omega_s \tag{3.66}$$

For the first solution,

$$s_1^2 = -(\omega_s^2 + \Omega_s^2) + 2\omega_s \Omega_s = -(\omega_s - \Omega_s)^2 \tag{3.67}$$

For the second solution,

$$s_2^2 = -(\omega_s^2 + \Omega_s^2) - 2\omega_s\Omega_s = -(\omega_s + \Omega_s)^2 \tag{3.68}$$

Therefore,

$$s_1 = \pm j(\omega_s - \Omega_s) \text{ or } s_2 = \pm j(\omega_s + \Omega_s) \tag{3.69}$$

i.e. in the rotating frame of reference, there is observed a splitting of the two equal original natural frequencies ω_s into the natural frequencies $\omega_s \pm \Omega_s$.

Let us consider a numerical example, for a mass m_s of the sun gear as 2 kg while the isotropic support stiffness is 2×10^6 N/m. For the isotropic bearing support stiffness, the natural frequencies of the sun gear can be determined using equation (3.69). This is done independently as a numerical check using an eigenvalue solution of equation (3.54) in MATLAB. The natural frequencies are plotted against the rotational speed of the rotating frame of reference and shown in the frequency map in Figure 3-16.

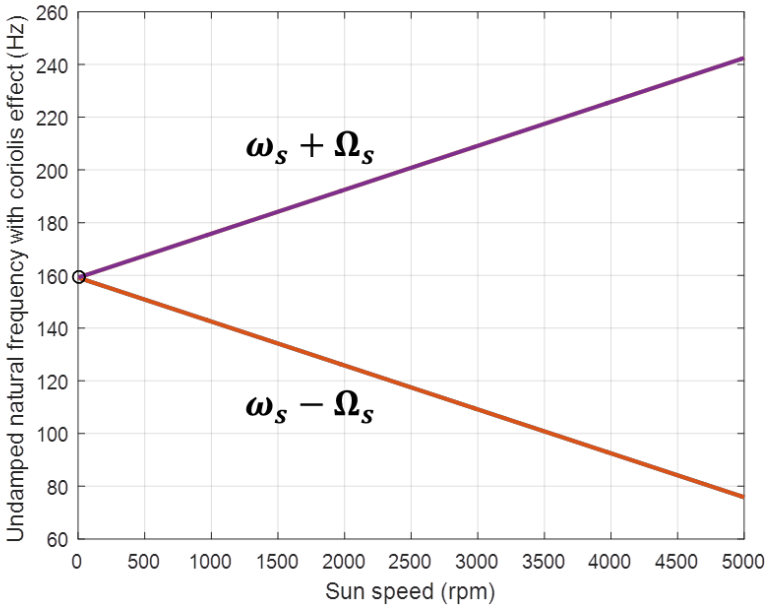

Figure 3-16 Frequency map showing the variation of the natural frequencies with the rotational speed of the sun gear as predicted and observed using a rotating coordinate system.

There are two identical natural frequencies for the non-rotating sun gear, because the support stiffness is isotropic i.e. the same in both the *x* and *y* directions. Figure 3-16 shows how the natural frequencies are changing due to the rotational speed of the sun gear. One of the two natural frequencies is increasing while the other is decreasing as the speed increases. This is due to the rotating coordinate system used for the modelling and analysis of the system. The frequencies can be referred to as pseudonatural frequencies, because a rotating frame of reference was used to investigate a system

with isotropic bearing stiffness. It is worth mentioning that for an observer who is observing the motion from a fixed frame of reference, the observer will see a different motion, hence different natural frequencies. For this isotropic bearing support case, the fixed observer will only see a single natural frequency corresponding to two modes comprising either a purely vertical or purely horizontal motion of the sun gear. The analysis given by Friswell [48] considers the general case when the support is not isotropic (i.e. $(k_x \neq k_y)$. As the gear rotates, it experiences a time varying support stiffness in the rotating coordinate directions. The natural frequencies of the stationary gear in the two fixed coordinates are then different. Equations (3.51 – 3.54) are subsequently changed and the two natural frequencies in the rotating frame of reference are obtained.

In practice, measurement using a rotating frame of reference is equivalent to using accelerometers that are rotating i.e. fixed to the rotating system. This may be possible with the use of wireless accelerometers, but it may be difficult to measure the natural frequencies of a rotating system especially at high speed. This is because there will be potentially more than one source of excitation when the system is rotating.

3.4.2 Numerical study using a planetary gear model

In this sub-section, numerical studies was undertaken to obtain the natural frequencies and vibration modes of a planetary gear using the equations (3.23) and (3.50). The parameters in Table 3-1 as used by Lin and Parker [14] will be used in this section to predict the natural frequencies and vibration modes of planetary. The reason for this is to confirm if the model will predict the same natural frequencies and eigenvectors as shown in their paper in [14]. It is imperative to state that Lin and Parker assumed that the carrier speed is small, hence they neglected the Coriolis terms in the equation of motion using a rotating frame of reference. In this numerical study, both fixed and rotating frames of reference will be considered and the effect of a wide range of carrier speed on the natural frequencies would be investigated. This would be shown on a frequency map or Campbell's diagram. However natural frequencies of a planetary gear with 2, 3, 4, 5, 6 planets will be shown to see how the difference between the modes.

Table 3-1 Planetary gear parameters by Lin and Parker

Parameter description	Carrier	Ring	Sun	Planet
Mass (kg)	3.43	2.35	0.40	0.66
The ratio of mass moment of inertia to the square of the radius I/r^2 (kg)	6.29	3.00	0.39	0.61
Base circle diameter (m)	176.8	275.0	77.4	100.3
Bearing stiffness (MN/m)	$K_p=K_s=K_r=K_p=100$			
Mesh stiffness (MN/m)	$Ks_n=Kr_n=500$			
Torsional stiffness (MNm/rad)	$K_{ru}=1000$, $K_{su}=K_{cu}=0$			
Pressure angle (degrees)	$\alpha_s=\alpha_r=24.6$			

For a fixed frame of reference, the standard eigenvalue problem considering equation (3.23) is written as:

$$\omega_i^2 \mathbf{M}\boldsymbol{\phi}_i = (\mathbf{K}_b + \mathbf{K}_m)\boldsymbol{\phi}_i \tag{3.70}$$

The natural frequencies and the eigenvectors using a fixed frame of reference are denoted by ω_i and $\boldsymbol{\phi}_i$ respectively.

For a rotating frame of reference, the free vibration response of the planetary gear for a linear time invariant case were determined using the general equation of motion in equation (3.50), neglecting the damping terms, the equation becomes

$$\bar{\mathbf{M}}\ddot{\bar{\mathbf{q}}} + \Omega_c \mathbf{G}_y \dot{\bar{\mathbf{q}}} + (\bar{\mathbf{K}}_b + \bar{\mathbf{K}}_m - \Omega_c^2 \mathbf{K}_\Omega)\bar{\mathbf{q}} = \mathbf{0} \qquad (3.71\text{ (a)})$$

The eigenvalues of the equation (3.71(a)) can be determined using a state space equation written as

$$\begin{bmatrix} \mathbf{0} & \mathbf{I} \\ -\mathbf{M}^{-1}(\bar{\mathbf{K}}_b + \bar{\mathbf{K}}_m - \Omega_c^2 \mathbf{K}_\Omega) & -\mathbf{M}^{-1}(\Omega_c \mathbf{G}_y) \end{bmatrix} \qquad (3.71\text{ (b)})$$

where **I** is an identity matrix. In a case where the Coriolis terms were neglected, the standard eigenvalue problem becomes

$$\bar{\omega}_i^2 \bar{\mathbf{M}} \bar{\boldsymbol{\phi}}_i = (\bar{\mathbf{K}}_b + \bar{\mathbf{K}}_m)\bar{\boldsymbol{\phi}}_i \qquad (3.72)$$

The natural frequencies and the eigenvectors using a rotating frame of reference are denoted by $\bar{\omega}_i$ and $\bar{\phi}_i$ respectively. Considering equation (3.72), the eigensolutions of a planetary gear system with three, four, five and six planets were simulated using the parameters in Table 3-1 and the result for their natural frequencies are given in Table 3-2. The results match with the ones in Lin and Parker's publications which considers three, four and five planet gears. The natural frequencies of a model with six planet gears were added as further work in this research. The multiplicity (*m*) in Table 3-2 implies the number of times a particular natural frequency of the planetary gear system occurs. For instance, for a planetary gear with three planets, a natural frequency of a translational mode, 743 Hz occurs twice in the third row and second column of the Table 3-2 This implies that the multiplicity of this natural frequency is two.

Table 3-2 Natural frequencies of planetary gear system with their multiplicity from 3 to 6-planet model using a rotating frame of reference.

Number of planets (N)	3	4	5	6
	0	0	0	0
Rotational mode frequencies (Hz)	1476	1537	1567	1581
multiplicity=1	1930	1971	2006	2033
	2658	2626	2615	2624
	7463	7774	8065	8343
	11775	13071	14253	15346
	743	727	710	693
Translational mode frequencies (Hz)	1102	1091	1072	1049
multiplicity=2	1896	1893	1888	1885
	2276	2343	2425	2514
	6986	7190	7382	7567
	9648	10438	11172	11862
Planetary mode frequencies (Hz)		1808	1808	1808
multiplicity=N-3		5964	5964	5964
		6982	6982	6982

3.4.3 Mode description

There are some unique properties in the vibration modes which are shown below for a planetary gear system with four planet gears. The unique properties are due to the fact that the planets' arrangement is symmetrical i.e. they are equally spaced.

a) Rotational mode: This mode has a multiplicity of 1 for different numbers of planets and there is no translation of the carrier, ring and sun. Six natural frequencies always correspond to this mode and their mode shapes are of the form $\begin{bmatrix} 0 & 0 & u_i & P_1 & P_2 & P_3 & P_4 \end{bmatrix}^T$ i= *c*, *r* and *s*; where *c*, *r* and *s* corresponds to the carrier, ring and sun respectively, and P_1, P_2, P_3 and P_4 are the displacements of the planets. Also, all the planets have the same deflection as for a rigid body mode as shown in Figure 3-17.

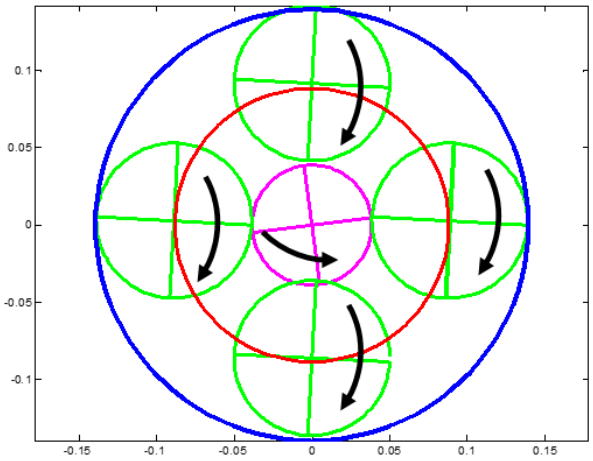

Figure 3-17 Rigid body rotational mode at 0 Hz.

b) Translational mode: This mode as shown in Figure 3-18, has a multiplicity of 2 for different number of planets and there is no rotation of the carrier, ring and sun. There are always twelve natural frequencies for this mode and their mode shapes is of the form $\begin{bmatrix} x_i & y_i & 0 & P_1 & P_2 & P_3 & P_4 \end{bmatrix}^T$ i=*c*, *r* and *s*, where P_1, P_2, P_3 and P_4 are the displacements of planets.

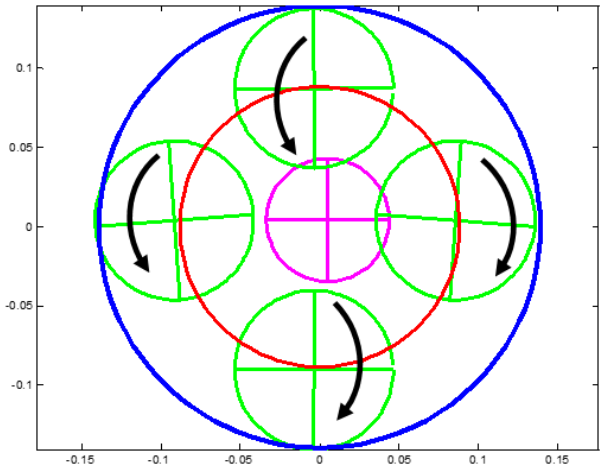

Figure 3-18 Translational mode at 1893 Hz.

c) Planet mode: This mode as shown in Figure 3-19, has a multiplicity of 3 for a different number of planets and there is neither rotation nor translation of the carrier, ring and sun. This implies that only the planet gears are moving in this mode. The natural frequencies in this case depend

on the number of planets in the planetary gear system. The mode shape has zero displacement of the carrier, ring, sun and planet in this category is of the form $\begin{bmatrix} 0 & 0 & 0 & P_1 & P_2 & P_3 & P_4 \end{bmatrix}^T$.

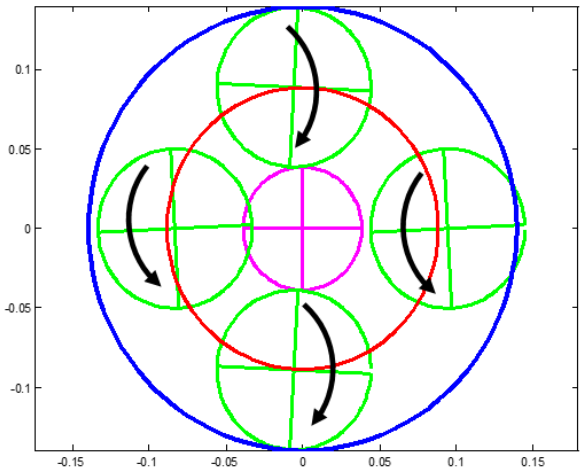

Figure 3-19 Planet mode at 1808 Hz.

Also, the natural frequencies of a planetary gear with four planets (because it exhibits all the mode types) was investigated using equation 3.71 (b) over a wide range of carrier speed and shown in the frequency map in Figure 3-20.

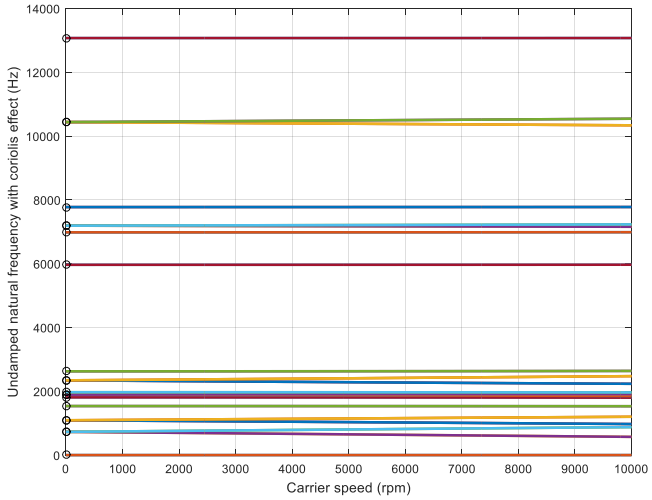

Figure 3-20 Frequency map showing the variations of the undamped natural frequencies with the carrier speed for a four-planet model.

It was discovered that the natural frequencies when a fixed frame of reference was used is the same as the natural frequencies when a rotating frame of reference was used, provided that the carrier speed is

low. The zoomed view of the frequency map is shown in Figure 3-21. It is obvious that some natural frequencies are splitting as the carrier speed increases. These are the frequencies of all the translational modes. The frequencies of rotational and planet modes are not splitting.

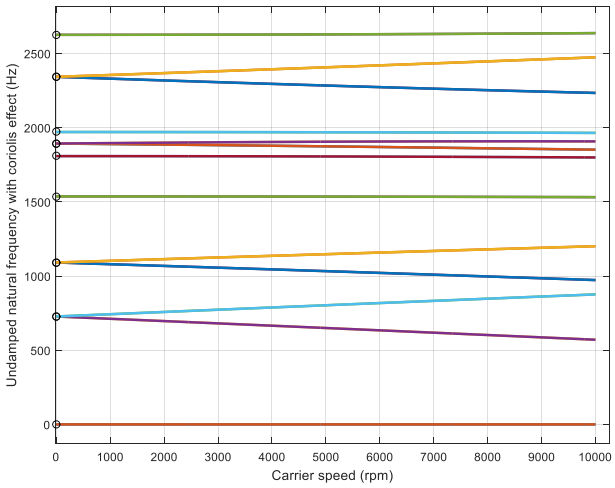

Figure 3-21 Zoomed view of a frequency map showing the splitting of the natural frequencies of only the translational modes as the carrier speed is increasing for a four-planet model.

Furthermore, natural frequencies and eigenvectors for a planet gear with two planet gears were determined using equation (3.72) so that it can be compared with the work of Lin and Parker. The results are shown in table 3-3 and for this case, there are fifteen natural frequencies and modes.

Table 3-3 Natural frequencies of planetary gear model with two planet gears.

S/N	Natural frequencies (Hz)	Mode type
1	0	Rotational mode
2	594	Translational mode
3	805	Translational mode
4	1038	Translational mode of the ring gear only
5	1129	Translational mode
6	1362	Rotational mode
7	1890	Rotational mode
8	1975	Translational mode
9	2254	Translational mode
10	2516	Translational mode of sun gear only
11	2714	Rotational mode
12	7124	Rotational mode
13	7190	Translational mode
14	10329	Rotational mode
15	10438	Translational mode

It is obvious from Table 3-3 that there is no planet mode in a two-planet model like a three-planet model. This implies that a planet mode can only be obtained in a planetary gear model with a minimum of four planet gears as shown by Lin and Parker [14]. The multiplicity (i.e. occurrence) of all the natural frequencies in this case is one unlike models with more than two planet gears. In this case, if the Coriolis terms were considered, there cannot be frequency split because the multiplicity of the translational mode is not 2 but 1. It was later discovered in chapter 4 that the multiplicity of the translational mode could be two for a 2-planet model depending on the stiffness of the bearing. Furthermore, only the ring gear is translating in the *x* and *y* directions in the fourth mode while the sun gear is exhibiting the same behaviour in the tenth mode. This is a unique behaviour which is peculiar to a planetary gear train with only two planet gears. This is not applicable to a planetary gear with 3, 4, 5 and 6 planet gears as shown by Parker [14].

3.5 Conclusion

A planetary gear model has been derived using both a fixed and rotating frame of reference for comparison. The model can be used to predict the dynamic behaviour of a planetary gear with one or more planet gears. Generally in both frames of reference, the mass matrix is dynamically uncoupled while the bearing stiffness matrix is statically uncoupled. The overall stiffness matrix is statically coupled using both frames of reference because of the sun-planet and planet-ring mesh stiffnesses as well as the contact between the carrier and the planet gears. The linear model is assumed to be time invariant and should be suitable for predicting the dynamic response of a planetary gear using either a fixed or rotating frame of reference. The models with isotropic bearing stiffnesses of the carrier, ring sun and planet gears were used to predict the free vibration response of the system. The natural frequencies of translational modes changed when increasing the carrier speed. This is because the translational modes have a multiplicity of two, therefore the frequency of one mode is increasing while the frequency of the other mode is decreasing as the carrier speed increases. This is known as frequency split due to the Coriolis effect.

The planetary gear system with two planets has not been studied before. In general, the following were discovered in this study:

a) There is no difference in the free response of the system when using either a fixed or rotating frame of reference provided that the carrier speed is below 100 rpm or set to zero in the latter.
b) For a two-planet model, the natural frequencies of the translational modes in a model with two planet gears only occurs once. This implies that the translational modes have a multiplicity of one. The models with more than two planets do not exhibit this behaviour. This is investigated further in chapter five where the stiffness of the bearings are reduced.

c) There is a translational mode where only the ring gear is vibrating and another translational mode where only the sun gear is vibrating.

The next chapter will focus on the design of a test rig which will be used to determine the bearing stiffnesses, sun-planet and ring-planet mesh stiffnessees the component masses and their moment of inertias. An update will be done on Table 3.1 and the parameters will be used to validate the model and subsequently some forced responses will be predicted in Chapter 5.

Chapter 4 Test rig design, estimation of the planetary gear parameters and frequency response using a rotating frame of reference

The mathematical model derived in chapter three will be verified by comparison to experimental results by suitable model predictions and measured data. In order to do this, an applicable planetary gear test rig must be designed and developed. In most planetary gear vibration experiments, accelerometers are mounted on the housing because there is no access to measure the vibration of the components inside the housing. This test rig was configured such that the independent vibration of carrier, ring, sun and planet gear can be measured when they are stationary and rotating. Some parameters estimated from the test rig will be used for the mathematical model; therefore the parameters previously used in chapter three can be updated. Therefore, this chapter focuses on the design and development of a vibration test rig for vibration measurement, as well as the experimental estimation of the bearing stiffnesses of the carrier, sun and planet gears. The stiffness of a stationary ring gear was also estimated. The bearing stiffness was determined dynamically using an instrumented hammer test. Furthermore, the mesh stiffness and the mass moment of inertia of the components were determined. The main purpose of doing this is to use the stiffnesses specified in the analytical model derived in chapter three to predict the natural frequencies, vibration mode shapes and the damping ratios present for the planetary gear.

It has been verified previously in chapter 3 that the natural frequencies and mode shapes of the planetary gear system using either a fixed or rotating frame of reference are the same provided the carrier speed is low when using a rotating frame of reference. Also, the effect of carrier speed on the undamped natural frequencies of the system has previously been shown in chapter 3, where the natural frequencies are either increasing or decreasing at high speed. It is necessary to also show how the rotational speed of the carrier affects the response. For this chapter, the frequency response function of the carrier, ring, sun and planet gears are shown using a rotating frame of reference at different carrier speeds. In this case, it was assumed that the bearing stiffnesses are isotropic. The study of planetary gear dynamic response to excitation using a rotating coordinate system at high speed is rare. The effect of the carrier speed on the excited low and high frequency were discussed. Also, the effect of the carrier speed on the damping ratio was studied to know if it is significant or not. Furthermore, the positions of the damped and the undamped poles in the *s*-plane are shown at different carrier speeds. The purpose of doing this is to know if the carrier speed can either increase or decrease the damping in the system significantly.

4.1 Design considerations and brief description of the test rig

The necessary test rig comprises mainly of the planetary gear train, the frame, the bearing supports, the input and output shafts, an electric motor, circlips, planet spindles, keys and the bearing housings. For modal testing, the external load on the planetary gear train was not considered. Also, for vibration measurements, instrumentation such as accelerometers were used to measure the vibration and an instrumented impact hammer to excite the system. The planetary gear design adopted comprises two pinions as planets, one gear or wheel as sun, a ring gear and the carrier as shown in Figure. 4-1. The sun and planet gears, when chosen, specified and subsequently purchased as manufactured items from ONDRIVES [49] and assembled together. The carrier and the ring gear were designed by the author and manufactured in the university's Engineering Design and Manufacturing Centre (EDMC). The shearing force and the bending moments of the shafts are not of interest in this research, therefore they will not be shown in the design calculations.

Most of the planetary gears used in the vibration test rig are built and enclosed such that there are no spaces to mount accelerometers on them during operation. One of the novelties in this research is the design and construction of a vibration test rig of a planetary gear which can accommodate accelerometers mounted on the carrier, sun and planet gears such that they will rotate with them during operation. This enhances independent measurement of the carrier, sun and planet gears. Hence, there will be no need to use a method like Time synchronous averaging (TSA) to know the frequencies that are related to the speed of carrier, sun or planet. Also frequencies that are not synchronized with a particular speed can be probably measured and analysed. Temporary fasteners are used to join the fixtures together which makes it easy to assemble and disassemble the test rig when necessary.

The following was considered in designing the test rig:

a. **Material selection**: Suitable materials were chosen for the components based on cost, availability and the function that they are to perform on the rig. For example, steel gears were chosen because they possess high strength and to avoid excess deflection of the teeth under static loading.
b. **Use of standard parts**: Parts like bearings, gears, keys and circlips were procured from ONDRIVE based on design standards. This makes the assembly and interchangeability of the parts as well as operation of the system possible.
c. **Convenient features and safety**: All the parts are well located for convenient control and safe operation of the test rig.

d. **Frictional resistance of the rotating parts**: For instance, rolling element bearings (which have low starting friction) were used (i) to avoid high starting friction of the rotating parts (ii) to achieve easy mounting and shaft alignment.
e. **Type of load on the output of the rig:** electrical load was chosen to be used on the rig.
f. **Maintenance:** The gear teeth were lubricated to avoid wear. Also, sealed rolling element bearings were chosen because they require less maintenance.
g. **Mechanism:** The carrier shaft was connected to an electric motor through a V-belt and two pulleys mounted on the electric motor and carrier shaft. This causes the rotation of the planet carrier mounted on the shaft. The two planet gears which are meshed with the sun gear rotate and revolve round the sun with the help of the planet carrier. The sun gear shaft serves as the output shaft and the external load was mounted onto it.

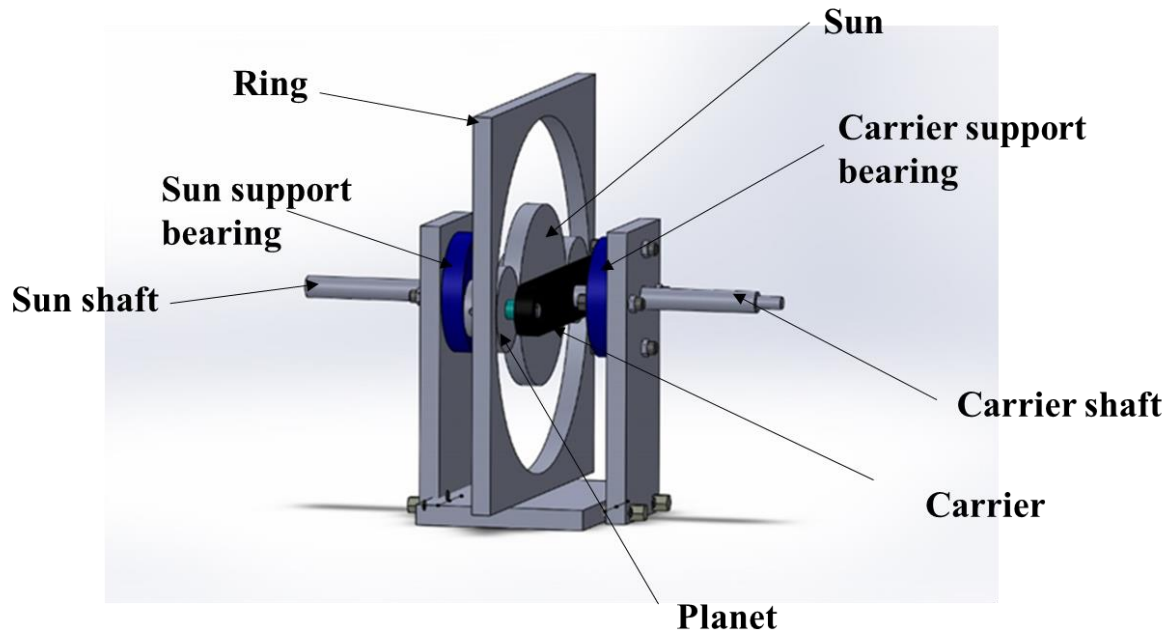

Figure 4-1 CAD model of planetary gear vibration test rig.

The carrier is shown in black in Figure 4-1 linked to the planet gears through two spindles, while the two bearing housing supports for the sun and carrier are shown in blue. The axes of rotation of the sun and the carrier are fixed unlike the planets, which makes the latter orbit round the sun gear as they rotate. The planet and sun have 45 teeth and 95 teeth respectively, while the ring gear with internal teeth arrangement has 185 teeth. As mentioned earlier, the input shaft is the carrier shaft connected to an electric motor while the output shaft is the sun shaft on which the external load was applied. The frames on both sides and the base rigidly supported the rig to avoid structural damage.

4.2 Gear terminologies

For simplicity, it is necessary to define some terms used in spur gears .Only the terms relevant to this research work will be defined. These terms are defined using Figure 4-2 as written by Gupta and Khurmi [50]. Figure 4-2 (a) shows the teeth which are not meshing with another teeth while Figure 4-2 (b) show the two teeth meshing together.

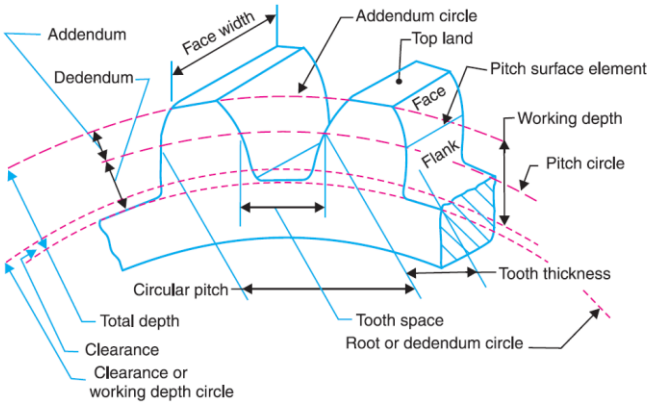

(a)

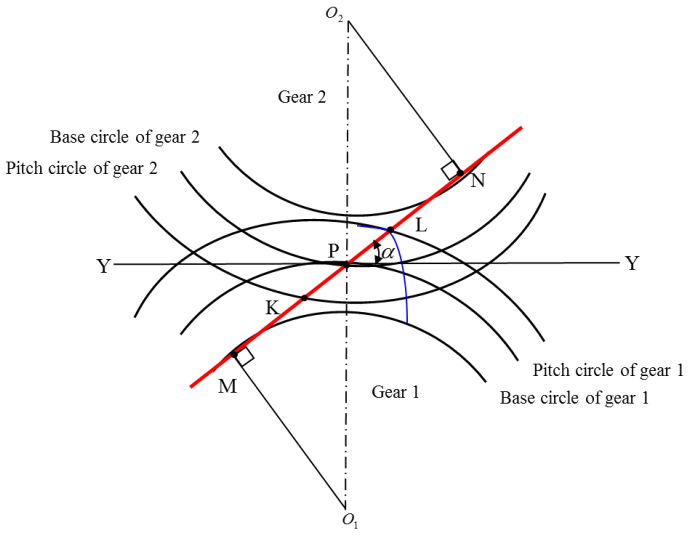

(b)

Figure 4-2 (a) Terms used in describing spur gears by Gupta and Khurmi [50]. (b) Two meshing gears with the pressure line shown in red.

The following terminologies will be used:

a. Pitch circle. It is an imaginary circle which by pure rolling action, transmits motion by friction as the actual gear. Its diameter is known as pitch circle diameter.
b. Addendum. It is the radial height of a tooth above the pitch circle and its circle is known as addendum circle.
c. Dedendum. It is the radial depth of a tooth below the pitch circle its circle is known as dedendum circle.
d. Pressure angle. It is the angle between the common tangent to the pitch circles (YY in Figure 4.2 (b)) and the pressure line (MN in Figure 4-2 (b)).
e. Pressure line. It is a line (red in Figure 4-2 (b)) tangential to the base circles of the two meshing gears.
f. Base circle. It is a circle that is tangential to the pressure line. The diameter of a base circle is the product of pitch circle diameter and cosine of the pressure angle.
g. Face width. It is the width of the tooth along its axial direction.
h. Pitch point. It is the point (P) where the two pitch circles of two mating gears are in contact (Figure 4-2 (b)).
i. Path of contact. It is the path followed by the point of contact of two teeth from the beginning to the end of mating. It is the line KL in Figure 4-2 (b).
j. Arc of contact. It is the arc measured on the pitch circle from the beginning to the end of mating.
k. Module. This is the ratio of the pitch circle diameter to the number of teeth.

4.3 Design calculations

The parameters of the sun and planet gears as received from the manufacturers are shown in Table 4-1. Other parameters like the speed ratio, design power, input and output torques and contact ratio are shown with equations in this section. The face width of all the gears is 15 mm. For perfect mating of the teeth, the modules of the ring, sun and planet gears are the same. The detailed engineering drawing can be found in the Appendix (C).

Table 4-1 Sun and planet gear parameters as received from the manufacturer

	No. of teeth	**Module (mm)**	**Addendum circle diameter, (mm)**	**Pitch circle diameter, (mm)**	**Base circle diameter (mm)**	**Pressure angle, α (degree)**
Sun gear	95	1.5	145.5	142.5	133.91	20
Planet gear	45	1.5	70.5	67.5	63.43	20

4.3.1 Design of the ring gear and the carrier

Mild steel was selected as the material because of its tensile strength. Figure 4-3 shows the schematic diagram of the ring, sun and planet gears with their pitch circle diameters. Let M and Z_r be the module and number of teeth on the ring gear respectively. The pitch circle diameter of the sun and planet gears are denoted by D_s and D_p respectively while the pressure angle of the ring gear is denoted by α_r.

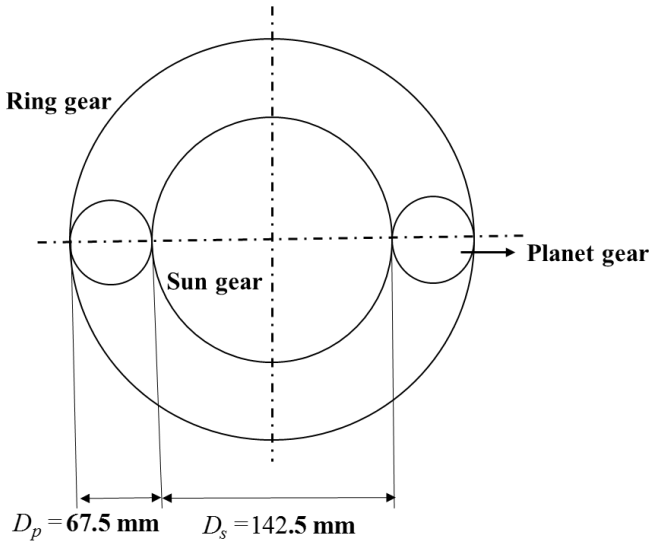

Figure 4-3 Pitch circle diameters of the gears.

The schematic diagram of the carrier is shown in Figure 4-4.

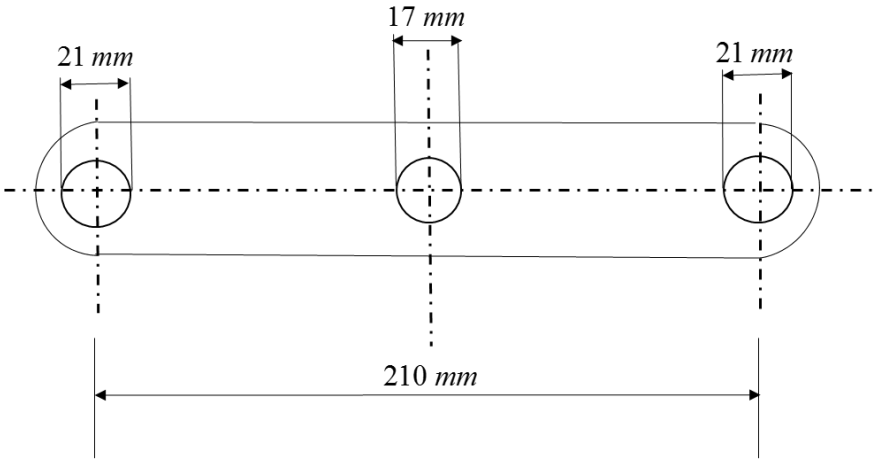

Figure 4-4 Carrier dimension.

The parameters of the ring gear and the carrier which were designed and manufactured are shown in the Table 4-2.

Table 4-2 Parameters of the carrier and ring gear.

S/N	Parameter	Formula	Numerical value (mm)
1	Module, M		1.5
2	Pitch circle diameter of ring gear , D_r (mm)	$D_r = (2D_p) + D_s$	277.5
3	Number of teeth on the ring gear, Z_r (mm)	$Z_r = D_r/M$	185
4	Addendum, a_r (mm)	$a_r = M$	1.5
5	Dedendum, d_r (mm)	$d_r = 1.25M$	1.875
6	Adddendum circle diameter (mm)	$D_r + 2M$	280.5
7	Dedendum circle diameter (mm)	$D_r - 2(\mathrm{d_r})$	273.75
8	Tooth depth	$\mathrm{a_r} + \mathrm{d_r}$	3.375
9	Base circle diameter of the ring gear (mm)	$D_r cos \propto_r$	260.76
10	Tooth thickness	$\pi M/2$	2.356
11	Centre distance of the planet gears on the carrier, c (mm)	$c = (2R_p) + D_s$	210

where, R_p is the radius of the planet gear.

4.3.2 Speed ratio and mesh frequency

Let Z_r, Z_s, and Z_p be the number of the teeth on the ring, sun and planet gears respectively while Ω_c, Ω_s and Ω_p are the rotating speeds of the carrier, sun and planet gears in rpm respectively. The speed ratio can be determined in tabular form as shown in Table 4-3 when the ring gear is chosen to be stationary. The schematic diagram showing that the ring gear is stationary is shown in Figure 4-5.

The number of teeth on the ring gear

$$Z_r = Z_s + 2(Z_p) = 95 + 2(45) = 185$$

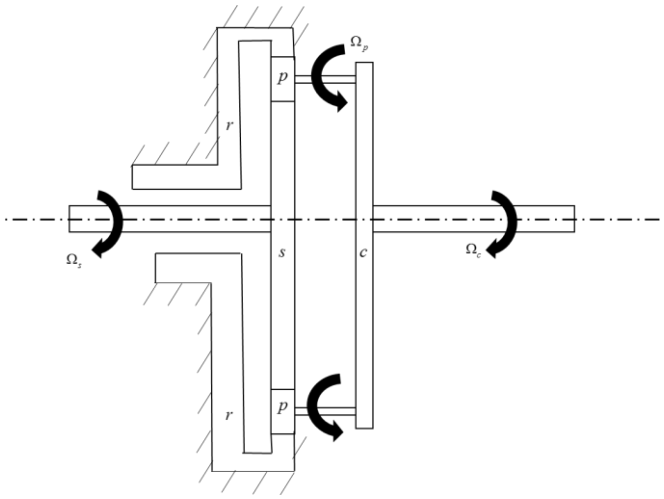

Figure 4-5 The mechanism of planetary gear train with the ring gear fixed.

Table 4-3 Table of speed ratio of the planetary type

Step	Description of motion	Carrier (c)	Ring (r)	Sun gear (s)	Planet gear (p)
1	Rotate the ring gear once -1 (i.e clockwise) while fixing the carrier	0	-1	$\frac{Z_r}{Z_s}$	$-\frac{Z_r}{Z_p}$
2	Rotate all at once	+1	+1	+1	+1
3	Add up	+1	0	$1+\frac{Z_r}{Z_s}$	$1-\frac{Z_r}{Z_p}$

The carrier is the input while the sun is the output. Assuming the carrier moves 1 rpm, the speed ratio of the carrier to the sun gear considering the last row and column 5 of Table 4-3 is

$$\frac{\Omega_c}{\Omega_s} = \left(1+\frac{Z_r}{Z_S}\right)^{-1} \tag{4.1}$$

Equation (4.1) can be re-written as:

$$\frac{\Omega_c}{\Omega_s} = \frac{Z_s}{Z_s + Z_r} \tag{4.2}$$

Thus, the speed ratio of the carrier to sun gear is 0.3393 i.e. if the carrier rotates 1 rpm, the sun will rotate at 2.947 rpm. The same procedure applies to the speed ratio of the carrier to planets considering the last row and column 6 of Table 4-3 is

$$\frac{\Omega_c}{\Omega_p} = \frac{Z_p}{Z_p - Z_r} \tag{4.3}$$

Therefore, the speed ratio of the carrier to the planet gear (taking the absolute value) is 0.321 i.e. if the carrier rotates 1 rpm, the planet gear will rotate at 3.11 rpm.

The contact between the teeth of two mating gears is called mesh. The mesh frequency, f_m in Hz, is the product of the carrier speed and the number of teeth on the ring gear [23]. There will be further explanation on the mesh frequency in chapter 6. Therefore, the mesh frequency can be expressed as

$$f_m = \frac{Z_s}{Z_s + Z_r}(\Omega_s / 60)Z_r = (\Omega_c / 60)Z_r \tag{4.4}$$

4.3.3 Input and output torques

The torque can be calculated from the relationship between the power and the rotating speed.

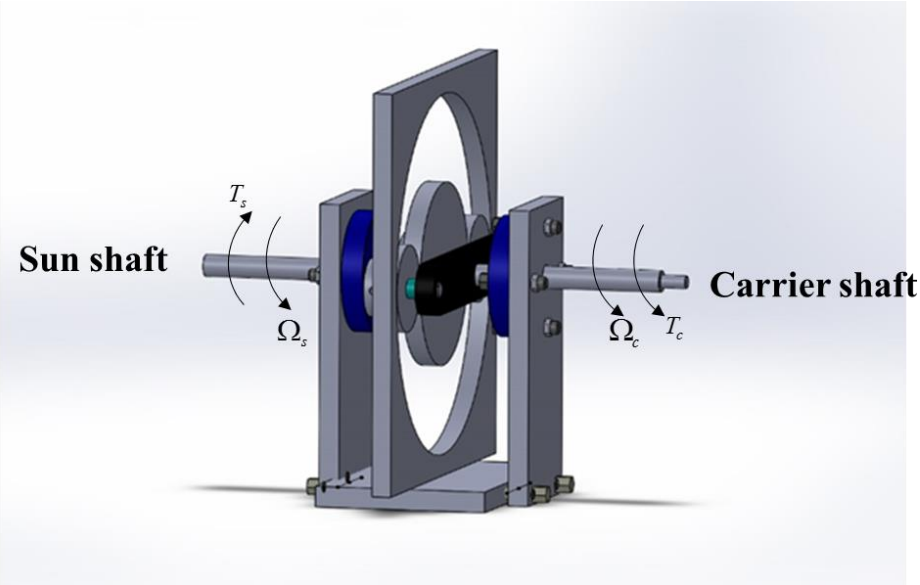

Figure 4-6 Torque in planetary gear trains.

Figure 4-6 shows the torques acting on a planetary gear train. A torque T_c applied at the input by an electric motor is transmitted to the output as T_s. The design power was determined based on the service factor, which is a measure of overloading capacity at which an electric motor can operate to avoid breakdown. However, the service factor, due to the operating hours of the electric motor at the input in a day is chosen to be 1 for this test rig. The power rating of the motor is 1 horsepower (0.745 kW).

The input torque applied on the carrier can be written as

$$T_c = \frac{60P_i}{2\pi\Omega_c} \tag{4.5}$$

where, T_c and P_i are the input torque and power respectively. Likewise, the output torque is on the sun gear and can be expressed as

$$T_s = \frac{60P_o}{2\pi\Omega_s} \tag{4.6}$$

where T_s and P_o are the output torque and power respectively. If the angular acceleration is zero, i.e. at constant angular velocity and the input and output shafts are rotating in the same direction, then the

input and the output torques will be in opposite directions i.e. T_c= -T_s . Therefore, from equations (4.5 and 4.6),

$$\frac{P_i}{\Omega_c} = -\frac{P_o}{\Omega_s} \tag{4.7}$$

This implies that the output power depends on the input power and the rotational speeds of the carrier and sun gear.

4.3.4 Gear contact ratio

The gear contact ratio is an important parameter, which is sometimes used to control gear noise and vibration passively**.** The higher the contact ratio, the lesser the gear vibration and noise. The contact ratio between the sun and planet gear are determined as follows [50]:

$$l_s = \sqrt{(R_a)^2 - R^2\cos^2 20^o} - R\sin 20^o \tag{4.8}$$

$$l_p = \sqrt{(r_a)^2 - r^2\cos^2 20^o} - r\sin 20^o \tag{4.9}$$

where**,** l_s, l_p, R_a and r_a are the length of path of approach, length of path of recess, addendum circle radii of the sun and planet gears respectively, while *R* and *r* are pitch circle radii of the sun and planet gears respectively. The diameters of the addendum and pitch circles of the sun and planets were all given in Table 4.1 as well as their pressure angles. Therefore, the lengths of path of contact l_{c1} and arc of contact l_{a1} are determined as

$$l_{c1} = l_s + l_p = 8.2442 + 5.5945 = 13.84 \text{ mm} \tag{4.10}$$

$$l_{a1} = \frac{13.84}{\cos 20^0} = 14.73\text{mm} \tag{4.11}$$

The contact ratio between sun and planet gears was calculated as $= \frac{14.73}{\pi M} = 3.125$. This implies that there are always at least three pairs of teeth in contact for the sun-planet mesh. Likewise, the contact ratio between planet and ring gear is calculated as follows:

$$l_r = \sqrt{(R_{rd})^2 - R_r^2\cos^2 20^o} - R_r\sin 20^o = 8.9704 \text{ mm} \tag{4.12}$$

where**,** l_r, R_{rd} and R_r are the length of path of recess, addendum (or inner) and pitch circle radii of the ring gear respectively. The length of path of approach is equal to l_p. The lengths of path of contact l_{c2} and arc of contact l_{a2} are determined as

$$l_{c2} = l_r + l_p = 8.97 + 5.60 = 14.57 \text{ mm} \quad (4.13)$$

$$l_{a2} = \frac{14.57}{\cos 20^0} = 15.51 \text{mm} \quad (4.14)$$

The contact ratio between planet and ring gears was calculated as $= \frac{15.51}{\pi M} = 3.29$. This implies that there are always at least three pairs of teeth in contact for the planet-ring mesh. Therefore, the minimum number of pairs of teeth in contact for the ring-planet is three like that of sun-planet contact.

4.4 Determination of the bearing stiffnesses

The bearing stiffnesses of the components are one of the important parameters used to determine the natural frequencies and the mode shapes of planetary gears. According to Kramer [51], the stiffness of a rolling element bearing can be approximated using the equation (4.15).

$$k_{vv} = k_b n_b^{2/3} d^{1/3} f_s^{1/3} \cos^{5/3} \alpha \quad (4.15)$$

where $k_{vv}, k_b, n_{b,} d, f_s$ and α are the vertical bearing stiffness, a constant = $13 \times 10^6 \text{ N}^{2/3}\text{m}^{-4/3}$, number of steel ball in the race, diameter of the ball in the race, vertical static load and the contact angle. For this study the vertical stiffness calculated for the carrier, sun and planet gears using equation (4.15) are 14.5, 15.3 and 0.81 MN/m respectively. Also, the horizontal stiffness can be calculated from the vertical stiffness depending on the number of balls. Kramer gives the ratio of the horizontal to vertical stiffness to be 0.46 and 0.64 for a bearing with 8 and 12 balls respectively. The planet bearing has 8 balls while the carrier and sun bearings, hence the approximated horizontal stiffnesses of the carrier, sun and planet gears are 9.28, 9.79 and 0.37 MN/m respectively.

However, the bearing stiffnesses of the carrier, sun and planet gear were experimentally measured by Tristan and Parker using a hydraulic jack to apply a known force on them [52]. A precise laser was used to measure the deflection and the force versus deflection curve was plotted. The experimental bearing stiffnesses of the component are taken from the slope of the least squares linear curve fit. They assumed the bearing stiffnesses are equal in radial directions. Nithin [53] determined the stiffness of a deep groove ball bearing by inserting the shaft into the inner race of the bearing. Both ends of the shaft were clamped so that the system can behave like a single degree of freedom (SDOF) system. The bearing was excited with an instrumented hammer and the accelerance was measured. The accelerance which must show 40 dB decade per slope on the stiffness line was converted to

receptance. The receptance was inverted to get the dynamic stiffness and the value was taken as the stiffness of the bearing.

For this study, the stiffnesses of the support bearings of the carrier, ring, sun and planet gears were not supplied by the manufacturers. These parameters are needed to predict the behaviour of the system using the lumped parameter model. Considering the available facilities and simplicity, a receptance method of estimating bearing stiffness was used in this study which was compared with those ones determine analytically using equation (4.15).

An experiment was conducted using modal testing to determine the stiffnesses of the support bearing. In this experiment, the components were mounted on the shaft in the frame. The bearings were also mounted such that the whole component (e.g. a carrier) under test behaves like a single degree of freedom (SDOF) system when excited with the impact hammer. For instance, the impact hammer was used to excite the carrier in the horizontal direction and the point accelerance was measured.

The experimental set-up for the carrier is shown in Figure 4-7. This comprises the bearing attached to the frame through the bearing housing, a shaft, a carrier and the base which was attached to a seismic base. During this test, the components were stationary. The shaft was assumed to behave as a rigid body so that the system can behave like a SDOF system (Figure 4-7 (a) and (b)). The mass and stiffness of the system are denoted by m_b and k_b. The hardware for the measurement comprised a signal analyser, an instrumented impact hammer, accelerometers and a computer to display the results. The sensitivity of the impact hammer was 2.25 mV/N while the sensitivity of the accelerometers was 1.00 mV/ms^{-2}. The frequency resolution was 1.563 Hz, the window length or maximum time was 640 ms and the sampling frequency was 2.56×10 kHz. This gives 6400 as a number of data points. The sensor was mounted on the carrier in the radial direction using wax. The instrumented hammer and the sensor were both connected to the signal analyser. The instrumented impact hammer was used to excite the carrier horizontally and vertically i.e. x and y directions respectively for different cases. The signals were displayed on the computer and any clipped data were rejected. The coherence of the data was checked to be good i.e. they are 90% and above before they were accepted for interpretation.

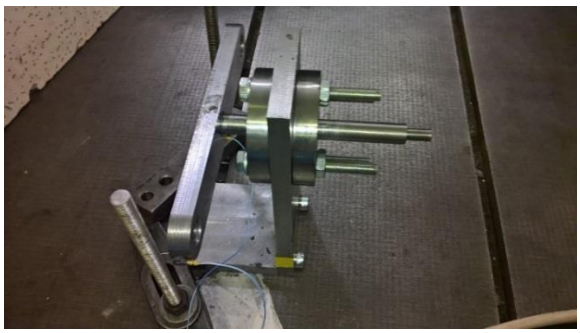

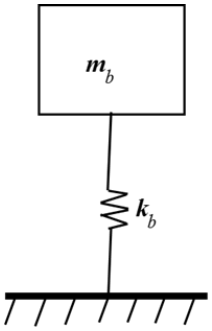

(a) (b)

Figure 4-7 Set-up to determine carrier bearing stiffness using the (a) experimental and (b) analytical models.

The low frequency stiffness line in the receptance plots was used to estimate the bearing stiffness. Stiffness was obtained by taking the average of the receptance values of points from 20 to 50 Hz. The average value of receptance was inverted and taken to be the stiffness.

Therefore, the estimated stiffness of the carrier in the horizontal direction is approximately $0.502\times10^{6}\,\mathrm{N/m}$. This value for the stiffness was used in the single degree of freedom lumped parameter model to compare the results which were plotted together in Figure 4-8 (a). It shows that the lumped parameter model is reasonably accurate when considering it as a SDOF. The dynamic stiffness measured from the experimental model were taken as the stiffness value in the dynamic model. The effective mass of the carrier was also determined from the mass line of the accelerance which is in Appendix 4 as 1 kg. The mass of the carrier was measured on a digital weighing balance as 1.03 kg to confirm the estimated mass from the experiment. The loss factor estimated from a SDOF circle fit for the carrier at 142 Hz in *x* direction is 0.3 while that of *y* direction at 288 Hz is 0.4. These were applied as hysteretic damping in the analytical model and shown in both Figures 4-8 and 4-9. The same method was used for the ring, sun and planet gears.

This procedure was repeated to determine the bearing stiffness of the carrier in the vertical direction and those of ring, sun and planet gears in both directions. The set up for the sun gear is shown in Figure 4-9 and the point receptances in both directions are shown in Figure 4-10. The receptances of the planet and ring gears are shown in Figures 4-11 and 4-12 respectively. In general, there is reasonable agreement between the responses from the model and experiments. However, this is not the case for the carrier in the vertical direction (Figure 4-8 (b)) where it behaves like a mass at low frequencies. This may be due to the fact that it was not clamped well enough during the experiment giving rise to a mounting resonance below 10 Hz.

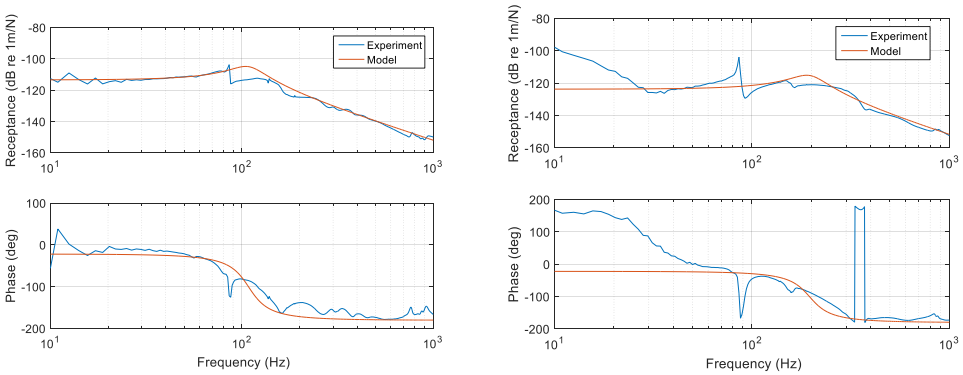

(a) (b)

Figure 4-8 Point receptance of the carrier showing its bearing stiffness at low frequencies in the (a) horizontal (0 to 180^o), the coherence is good from 23 Hz and (b) vertical directions (90^o to 270^o), the coherence is good from 38 Hz.

Figure 4-9 Set-up to determine sun gear bearing stiffness.

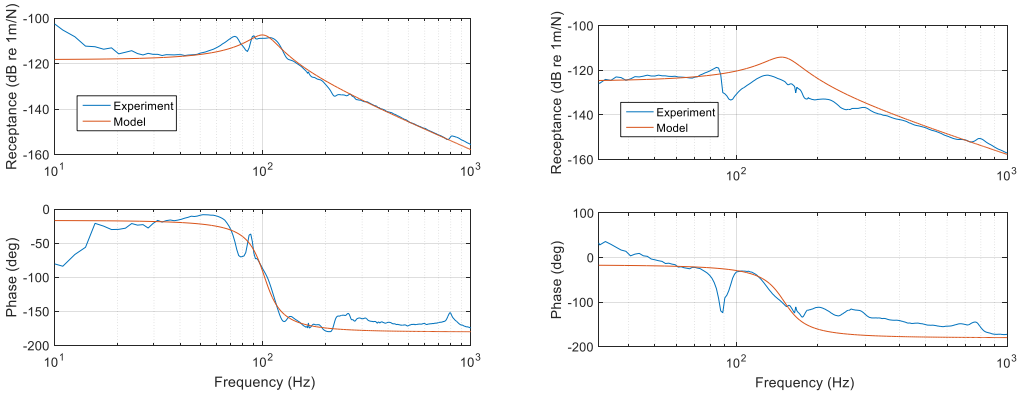

(a) (b)

Figure 4-10 Point receptance of the sun gear showing its bearing stiffness at low frequencies in the (a) horizontal and (b) vertical directions. The coherence is good from 20 Hz and 31 Hz respectively.

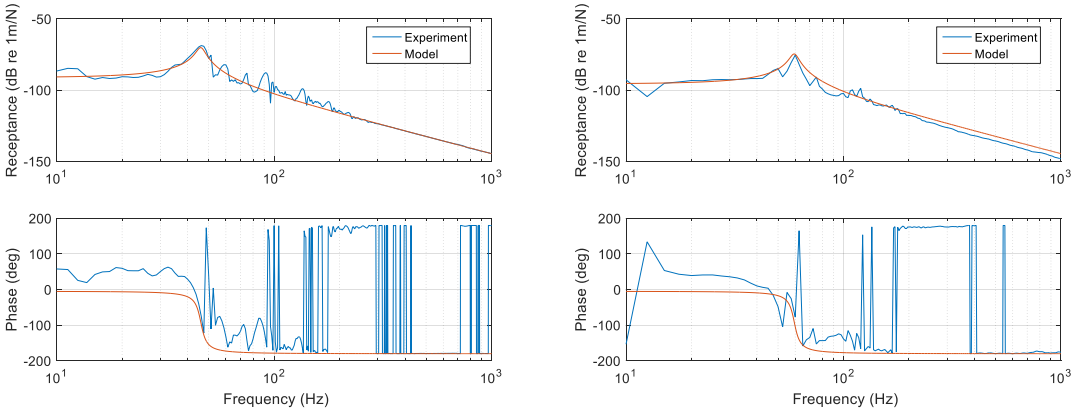

(a) (b)

Figure 4-11 Point receptance of the planet gear showing its bearing stiffness at low frequencies in the (a) horizontal and (b) vertical directions. The coherence are good from 16 Hz and 20 Hz respectively.

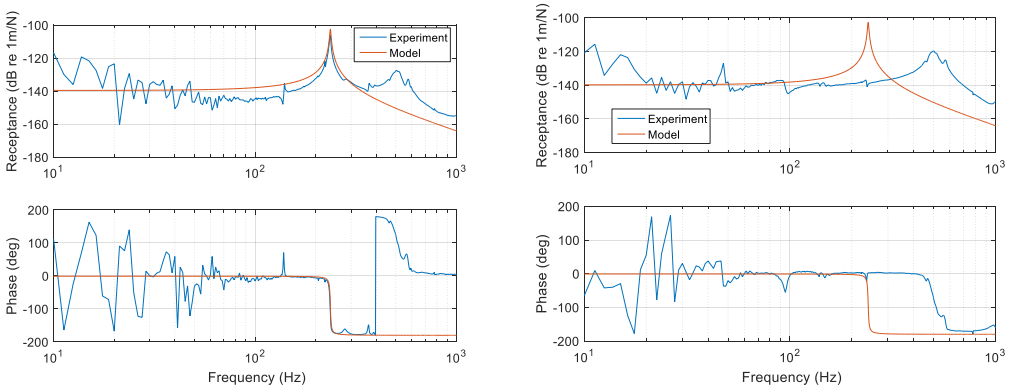

(a) (b)

Figure 4-12 Point receptance of the ring gear showing its stiffness at low frequencies in (a) horizontal and (b) vertical directions.

The coherence is good from 96 Hz in Figure 4-12 (a) and from 75 Hz in Figure 4-12 (b). There is a limitation in determining the stiffness of the ring gear in the vertical direction (Figure 4-12 (b)) because it was constrained in the vertical direction (i.e. bolted to the base). Therefore there is a probability that the whole mass did not move as a rigid body when exciting it with the instrumented hammer in the vertical direction. The stiffness in the vertical direction cannot be determined accurately. In this case, the stiffness in the vertical direction will be assumed to be equal to that of horizontal direction. The stiffness in the horizontal direction is 1.64×10^7 N/m.

The bearing stiffnesses determined analytically using equation (4.15) are greater than the ones estimated from the experiment. The estimated values for the bearing stiffnesses and stiffness of the ring gear determined are summarised in Table 4-4. It is believed that the estimated ones will be more accurate and acceptable than the ones determined analytically. Therefore the estimated ones will be used in this study.

Table 4-4 Bearing stiffness values.

Component	Estimated horizontal Stiffness (MN/m)	Estimated vertical stiffness (MN/m)	Ratio of estimated horizontal to vertical stiffness	Analytical horizontal stiffness (MN/m)	Analytical vertical stiffness (MN/m)	Ratio of analytical horizontal to vertical stiffness
Carrier	K_{cx}=0.50	K_{cy}=1.43	0.350	9.28	14.5	0.64
Ring	K_{rx}=16.40	K_{ry}=16.40	-	-	-	-
Sun	K_{sx}=0.68	K_{sy}=1.35	0.500	9.79	15.3	0.64
Planet	K_{px}=0.027	K_{cy}=0.049	0.551	0.37	0.81	0.46

Also, the ratio of horizontal stiffness to vertical stiffness of the bearing was investigated to check if the values are closer to the one given by Friswell from the analytical method [48]. The comparisons between the estimated and analytical ratio are close except for the case of the carrier where the estimated ratio is 0.35 while the analytical ratio is 0.64 (Table 4-4).

4.5 Estimation of sun-planet and planet-ring mesh stiffnesses by a fitting method

It is necessary to determine the mesh stiffness of a gear system before the natural frequencies and the mode shapes can be predicted. The mesh stiffness is the mesh force per deflection at the contact between the meshing teeth [54]. It can vary when the number of teeth in contact changes or when the load fluctuates. In this study, the mesh stiffness is assumed to be constant for determination of natural frequencies and mode shapes. Various methods have been used to determine the mesh stiffness of a gear system analytically and using finite element analysis. Howard et al. [55] modelled the tooth stiffness using finite element analysis (FEA). Instead of modelling the bending stiffness, the static torsional mesh stiffness was considered and converted to a linear stiffness for use in their dynamic model. Wadkar and Kajale in their study [56] show how the single pair torsional stiffness and double pair torsional stiffness of meshing pinion and gear can be determined. They defined torsional stiffness as the ratio of applied torque to an angular rotation of gear body. i.e. $K=T/\theta$, where K, T and θ are the torsional stiffness, applied torque and the angular rotation of gear body. The transverse plane angular rotation of the gear body θ are caused by bending and shear when the gear is stationary using equation 4.16.

$$\theta = \frac{B+H}{R} \tag{4.16}$$

where *B*, *H* and *R* are the tooth displacement caused by bending and shearing at the contact, tooth displacement caused by contact deformation and the radius of the base circle. They determined the equivalent torsional stiffness of single pair of meshing teeth using by assuming that the meshing are springs in series.

$$K_{eq} = \frac{K_p K_g}{K_p + K_g} \tag{4.17}$$

where K_p and K_g are the torsional mesh stiffnesses of the pinion and gear respectively. This procedure can be used to determine the torsional mesh stiffness. However, to determine the accurate displacement caused by shearing and bending may not be trivial. Chang et al. [57] proposed a model for determination of mesh stiffness of cylindrical gears using a combination of local contact analysis and finite element method (FEM). The two and three-dimensional finite element models which can be used to determine mesh stiffness were developed by Kiekbuch et al. [58]. The two-dimensional model is suitable to simulate a variety of different gear pairs in a short period of time. A formula for combined torsional mesh stiffness of spur gear was derived from the analysis of the two-dimensional model. They assumed that the stiffnesses of the body, teeth and contact zone can be arranged as three springs in series such that the combined torsional stiffness K_i for each pinion and gear will be

$$K_i = \frac{(K_{B,i})(K_{T,i})(K_{c,i})}{K_{B,i} + K_{T,i} + K_{c,i}} \tag{4.18}$$

where $K_{B,i}$, $K_{T,i}$ and K_{ci} are stiffnesses of the gear body, tooth and the contact respectively with *i* denoting pinion or gear. The combined torsional mesh stiffness of the pinion and gear are then determined in series. Sanchez [59] et al. presented a model for evaluation of spur gear mesh stiffness which includes bending, shear, compressive and contact deflections. The stiffness is evaluated at any point of the path of contact by an analytical equation. The load at any point of contact can be determined from the analytical equation.

All the aforementioned methods of determining the mesh stiffness are not trivial. In this study, the sun-planet and ring-planet mesh stiffnesses were determined by fitting a relationship between the natural frequencies measured from the experiment and those predicted by the model. This is a new and easier method of estimating mesh stiffness of a planetary gear. It takes into consideration the measured natural frequencies of the system.

For sun-planet mesh frequency estimation, the ring gear was excluded during the experiment. Therefore, only the carrier, sun and planet gears were present. A reasonable range of estimated values

for the mesh stiffness were assumed between 10^6 and 10^9 N/m. The contact stiffness matrices was decomposed (as shown in Appendix 3) in order to achieve this. The relationship in Equation (4.19) was used to determine the mesh stiffness by choosing to minimise an error function, Є.

$$\epsilon = \sum_{i=1}^{n} \frac{(\omega_{ie} - \omega_{ip})^2}{(\omega_{ip})^2} \tag{4.19}$$

where, *n* is the chosen number of modes to be used in the estimation process, while ω_{ie} and ω_{ip} are the natural frequencies of *i*th mode from the experiment and the predictions respectively. A table showing the natural frequencies are shown in the Appendix B. Each pair of estimated and predicted natural frequencies was chosen based on the closeness in their values. Some of the measured natural frequencies cannot be identified by the analytical model because the model can only capture the translational, rotational modes and the assumptions in the lumped parameter model.

The two different lines of the error function Є against the sun-planet mesh stiffness are used in the model shown in Figure 4-13 (a). The value chosen was determined using three natural frequencies in the first case and four natural frequencies in the second case from both experiment and predictions. The minimum value in the error function corresponds to an estimated mesh stiffness of 1.0×10^7 N/m and this was taken as the sun-planet mesh stiffness in the analytical model. The same procedure was repeated when a ring gear was included on the test rig in order to estimate ring-planet mesh stiffness. The estimated ring-planet mesh stiffness as shown in Figure 4-13 (b) is 1.5×10^7N/m. The average of sun-planet and planet-ring mesh stiffnesses estimated is 1.25×10^7N/m. This value was subsequently used as the mesh stiffness for both the sun-planet and planet-ring contact. Since the same numbers of pairs of teeth are in contact at any point in time the sun-planet and planet-ring mesh, both mesh stiffnesses should be the same.

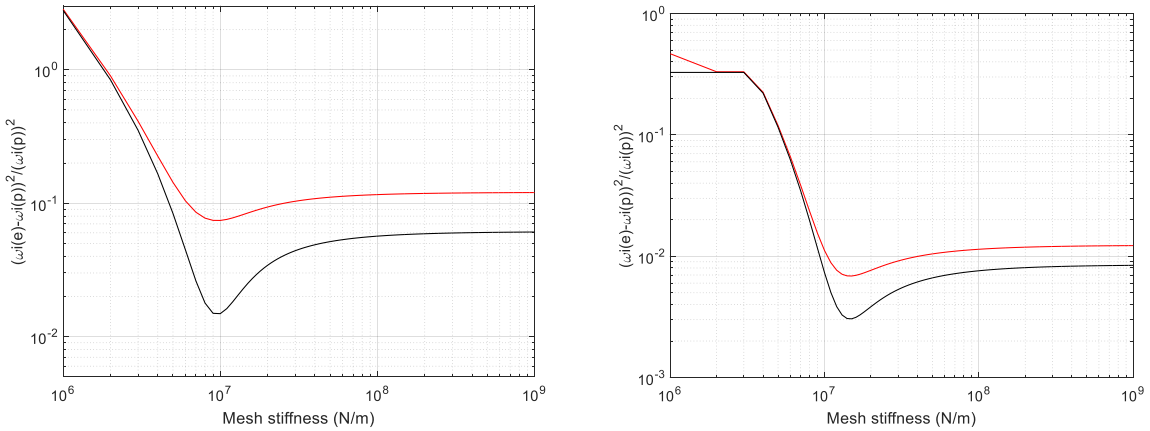

(a) (b)

Figure 4-13 Determination of the mesh stiffness by minimising the error in the squared difference in the predicted and estimated natural frequencies as a function of the mesh stiffness (a) Sun-planet mesh (b) Planet-ring mesh.

The red line denoted the error function when four natural frequencies were chosen while the black is for the error when three natural frequencies were chosen.

4.6 Estimation of the mass moment of inertia of the components and the torsional stiffness of the ring gear

The masses, mass moment of inertias of carrier, ring, sun and planet gears were evaluated and tabulated in Table 4-5. Their geometric shapes were considered for the calculations of the mass moment of inertia which was subsequently divided by the square of the radii of the pitch circles. The carrier mass moment of inertia was divided by its horizontal length as shown in Figure 4-4. These will be used in the mathematical model which has been derived in chapter three. The equations for calculation of the moment of inertia of the carrier, ring, sun and planet gears with relevant diagrams are shown in Appendix B.

Table 4-5 The estimated masses and mass moment of inertia of the planetary gear.

Component	**Masses (kg)**	**Mass moment of inertia, I (kgm^2)**	**I/r^2 (kg)**
Carrier	1.00	0.0377	2.41
Ring	4.30	0.1197	6.22
Sun	2.00	0.0051	1.00
Planet	0.43	0.000254	0.22

Also, the torsional stiffness of the ring gear was calculated to be $2.54 \times 10^8 \text{Nm/rad}$. This can be found in Appendix B.

4.7 The determination of viscous damping

For the numerical analysis using a rotating frame of reference, the viscous damping coefficient was calculated using equation (4.20) taking the damping ratio ζ as 0.01. The reason for doing this is to see clearly the resonance peaks of the system when an external force is applied.

$$\zeta_i = \frac{c_i}{2\sqrt{k_i m_i}} \; ; \; i=c, r, s \text{ and } p \qquad (4.20)$$

The values of c_i, k_i and m_i are the viscous damping coefficient, stiffness and mass of the carrier, ring, sun and planet gears. The estimated viscous damping coefficients are shown in Table 4-6.

4.7.1 4.7.1 The effect of the different carrier speed on the damping ratios

In this subsection, the effect of carrier speed on the damping ratios was studied. This was compared to the damping ratios obtained at each damped natural frequencies when using a fixed frame of reference. For this comparison between both frames of reference, the parameters in Table 4-6 were considered for both cases. The modal damping ratio of the m^{th} mode was determined analytically from the calculated eigenvalues as follows assuming a viscous damped mode i.e.

$$s_{1,2} = -\zeta\omega_n \pm j\omega_n\sqrt{1-\zeta^2} \qquad (4.21)$$

where, σ, ζ, ω_n and ω_d are the real parts of the complex eigenvalue and the damping ratio, natural frequency and damped natural frequency respectively.

$$\sigma = -\zeta\omega_n \; ; \; \omega_d = \omega_n\sqrt{1-\zeta^2} \qquad (4.22 \text{ (a) and (b)})$$

Therefore, equation (4.13) becomes

$$s_{1,2} = \sigma \pm j\omega_d \qquad (4.23)$$

ω_n can be made the subject of the formula from equation 4.22 (a) and (b) such that they will be equal and the modal damping ratio can be determined based on the damped natural frequency and σ. The modal damping ratio of the m^{th} mode is therefore expressed as

$$\zeta_m = \sqrt{\frac{\sigma_m^2}{\sigma_m^2 + \omega_{dm}^2}} \tag{4.24}$$

where, σ_m and ω_{dm} are the real part of the complex eigenvalue of m^{th} mode and its damped natural frequency respectively. The calculated modal damping are shown using coloured lines in Figure 4-14 for the carrier speeds 0 to 2000 rpm in 500 rpm increments.

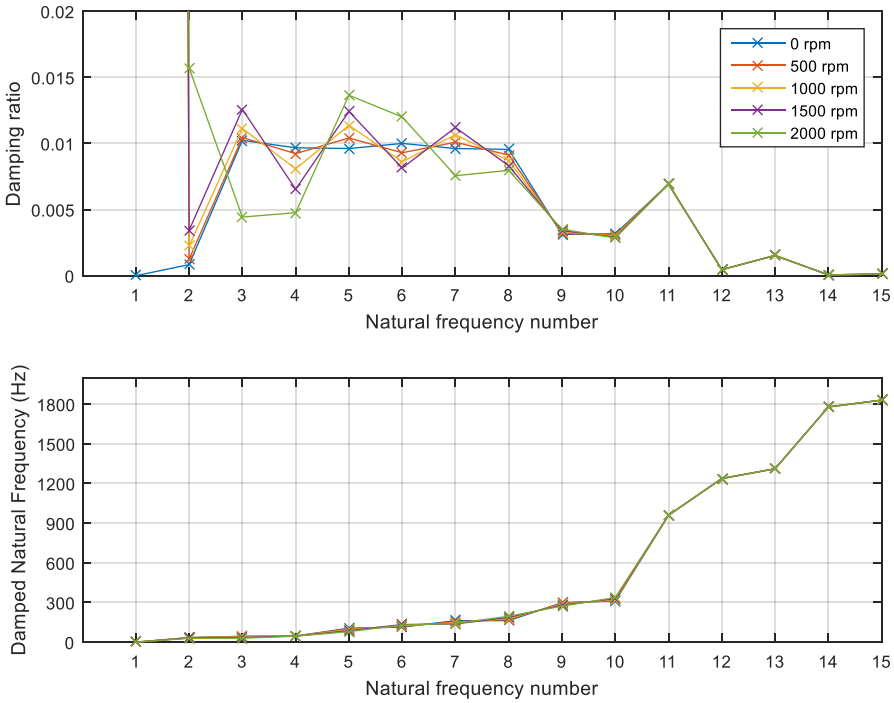

Figure 4-14 **The effect of the carrier speed on the modal damping ratios at 0 to 2000 rpm.**

It is obvious in Figure 4-14 that there is no significant difference in the modal damping ratios between 0 and 500 rpm from the second to eight mode, but the difference is obvious from 1000 rpm for these modes. The case is different for the ninth to fifteenth mode because the modal damping ratios are almost invariant at the carrier speeds considered. This implies that the Coriolis effect has no influence on the modal damping ratios at higher order modes, from 272 Hz but has an effect on the lower modes at 1000, to 2000 rpm.

4.8 The frequency response at different carrier speed using a rotating frame of reference

In many publications where a rotating coordinate system was used, the Coriolis terms are usually ignored because they do not have effect on the natural frequencies of the system at low rotational

speeds. The aim in this section is to investigate and report how the Coriolis effect affects the response at high carrier speeds. Five different carrier speeds at intervals of 500 rpm were chosen to demonstrate and compare the frequencies excited when a unit force is applied on a system component in the horizontal, vertical and rotational directions. Therefore, the bearing stiffness must be isotropic in this case, so the average of the stiffnesses of carrier, ring, sun and planet gears in both the horizontal and vertical directions as written in Table 4-4 were taken and used at this point. They are shown in Table 4.6 and will be used in all the subsequent studies in this research when using either a fixed or rotating coordinate system for analysis unless otherwise stated.

Table 4-6 Parameters of the system when using a rotating frame of reference

Parameter description	**Carrier**	**Ring**	**Sun**	**Planet**
Mass (kg)	1.00	4.30	2.00	0.43
I/r^2 (kg)	2.41	6.22	1.00	0.23
Base circle diameter (m)	176.8	261.00	134.00	63.40
Bearing stiffness (N/m)	0.965×10^6	1.64×10^7	1.02×10^6	3.82×10^4
Bearing damping coefficient (Ns/m) using 0.01 as the damping ratio	19.65	53.22	28.57	2.56
Mesh stiffness (N/m)	1.25×10^7			
Torsional stiffness of the ring gear (Nm/rad)	2.54×10^8			
Torsional damping coefficient of the ring (Ns/m) using 0.01 as the damping ratio	661			
Pressure angle (degree)	$\alpha_s=\alpha_r=20$			

The above parameters were used to determine the natural frequencies and the mode shapes of the system using equation (3.56) in chapter 3. This is a case whereby a rotating frame of reference was used for the analysis neglecting the Coriolis terms. The natural frequencies and the mode type are shown in Table 4-7.

Table 4-7 Natural frequencies using a rotating frame of reference and isotropic bearing stiffnesses

S/N	Natural frequencies (Hz)	Mode type
1	0	Rotational mode
2	34.7	Rotational mode
3	44	Translational mode
4	46.1	Rotational mode
5	105.7	Translational mode
6	113.7	Translational mode
7	162.5	Translational mode
8	162.9	Translational mode
9	298.7	Translational mode
10	310.8	Translational mode
11	959.7	Rotational mode
12	1237.2	Translational mode
13	1311.1	Rotational mode
14	1778.8	Translational mode
15	1830.5	Rotational mode

The mode shapes of the rotational and translational modes at 34.7 and 162.5 Hz respectively are shown in Figure 4-15.

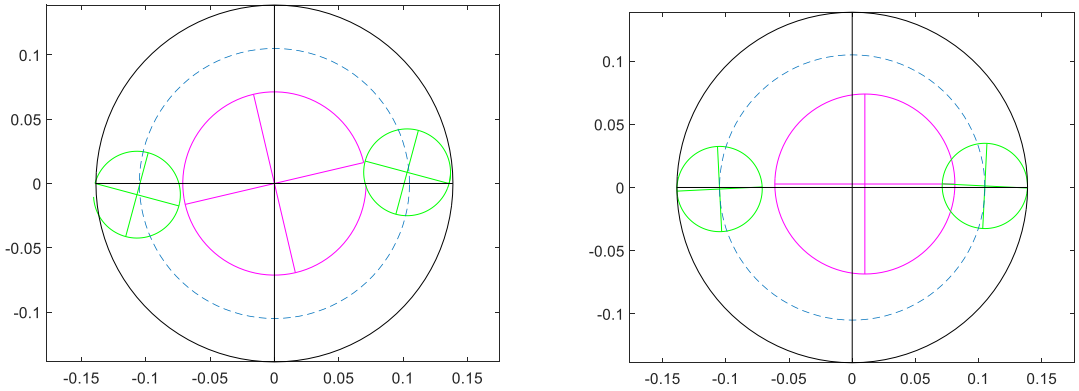

(a) (b)

Figure 4-15 (a) Rotational mode at 34.7 Hz (b) Translational mode at 162.5 Hz.

At 34.7 Hz, the sun and planet exhibit significant displacement in the rotational direction (Figure 4-15). Also, at 162.5 Hz, it shows that the sun was more significantly displaced in the horizontal direction than the vertical direction.

The carrier, ring, sun and planet gears were excited in the horizontal, vertical and the rotational direction using a rotating frame of reference and their point receptances are shown in Figures 4-16 to 4-19 respectively. The various carrier speeds considered are shown in different colours for clarity with the black line as a reference. Also, the Coriolis effect on the natural frequencies of the system considering a wide carrier speed range was shown on a frequency map to confirm if there is any frequency split shown on the frequency response function.

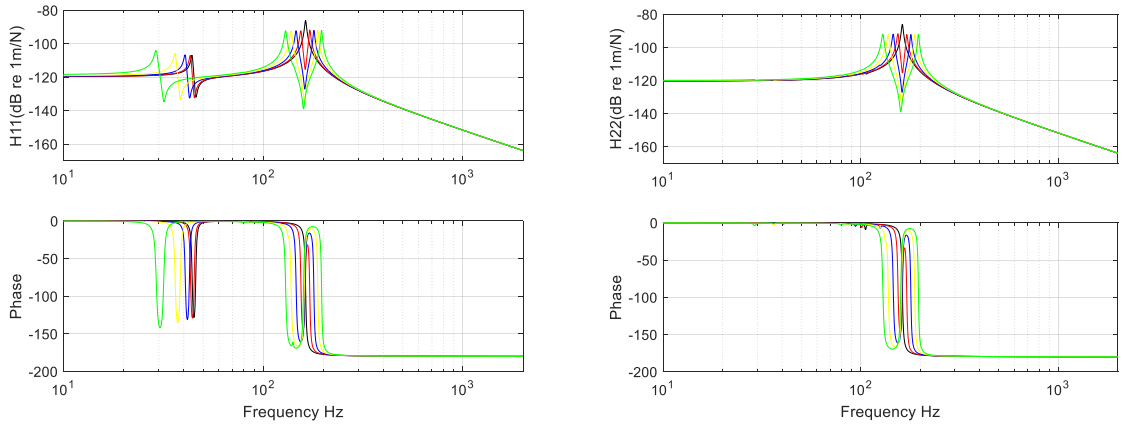

(a) (b)

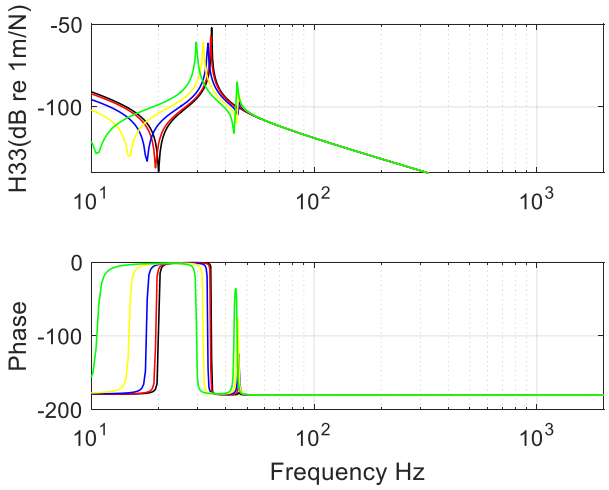

(c)

Figure 4-16 Predicted point receptance of the carrier in the (a) horizontal (b) vertical and (c) rotational directions at different speeds. The point receptance at 0, 500, 1000, 1500 and 2000 rpm are shown in black, red, blue, yellow and green lines respectively.

Figure 4-16 (a) show the carrier frequency response in the horizontal direction. There is a peak at 44 Hz when the carrier speed is zero (i.e. when there is no Coriolis effect) and this is a translational mode. There is no significant difference between the resonance frequencies at the carrier speeds 0 and 500 rpm. The difference becomes significant when the carrier speed reaches 1000 rpm and above because of the Coriolis effect. At higher frequencies, the resonance frequency when there was no Coriolis effect is 162.5 Hz and there was a frequency split for the carrier speeds above 500 rpm. This is due to the fact that there are two frequencies of 162.5 and 162.9 Hz when there is no Coriolis effect in the system which split as the carrier speed increases. It has been shown in Chapter three that the analytical model with two planet gears does not exhibit this behaviour whereby there will be two

similar natural frequencies of translational modes. Lin and Parker [14] said this kind of mode has a multiplicity of two. However, the stiffnesses used for the analysis in Chapter three are more than the ones used in this section, so this may be responsible for the occurrence of two similar frequencies splitting as the carrier speed is increasing in the two-planet model. The higher frequencies excited in the vertical direction also show the same trend as in the horizontal direction. Without the Coriolis effect, a rotational mode was excited in the rotational direction (Figure 4-16 (c)) at 34.7 Hz. The difference in the resonance frequencies is not significant at the lower speed 500 rpm. The difference is significant from 1000 rpm most especially at 2000 rpm, but less significant when compared to the translational mode excited at low frequencies in the horizontal direction (Figure 4-16 (a)). It is obvious that the frequency of the rotational mode does not split. For three directions, the responses when there is no Coriolis effect is about 6 dB higher than the responses at higher carrier speeds. This was mentioned considering that the same viscous damping coefficient was applied to the components in both the horizontal and vertical directions.

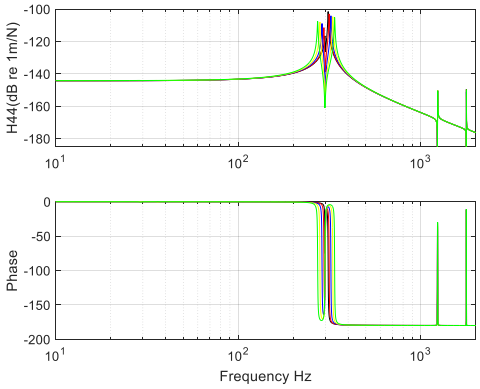

(a)

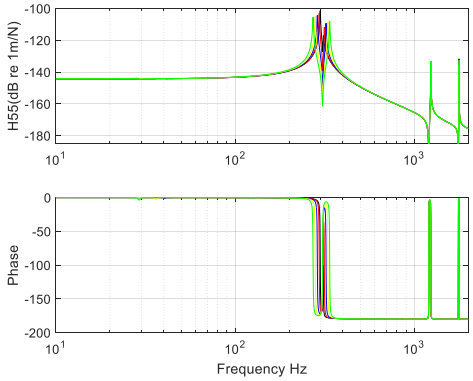

(b)

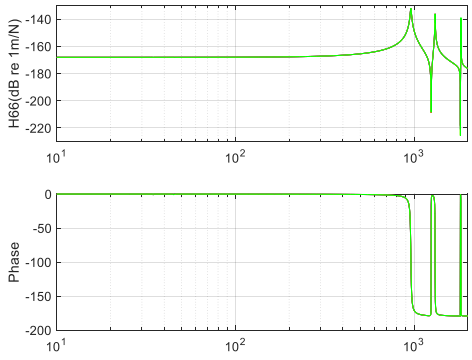

(c)

Figure 4-17 Predicted point receptance of the ring gear in the (a) horizontal, (b) vertical and (c) rotational directions at different speeds. The point receptances at 0, 500, 1000, 1500 and 2000 rpm are shown in black, red, blue, yellow and green lines respectively.

Two frequency peaks can be seen in the horizontal and vertical directions of the ring gear at 298.7 and 310.8 Hz without the Coriolis effect (Figures 4-17 (a) and (b)). When the carrier is rotating at 500 rpm, there is a little difference in the resonance frequencies. The difference becomes obvious at the carrier speeds above 1000 rpm. In the rotational directions, there is no difference in the resonance frequencies with and without the Coriolis effect. This implies that Coriolis effect has no influence on the rotational modes of the ring because of its high torsional stiffness i.e. the ring gear is effectively stationary.

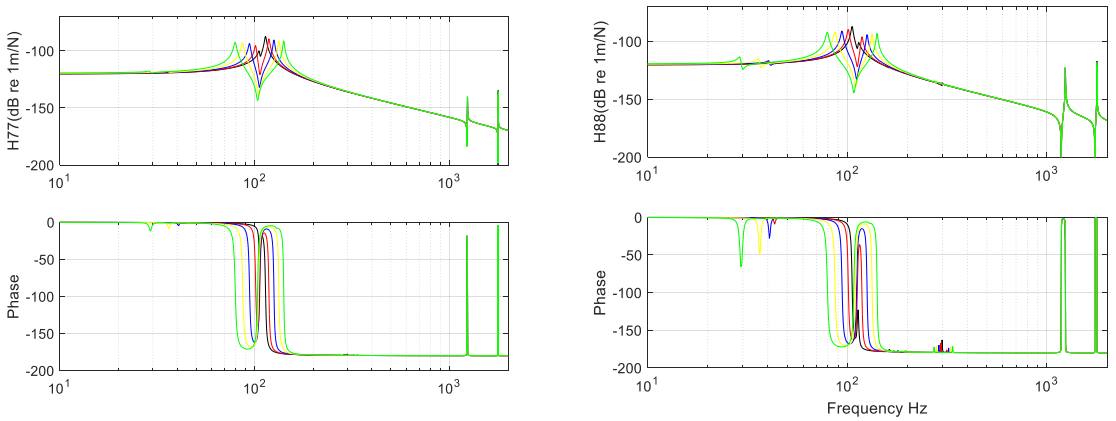

(a) (b)

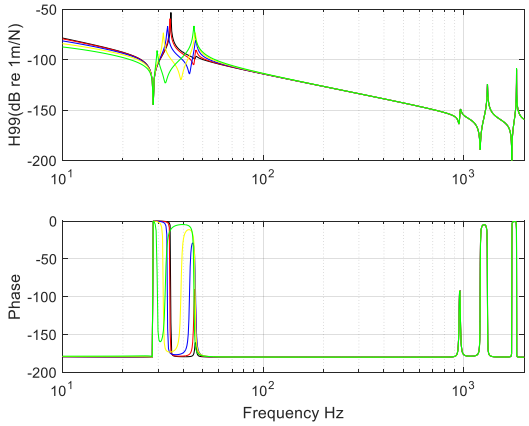

(c)

Figure 4-18 Predicted point receptance of the sun gear in the (a) horizontal, (b) vertical and (c) rotational directions at different speedsThe point receptances at 0, 500, 1000, 1500 and 2000 rpm are shown in black, red, blue, yellow and green lines respectively.

There is a low-amplitude peak on the sun gear at 105.7 Hz without the Coriolis effect, while the resonance frequencies at the carrier speed above 500 rpm can be seen at lower frequencies (Figure 4-18 (a) and (b)). As in the case of the carrier, the resonance frequency at 0 and 500 rpm are not significantly different from each other with a difference of only 4 Hz. The case is different for excitations above 1000 rpm. The higher the carrier speed the lower the resonance frequencies. The second mode was excited in the absence of Coriolis effect with resonance occurring at 113.7 Hz. In this mode, the resonance frequency is increasing as the carrier speed is increasing.

In the rotational direction (Figure 4-18 (c), the frequency of the corresponding to a rotational mode is 34.7 Hz when there is no Coriolis effect. As the carrier speeds increases, the resonance frequencies are reducing, although there is no significant difference between the frequencies excited at 0 and 500 rpm. Another rotational mode was excited at 46.1 Hz for a stationary coordinate system while the other resonance frequencies at for rotational speeds above 500 rpm are not significantly different. This shows again that the Coriolis effect does not have a significant influence on the rotational modes of the system at high carrier speeds.

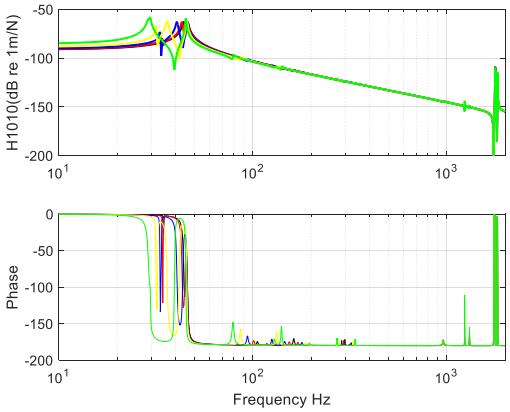

(a)

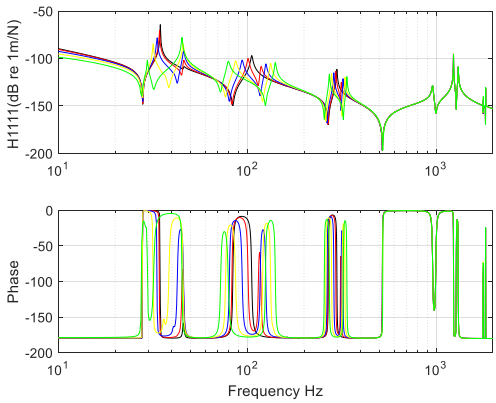

(b)

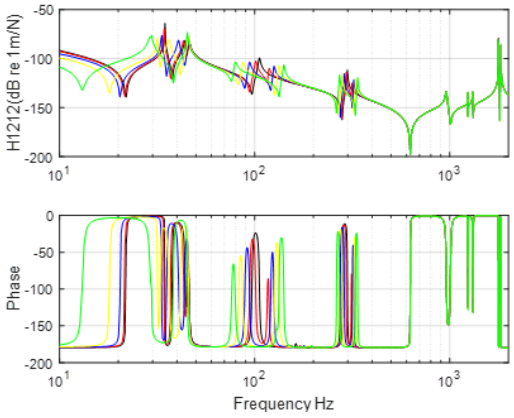

(c)

Figure 4-19. Predicted point receptance of the first planet gear in the (a) horizontal, (b) vertical and (c) rotational directions at different speeds The point receptances at 0, 500, 1000, 1500 and 2000 rpm are shown in black, red, blue, yellow and green lines respectively.

The point receptances of the first planet gear are shown in Figures 4-19. The corresponding point receptances of the second planet gear are in Appendix 5, because they are identical. A careful observation shows that a rotational mode at 34 Hz as shown in Figure 4-18 (a) was not visible when the carrier is not rotating but can be seen at the speed of 500 rpm. It is obvious for this mode that the resonance frequencies are decreasing as the carrier speed increases. Also, at a translational mode 44 Hz when there is no Coriolis effect, the frequencies are decreasing with increased carrier speed. The carrier speed has no significant effect on another rotational mode excited at 46.1 Hz. In Figure 4-18 (b), the resonance frequencies at 34.7 Hz, 105.7 and 298.7 Hz are decreasing with increased carrier speed because they translational mode. Although there are no peaks at 113.7 and 310.8 Hz when there is no Coriolis effect, but resonance peaks can be seen at 118.7 and 315 Hz when the carrier speed is 500rpm. The resonance frequencies are increasing at these two frequencies with increased carrier

speed. The two frequencies correspond to two translational modes. The resonance frequency of a rotational mode at 46.1 Hz remain significantly unchanged as well as the resonance frequencies from 959.7 Hz and above. The same trend in the vertical direction of the planet frequency response can be seen in the response at the rotational direction.

In general, the trend in the responses considering the Coriolis effect depends on the mode type. In other words, the resonance frequencies decrease as the carrier speed increases for frequencies excited between 34 and 105 Hz but with no significant effect on the rotational modes. The resonance frequencies are either decreasing or increasing as the carrier speed increases for frequencies between 118.7 and 315 Hz. All the modes excited (both rotational and translational modes) above 959.7 Hz remain unchanged with increasing carrier speed, therefore the frequencies excited within this range does not change even by a small amount due to Coriolis effect. This observation is peculiar to a two-planet model.

The frequency map which shows how the carrier speed is affecting the undamped natural frequencies is shown in Figure 4-20.

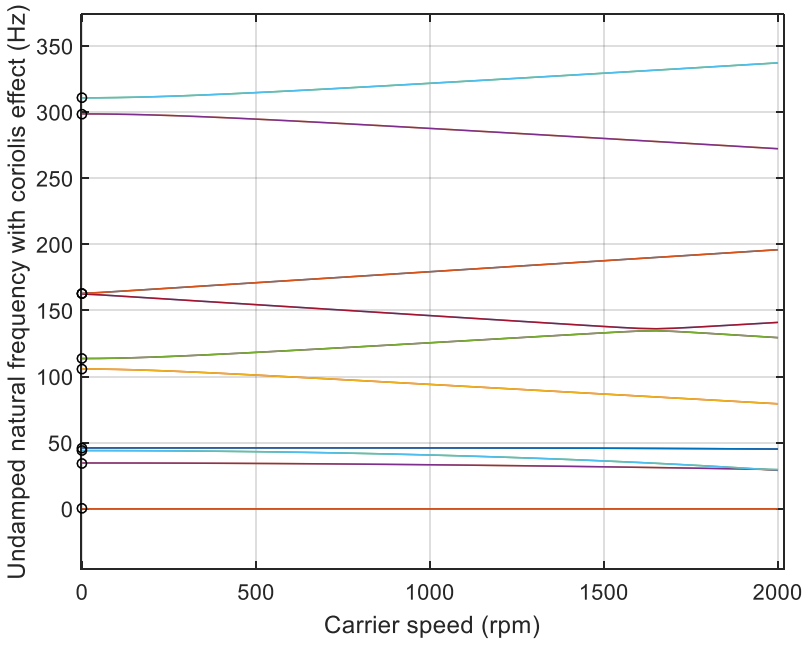

Figure 4-20 Zoomed view of a frequency map showing the split at 162.5 and 162.9 Hz as the carrier speed increases for a two-planet model.

The frequency map shows two translational modes number 7 and 8 at 162.5 and 162.9 Hz which split as the carrier speed is increases.

4.9 Location of the poles in the s-plane

The positions of the damped poles in the s-plane are presented to see if the Coriolis effect can produce shifts to the right hand side of the complex plane which indicates potential instability in the system.

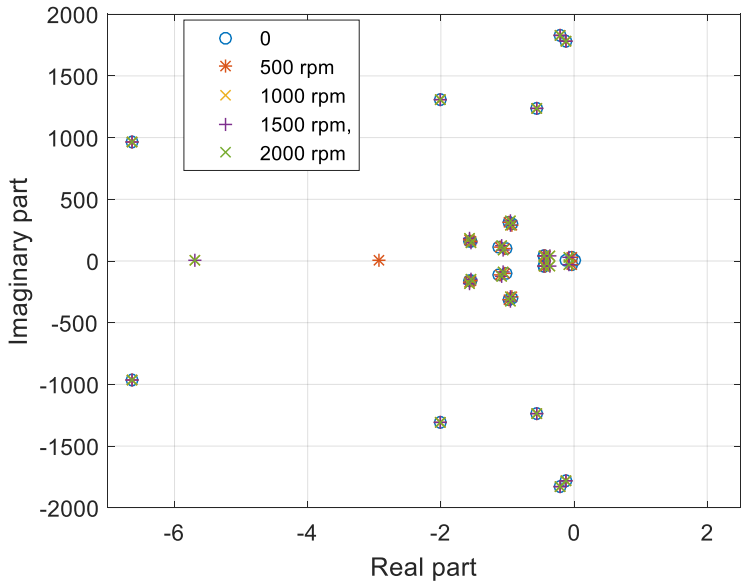

Figure 4-21 Positions of the damped poles in the s-plane at different carrier speeds.

Figure 4-21 shows that the damped poles are not significantly affected by the Coriolis effect due to the rotational coordinate system which is attached to the carrier. Also the poles are not shifting to the right hand side due to the high carrier speed which indicate potential instability in the system.

4.10 Conclusions

A suitable vibration test rig for a planetary gear system has been designed and developed for vibration tests and model validation. The test rig was configured such that an accelerometer can be mounted on the carrier, ring, sun and planet gear separately at the same time when they are stationary or rotating. The novelty in this is that, the independent vibration of each of them can be measured with the accelerometers rotating with the components during operation. Also, the test rig was built in such a way that it will be easier to assemble or disassemble when necessary.

The configuration of the test rig makes it possible to be used for experimental estimation of the bearing stiffnesses of the carrier, ring, sun and planet gears when it is not rotating. The estimated bearing stiffnesses were compared to the stiffnesses determined analytically and the ones of analytical are significantly larger. The estimated bearing stiffnesses will be used instead of the analytical ones. The ratio of the horizontal to the vertical bearing stiffness was also investigated and compared with

the results in the literature [48]. It shows that the ratios are close for cases of the sun and planet bearing. The mesh stiffness was also determined using a fitting method which includes the measured natural frequencies. This is another novelty in this chapter as the sun-planet and planet-ring mesh stiffnesses were estimated by a fitting method. The values of both the bearing and mesh stiffnesses will be used in the lumped parameter analytical model to predict both the free and forced responses of the planetary gear in the subsequent chapters.

The effect of carrier speed (i.e. Coriolis effect) on the modal damping ratios of the system was investigated. Out of fifteen modes, it shows there is no significant change on the modal damping ratios from the first to the eighth mode while the damping ratios from ninth to the fifteenth mode remain unchanged.

Also the effect of the carrier speed on the resonance frequencies was studied for each component in the different directions. In general, the dynamic behaviour is not significantly affected by a Coriolis effect at a carrier speed below 500 rpm. Above 500 rpm the behaviour may seem to be different until 1000 rpm where the change in frequency is obvious for the translational mode. The Coriolis effect either decreases or increases the resonance frequencies in the component does not have a significant effect on the rotational mode excited. All the excited modes (both rotational and translational) above 960 Hz remain unchanged with increase in the carrier speed, therefore they are not influenced by the Coriolis effect probably because of higher stiffness. It was discovered that there is a translational mode (approximately 163 Hz) with a multiplicity of two in the model with two planet gears. In this case, the stiffness values of the bearings have reduced compare to the one in chapter 3. Therefore, the frequency will split at high carrier speeds when using a rotating frame of reference.

The next chapter focuses on modal testing carried out on the test rig when it was stationary. The results of the modal test will be compared to the predictions from the analytical model.

Chapter 5 Comparison between the predictions and measurements with forced vibration response

In the previous chapter the parameters needed for the analytical model have been determined. This chapter focuses on comparing the predictions from the analytical model with the measured natural frequencies. In this case, a fixed frame of reference was used to analyse the dynamic model, and the anisotropic bearing stiffnesses determined in Chapter 4 were used. For the modal test, the frequency and loss factor are shown.

The forced response at the mesh excitation frequency was predicted using the analytical model and this was compared to the measured response from the spinning test.

5.1 Experimental modal analysis: non-rotating planetary gear

The processing of the vibration data from the planetary gear system was carried out using modal analysis, in order to validate the results obtained from the lumped parameter model.

The set-up for the modal testing is shown in Figure 5-1. The impact hammer with a steel tip (model number PCB 086C03) was used. The sensitivities of the hammer and the accelerometers are 2.25 mV/N and 1.00 mV/ms^2 respectively. The two accelerometers (model number PCB 352C22) measuring the response in the horizontal (x) and vertical (y) directions of the planetary gear components were acquired. The frequency span was set to be 10 kHz while the number of sampling points is 3200. The sampling time is thus 0.32 s. The frequency resolution, df, equals 3.125 Hz which is good enough to distinguish between two close natural frequencies. The accelerometers were carefully mounted with wax on the components to be tested in both the horizontal and vertical directions. The clipped data were rejected while the signals with good coherence were accepted for processing. The acquired data namely acceleration and force for computation of the accelerance is converted from analogue voltage signals by the analyser. The natural frequencies and loss factors were subsequently determined from processing the point accelerance measured on each component of the system.

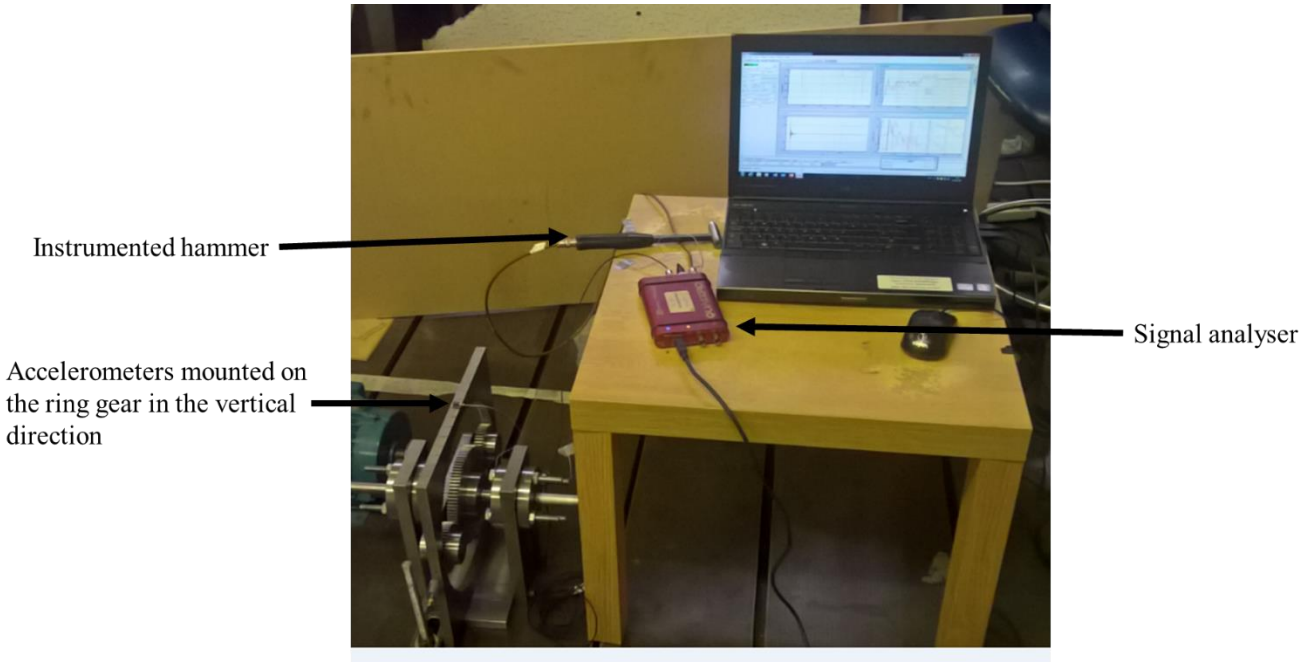

Figure 5-1 Planetary gear vibration test on the ring gear in both the horizontal and vertical directions.

5.2 Validation of the analytical model

Viscous damping was added into the analytical model in parallel to the bearing stiffness of the carrier, ring, sun and the planet gears based on the measured loss factor measured at the first excited mode. However, there are some cases where the viscous damping estimated is slightly greater than the one used. For instance, the loss factor measured for the first excited mode (84.37 Hz) of the carrier in the horizontal direction is 0.3. This implies the damping ratio is 0.15 but 0.2 was used in the analytical model which is not significantly different.

The frequency responses in the rotational direction are not shown in the model validation, because they were not measured. The parameters in Tables 4-4 and 4-5 were used to determine analytically the natural frequencies and mode shapes of the system. In this case, the bearing stiffnesses are not the same in all directions, so a fixed frame of reference was chosen as the coordinate system. The analytical and measured point receptances of the carrier, sun, planet and ring gears were plotted and shown together for each them in *x* and *y* directions respectively.

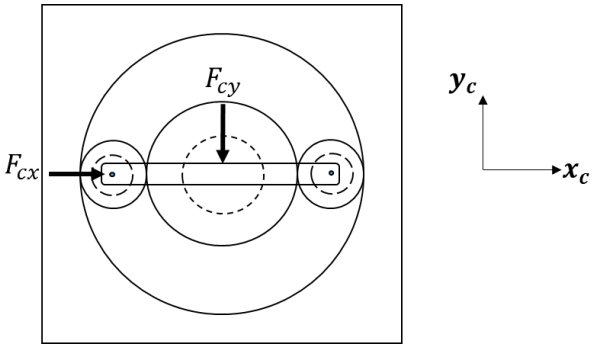

Figure 5-2 Locations where the carrier was excited in x and y directions.

A unit force, F_{cx} was applied to the carrier in the horizontal direction and subsequently in the vertical direction, F_{cy} as shown in Figure 5-2 to show the points of excitation and measurement in the experimental and the analytical models. An accelerometer mounted on the opposite side measures the point accelerance which was later converted to receptance. The point accelerance and Nyquist circle at 84.37 Hz are shown in Figures 5-3 (a) and (b). The frequencies of the modes measured on the carrier in this direction are shown in Table 5-1.

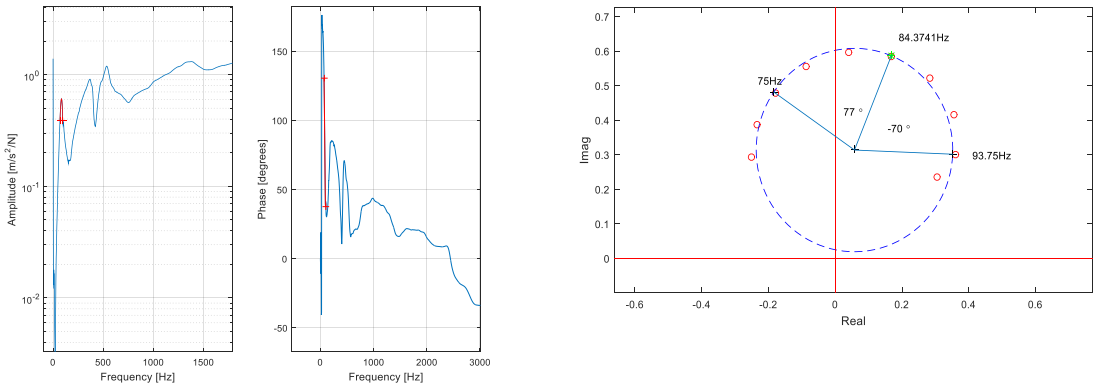

(a) (b)

Figure 5-3 (a) Point accelerance and (b) Nyquist circle of the carrier in *x* directions at 84.37 Hz.

Table 5-1 Modal parameters of the carrier in x direction

Mode	Frequency (Hz)	Loss factor	Modal diameter	Phase	Angle to +ve imag axis (deg)
1	84.37	0.300	0.589	+ve	-22
2	365.80	0.180	0.478	+ve	-45
3	537.47	0.114	0.592	+ve	-64
4	7631.21	0.009	2.140	-ve	-168

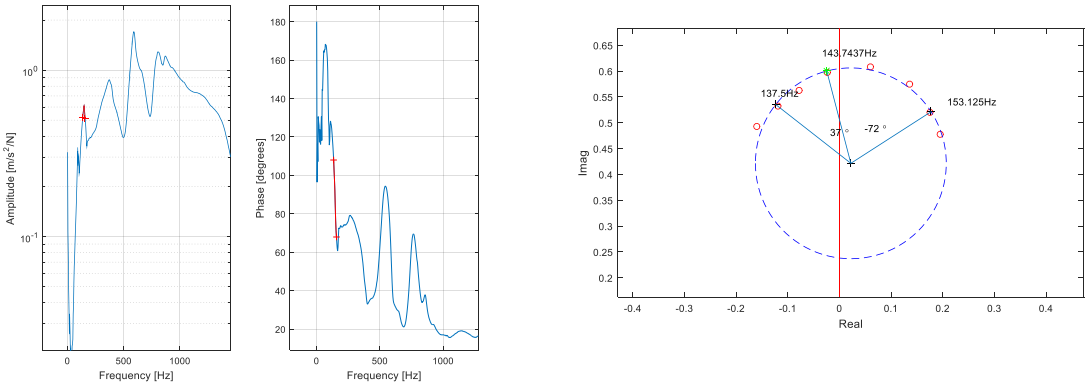

(a) (b)

Figure 5-4 **(a) Point accelerance and (b) Nyquist circle of the carrier in y directions at 143.7 Hz.**

The point accelerance and Nyquist circle at 143.7 Hz are shown in Figures 5-4 (a) and (b). The frequencies and other modal parameters measured on the carrier in y direction are shown in Table 5-2.

Table 5-2 Modal parameters of the carrier in y direction

Mode	Frequency (Hz)	Loss factor	Modal diameter	Phase	Angle to +ve imag axis (deg)
1	143.70	0.204	0.369	+ve	15
2	369.00	0.215	0.395	+ve	-34
3	587.60	0.073	1.130	+ve	-24
4	1984.00	0.053	8.060	+ve	-10
5	3781.00	0.067	9.460	+ve	17
6	7628.00	0.079	11.100	-ve	-114

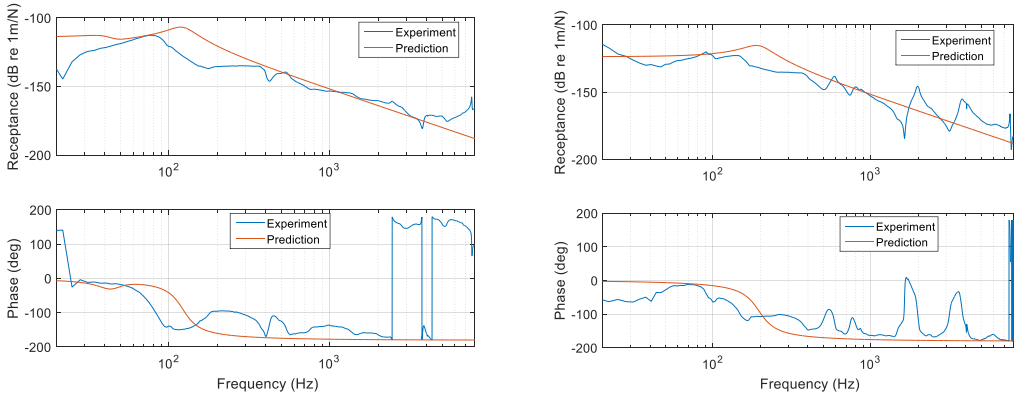

(a) (b)

Figure 5-5 Point receptance of the carrier in both the (a) *x* and (b) *y* directions.

The predicted and measured receptances are shown graphically for each direction for comparison. Figure 5-5 (a) shows the receptance in the *x* direction where the coherence of the measured signal is acceptable from 31.5 Hz. There is poor matching between two damped peaks at 84.37 and 121.9 Hz from the predicted and measured results respectively. The predicted mode, corresponding to 121.9 Hz, is a translational mode where the carrier, sun and planet gears are translating. There is a significant amount of damping in the measured receptance because the peak is not sharp. This may be due to dissipation from the bearing and friction or coulomb damping between the teeth of the sun and planet gears in the system. The case is different when the planetary gear system is rotating, this will be shown in Chapter 6. In the *y* direction of the carrier (Figure 5-5 (b)), the measured and predicted receptances show a better degree of agreement. The coherence of the measured signal in this direction is good from 44 Hz. The first excited mode corresponding to 195 Hz is a translational mode. There are two peaks at 1984 and 3781 Hz in the measured frequency responses which were not predicted by the analytical model.

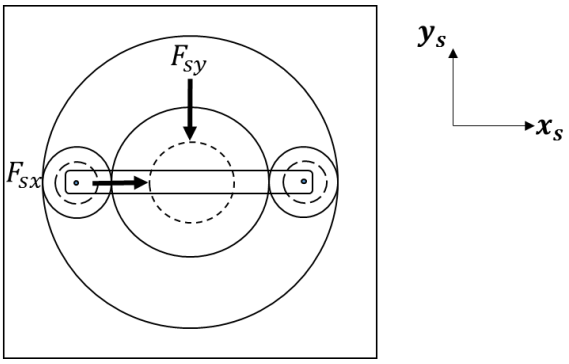

Figure 5-6 Locations where the sun gear was excited in *x* and *y* directions.

The sun gear was excited with an instrumented hammer in the horizontal direction and subsequently in the vertical direction as shown in Figure 5-6.

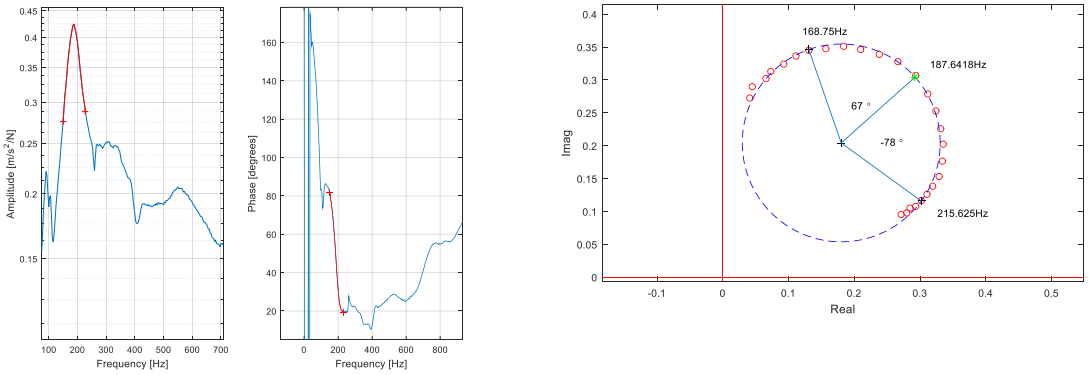

(a) (b)

Figure 5-7 (a) Point accelerance and (b) Nyquist circle of the sun gear in x direction at 187.6 Hz.

The point accelerance and Nyquist circle are shown in Figure 5-7 (a) and (b) while the modal parameters are shown in Table 5-3.

Table 5-3 Modal parameters of sun gear in x direction

Mode	Frequency (Hz)	Loss factor	Modal diameter	Phase	Angle to +ve imag axis (deg)
1	90.66	0.204	0.102	+ve	17
2	187.64	0.339	0.301	+ve	-48
3	1341.23	0.217	0.514	+ve	-52

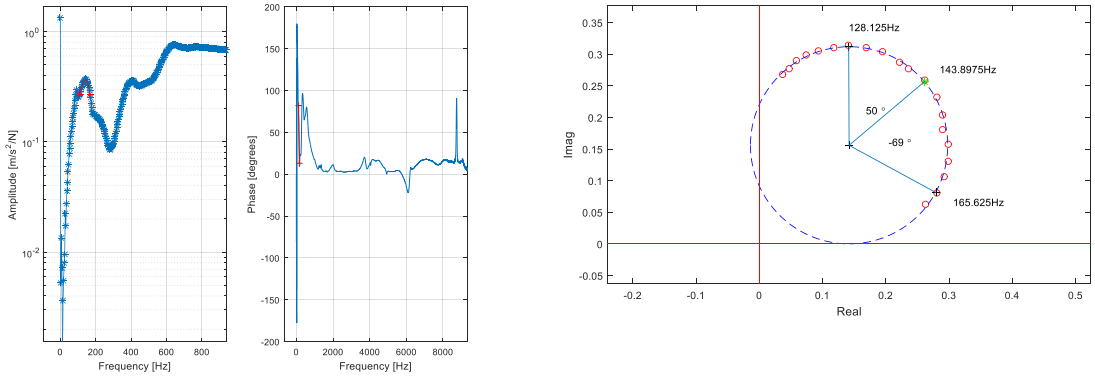

(a) (b)

Figure 5-8 **(a) Point accelerance and (b) Nyquist circle of the sun gear in y direction at 143.9 Hz.**

Table 5-4 Modal parameters of sun gear in y direction

Mode	Frequency (Hz)	Loss factor	Modal diameter	Phase	Angle to +ve imag axis (deg)
1	143.9	0.453	0.312	+ve	-52

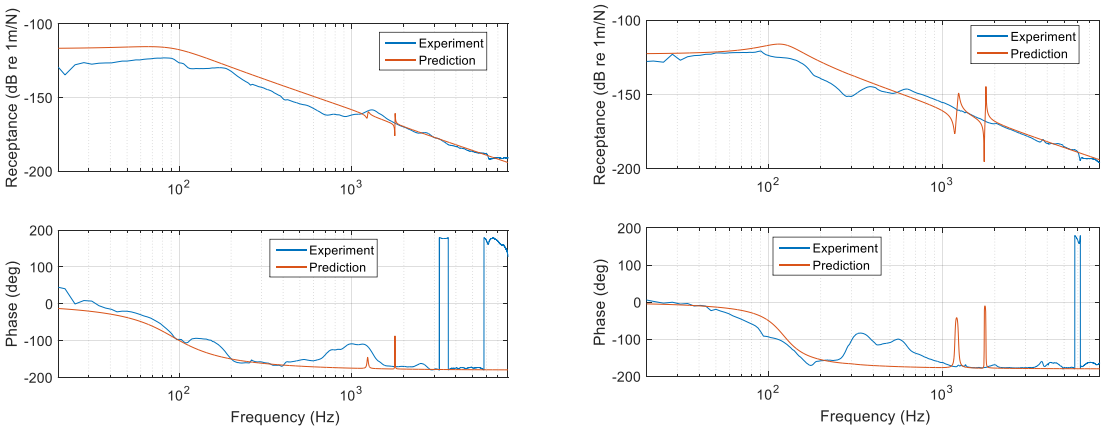

(a) (b)

Figure 5-9 Point receptance of the sun in both the (a) x and (b) y directions.

The measured and predicted receptances in the *x* direction are shown in Figure 5-9 (a), where the coherence for the measurements is good from 44 Hz. Both the measured and predicted receptances show a fair degree of agreement especially between 2.5 to 8 kHz. There is a peak in the predicted receptance (1779 Hz) which was not measured. This is more significant in the predicted receptance in the *y* direction (Figure 5-9 (b)) as well as another peak at 1237.3 Hz. The coherence is good from 35 Hz in the vertical direction. The corresponding modes for these two peaks as predicted and shown in Table 5.1 are translational modes.

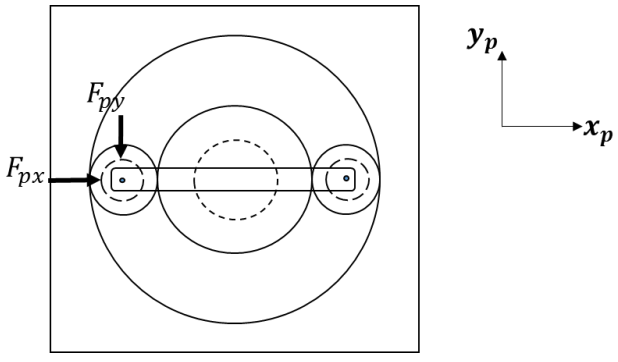

Figure 5-10 **Locations where the planet gear was excited in x and y directions.**

The planet gear was subsequently excited in the same way as shown in Figure 5.10 and the natural frequencies are shown in Tables 5-5 and 5-6.

Table 5-5 Modal parameters of planet gear in x direction

Mode	Frequency (Hz)	Loss factor	Modal diameter	Phase
1	184.40	0.315	0.584	+ve
2	362.45	0.151	0.280	+ve

Table 5-6 Modal parameters of planet gear in y direction

Mode	Frequency (Hz)	Loss factor	Modal diameter	Phase	Angle to +ve imag axis (deg)
1	156.36	0.465	1.46	+ve	-30
2	356.40	0.354	1.26	+ve	-61
3	2034.50	0.055	1.89	+ve	-69

The accelerance and Nyquist circle are in Appendix C

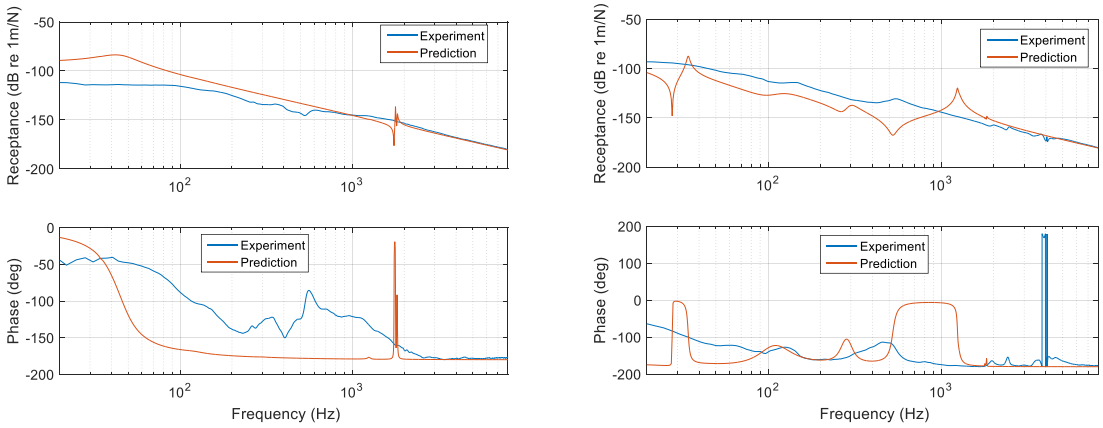

(b) (c)

Figure 5-11 **Point receptance of the planet in both the (a) x and (b) y directions.**

The measured and predicted receptance in the *x* direction are shown in Figure 5-11 (a). The coherence of the measured signal is acceptable from 40 Hz upwards. For the model, two predicted resonance peaks can be seen in the horizontal direction at 42.3 Hz and 1779 Hz. The peak at 42.3 Hz is damped while the second one at 1779 is lightly damped. Both peaks correspond to the class of translational modes although the planet gears are moving in the three translational and rotational directions. The measured and predicted responses only agree at frequencies above 2 kHz. Also, the predicted receptance show two peaks at 34.6 and 1237 Hz in the *y* direction (Figure 5-11 (b)). The coherence of the measured signal is acceptable from 13 Hz. The first excited mode corresponds to a rotational

mode while the second one at 1237 Hz is a translational mode. This implies from the predictions that both translational and rotational modes can be excited in the *y* direction of the planet gears probably because it is tangential to the rotational coordinate of the carrier and planet gears. The behaviour of the measured and predicted results agrees at frequencies above 3 kHz.

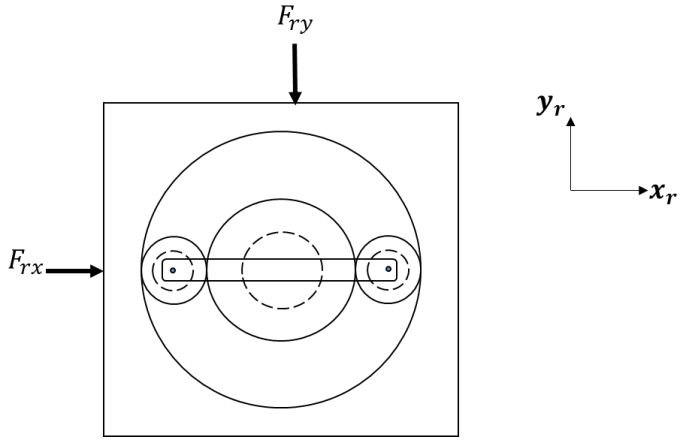

Figure 5-12 **Locations where the ring gear was excited in *x* and *y* directions.**

The ring gear was subsequently excited in the same way as shown in Figure 5-12. The modal parameters are shown in Tables 5-7 and 5-8.

Table 5-7 Modal parameters of ring gear in x direction

Mode	Frequency (Hz)	Loss factor	Modal diameter	Phase	Angle to +ve imag axis (deg)
1	275.00	0.175	1.02	+ve	-55
2	506.20	0.125	1.20	-ve	-164
3	2281.43	0.053	1.08	+ve	-15
4	4200.00	0.078	22.20	-ve	-177
5	7780.00	0.052	22.00	-ve	108

.

Table 5-8 Modal parameters of ring gear in y direction

Mode	Frequency (Hz)	Loss factor	Modal diameter	Phase	Angle to +ve imag axis (deg)
1	515.56	0.140	4.38	-ve	173
2	1117.00	0.118	1.01	-ve	138
3	1640.57	0.039	2.03	-ve	130
4	2300.00	0.054	6.42	-ve	158
5	4249.80	0.051	11.90	-ve	-163

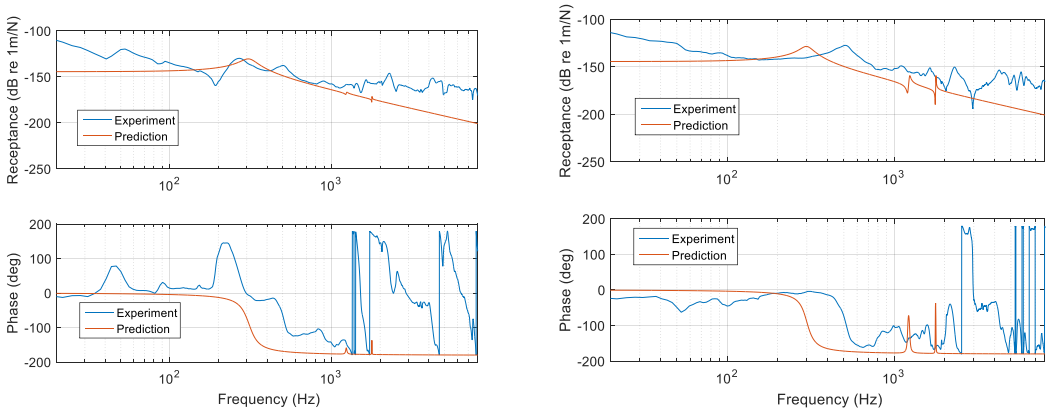

(b) (c)

Figure 5-13 Point receptance of the ring in both the (a) x and (b) y directions.

Figure 5-13 (a) shows both the measured and predicted receptances in the *x* direction. The measured signal from this direction is acceptable from 50 Hz. A peak frequency was measured at 275 Hz and another one was predicted at approximately 311 Hz. The difference between them is significant. The predicted frequency is related to a translational mode where only the ring gear is translating among the central members of the planetary gear system. In the *y* direction (Figure (5-13 (b)), the measured signal is acceptable from 30 Hz. A damped peak at 299 Hz was predicted which is a frequency of translational mode while a measured peak can be seen at 516 Hz. There is poor agreement between the peaks and the behaviour at low and high frequencies in this direction. This may be due to the fact that there is a limitation in measuring a reasonably accurate stiffness of the ring gear in the *y* direction as mentioned earlier in Chapter 4.

Table 5-9 Predicted and measured natural frequencies of a two-planet model of a planetary gear system.

S/N	Predicted natural frequencies (Hz)	Mode type	Measured natural frequency (Hz)	% difference
1	0.00	Rotational mode of the carrier and sun	-	
2	34.60	Rotational mode	-	
3	42.30	Translational mode	-	
4	46.10	Rotational mode of the carrier and sun of the ring	-	
5	92.00	Translational mode	90.66	1.48
6	121.90	Translational mode	143.70	15.17
7	122.90	Translational mode	143.70	14.47
8	195.40	Translational mode	187.64	4.14
9	298.80	Translational mode	275.00	8.65
10	310.90	Translational mode of ring gear only	356.64	12.83
11	959.70	Rotational mode	-	
12	1237.30	Translational mode	1117.00	10.77
13	1311.10	Rotational mode	1341.23	2.25
14	1778.80	Translational mode (carrier moves only in *x* direction while ring and planet moves in *x* and *y* directions)	1640.57	8.43
15	1830.50	Rotational mode of both the ring and sun gears	1984.00	7.74

Table 5-9 shows the predicted and measured natural frequencies of the particular planetary gear system modelled. The percentage difference was estimated between the measured and predicted natural frequencies and it shows that the sixth, seventh and tenth modes are not as accurate as for the other modes because their natural frequencies greater than nine percentage points higher than the predicted ones. The mode shapes of corresponding to 0, 92 and 122.9 Hz are shown in Appendix C.

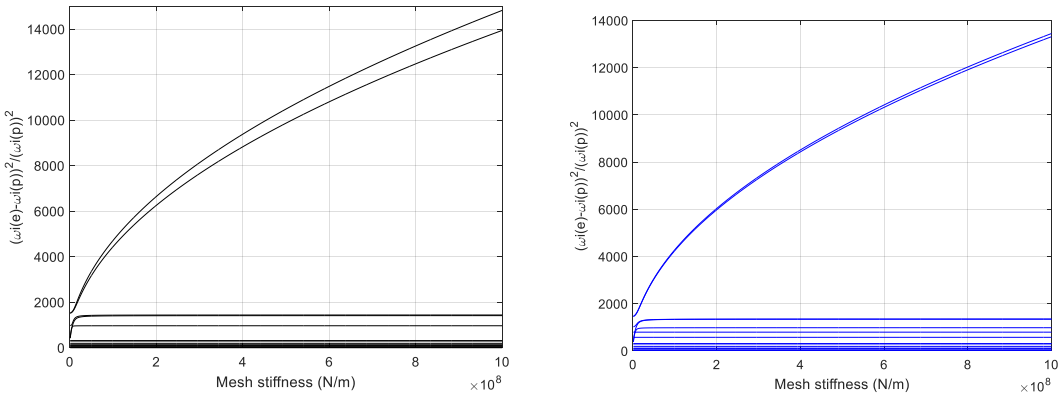

(a) (b)

Figure 5-14 Sensitivity of the natural frequencies to the (a) sun-planet mesh stiffness and (b) planet-ring mesh stiffness.

The sensitivity of the sun-planet and planet-ring mesh stiffness was determined using the analytical model and shown in Figures 5-14 (a) and (b). It shows that the natural frequencies from 1779 Hz are sensitive to these mesh stiffnesses while the lower frequencies are not significantly sensitive to the mesh stiffnesses. This is in agreement with the study shown by Lin and Parker where they show the sensitivity of the natural frequencies to the sun-planet mesh stiffness [22]. The method used to estimate the sun-planet and planet-ring mesh stiffnesses is relatively simpler. The values of the mesh stiffnesses determined are believe to be close to the accurate value.

5.3 Forced vibration responses

This section focuses on studying the response of planetary gear system to transmission error as an externally applied force at the mesh. The force is assumed harmonic (i.e. sinusoidal) for easier calculation and interpretation. The force was added by adding a forcing function to the equation of motion (3.49), as previously derived in chapter 3 of this report. A rotating frame of reference was chosen as a coordinate system for this study. The mesh force was applied at the ring-planet and sun-planet mesh of the system.

The response is obtained in time domain by writing equation (3.49) in state space form and using the ODE 45 solver in MATLAB to solve the differential equation written in equation (5. 1).

$$\frac{d}{dt}\begin{pmatrix}\mathbf{q}\\ \dot{\mathbf{q}}\end{pmatrix} = \begin{bmatrix}\mathbf{0} & \mathbf{I}\\ \mathbf{M}^{-1}(\mathbf{K}_b + \mathbf{K}_m + \Omega_c\mathbf{K}_d - \Omega_c\mathbf{K}_\Omega^2) & \mathbf{M}^{-1}(\Omega_c\mathbf{G} + \mathbf{C}_b)\end{bmatrix}\begin{pmatrix}\mathbf{q}\\ \dot{\mathbf{q}}\end{pmatrix} + \begin{pmatrix}\mathbf{0}\\ \mathbf{M}^{-1}\mathbf{F}_m\end{pmatrix} \qquad (5.1)$$

The notations have been defined previously in equation 3.50 except for $\mathbf{q}, \dot{\mathbf{q}}$ and $\boldsymbol{F_m}$ which denotes the generalized displacement, velocity and force vectors respectively. Therefore, the component force

vectors in a force vector $\mathbf{F}_m$ on the carrier, ring, sun and planet gears respectively are written in equations (5.2 - 5.6).

$$\mathbf{F}_c = \begin{bmatrix} 0 & 0 & 0 \end{bmatrix}^T \tag{5.2}$$

$$\mathbf{F}_r = \begin{bmatrix} K_{rn} e_{rn} \sin\psi_{rn} & K_{rn} e_{rn} \cos\psi_{rn} & K_{rn} e_{rn} \end{bmatrix}^T \tag{5.3}$$

$$\mathbf{F}_s = \begin{bmatrix} K_{sn} e_{sn} \sin\psi_{sn} & K_{sn} e_{sn} \cos\psi_{sn} & K_{sn} e_{sn} \end{bmatrix}^T \tag{5.4}$$

$$\mathbf{F}_n = \begin{bmatrix} -(K_{rn} e_{rn} + K_{sn} e_{sn}) \sin\alpha & -(K_{rn} e_{rn} + K_{sn} e_{sn}) \cos\alpha & -(K_{rn} e_{rn} + K_{sn} e_{sn}) \end{bmatrix}^T \tag{5.5}$$

Since it was assumed that the excitation force is time harmonic, then

$$e_{rn} = E_{rn} \sin\omega_m t \tag{5.6}$$

where, E_{rn} is the amplitude of the transmission error applied (0.00105 mm) between sun-planet and planet-ring meshes.

The transmission error between planet and gear e_{rn} is assumed to be the same as sun-planet e_{sn}. The mesh frequency which is the product of carrier speed (Ω_c) and the number of teeth on the ring gear is denoted by ω_m. The harmonic force on the planet gear is equal and opposite of the forces on the sun and ring gears. The predicted results were shown in Figures 5-15 and 5-16.

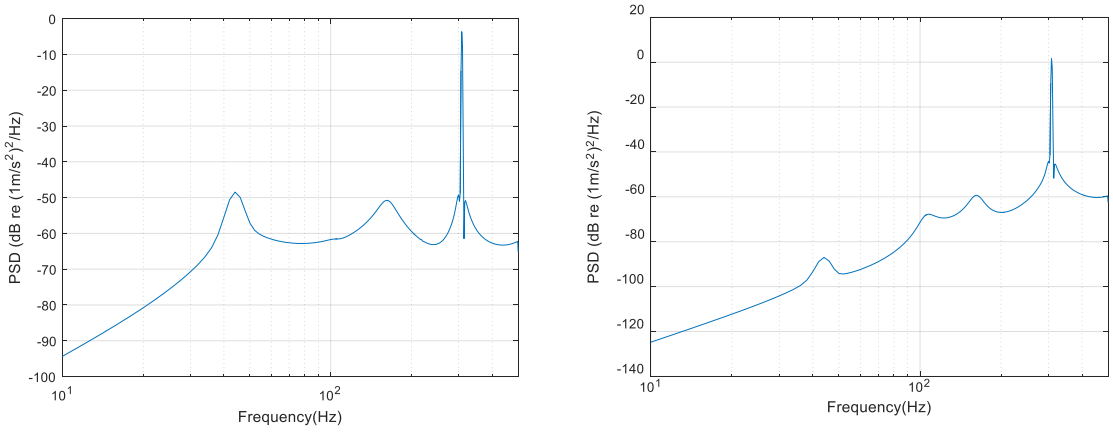

(a) (b)

Figure 5-15 The predicted power spectral density of the carrier radial acceleration response at a rotational speed of 100 rpm in the (a) horizontal and (b) vertical directions.

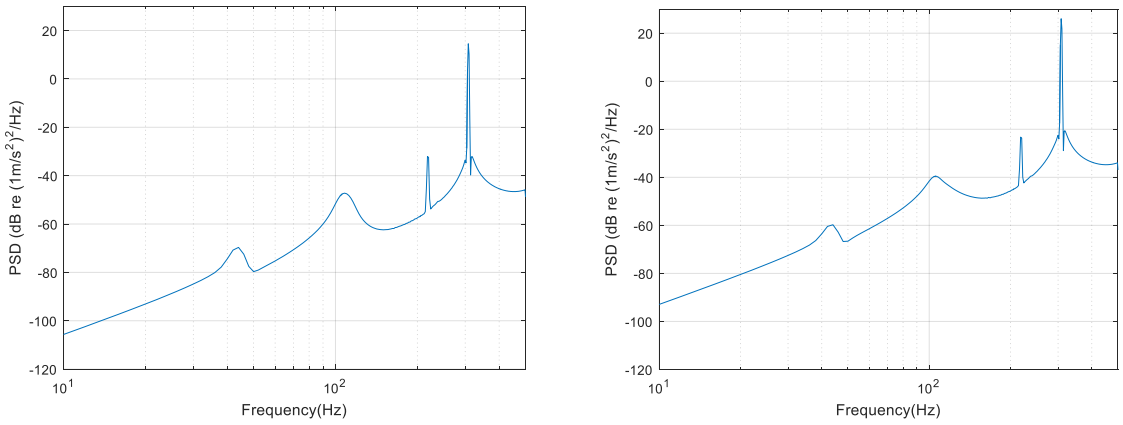

(a) (b)

Figure 5-16 The predicted power spectral density of the sun gear radial acceleration response at a rotation speed of 100 rpm in the (a) horizontal and (b) vertical direction.

Figures 5-15 (a) and (b) show the predicted acceleration power spectral densities (PSD) of the carrier in both the horizontal and vertical directions with the mesh frequencies dominating the spectrum. In this case, the carrier speed is 100 rpm which makes the mesh frequency 308 Hz. There are some other frequencies in the spectrum as shown in Figure 5-15 (a) which are 44 and 162 Hz while another one was excited at the vertical direction Figure 5-15 (b) at 162 Hz. Figure 5-16 (a) and (b) show the acceleration PSDs of the sun gear in the horizontal and vertical directions. They also show excitation at 44 Hz.

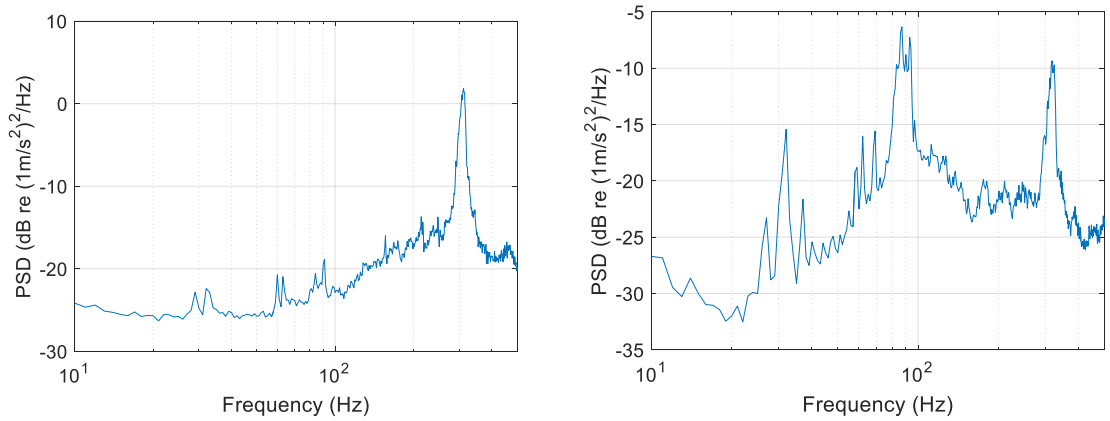

(a) (b)

Figure 5-17. The measured power spectral density of the acceleration response at a rotational speed of 100 rpm (a) Carrier in radial direction (b) Sun gear in radial direction.

Figures 5-17 (a) and (b) show the measured acceleration power spectral densities of the carrier and the sun gear in the radial direction respectively. The dominant frequency content in both figures is also the mesh frequency at 318 Hz. There is small difference in the predicted and measured mesh frequencies, because the ideal speed of the sun gear is supposed to be 295 rpm, but the actual speed is 305 rpm, hence the mesh frequency which is a function of speed increases. For a sun gear vibration (Figure 5-17 (b)), there are symmetric sidebands around a frequency at 32 Hz. The frequencies at the lower and upper side band are 27 and 37 Hz respectively. The measured speed of the sun gear is 305 rpm (5.08 Hz). It shows that the lower and upper sidebands are ± 5 Hz to the frequency at 32 Hz. This frequency may be associated with a particular fault on the sun gear. It shows that the experiment can detect more forces exciting the system than the model being considered. More investigations on some faults at lower frequencies are discussed in the next chapter.

5.4 Conclusions

The measured parameters of a planetary gear train were used in the analytical model and the frequency response was compared with that of the modal testing. Although the agreement is not perfect, the model seems to represent the main physical features of the system. Probably higher degree of agreement can be achieved if mesh damping was determined and included in the model. For the ring gear there is inaccuracy in measuring the stiffness in the vertical direction as discussed in chapter 4. Therefore for better agreement, the mesh damping and stiffness of the ring gear in the vertical directions must be accurately estimated. Also determined, was the sensitivity of the sun-planet and planet-ring mesh to the natural frequencies of the system; only the high natural frequencies (above 1311 Hz) are significantly affected by the mesh stiffness, the lower frequencies are governed by the bearing frequencies. The modal testing will help to distinguish between the frequencies that are related to natural modes and rotational speeds in the frequency spectrum of the spinning test.

The analytical model has been used to predict the mesh response of the system to mesh excitation. The next chapter will focus on the analysis of the results from the spinning test at different rotating speeds and loads as well as identification of vibration source in the system during operation.

The next chapter will focus on the spinning test where a planetary gear system is operating to transmit power from the input to the output. Different electrical loads will be applied and the independent vibration of the carrier, sun and planet gears will be measured. Also vibration source in the system will be identified using a method known as Principal component analysis (PCA) where the vibration level of the individual component will be determined in order of preponderance.

Chapter 6 Spinning Testing and Vibration Source Identification

In the last chapter, the natural frequencies and some other modal parameters of a planetary gear system were measured using modal testing. The measured natural frequencies will be one of the frequencies of interest in this chapter where a spinning test will be carried out to know the effect of loads and speeds on the response of the system during operation.

Therefore, this chapter focuses on the dynamic response of the planetary gear train (PGT) when rotating at different rotational speeds under different loads and identification of vibration sources. This is necessary, because it will show how the system behaves before active control is implemented. Also with the natural vibration mode, the vibration response of the carrier, sun and planet gears at mesh frequencies will be investigated. Investigation will be done to determine their level of vibration responses when changing the load and the rotational speed and these will be compared. Also, a method known as principal component analysis (PCA) will be applied to identify the vibration sources in the planetary gear for at different speeds.

One of the sources of vibration in planetary gears is the vibration generated from the sun-planet mesh as explained by Miao and Zhou [60]. This mesh vibration is transmitted to the stationary casing via the sun gear, its shaft and bearing. Another transmission path as explained by them is the vibration from the sun-planet mesh which passes through the planet gear and its bearing to the carrier and its shaft and from there to the carrier bearing and to the casing of the gearbox. A second source is the mesh vibration generated from the planet-ring mesh. This vibration is transmitted directly to the ring gear and the casing. However, it was stated by McFadden and Smith [36], that if an accelerometer is placed on a stationary ring gear, the dominant vibration that can be measured by the accelerometer is the one generated by the planet-ring mesh. Therefore, it is believed that the true dynamic behaviour of the carrier, sun and planet gears may not be fully captured by accelerometers placed either on the stationary ring gear or casing. One of the benefits of measuring the response using a rotating frame of reference (i.e. where the accelerometers rotate with the component), according to Jarvinen [61] is that all the measured signals are from the true dynamics of the rotating components being measured. Vibration signals of a rotating component measured from fixed ring gear or casing (i.e. fixed frame of reference) are characterized by some factors (like signal distortion, vibration of the casing etc.) that do not correlate with the true motions of the rotating component. Smith said such a vibration signal is likely to contain a substantial amount of extraneous information [62]. In a case like this, time synchronous averaging (TSA) can be used to remove unwanted signals that are not related to the

component speed [6]. However, if there is a frequency relating to the natural mode, it will be filtered out of the frequency spectrum [5].

One of the main objectives of this chapter is to determine the effect of load and rotational speed on the dynamic response of a planetary gear system. These responses are measured independently on the components using MEMS accelerometers which rotate with them unlike what many researchers do. Section 6.1 covers the coordinate system used in measuring vibration response of planetary gears and causes of sidebands in the spectrum while section 6.2 covers the set-up and data acquisition. Section 6.3 covers the effect on the dynamic response when both the speed and the load are changing, the effect when the load is constant at varying speed and the effect when the speed is constant, and the load is changing. Another objective is to identify the vibration source using a statistical method known as principal component analysis (PCA). PCA can help to determine the optimal location where control force can be applied in the case of active vibration control. Therefore, section 6.4 focuses on the principal component analysis where the vibration sources of the planetary gear system were investigated. This was done by forming a correlation matrix using the PSDs of the measured signals. The singular value decomposition was utilized to determine the eigenvalues and the eigenvectors which are useful parameters in the vibration source identification. The evaluated virtual coherence assists in determining how much the principal components are contributing to each physical source.

6.1 Vibration measurement of planetary gears and coordinate system

An accelerometer mounted on the casing of a planetary gearbox measures a filtered vibration response of the original vibration signal characterized by a significant noise contamination. This makes it more challenging to process signal in order to detect fault successfully [5]. There are some experiments where a slip ring has been used with the instrumentation to measure the vibration of the rotating components. In this case, there may be some unwanted signals (noise) in the frequency spectrum due to electrical noise and contacts within the slip ring like the experiment conducted by Smith [62] and Ericson et al. [63] .

According to McFadden [36], most of the experiments where gear vibrations were investigated, the accelerometers are either mounted on a stationary member or the stationary casing. In this case, an accurate vibration amplitude may not be obtained because the level of vibration transmitted from the components to the casing may not be the actual vibration level of the rotating components. The accelerometer may capture some dynamic response that is not the response of the intended rotating component to be measured. De Smidt [64] suggested in his thesis after mounting accelerometers with slip rings on the carrier that with the future improvement in wireless technologies, the internal measurement of vibration of planetary gear will be more viable.

In this research, the response of the planetary gear is obtained experimentally by using wireless micro-electro-mechanical system (MEMS) accelerometers which can rotate with the planetary gear components. It is important to state that this kind of experiment is not common because the vibration of the rotating components cannot be measured by typically available accelerometers, which use cables to transmit signals. The MEMS accelerometers were mounted on each of the rotating components of the planetary gear, and their time histories were obtained. These sensors, give the possibility of measuring the vibration of the rotating elements on-site. The low frequency range associated with rotation gives the symptoms of basic mechanical faults like unbalance, misalignment, looseness etc. This frequency spans between one to ten multiplied by the rotational frequency [65]. These frequencies are measured by the MEMS accelerometers which helps to detect the misalignment and effect of load and rotational speed on it. The frequency response in this study was subsequently obtained by a Fast Fourier Transform (FFT) algorithm and analysed for interpretation.

6.1.1 Sidebands and its causes in planetary gear vibration signal

Most measured vibration and noise signals measured from planetary gear exhibit sideband around the mesh frequency [35]. On this note, it is necessary to discuss the basic meaning of sideband. Sideband is defined as a band of frequencies higher or lower than the centre or dominant frequency. The dominant frequency in this case is the mesh frequency. Sidebands are formed due to frequency, amplitude or phase modulation of the signal at the mesh. The frequency of the sidebands is equal to the mesh frequency plus and minus the rotational speed of the components in each case i.e. the carrier, sun and planet gears. For instance, if the frequency of the sideband is equal to the mesh frequency plus the rotational speed of a planet gear, it called an upper side band [36] and [66]. Conversely, if the sideband is equal to the mesh frequency minus the rotational speed of a planet gear it is called a lower side band.

According to Inalpolat and Kahraman [35] there will be sideband in planetary gear vibration signals if

- the planet load sharing characteristics impact the amplitude modulation as well as the dynamic mesh forces.
- the planet passes through the location of a fixed transducer mounted on a stationary ring gear or casing. In this case there will be variation in the amplitudes of vibration which causes amplitude modulation.
- there are eccentricities and run-out errors of the gears and the carrier, tooth thickness, tooth to tooth spacing and indexing errors.

- there is a change in the deformation of the components with planet pass, tooth pass or ring gear spline pass as observed by the gears.
- there is a large number of manufacturing errors. These can cause variations which are capable of modulating the dynamic gear mesh forces in three different forms which are amplitude, frequency and phase modulations.

6.2 Experimental set up and data acquisition

The test rig without load has been described in the previous chapter. Here, load has been attached to the rig as shown in (Figure 6-1 (a)). The test rig comprises mainly a carrier, a ring, a sun and two planet gears, two bearings with housing, a generator, a resistor box, two timing belts and a speed regulating unit. The ring gear is fastened to the base to make it stationary. There are two identical bearing housing supports, one for the sun gear and the other for the carrier. The maximum capacity of the generator (Parvalaux model number 329321/06G) as shown in Figure 6-1 (a) is 125 W while the maximum speed is 3000 rpm. It was used to generate the electrical power at the output. The field windings of the motor were excited by an applied DC voltage using a rectifier. The sun gear shaft of the planetary gear train (PGT) drives the generator via a timing belt at a faster speed, such that the speed ratio of the carrier to sun gear is 1 to 2.95. The advantage of using a belt according to Tristan [67] is that it serves as a mechanical filter isolating the planetary gear system from the driving motor and the generator. This excites the armature windings of the motor and an electrical voltage is generated. The amount of power generated depends on the rotational speed of the sun gear driving the generator, which in turn depends on the rotational speed of the carrier and the planet gears. The speed ratio of the carrier to planet gear is 1 to 3.11. The speed ratio of the sun gear to that of the generator is approximately 1 to 1.50.

Three 3-axis Axivity MEMS accelerometers, one of which is shown in each of Figures. 6-1 (b), (c), and (d) were used to measure the acceleration of the carrier, sun and planet gears. The measuring device is suitable for use in various environments, and it has resistance to water. The memory size is 512 MB NAND flash which is non-volatile. The sampling frequency range is 12.5 – 3200 Hz, while the acceleration amplitude ranges of the sensor are $\pm 2, \pm 4, \pm 8, \text{and } \pm 16g$. There is a configuration software and analytical tool known as the AX3 OMGUI. This is used to set up and configure the accelerometer before the measurement. It is also used to download and obtain the recorded data (in the form of a time history) from the experiment. It helps to convert the binary AX3 recorded data from the experiment for subsequent data processing and analysis. The accelerometer has a real time quartz internal clock, where the desired time to start measuring the vibration is set. The precision is

typically ± 50 parts per million (ppm) as specified by the manufacturer. For PCA, the accelerometers are set to start at the same time throughout the spinning test for the purpose of synchronization.

In all of the experiments, the sampling rate was set to 1600 Hz. However, it was discovered that the actual sampling rate is always different from configured sampling frequency. The actual sampling rate was obtained by dividing the number of the sampled data points by the sampled time after the measurements have been downloaded. If the sampling rate is not up to 1600 Hz, the signal length acquired was interpolated to resample and hence achieve the configured sampling rate. The PSDs were obtained using a Hamming window with 50% overlap. The frequency resolution of 1 Hz was used for the frequency analysis

The three accelerometers were mounted on the rotating components, namely; the carrier, the sun and one of the planet gears as shown in Figure 6-1 (b), (c), and (d) respectively. Their vibrations were measured separately when spinning. The accelerometers are capable of measuring the vibrations in all three translational directions i.e. in the radial, tangential and axial coordinates in the cases of the carrier and sun gear. The horizontal and vertical directions were measured on the planet gear because of the available space to accommodate the accelerometer (Figure. 6-1 (b)). The flash memory of the accelerometer after removal from the gear is linked by a USB enabled microcontroller. This allows the measured vibration signal (in the form of time history) to be accessed on the computer and exported to MATLAB for frequency analysis.

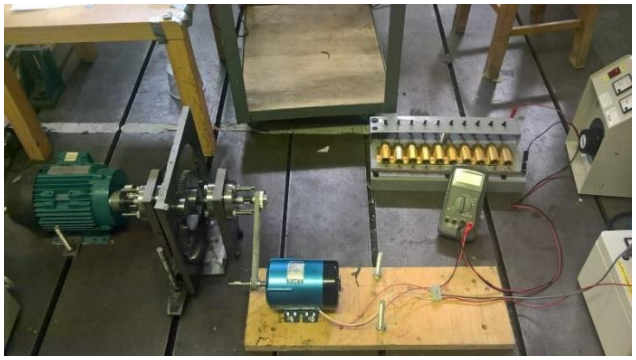

(a)

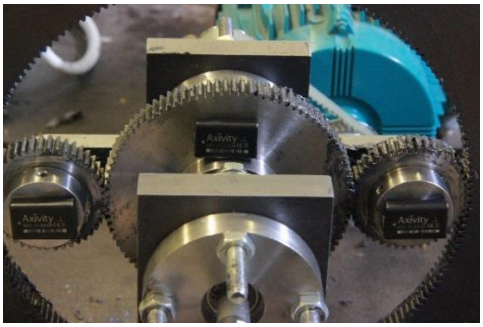

(b) (c)

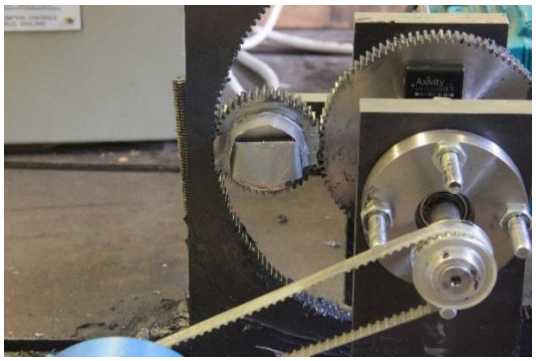

(d)

Figure 6-1 Test rig and 3-axis MEMS accelerometer with dimension 23×32.5×8.9 mm. The accelerometers were attached to the components with wax and Garvey tape.

The configuration considered is the planetary type of epicyclic gear as shown in Figure. 6-2, where the ring gear is stationary. The speed ratio is the ratio of the input speed to the output speed which has been shown in Chapter 4.

The dominant or mesh frequency in the vibration spectrum is then equal to product of the number of teeth on the stationary component (i.e. ring gear) and the rotational speed of the carrier at the input.

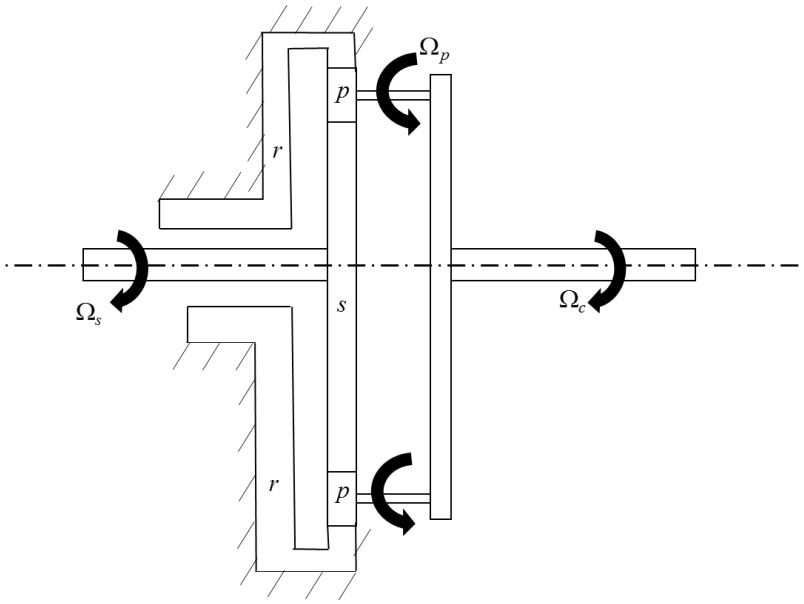

Figure 6-2 Planetary type of epicyclic gear. The notations *c*, *r*, *s* and p are the carrier, ring, sun and planet gears respectively.

The mesh frequency can also be determined from the components using equation (6.1) written as

$$f_m = z_r(\Omega_r - \Omega_c) = z_s(\Omega_s - \Omega_c) = z_p(\Omega_p + \Omega_c) \tag{6.1}$$

where, $f_m, z_s, z_r, z_{p,} \Omega_s, \Omega_r, \Omega_p$ and Ω_c are the mesh frequency, number of teeth on the sun gear, ring gear, planet gear, rotational speeds of the sun gear, ring gear, planet gear and the carrier respectively. For a stationary ring in equation 6.1, Ω_r is equal to zero. When using the ring gear to calculate the mesh frequency in the equation 6.1, the absolute value of the carrier speed is considered [68].

Two configurations were considered in the spinning test. One is the case where the PGT was idle (i.e. unloaded) and the second is the case where the PGT was loaded using a generator attached to the output shaft via a timing belt. The generator was configured to generate electric power and the output voltage was used to determine the output power. A resistor box containing resistors of different resistances was used to apply different electrical load on the generator. The results show the time histories and the power spectral densities (PSD) of the components starting from the low speed. Later, the PSD of each component at different speeds were obtained.

6.3 Dynamic response of the rotating planetary gear

6.3.1 Combined effects of different loads and speeds on the dynamic response

The sub-section aims to determine how different resistance loads and speeds affect the dynamic behaviour of a planetary gear system from an unloaded condition to a loaded condition. This scenario occurs in day to day activities in some countries where there is no regular power supply. In this situation, a power generator can be used to generate power. If the generator is started initially, it will be allowed to run for few minutes without any load and later it will be loaded from a light load to a heavy load. This section aims to see the dynamic effect on the planetary gear at different loads and corresponding rotational speeds. The measured natural and mesh frequencies are the frequencies of interest.

The rotational speed of the carrier when the planetary gear train was unloaded is 117 rpm, although the tachometer reading shows 120 rpm being the chosen speed.. At this carrier speed, the open circuit output voltage is 32.5 V. Subsequently, an electrical load of 10, 23.5, 33, 47 and 100 Ohms were loaded using a decade box which contains different resistance loads. The change in the resistance load also leads to a change in the voltage and the speeds when loaded. The values of the power at the output was calculated from the output voltage and the electrical resistance using equation (6.2).

$$P = \frac{V^2}{R} \tag{6.2}$$

where P, V and R are the output power in Watts, output voltage in Volts and the electrical resistance in Ohms respectively. The effect of the load resistance on the output power generated is shown in Figure 6-3 where the maximum power generated is approximately 6.4 Watts. The corresponding resistance loads at the maximum power is 47 Ohms.

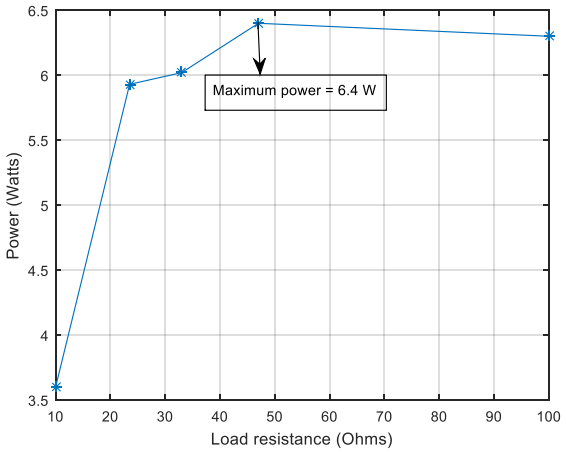

Figure 6-3 The effect of the load resistance on the generated output power. The maximum output power was generated when the load resistance was 33 and 47 Ohms.

A typical time history of the acceleration of the carrier in the radial direction is shown in Figure. 6-4 (a), which was then transformed to the frequency domain using a Fast Fourier Transform (FFT) routine available in MATLAB to obtain the frequency content shown in Figure 6-4 (b). The PSDs were calculated and plotted using the "pwelch" routine available in MATLAB in order to show the strength of the signal at each frequency. The time history and the frequency content of the carrier response in the tangential direction is shown in Figure D6.1 in Appendix D.

It is imperative to state that the frequencies of interest in this study are the frequencies of rotation, natural mode and the mesh vibration. Another frequency considered is the one measured on the sun gear which is probably related to misalignment, unbalance, looseness etc. The tangential component of the response at the mesh frequencies in all cases considered, is taken more serious because of the capability of the tangential force acting at the mesh to bend the gear teeth as stated by Gupta and Khurmi [69].

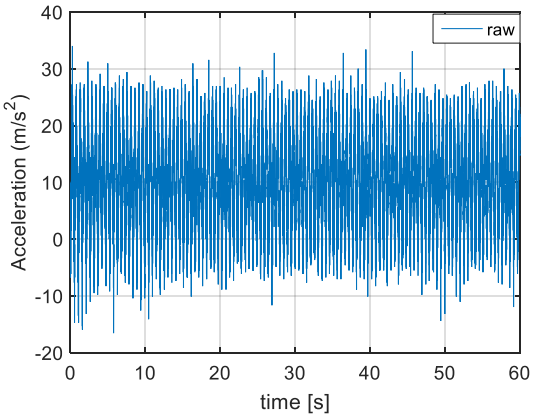

Figure 6-4. Time history of the unloaded carrier acceleration in the radial direction.

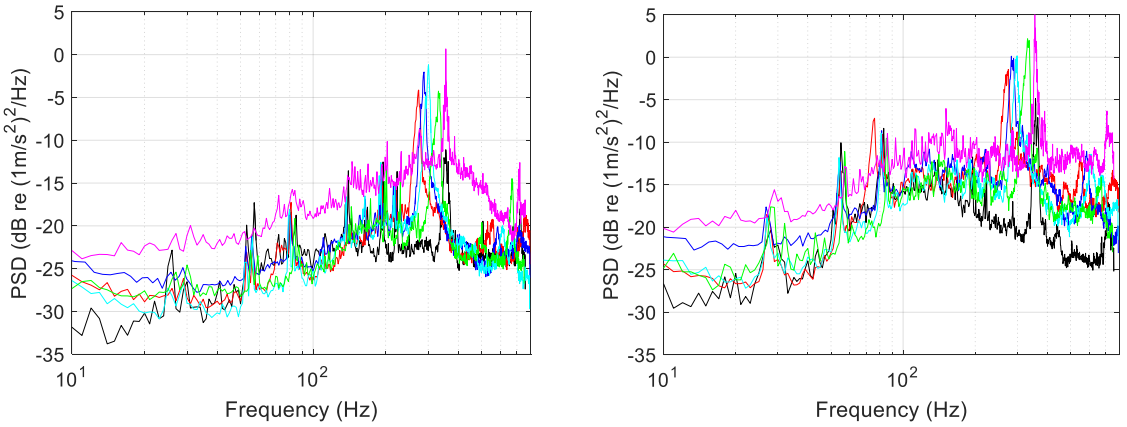

(a) **(b)**

Figure 6-5 The power spectral density of the carrier acceleration in the (a) radial direction (b) tangential direction. The PSD of the unloaded, 10, 23.5, 33, 47 and 100 Ohms are shown in black, red, blue, cyan, green and magenta lines respectively.

The rotational speeds, load resistances and the mesh frequencies of the carrier (which can be seen in Figure 6-5) are shown in Table 6-1.

Table 6-1 The rotational speeds, load and mesh frequencies of the carrier when varying the speed and load.

Rotational speed (rpm)	Load resistance (Ohms)	Mesh frequency (Hz)
117	0.00	357
89	10.00	274
91	23.50	288
98	33.00	301
108	47.00	331
116	100.00	355

The mesh frequencies are different for different loading conditions due to the different carrier speeds. Figure 6-5 (a) shows that the radial mesh frequency increases as the load is increasing except for the load where the maximum electric power (6.4 W) was generated. The radial response at the mesh frequency when unloaded is significantly lower than others.

The acceleration PSD of the carrier acceleration in the radial direction shows some frequencies close to the measured natural frequencies measured on the carrier in chapter 5. The frequencies are 80.3, 81, 82, 84, 85, 87, 137, 138, 140, 144 Hz which can be seen in Figure 6-5 (a) and some other PSDs at

different rotational speeds. The highest PSD level for frequencies between 80 and 87 Hz was obtained at a load of 10 ohms which is a light load compared to the others. There is no visible peak within this frequency range corresponding to 100 Ohms. The PSD levels of other peaks within the frequency range are not significantly different from one another. For frequencies between 137 and 144 Hz, the highest PSD was obtained when the system is unloaded while the PSD levels of other peaks within this range are almost the same.

Therefore, for carrier in the radial direction, the response at the mesh frequency increases with increase in load and rotational speed for loaded case. A reduced response was obtained when unloaded and when generating maximum power at a load resistance of 47 Ohms. The responses at frequencies close to a measured natural frequency of 84 Hz are relatively high when unloaded and when a light load resistance of 10 Ohms was applied. This implies that a light load or unloaded condition can lead to a significant response at this frequency.

The acceleration PSD in the tangential direction (Figure 6-5 (b)), shows that the highest response at the mesh frequency was obtained when the maximum load was applied. The PSD levels at the mesh frequency increase as the load and speed are increased for the loaded case. The PSD level at the mesh frequency when unloaded is the lowest. For the tangential response at the mesh frequency, the PSD level at 47 ohms is not relatively lower than other responses when loaded like the radial response. The acceleration PSD level of the frequencies between 80 and 85 Hz shows that the responses are not significantly different from one another at different speeds and loads. There is a significant response at 76 Hz corresponding to a load resistance of 10 Ohms.

Therefore, it can be deduced that the response level of the carrier at the mesh frequency in both the radial and tangential directions for varying rotational speeds and loads are not the same. This due to the fact that the external load applied is acting more at the mesh in a tangential direction than the radial direction. Generally for the carrier, the level of the responses at mesh and natural frequencies in the tangential direction is relatively higher than the radial direction.

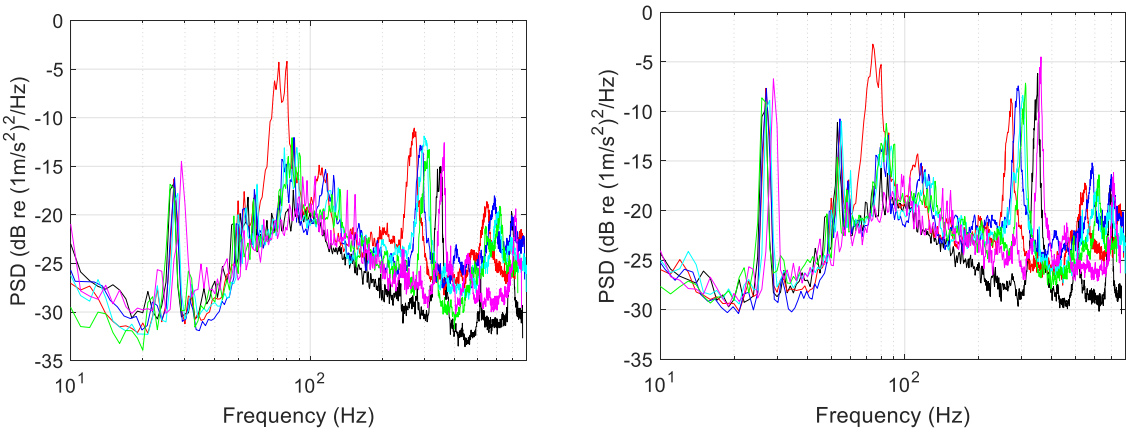

(a) **(b)**

Figure 6-6 The power spectral density of the sun gear acceleration in the (a) radial and (b) tangential directions. The PSD of the unloaded, 10, 23.5, 33, 47 and 100 Ohms are shown in black, red, blue, cyan, green and magenta lines respectively.

The rotational speeds, load and mesh frequencies of the sun gear which was determined from Figure 6-6 are shown in Table 6-2.

Table 6-2 The rotational speeds, load and mesh frequencies of the sun gear when varying the speed and load.

Rotational speed (rpm)	Load resistance (Ohms)	Mesh frequency (Hz)
332	0.00	350
261	10.00	272
267	23.50	291
291	33.00	304
296	47.00	312
343	100.00	361

The response of the sun gear in the radial direction is shown in Figure 6-6 (a). The response at the mesh frequency when a load (10 Ohms) was applied is the most significant considering the PSD level. This may be as a result of light load which is insufficient to ensure that there is a proper contact between the meshing teeth of the sun and planet gears [7]. This can lead to damage at the mesh due to impact when the teeth are coming into contact again after disengagement. There is no significant difference between the responses at other mesh frequencies except for the unloaded case where the response is relatively lower.

For the peaks between 80 and 88 Hz, the response at a light load of 10 ohms is the highest. There are responses at 131, 133 and 143 Hz which correspond to loads of 33, 47 and 100 Ohms respectively. Their PSD levels are almost the same.

For the tangential direction of the sun gear, the PSD level at the mesh frequencies are slightly increasing as the load increases (Figure 6-6 (b)). The two most significant responses at the mesh frequency in this direction can be seen when at the maximum load resistance (100 Ohms) and when unloaded. This probably may be confirming what Derek [7] stated in his book about high loads which can also lead to contact loss if the errors are larger than the deformation at the tooth and the inertia of the system is high. The mass of the sun gear is relatively larger than those of the carrier and planet gears. Therefore, it is possible to have a higher response at the mesh frequency when the load is relatively high. This is different when compared to the mesh response in the radial direction. Another possibility is that the load may act more at the teeth mesh in the tangential direction than the radial direction.

There is a response on the sun gear at 74 Hz for a 10 Ohms load resistance which is more significant than the mesh frequency. Among the responses between 80 and 88 Hz, the response at 10 Ohms is the highest followed by the one at 47 Ohms where maximum power was generated. Other responses within this frequency range are almost the same in PSD level. Only the PSD when a maximum load was applied shows a peak at 143 Hz with a smaller PSD level compared to that of carrier in the tangential direction (Figure 6-5 (b)).

There are frequency peaks between 26 and 29 Hz on the sun gear in both the radial and tangential directions. These frequencies are probably associated with mechanical faults like misalignment, unbalance etc. as stated by Jan et al. [65]. The independent measurement of vibration has made it easier to detect faults associated with mechanical fault on each component without any complicated signal processing method. The levels of the responses within this frequency range are almost the same except for the response at maximum load and rotational speed of the sun gear which is higher. Therefore, the response is more significant at the maximum load and rotational speed.

In general, like the carrier, the response at the mesh frequency of the sun gear is higher in the tangential direction than the radial direction.

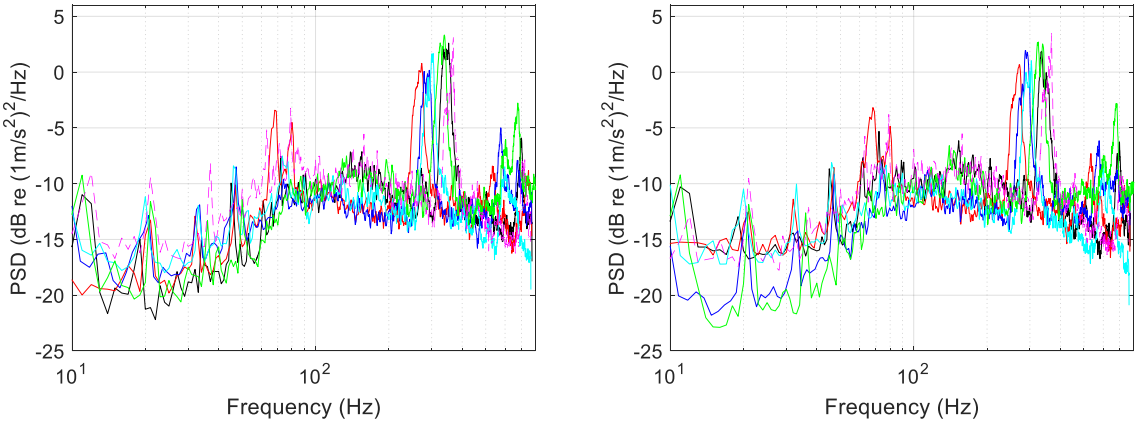

(a) **(b)**

Figure 6-7 The power spectral density of the planet gear acceleration in the (a) x and (b) y directions. The PSD of the unloaded, 10, 23.5, 33, 47 and 100 Ohms are shown in black, red, blue, cyan, green and magenta lines respectively.

The rotational speeds, load and mesh frequencies of the planet gear which was determined from Figure 6-7 are shown in Table 6-3.

Table 6-3 The rotational speeds, load and mesh frequencies of the planet gear when varying the speed and load resistance.

Rotational speed (rpm)	Load resistance (Ohms)	Mesh frequency (Hz)
352	0.00	350
267	10.00	272
292	23.50	287
298	33.00	304
338	47.00	338
359	100.00	368

Although the PSD level of the responses at the mesh frequencies are almost the same, the maximum response in *x* and *y* directions at the mesh frequency was determined on the planet gear when loads of 47 and 100 Ohms (which are relatively heavy) were applied (Figure 6-7 (a) and (b)). There are some frequencies excited in both directions which are close to the second harmonics of the mesh frequencies at different speed and loads. The most significant response occur at the mesh frequency corresponds to 47 ohms where the maximum power was generated.

The most significant response close to the measured natural frequencies between 79 and 89 Hz occurred at a maximum load resistance of 100 Ohms and another response at a load of 10 Ohms. There are responses within a frequency range of 150 and 158 Hz and a natural frequency of 156.36 Hz

was measured on the planet gear and shown in Table 5-6. The most significant response within this frequency range occurred when a maximum load of 100 Ohms (Figure 6-7 (a) and (b). This implies the level of response relating to the natural mode on the planet gear under varying load and speed does not depend on the magnitude of load and speed. They can be high or low when lightly loaded or heavily loaded.

6.3.2 Dynamic response under constant load of 100 ohms and different speeds

In this sub-section, the dynamic response of planetary gear under a constant load resistance of 100 Ohms will be investigated. The carrier, sun and planet gears speeds are varied by varying the input speed. Generally, the output power increases as the speed is increased. Therefore, for a constant load, increased speed leads to an increase in the output power transmitted as shown in Figure 6-8.

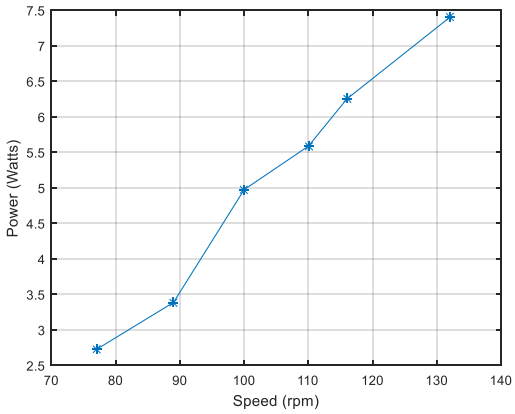

Figure 6-8 The effect of rotating speed on the power generated under constant load of 100 Ohms.

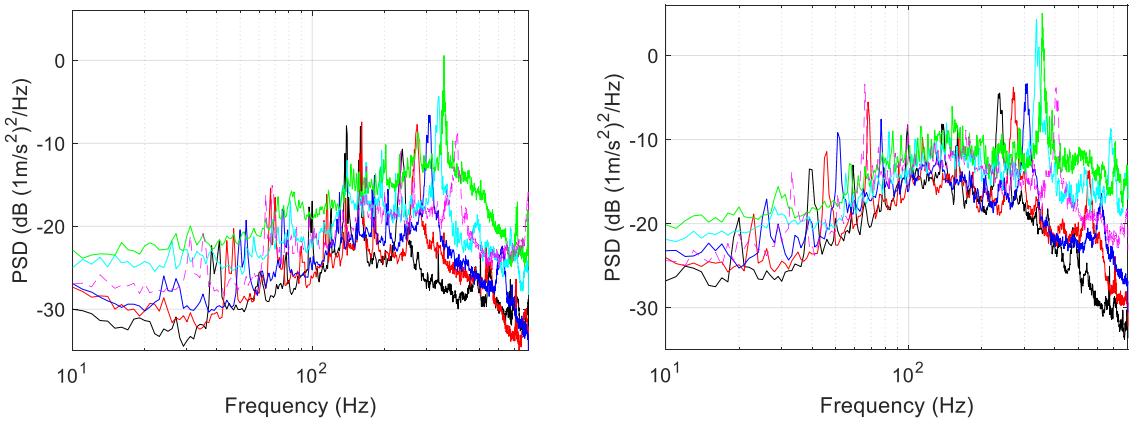

(a) **(b)**

Figure 6-9 The power spectral density of the carrier acceleration in the (a) radial (b) tangential directions under a constant load resistance of 100 Ohms. The rotational speeds 77, 89, 100, 110, 116 and 132 rpm are shown in black, red, blue, cyan, green and magenta lines respectively.

In (Figure 6-9 (a) and (b)), some frequencies are excited in one direction only but the frequencies of interest are the frequencies of the modes as measured, mesh frequencies and some of its harmonics if they are significant.

The rotational speeds and mesh frequencies of the planet gear at a constant load of 100 Ohms are shown in Table 6-4.

Table 6-4 The rotational speeds and mesh frequencies of the planet gear when varying the speed at a constant load of 100 Ohms.

Rotational speed (rpm)	Mesh frequency (Hz)
77	238
89	274
100	310
110	338
116	355
132	404

The vibration response of the carrier in the radial direction is shown in Figure 6-9 (a). The response at the mesh frequency is slightly increasing till it reaches a rotational speed of 116 rpm corresponding to a frequency of 355 Hz. This frequency was measured on the planet gear and another closer value was measured on the carrier (Tables 5-1 and 5-6). The response at the highest speed of 132 rpm is significantly lower considering its acceleration PSD level. Probably, the high response at a mesh frequency of 355 Hz is due to the fact that the mesh frequency coincides with one of the natural

frequencies of the system. Hence, for the carrier in radial direction, the mesh response was increasing with increment in the rotational speed up to 116 rpm. The response later reduced at 132 rpm with a corresponding mesh frequency of 407 Hz. It is possible that the natural frequency of the system has been excited in this case. It may be necessary to investigate further the response level at a higher speed (which will not excite the natural frequency of the system) to know if it will decrease or increase. There is a limitation with the current equipment. The range of the accelerometer is not enough to measure the vibration of the gears especially the planet at higher speeds.

Therefore, for a constant load, high speed and power generated can lead to a significant response of the carrier in the radial direction at the mesh frequency but the response can reduce at a higher speed.

There are three obvious groups of frequency peaks of interest in the radial direction of the carrier at frequencies lower than the mesh frequencies (Figure. 6-9 (a)). They are 76, 78, 79, 81, 86, 130, 138, 139, 140, 145 and 156 Hz. It is obvious that some of these frequencies are close to one another depending on the rotational speed of the carrier. Also they are close to the measured natural frequencies. For a frequency range between 76 and 86 Hz, there is a significant response at 76 and 81 Hz with corresponding speed of 100 and 110 rpm respectively. The responses at 89 and 77 rpm are lower while the response at 132 rpm is the lowest. There is no peak within this frequency range in the PSD of 116 rpm. However, for the frequency range between 130 and 145 Hz, the most significant response is recorded at the lowest rotational speed (77 rpm) followed by the response at 110 rpm.

It appears that the increasing speed does not lead to an increment in the response level at the natural frequencies in the radial direction of the carrier at a constant load of 100 ohms. Nevertheless one can deduce that the natural modes are significantly excited in the radial direction of the carrier at relatively low speeds.

The response of the carrier in the tangential direction is shown in Figure 6-9 (b). The mesh frequency is increasing with increment in speed till 116 rpm which is the most significant response at the mesh frequency at a rotational speed of 116 rpm with a corresponding frequency of 355 Hz. Like the radial direction the highest response at the mesh appeared at 355 Hz. The acceleration PSD level shows that the tangential response at the mesh frequency of the carrier is more than the radial response at the mesh frequency. The level of response at mesh frequency (404 Hz) which corresponds to the highest rotational speed of the carrier (132 rpm) is significantly lower (approximately 8 dB) than the response level at 116 rpm. High level of response can be avoided at mesh frequency by carefully selecting the rotational speed such that the frequency of the mesh force will not coincide with any of the natural frequencies of the system.

Some peaks can be seen in Figure 6-9 (b) between 77 and 88 Hz, 131 and 143 Hz and a peak at 151 Hz. The most significant response among the first frequency range can be seen at 77 Hz with a corresponding rotational speed of 100 rpm. The highest response level in the second frequency range was recorded at 139 and 143 Hz with corresponding rotational speeds 77 and 110 rpm respectively. For this frequency range, the peaks are not obvious for the rotational speeds at 89, 100, 116 and 132 rpm. The response at the frequency of 151 Hz is significant and the corresponding rotational speed of the carrier is 116 rpm which is relatively high.

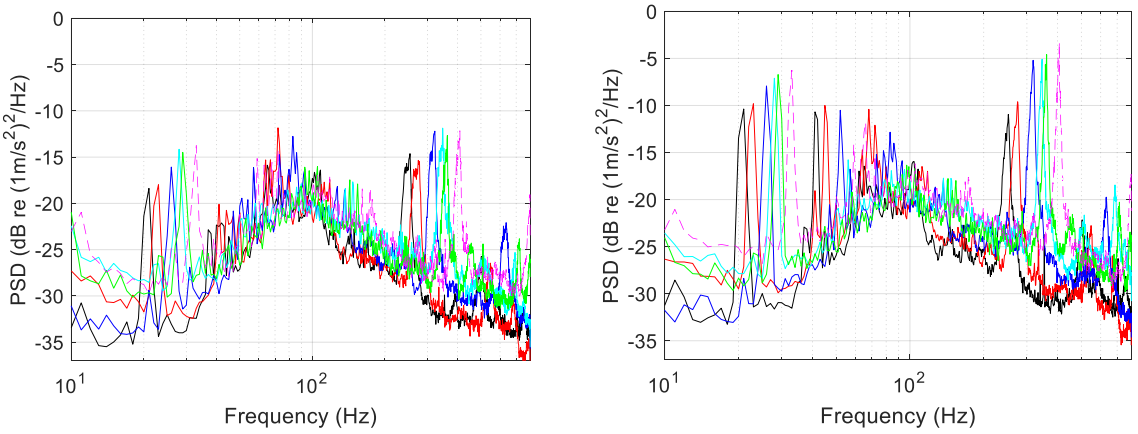

(a) (b)

Figure 6-10 The power spectral density of the sun gear acceleration in the (a) radial and (b) tangential directions under a constant load resistance of 100 Ohms and different speeds. The rotational speeds 240, 262, 304, 328, 342 and 386 rpm are shown in black, red, blue, cyan, green and magenta lines respectively.

In figure (6-10), the mesh frequency of the sun at the minimum speed of 240 rpm is 254 Hz. The mesh vibration response of the sun gear in the radial direction is shown in Figure 6-10 (a). The responses at the mesh frequencies of 254 and 275Hz corresponding to low rotational speeds of 240 and 262 rpm are relatively low. The mesh responses at rotational speeds of 304, 328, 343 and 386 rpm are higher and are not significantly different from one another. Based on this result, it can be deduced that the radial response of the sun gear at mesh frequency can be influenced by high speed for a constant load resistance.

There are two significant responses at frequencies of 72 and 73 Hz corresponding to rotational speeds 262 and 386 rpm. The acceleration PSD levels of other peaks within this frequency range are not significant. The responses between 80 and 87 Hz show that the PSD level of the frequency corresponding to 304 rpm is the highest. The levels of all other peaks within this frequency range are

approximately the same and low. For the frequency range between 137 and 147 Hz, the PSD levels of the responses are approximately the same.

In the tangential direction of sun gear, the response at the mesh frequency (starting from 252 Hz) is increasing as the rotational speed is increasing. The level of mesh response corresponding to speeds of 328 and 342 rpm are approximately the same because of the small speed difference between them. The level of this response increases further at a maximum speed of 386 rpm corresponding to mesh frequency of 407 Hz (Figure 6-10 (b)). The peaks at different mesh frequencies show clearly that the response increases with increment in the rotational speed of the sun gear. This means that the tangential mesh response of the sun gear increases as the speed is increasing.

Considering the responses between 72 and 84 Hz, the ones corresponding to the relatively low speed of 89 and 100 rpm are more significant. For the frequency range between 137 and 147 Hz, the response levels are approximately the same for rotational speeds from 100 to 116 rpm. The response at 240 and 386 rpm are relatively low. There is no obvious peak at 89 rpm within the frequency range. One cannot really infer that the level of tangential responses at the frequencies closed to the measured natural frequencies are actually influenced by the rotational speed of the sun gear.

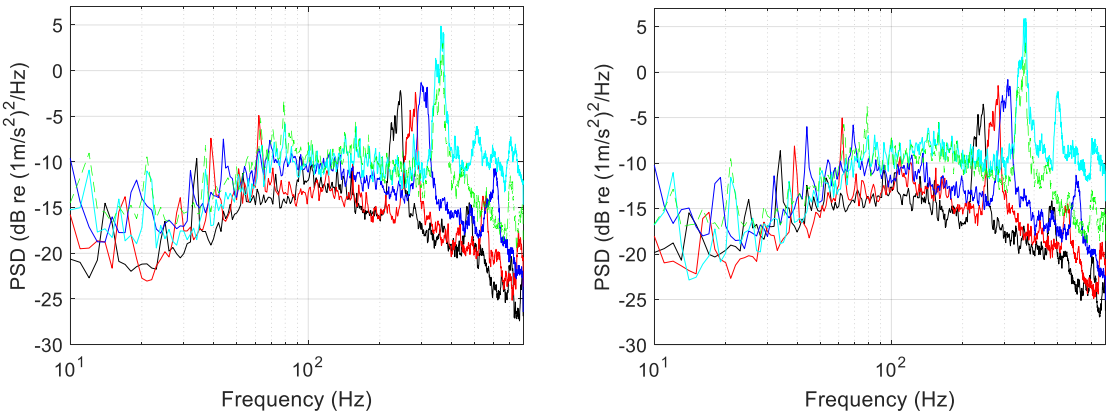

(a) **(b)**

Figure 6-11 The power spectral density of the planet gear acceleration in the (a) *x* and (b) *y* directions under a constant load of 100 Ohms and different speeds. The rotational speeds 238, 276, 309, 362 and 360 rpm are shown in black, red, blue, cyan and green lines respectively.

The response of planet gear in x direction at the mesh frequency shows that the most significant response appeared at the 361 Hz when the rotational speed is 362 rpm (Figure 6-11 (a)). This is the maximum speed of planet gear in this case study. Although, it is not supposed to be the highest speed considering the speed ratio of the gear train. There may be little fluctuation of the applied load acting on the planet gear at this speed, if the load reduces this may have effect on the speed which is

supposed to be 342 rpm theoretically. Therefore, the most significant radial response of the planet gear at the mesh frequency occurred at the maximum speed. The next radial response at mesh frequency in order of PSD level occurred at a rotational speed of 360 rpm speed corresponding to the speed where the highest power was generated (Figure 6-8). Two significant peaks appeared at 79 and 80 Hz corresponding to a rotational speed of 360 and 362 rpm respectively. This implies that for a planet gear under a constant load but varying speed, the response relating to the natural mode is more significant at higher speed than lower speed.

The response level and pattern in *y* direction is the almost same with the ones in the *x* direction because they are both radial. The acceleration PSD level of the response in *y* direction at the mesh frequency is slightly higher (Figure 6-11 (a) and (b)). Also, a frequency was significantly excited in *y* direction at 505 Hz at a relatively high rotational speed of the planet gear. This frequency was measured on the ring gear in *x* direction in chapter 5. The corresponding response of the planet gear when the input speed (i.e. the carrier speed) was 132 rpm could not be measured as a result of signal clipping due to the dynamic range of the accelerometer.

6.3.3 Dynamic response under a constant speed 100 rpm and different loads

The dynamic response of planetary gear under a constant speed and varying load resistance was examined in this section. Although there are some little differences in the speed when changing the load resistance, the difference is assumed to be insignificant. The rotational speed varies from 100 rpm (1.667 Hz) to 103 rpm (1.717 Hz), therefore, the difference is assumed to be negligible on the dynamic response of the system. The effect of the load resistance on the output power is as shown in Figure (6-12). The power generated was increasing as the resistance load applied was increasing up to 6.65 W at a corresponding load resistance of 23.5 Ohms. The power starts decreasing from 6.65 Watts as the load increases until it reaches 4.97 W at a corresponding load resistance of 100 Ohms which is the maximum load applied. If the rotational speed is increased at this load the power generated will also increase like the case shown in Figure 6-8.

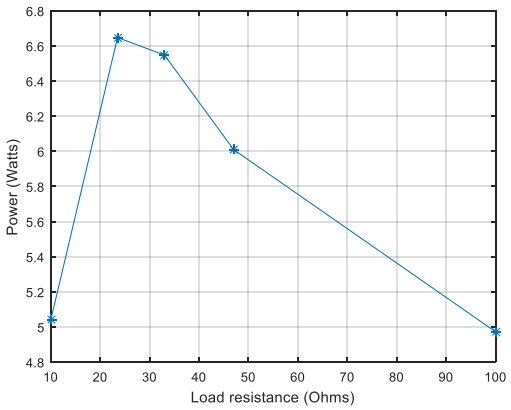

Figure 6-12 The effect of the load resistance on the output power at a constant gear speed of 100 rpm.

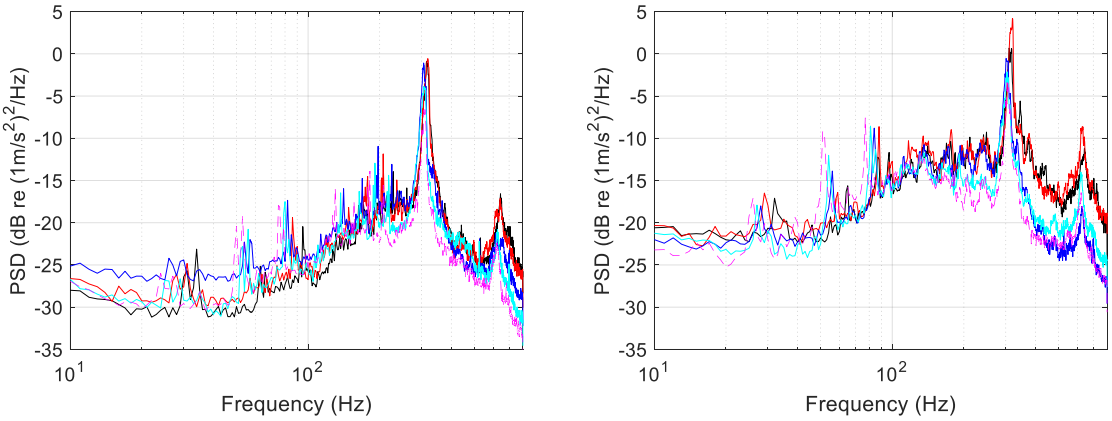

(a) **(b)**

Figure 6-13 The power spectral density of the carrier acceleration in the (a) radial and (b) tangential directions under a constant speed of 100 rpm at different resistance loads. The load resistance of 10, 23.5, 33, 47 and 100 Ohms are shown in black, red, blue, cyan and magenta lines respectively.

The response of the carrier in the radial direction is shown in Figure 6-13 (a). The mesh frequency at each load resistance dominates the vibration spectra in both the radial and tangential directions. From Figure 6-13 (a), it is obvious that the values of all the mesh frequencies at an assumed constant speed are not significantly different from one another. The mesh frequencies are 315, 319, 306, 306 and 310 Hz at applied loads of 10, 23.5, 33, 47 and 100 Ohms respectively. There are little variations in the mesh frequencies due to little variation in the rotational speed. The vibration response level at the mesh frequency is higher at loads of 10, 23.5 and 33 Ohms than when heavier loads of 47 and 100 Ohms. They are 3.8 and 5.1 dB lower respectively than the first three responses which are approximately the same. The power generated at this loads are relatively low as shown in Figure 6-12.

Therefore the radial responses of the carrier at the mesh frequency are more significant at relatively lighter loads for a case where the rotational speed is constant or not changing significantly.

The response believed to be related with the natural mode between 75 and 86 Hz are significant at loads of 33, 47 and 100 Ohms than the responses at a light load of 23.5 Ohms. The frequency peaks at 82, 80, 75 Hz correspond to the applied loads of 33, 47 and 100 Ohms respectively There is no peak at 10 Ohms within this frequency range. For responses within 130 and 148 Hz, the acceleration PSD levels are relatively higher at loads of 33, 47 and 100 Ohms. The carrier radial response at the frequencies close to the measured natural frequencies is high at higher load when the rotational speed is constant.

The most significant response of the carrier in the tangential direction at the mesh frequencies occurred when the applied load was 23.5 Ohms (Figure 6-13 (b)). This is a load where maximum power was generated. Also, the response is higher at loads corresponding to 10 and 33 Ohms than 47 and 100 Ohms. This implies that the response at the mesh frequency in the tangential direction is higher at light loads especially at a load where maximum power was generated. The level of tangential response of the carrier at the mesh frequency depends on the load and power; it is high at a light load where maximum power is being generated.

Five peaks relating to the five loads occurred from 77 to 88 Hz and it shows that frequencies are reducing as the load is increasing (Figure 6-13 (b)). Furthermore, the highest PSD level within the frequency range is obtained at 77 Hz when a load of 100 Ohms was applied. The acceleration PSD level of the peak corresponding to 10 Ohms (87 Hz) is the smallest within the frequency range while the levels of other peaks are almost the same. This implies that the most significant carrier response at a frequency range close to a measured natural frequency occurred when a relatively heavy resistance load (100 Ohms) was applied. Considering a frequency range between from 135 to 143 Hz, the response at a relatively light resistance load of 23.5 Ohms is the most significant.

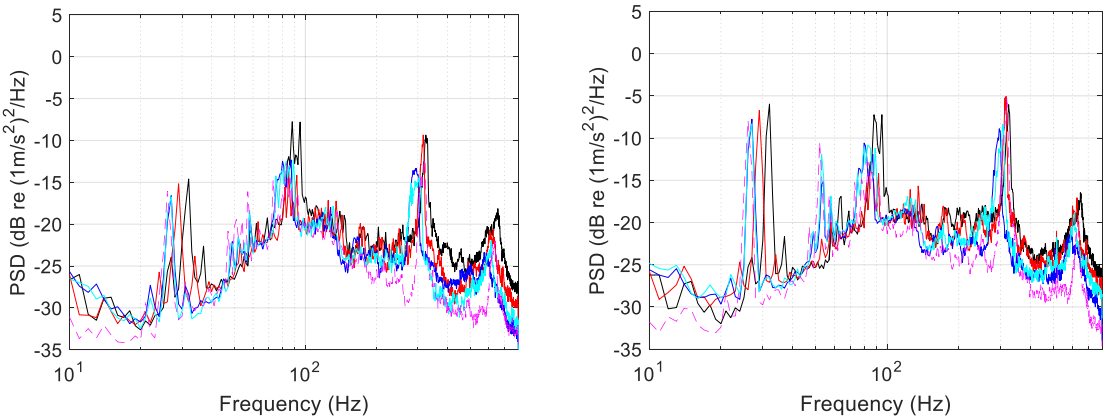

(a) **(b)**

Figure 6-14 Power spectral density of the sun gear acceleration in the (a) radial and (b) tangential directions under an average constant speed of 300 rpm at different resistance loads. The resistance loads of 10, 23.5, 33, 47 and 100 Ohms are shown in black, red, blue, cyan and magenta lines respectively.

The acceleration PSD of the sun gear in the radial direction is shown in Figure 6-14 (a). The most significant response at the mesh frequency occurred at the light loads of 10 and 23 Ohms. The corresponding mesh frequencies at these loads are 324 and 316 Hz respectively. The acceleration PSDs of the peaks corresponding to other load are relatively lower. Hence, the response of the sun gear at mesh frequency in the radial direction is high when the applied load is relatively light.

There are two peaks at 88 and 95 Hz when a light load of 10 Ohms was applied. Their acceleration PSD level shows the sun gear was significantly excited at these frequencies more than the most significant response at mesh frequency. It shows clearly that the most significance response of the sun in the radial direction at a constant speed occur when a load of 10 Ohms was applied.

The response of the sun gear in the tangential direction is shown in the power spectrum (Figure 6-14(b)). The peaks at the mesh frequency show that the most significant response occurred when resistance loads of 23.5 and 100 Ohms were applied. Therefore, there can be a significant tangential response of the sun gear at mesh frequency at a light load (probably if the maximum power is being generated) or at a relatively heavy load. This is for a case of constant speed and varying load. The tangential responses at a measured frequency associated with a natural mode are significant at 88 and 95 Hz when the applied load of 10 Ohms was applied like the radial response.

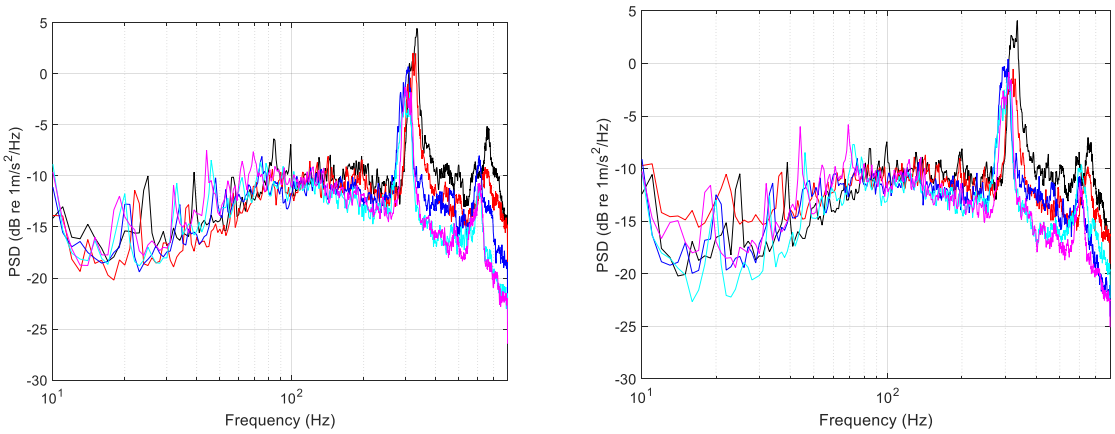

(a) (b)

Figure 6-15 Power spectral density of the planet gear acceleration in the (a) *x* and (b) *y* directions under a constant speed of 100 rpm at different resistance loads. The resistance loads of 10, 23.5, 33, 47 and 100 Ohms are shown in black, red, blue, cyan and magenta lines respectively.

The most significant response in *x* direction of the planet gear at the mesh frequency occurred when a relatively light load of 10 Ohms was applied (Figure 6-15 (a)). The power generated by the system at 10 Ohms is relatively low. Also, the lowest response corresponds to maximum load where the minimum power was generated. Since the response is high for the former case and low for the latter case such that low power was generated in both cases, the response is independent of power generated but the light load applied. The acceleration PSD level at the mesh frequency decreases as the load increases.

Two frequencies (84 and 99 Hz) which are close to the measured natural frequencies were significantly excited when a light resistance load of 10 Ohms was applied. The response at the mesh frequency and frequencies close to the measured natural frequencies are the same for planet in *y* direction. Therefore for a planet gear rotating at a constant speed different load, it can be inferred that the response at the mesh and predicted natural frequencies are significantly more excited at relatively lighter load than heavier load.

6.4 Summary on dynamic responses under different conditions

6.4.1 Combined effect of load resistance and rotational speed on the dynamic response

For a case where the rotational speed and load are increasing simultaneously; the radial and tangential responses of the carrier at the mesh frequency increase. The radial and tangential carrier responses at the mesh frequency are typically low when unloaded. In this case, where the rotational speed is

varying, the carrier response is low when the load is light or when the system is unloaded. For the sun gear, the radial response at the mesh frequency is high at a light load and low rotational speed. This is because of the insufficient load to keep the mating teeth together for proper contact, which causes impacts when they are engaging and disengaging. This can lead to damage of the teeth. The tangential response of the sun gear at the mesh frequency increases as the load increases. The radial response of the sun gear at the mesh frequency is low when unloaded while the tangential response is relatively high. For the planet gear, the response at the mesh is high at higher resistance loads of 47 and 100 Ohms than the remaining lighter loads. The response of the planet at the mesh can also be significant when unloaded.

The response levels of the carrier at a frequency associated with a natural mode are almost the same covering a frequency range of 80 to 86 Hz, except for a case where a resistance load of 10 Ohms was applied. This implies they are not significantly affected by the increasing rotational speed and load. The tangential response of the carrier is significant at a higher frequency of 151 Hz at a heavy load. The response of the carrier at a heavy resistance load of 100 Ohms dominates the response at the higher frequency band in both directions. For the sun gear, the radial response is high at 80 Hz for a light load. This is probably a resonance frequency because 80 Hz is close to 84. 37 Hz measured on the carrier. This may be the reason why the response at this frequency is more significant than the response at the mesh frequency 274 Hz for the same load. Since the force exciting this natural frequency cannot be an unbalanced force, whose frequency is 1.48 Hz, or the mesh force whose frequency is 274 Hz, it is necessary to investigate it. It is probably a force associated with a defect associated with the bearing. The tangential response of the sun gear at a light resistance load of 10 Ohms is the most significant. The response of the planet is high at a light and heavy resistance loads between 79 and 89 Hz and high at a frequency of 158 Hz corresponding to 100 Ohms. There is no clear indication that the load and speed affects the dynamic response of the planet at a frequencies associated with the natural modes when the rotational speeds and load are changing.

Misalignment may be caused by an error in the system during assembling has been diagnosed in planetary gear at a low frequency range by Abdalla et al [70] using a method known as Modulation Signal Bispectrum (MSB) . The response was measured by an accelerometer mounted on the housing. In this study, the PSD of the sun gear shown in Figure 6-6 (a) and (b) when the rotational speed and load are varying shows a frequency range associated with misalignment as discussed previously in section 6.1. A significant response was measured on the sun gear at 27 Hz when unloaded. This response is more significant at maximum load and rotational speed of the sun gear. The change was obvious at a maximum load resitance of 100 Ohms where the frequency is 29 Hz. The presence of lower and upper sidebands having relatively lower amplitude can be seen around the frequency, which

may indicate faults on the sun gear at both frequencies. This fault is probably a misalignment of sun shaft, so unbalance occurs. The frequency associated with this fault is within the range of low frequency which signifies mechanical faults. This shows another benefit of measuring vibration of a planetary gear individually using an accelerometer that can rotate with it. There is no need to employ any signal separation or extraction technique before a mechanical fault like misalignment can be detected.

6.4.2 Effect of varying the rotational speed on the dynamic response at a constant resistance load

The radial response of the carrier at the mesh frequency increases with an increase in the rotational speed up to 116 rpm. At this rotational speed there is resonance because the mesh frequency of 355 Hz that is close to one of the natural frequencies of the system at 356.4 Hz measured on the planet and 365.8 Hz measured on the carrier. Above this speed, at 132 rpm, the level of the response reduced. For the tangential response of the carrier at the mesh frequency, the response levels are almost the same except at 336 and 355 Hz, which correspond to rotational speeds of 110 and 116 rpm respectively. The responses at these rotational speeds are high especially at 116 rpm because a natural mode was excited which leads to resonance. Therefore, an increase in the rotational speed leads to an increase in the radial response of the carrier at the mesh frequency but the most significant response occurred at the resonance frequency. The tangential response levels at the mesh frequency are the same except for the response at resonance frequency and the one close to it. The speed corresponding with this resonance should be avoided to prevent damage of the carrier.

The radial and tangential responses of the sun gear at the mesh frequency are significant at high speed and relatively low at low speeds. For the planet, the response at the mesh frequency is very high at high rotational speeds especially the one which corresponds to the resonance frequency of 356.4 Hz as mentioned earlier.

For the frequencies close to the natural modes, increase in the rotational speed does not clearly show an increased level of response of the carrier in both radial and tangential directions. The response of the sun gear in the radial direction seems unaffected by the rotational speed while the tangential response is high at low rotational speed. The response of the planet gear is significant at high speed, probably because it becomes more flexible as the rotational speed increases.

In summary, for a constant load and varying speed, the radial and tangential responses of the carrier, sun and planet gear at the mesh frequency increases as the rotational speed increases. For the frequencies relating to the natural modes, it is observed that increased rotational speed does not affect the response level of the carrier in both directions as well as the sun in the radial direction. The

response level of the sun in the tangential direction is relatively high for low speeds. The response of the planet gear at a frequency related to a natural mode is significant for high speeds.

The frequency associated with misalignment of sun gear and its response level increases in both directions as the rotational speed increases for the constant load.

6.4.3 Effect of varying the load resistance on the dynamic response at a constant rotational speed

The radial response of the carrier at the mesh frequency is high at lighter loads of 10, 23.5 and 33 Ohms than the heavier resistance loads of 47 and 100 Ohms. Most significant tangential response at the mesh frequency occurred at a light resistance load 23.5 Ohms, where the maximum power was generated. The most significant radial response of the sun gear at the mesh frequency occurred at light resistance loads of 10 and 23.5 Ohms. The power generated at 10 Ohms is low while the one generated at 23.5 Ohms is the maximum. Therefore, the power generated could not be responsible for the high response for the latter case but a light load applied. The tangential response of the sun gear at the mesh frequency is high at 10 and 100 Ohms which are light and heavy loads respectively. A light load could result in a high sun gear response because of the insufficient load to keep the meshing teeth together, thereby causing a large impact capable of causing tooth failure. Also, a heavy load can cause a high response if the errors are greater than the tooth deflection and the inertia of the sun gear is relatively high as presented by smith [7]. The significant response of the planet gear at the mesh frequency occurred for a light load of 10 Ohms. Therefore, for a constant speed, a light load could damage the carrier, sun and planets at a frequency relating to the teeth meshing except for the tangential response of the sun which is only significant for heavy loads.

For the responses relating to the natural mode, the radial response of the carrier are higher at relatively higher loads. The tangential response is high at a heavy load corresponding to a low frequency range (between 77 and 87 Hz), while the response over a relatively higher frequency range (135 and 143 Hz) is high at a light load resistance of 23.5 Ohms. The radial and tangential responses of the sun gear over a frequency range between 88 and 95 Hz are high at a light load of 10 Ohms. Therefore, a light load can damage the sun gear at a lower frequency, when the rotational speed is constant. The most significant response of the planet occurred for a light load resistance.

The frequency associated with misalignment on the sun gear and its response level, is increasing as the load decreases for a constant rotational speed.

6.4.4 General comparison

The radial and tangential responses of the carrier at the mesh frequency could be more than that of the sun gear if the bearing stiffness of the planet which connects it to the carrier is less than of the sun gear. This is because the vibration generated at the sun-planet mesh is transmitted through the planet to its bearing at the carrier-planet interface. This makes the tangential response of the carrier at the mesh frequency higher than that of the sun gear whose bearing is stiffer.

Generally, for the carrier and sun gear the response at the tangential direction is higher while the response of the planet gear in *x* and *y* directions are the highest.

The response relating to misalignment measured on the sun gear that follows shows a slight increase as the speed and load is increasing, increases as the speed is increasing for a constant load and increases as the load is decreasing for a constant speed. It exhibits different behaviours under different working conditions.

The effect of load and rotational speed has been investigated on the dynamic response of carrier, sun and planet gear. The next section will focus on the identification of vibration sources at each measuring point in the system.

6.5 Identification of vibration sources in a planetary gear transmission mechanism

Principal component analysis (PCA) is a mathematical algorithm used to transform a set of values which comprise correlated variables into set of uncorrelated variables. Principal component analysis (PCA) within a vibration context, can be utilized to identify and rank the vibration sources in the planetary gear. To determine the contribution of each component of the planetary gear to the vibration, it is important to apply PCA. The method can help to determine where to really apply the control forces when controlling the vibration.

Huang and Ferguson [71] used a PCA method and virtual coherence techniques to analyse cross-axis apparent mass in whole body vibration. Their aim is to identify the contributions and correlations between the cross-axis vertical (*x*- axis) and cross axis lateral (*y*-axis) in response to a longitudinal inline force (*z*-axis). They stated that the use of the ordinary coherence function to determine the extent to which the cross axis forces are correlated to the inline longitudinal force is unclear. The use of only PCA makes it difficult to establish the relationships between principal components and physical sources. Therefore, a technique known as virtual coherence (VC) has been useful in identifying the relationship between a principal component and physical sources. They concluded by

stating that the extent of correlation determined from the results could help to know the causes of cross-axis coupling which is common in biodynamic vibration response of the whole human body. Bellino et al. [72] , used a PCA technique to detect damage in a time-varying systems. They showed that this technique can be successfully used not only for time-invariant systems but time varying systems like a railway bridge. Their results show that the PCA technique can be used to detect damage in a time varying system as well as different levels of crack depth.

This section focuses on the application of principal component and virtual coherence methods to the measured responses from a carrier, sun and planet gears during operation. As mentioned earlier in section 6.2, the accelerometers are rotating with the components of the planetary gears unlike the past research works where the accelerometers are stationary. Moreover all the accelerometers were synchronized by configuring them to start and finish measurements at the same time. The power spectral density (S_{ii}) and cross spectral density (S_{ij}) were determined by using MATLAB routine "pwelch" and "cpsd" respectively. Like previous sections all the signals for a specific case were acquired in 60 seconds at different sampling rates but were interpolated to 1600 Hz using a MATLAB routine called "interp1". This makes the number of data points equal to 96000. The spectral analysis was performed using a Hamming window with overlap of 50% and the frequency resolution is 1 Hz in all cases.

They were subsequently used to form a correlation matrix shown in equation (6.3). The aim is to separate various signals being considered and determine the principal components. A command in MATLAB known as "svd" which means Singular Value Decomposition was used to achieve this and the principal components were determined.

The correlation matrix of all the signals measured for general case is built as follows:

$$\left[S_{xx}\right]=\begin{bmatrix} S_{11} & S_{12} & \cdots & S_{1m} \\ S_{21} & S_{22} & \cdots & S_{2m} \\ \cdots & \cdots & \cdots & \cdots \\ S_{m1} & S_{m2} & \cdots & S_{mm} \end{bmatrix} \tag{6.3}$$

Assuming there are n uncorrelated principal sources (or virtual sources) formed by an m different physically measured sources, then $n \leq m$. In this study, $m = n = 4$. Eigen decomposition of the correlation matrix $\mathbf{S}_{xx}$ at a specific frequency gives:

$$\mathbf{S}_{xx} = \mathbf{U}(f)\mathbf{\Lambda}(f)\mathbf{U}^{H}(f) \tag{6.4}$$

where, $\mathbf{\Lambda}(f)$ is a diagonal matrix containing nonzero eigenvalues in descending order. It represents the spectral density of the uncorrelated sources or virtual sources. The measured responses which are the physical sources are the linear combination of these principal components. Matrix $\mathbf{U}(f)$denotes the eigenvectors which are arranged in columns. It is the linear relationship between the physical and virtual sources. Each column in $\mathbf{U}(f)$at a specific frequency corresponds to a specific eigenvalue $\mathbf{\Lambda}(f)$ at the same frequency. The number of significant independent contributors or principal components depends on the number of high eigenvalues at any specific frequency.

However, the principal component analysis can reveal the virtual sources but virtual coherence can reveal the extent to which a virtual source can contribute to each physical source. The virtual coherence between the j^{th} virtual and i^{th} physical sources is the ratio of the contribution of the virtual source j to the power spectral density of the physical source [71]:

$$\mathbf{V}_{coh} = \frac{(abs(\mathbf{U}_{ij}(f)^{*}(\mathbf{\Lambda}_{jj}(f))^{1/2})^{2}}{\mathbf{S}_{ii}(f)} \tag{6.5}$$

where, $\mathbf{U}_{ij}(f)^{*}$ is the conjugate of the eigenvector coefficient of the *ith* physical source contributing to the *jth* virtual source: $\mathbf{\Lambda}_{jj}(f)$ is the *jth* eigenvalue of the principal component or virtual source. $\mathbf{S}_{ii}(f)$ is the power spectral density of the acceleration excitation.

The experiment started by measuring the vibration of the carrier, sun and planet gears when rotating at speeds of 103, 307.98 and 337.98 rpm respectively with a load resistance of 100 Ohms. The analysis considered a case whereby a carrier and planet were investigated and another case where a sun and planet were investigated. This was repeated for another case where the speeds of the carrier, sun and planet gears are 130, 376.98 and 412 rpm at a load resistance of 100 Ohms. Also, the analysis was done considering a carrier and two planet gears as well as sun and two planet gears.

6.5.1 Principal Component Analysis of the loaded carrier and planet gear

Investigations were carried out on measured responses in the radial and tangential directions of the carrier and horizontal and vertical directions of one of the planet gear when the planetary gear was loaded. In this case, $m = n = 4,$ therefore equation (6.3) is of the form:

$$\left[S_{xx}\right] = \begin{bmatrix} S_{11} & S_{12} & S_{13} & S_{14} \\ S_{21} & S_{22} & S_{23} & S_{24} \\ S_{31} & S_{32} & S_{33} & S_{34} \\ S_{41} & S_{42} & S_{43} & S_{44} \end{bmatrix} \tag{6.6}$$

where, the first subscript ‘1’ is the measured radial response of the carrier, ‘2’ is the measured tangential response of the carrier, ‘3’ and ‘4’ are the measured horizontal and vertical radial responses of the planet gear. The carrier speed in this case is 103 rpm (1.717 Hz), the speed of the planet gear is 337.98 rpm (5.6 Hz) and the load resistance is 100 Ohms. The theoretical mesh frequency is 317.65 Hz considering the number of teeth on the ring gear in equation (6.1), while the actual mesh frequency estimated from the calculated PSD is 317 Hz. In an actual sense, the mesh frequency may not be the same using the number of teeth on the sun or planet gear. For instance, the mesh frequency for this case, considering the number of teeth on the planet gear is 330.75 while the PSD shows a frequency of 345 Hz. Probably, the load acting at the teeth mesh is fluctuating. The interpolated signal length of the carrier and the planet is 96,000 and this is applicable to subsequent cases. For instance, the raw and interpolated acceleration signals as well as the zoomed view of the carrier are shown in Figures 6-16 and 6-17. Also, few points were chosen from the raw and the interpolated signals, and the mean square difference was determined to be small. The PSD was zoomed around the mesh frequency (317.65 Hz) for clarity purpose (Figure 6-17 (b)).

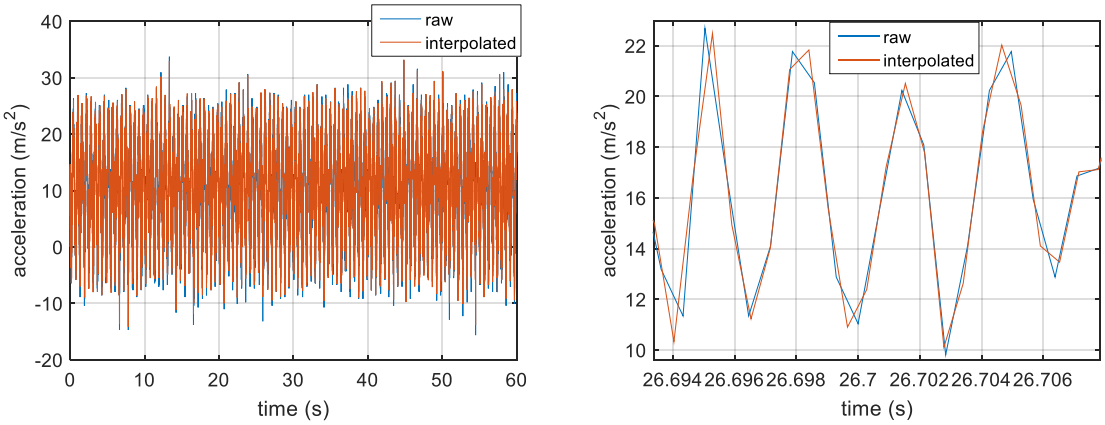

(a) (b)

Figure 6-16. (a) The time domain raw and interpolated acceleration signals of the carrier in the horizontal direction (b) zoomed view.

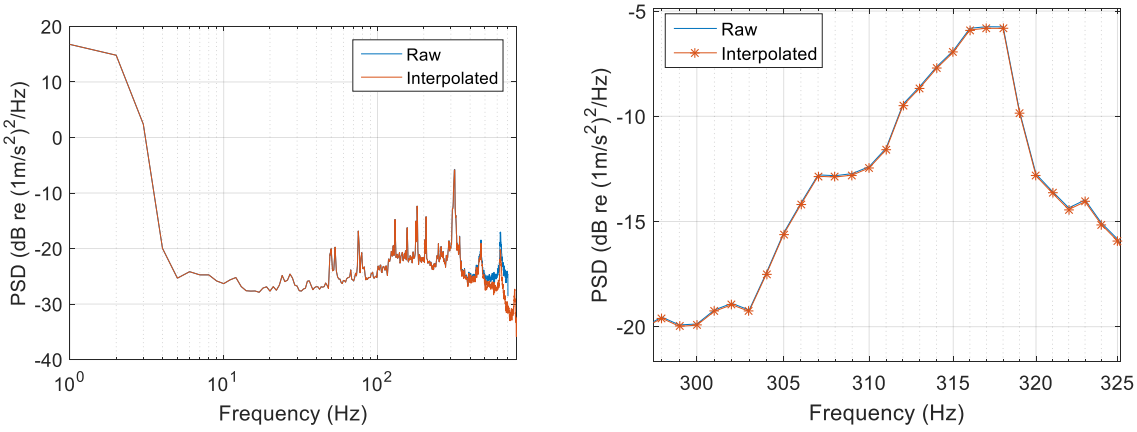

(a) (b)

Figure 6-17. (a) The frequency domain raw and interpolated acceleration signals of the carrier in the horizontal direction (b) zoomed view.

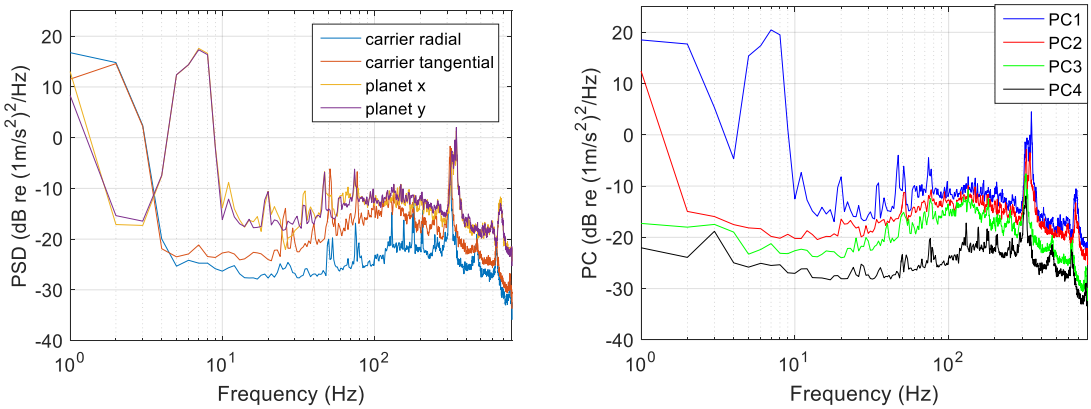

(a) **(b)**

Figure 6-18 (a) The power spectral density of the carrier and planet gears acceleration. (b) The eigenvalues of the principal components PC_1, PC_2, PC_3 and PC_4.

The two PSDs (yellow and violet lines in Figure 6-18 (a)) are of the planet gear acceleration in the *x* and *y* radial directions respectively. They are relatively higher than the PSDs of the carrier acceleration response. Generally, the responses are significant at the rotational speed and the mesh frequency. Figure 6-18 (b) shows that two principal components PC_1 and PC_2 are more significant, while the other two principal components are less significant. PC_1 contributes more at the rotational and mesh frequencies while PC_2 only contributes significantly at the mesh frequency. PC_1 and PC_2 are higher in magnitude than PC_3 and PC_4 over the wide range of frequency considered. To investigate further on the principal components, the virtual coherence and the eigenvectors were determined and plotted over a wide range of frequency.

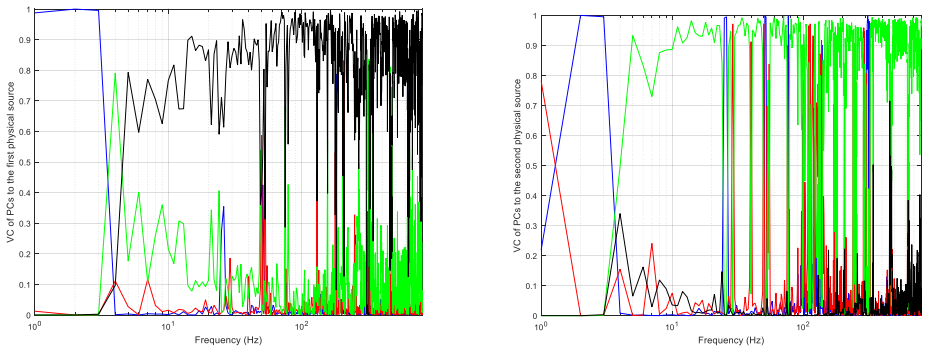

(a) **(b)**

Figure 6-19 Virtual coherence of the PC_1, PC_2, PC_3 and PC_4 showing their contributions to the (a) first physical source (radial direction of the carrier) and (b) second physical source (tangential direction of the carrier). The blue, red, green and black lines denote PC_1, PC_2, PC_3 and PC_4 respectively.

Figure 6-19 (a) shows the virtual coherence where the contributions of the PC_1 to all the physical sources can be seen over a range of frequencies (1 to 3 Hz) which includes the rotational frequency of the carrier. The contributions of PC_4 to the first physical source can be seen between 80 and 100 Hz which includes a frequency close to a measured natural frequency of the system. At the mesh frequency 317 Hz, it shows that there is no contribution from all the four PCs to the first physical source as the virtual coherence shows noisy signals at high frequencies.

The virtual coherence in Figure 6-19 (b) shows that PC_3 contributes to the second physical source (carrier tangential) from 10 to 24 Hz and from 30 to 90 Hz. The latter frequency band includes frequency related to the natural mode. PC_3 also contributes between 338 and 448 Hz which includes the mesh frequency of the planet gear which is 345 Hz.

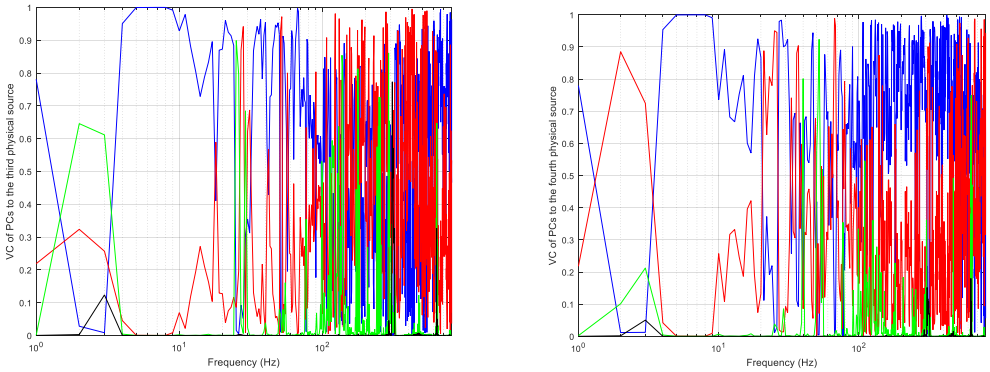

Figure 6-20 Virtual coherence of the PC_1, PC_2, PC_3 and PC_4 showing their contributions to the (c) third physical source (horizontal radial direction of the planet gear) and (d) fourth physical source (vertical radial direction of the planet gear). The blue, red, green and black lines denote PC_1, PC_2, PC_3 and PC_4 respectively.

In Figure 6-20 (a), it shows that PC1 contributes to the third physical source between 3.9 and 13 Hz which includes the rotational speed of the planet gear. PC_1 also contributes to the fourth physical source between 4 and 9 Hz (Figure 6-20 (b)). PC_2 almost show a contribution to the fourth physical source at 2 Hz. There is no PC contributing to the third and fourth physical source at higher frequencies especially the mesh frequency.

Only PC_1 contributes to all the physical sources at the frequencies of synchronous vibration (1.72 and 5.6 Hz). These are the two frequencies (corresponding to the rotational speed of carrier and sun gear) where the vibration may be as a result of unbalance or misalignment of shaft in the planetary gear train. The PSDs shows that the response at the frequency corresponding to the rotational speed is higher than the response at the mesh frequency. The virtual coherence shows noisy signal at high frequencies of the first, third and fourth physical sources. This analysis may serve as a diagnostic means of identifying the principal vibration source in planetary gear especially at the rotational and mesh frequencies of the carrier and planet gear.

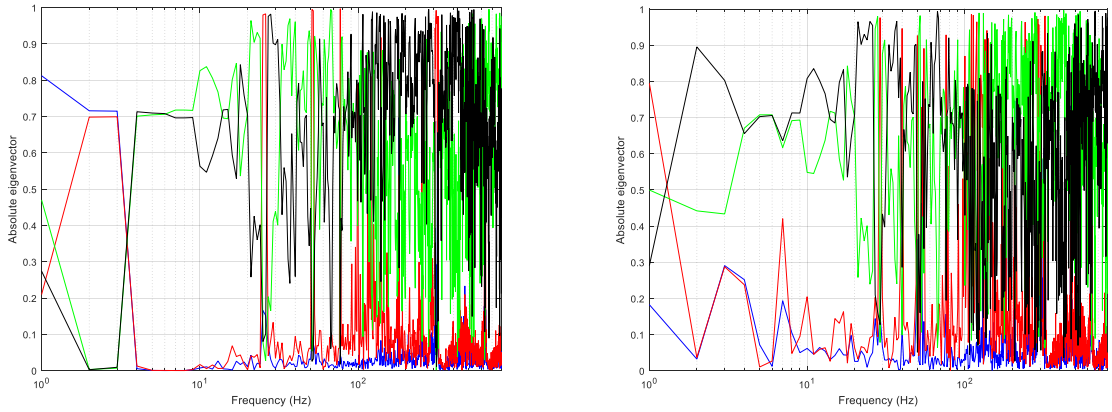

(a) **(b)**

Figure 6-21 Absolute values of eigenvector component of the first, second, third and fourth physical sources that relate with (a) PC_1 (b) PC_2. The blue, red, green and the black line denotes the absolute eigenvector components of first, second, third and fourth physical sources respectively.

The absolute eigenvector components of the first, second, third and fourth physical sources showing their correlation with PC_1 are shown in Figure 6-21 (a). It shows that the first and second physical sources correlate with PC_1 at low frequency corresponding to the rotational frequency of the carrier (1.72 Hz). The third and fourth physical sources correlate with PC_1 between 4 and 9 Hz which includes the rotational speed of the planet gear (5.6 Hz). There is no correlation between all the physical sources and PC_1 at high frequencies especially at the mesh frequency. The correlation of all

the physical sources with PC_2 is shown in Figure 6-21 (b). It shows that the fourth physical source correlates with PC_2 at a low frequency of 2 Hz.

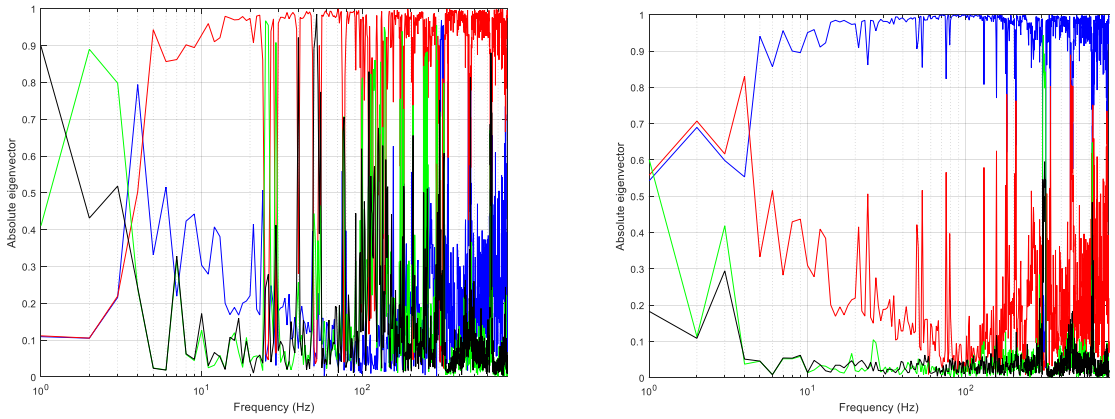

(a) **(b)**

Figure 6-22 . Absolute values of the eigenvectors of the first, second, third and fourth physical sources that relate with (a) PC_3 and (b) PC_4. The blue, red, green and the black line denotes the absolute eigenvector components of first, second, third and fourth physical sources respectively.

The correlation of the second physical source with PC_3 can be seen over a wide range of frequency as shown in Figure 6-22 (a). This frequency band includes the mesh frequency. It is very obvious that the first physical source correlate with PC_4 from 5 to 600 Hz (Figure 6-22 (b)).

In summary the values of the absolute eigenvector component confirms the dominant contribution of PC_1 to all the physical sources. It also shows clearly the linear relationship between the first physical source and PC_4 and the second physical source and PC_3.

6.5.2 Principal component analysis of the loaded sun and planet gears

An investigation was carried out on measured responses from the radial and tangential directions of the sun gear and horizontal and vertical directions of one of the planet gears when the planetary gear was loaded. The speed of the sun gear in this case is 307.98 rpm (5.133 Hz), the speed of the planet gear is 337.98 rpm (5.633 Hz) and the load resistance is 100 Ohms. The theoretical mesh frequency is 324.5 Hz considering the number of teeth on the sun gear in Equation 6.2 (b), while the actual mesh frequency from the PSD is 324 Hz. The mesh frequency of the planet gear (345 Hz) remains the same as in the previous section.

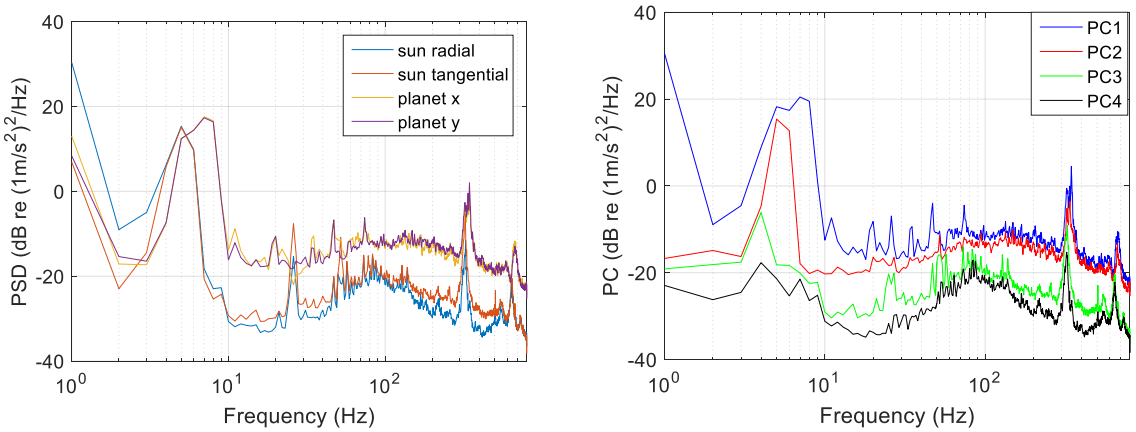

Figure 6-23 (a) The power spectral density of the sun and planet gear accelerations. (b) The eigenvalues of the principal components PC_1, PC_2, PC_3 and PC_4.

Figure 6-23 (a) shows that the PSD level of the planet gear is a higher than the sun gear at their rotational speeds of 5.633 and 5.133 Hz respectively. Also, the PSD of the planet gear is higher at the mesh frequency. Two principal components (PC_1 and PC_2) are most significant in this case (Figure 6-23 (b)). PC_1 contributes more than other PCs but all the PCs are considered because of the difference between the PCs is not big.

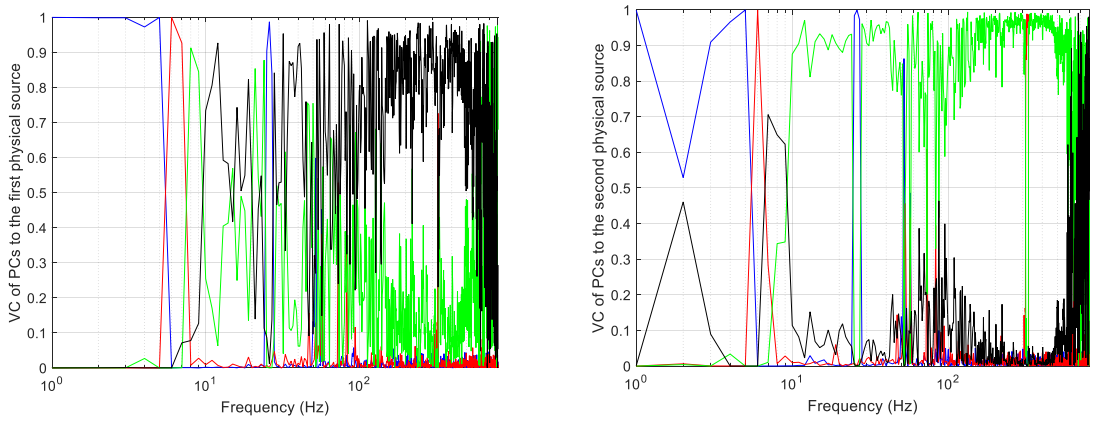

Figure 6-24 Virtual coherence of the PC_1, PC_2, PC_3 and PC_4 showing their contributions to (a) the first physical source (radial direction of the sun gear) and (b) the second physical source (tangential direction of the sun gear). The blue, red, green and black lines denote PC_1, PC_2, PC_3 and PC_4 respectively.

The contribution of PC_1 to the first physical source can be seen at a low frequency range from 1 – 5 Hz (Figure 6-24 (a)). The frequency range is close to the rotational frequency of the sun gear (5.13 Hz). It shows that PC1 is not contributing to the first physical source at higher frequencies. Figure 6-24 (b) show the contribution of PC_1 To the second physical source at a low frequency range between 3 and 5.2 Hz. PC_3 contributes from 14 to 42 Hz and from 170 to 490 Hz. The latter frequency band includes natural frequencies 187, 275, 356, 365 Hz and the mesh frequency measured in the system.

However it is obvious that the PC_3 contributes to the second physical source (sun tangential) at the sun mesh frequency of 324.5 Hz.

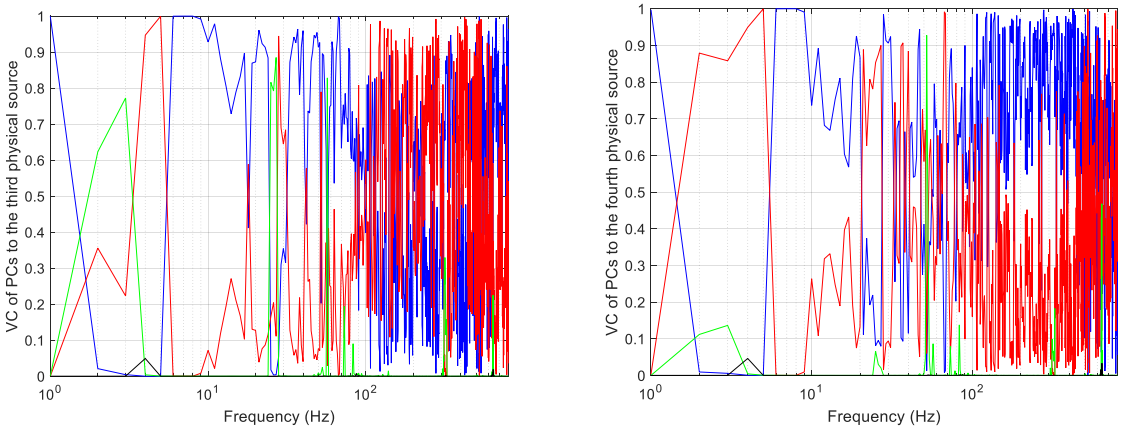

(a) **(b)**

Figure 6-25 Virtual coherence of the PC_1, PC_2, PC_3 and PC_4 showing correlation with (a) the third physical source (horizontal radial direction of the planet gear) and (b) the fourth physical source (vertical radial direction of the planet gear). The blue, red, green and black lines denotes PC_1, PC_2, PC_3 and PC_4 respectively.

PC_1 contributes to the third physical source from 5.5 to 11 Hz while PC_2 contribute to it from. 4 to 5 Hz (Figure 6-25 (a)). PC_1 contributes to the fourth physical source from 5.8 to 9 Hz while PC_2 contribute to it from 4 to 5 Hz (Figure 6-25 (b)).

In summary, it shows that PC_1 contributes to all the four physical sources at a low frequency range which include the frequencies corresponding to the rotational speed of both the sun and planet gear. PC_3 contributes to the second physical source (sun tangential) at a high frequency range which include the mesh frequency. The virtual coherence of other PCs does not show clear relationship at high frequencies especially at the mesh frequency.

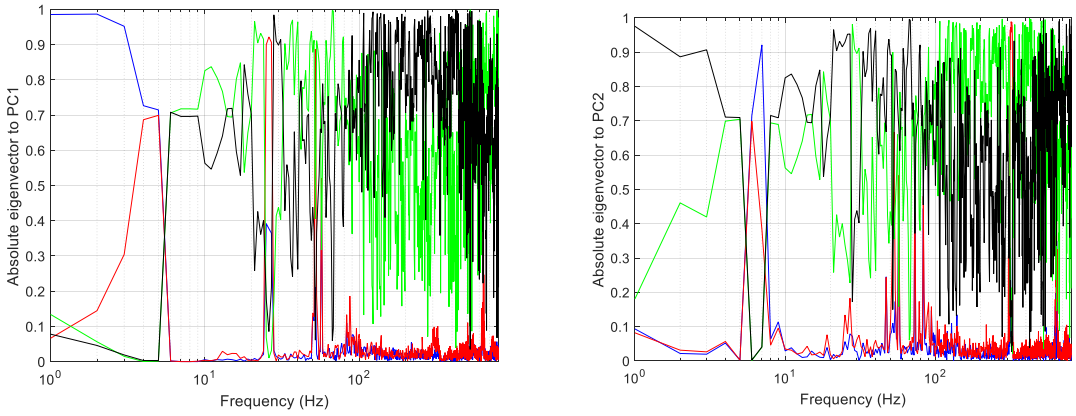

(a) **(b)**

Figure 6-26. Absolute values of the eigenvectors of the first, second, third and fourth physical sources that correlate with (a) PC_1 (b) PC_2. The blue, red, green and the black line denotes the absolute eigenvector components of first, second, third and fourth physical sources respectively.

The absolute values of eigenvector component in Figure 6-26 (a) shows that there is a linear relationship between the first physical source and PC_1 at low frequencies ranging from 1 to 3 Hz. Figure 6-26 (b) shows that there is a correlation between the fourth physical source and PC_2 from 1 to 3 Hz. The third physical source relates with PC_3 from 1 to 3.2 Hz while the second physical source relates with it at high frequencies. The second physical source relates with the PC_4 at a low frequency range.

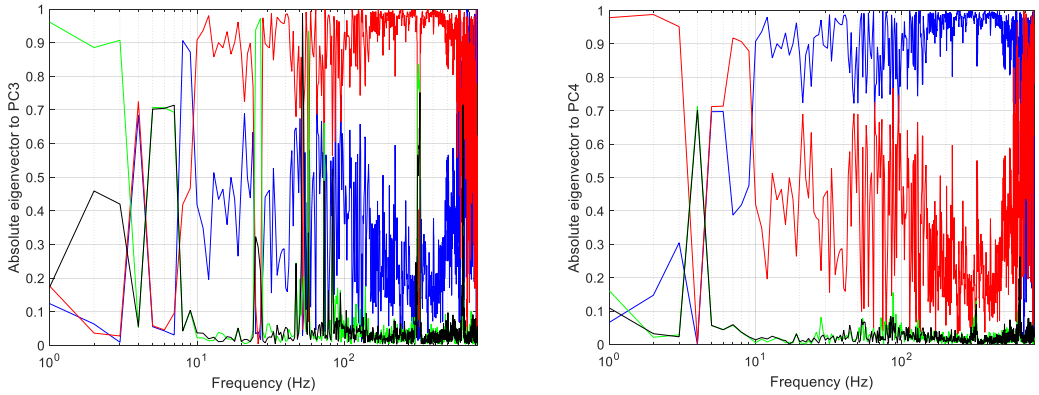

(a) **(b)**

Figure 6-27 Absolute value of eigenvectors of the first, second, third and fourth physical sources that correlates with (a) PC_3 (b) PC_4. The blue, red, green and the black line denotes the absolute eigenvector components of first, second, third and fourth physical sources respectively.

At high frequencies (including the mesh frequency), there is a relationship between the second physical source (tangential response of the sun gear) and PC3 (Figures (6-27 (a)). Also, the first physical source (radial response of the sun gear) correlates with PC4 from 25 to 45 Hz and from 145 to 500 Hz (Figure (6-27(b)).

For this case where sun and planet gear is being considered at a lower speed and high frequencies (which includes the mesh frequency), the virtual source of vibration contributing to the tangential response of the sun at the mesh frequency comes from PC_3. The virtual source contributing to the sun gear radial response is from PC_4. At low frequencies (which includes the frequencies corresponding to the rotational speed of the sun and planet gears), PCs 1 and 2 dominate in all the physical sources in a small range of frequency.

6.5.3 Principal Component Analysis of the loaded carrier and planet gear at higher speed

In this section, the PCA of the planetary gear was carried out at higher speed. The speed of the carrier in this case is 130 rpm (2.17 Hz), the speed of the planet gear is 412 rpm (6.87 Hz) and the load resistance is 100 Ohms. The theoretical mesh frequency is 400.8 Hz considering the number of teeth on the ring gear in Equation (6.2b), while the actual mesh frequency from the PSD is 397 Hz. The actual mesh frequency of the planet gear is 420 Hz. The PSDs of the carrier and planet, principal components, the contributions of the PCs to first and second physical sources and finally to the third and fourth physical sources are shown in Figures D6.2, D6.3 and D6.4 respectively in Appendix D. The results are not significantly different from the ones at the lower speed.

6.5.4 Principal Component Analysis of the loaded sun and planet gears at a higher speed

The PCA of the planetary gear was carried out at higher speed for the sun and planet gear. The radial and tangential directions of the sun gear and *x* and *y* directions of one of the planet gears when the planetary gear train was in operation were considered. The speed of the sun in this case is 376.98 rpm (6.28 Hz), the speed of the planet gear is 412 rpm (6.87 Hz) and the load resistance is 100 Ohms. The actual mesh frequencies of the sun and planet gears from the PSD are 397 and 420 Hz respectively. The PSDs of the sun and planet, principal components, the contributions of the PCs to first and second physical sources and finally to the third and fourth physical sources are shown in Figures D6.5, D6.6 and D6.7 respectively in Appendix D. The results are not significantly different from the ones at the lower speed.

6.5.5 Principal Component Analysis of the loaded carrier and planet gears at a lower resistance load

The PCA of the planetary gear was carried out at a lighter resistance load of 47 ohms for the carrier and planet gear. The radial and tangential directions of the carrier and *x* and *y* directions of one of the planet gears when were measured. The speed of the carrier in this case is 103 rpm (1.7 Hz), the speed of the planet gear is 319.98 rpm (5.33 Hz) and the load resistance is 47 ohms. The results in this sub section will be compared the ones in sub-section 6.5.1. The effect of reducing the load by approximately half was investigated. The mesh frequency of the carrier is 317 Hz while that of the planet is 315 Hz. The PSDs, PCs and the virtual coherence showing the contributions of the PCs to the first and second physical sources are shown in Figures D6.8 and D6.9 in Appendix D.

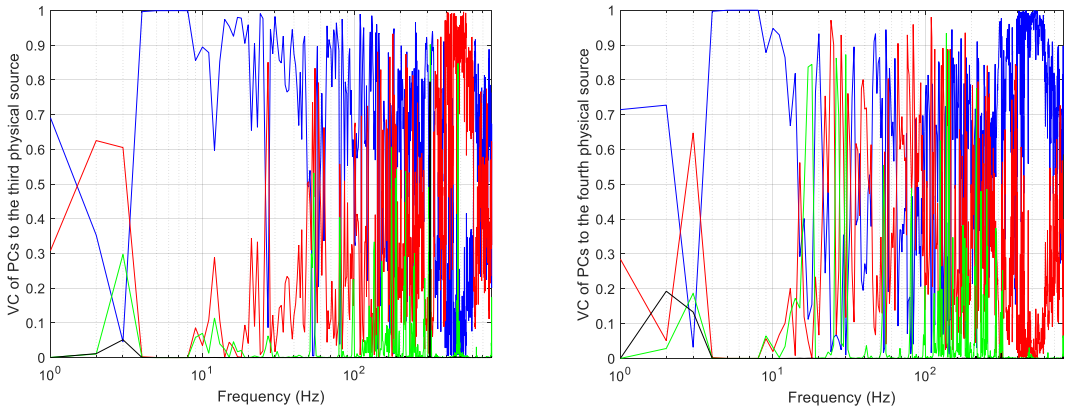

(a) **(b)**

Figure 6-28 Carrier-planet virtual coherence of the PC_1, PC_2, PC_3 and PC_4 at 47 ohms showing their contributions to the (c) third physical source (x direction of the planet gear) and (d) fourth physical source (y direction of the planet gear). The blue, red, green and black lines denotes PC_1, PC_2, PC_3 and PC_4 respectively.

The virtual coherence showing the contributions of PC_1 to the third and fourth physical sources are shown in Figure 6-28 (a) and (b) respectively. It shows that the contribution of PC_1 to the fourth physical source at higher frequency range is becoming clearer between 450 to 580 Hz (Figure 6-28 (b)). This shows that at a lighter resistance load, the virtual source of vibration contributing to the fourth physical source at high frequencies is becoming more obvious compared to unlike the virtual coherence at a heavier load of 100 ohms (Figure 6-20 (b)).

6.5.6 Principal Component Analysis of the loaded sun and planet gears at lower resistance load

The PCA of the planetary gear was carried out at a lower resistance load of 47 ohms for the sun and planet gear. The speed of the sun in this case is 294 rpm (4.9 Hz), the speed of the planet gear is 319.8 rpm (5.33 Hz) and the load resistance is 47 ohms. The actual mesh frequencies of the sun and planet gears from the PSD are 312 and 326 Hz respectively. The PSDs of the sun and planet, principal components, the contributions of the PCs to first and second physical sources and finally to the third and fourth physical sources are shown in Figures D6.10 and D6.11 respectively in Appendix D.

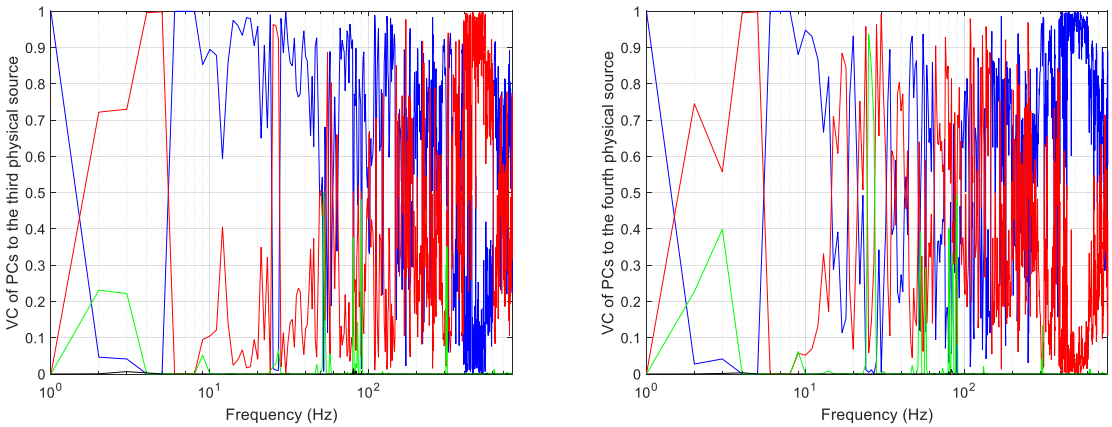

(a) **(b)**

Figure 6-29 Sun-planet virtual coherence of the PC_1, PC_2, PC_3 and PC_4 at 47 ohms showing their contributions to the (c) third physical source (x direction of the planet gear) and (d) fourth physical source (y direction of the planet gear). The blue, red, green and black lines denotes PC_1, PC_2, PC_3 and PC_4 respectively.

It is also obvious in Figure 6.29 (b) that PC_1 is contributing to the fourth physical source at high frequency. This is not obvious at a load of 100 ohms previously discussed. In general the PCs 1 and 2 do not correlate with the third and fourth physical sources at the mesh frequencies probably because there is mesh phasing. The number of teeth on the ring gear divided by the number of planet gears in this study is 92.5. Inapolat et al. [35] stated that if the ratio of number of teeth on the ring gear and number of planets is not equal to an integer, the planet gear are out of phase, therefore there is mesh phasing. It is necessary to conduct this experiment without phasing by increasing the number of planet gears in the planetary gear system such that the ratio will give an integer.

6.5.7 Summary on vibration source identification

The investigation has been carried out using PCA technique to identify the major source of vibration in the planetary gear considering two different rotational speeds under a constant resistance load. An

investigation was also done by reducing the load with the speed remaining constant. This is useful in providing information needed when monitoring or reducing vibration in a planetary gear system. The analysis was done directly on the signals measured individually on the carrier, sun and planet gears using MEMs accelerometers when rotating. First and foremost, a carrier and a planet gear were considered and subsequently a sun and planet gear was considered for two different rotational speeds. Also, the analysis was performed for a lower resistance load of 47 Ohms. In general, the following was discovered,

1. For a carrier and planet gear
    a. The major virtual source of vibration of all the physical sources at low frequencies (especially at the frequency of synchronous vibration) is PC_1, which relates with the planet *y* radial direction. Hence, the planet is the major source of synchronous vibration which may be due to unbalance in the load sharing or misalignment when coupling together the carrier, sun and planets.
    b. The major virtual source of vibration at high frequencies (especially at the mesh frequency) which dominates the first physical source (carrier radial) is PC_4. PC_4 relates with the carrier response in the radial direction.
    c. The major virtual source of vibration at high frequencies dominating the second physical source is PC_3 which relates with the tangential direction of the carrier response.
    d. The major virtual source of vibration dominating the third and fourth physical sources at high frequencies is unclear at 100 Ohms. When a lighter load of 47 Ohms was applied it becomes clearer that PC_1 which relates to planet in the *y* direction contributes to the fourth physical source over a high frequency range.
2. For sun-planet case
    a. PC_1 dominates all the physical sources at low frequencies including the frequencies corresponding to the rotational speeds of the sun and planet gears.
    b. The principal contributor to the first physical source at high frequencies is not clear at 100 ohms.
    c. The major contributor to the second physical source at high frequency is PC_3, which relates with the sun tangential response.
    d. The major contributors to the third and fourth physical sources are not clear at high frequencies for a load of 100 Ohms. However, at a light load of 47 ohms the major contribution comes from PC_1 over a narrow range of frequency.

3. For a constant load, there is no significant difference between the eigenvalues of the principal components, virtual coherence and absolute eigenvectors for the two rotational speeds considered.
4. Attention must be paid to $PC_1$when considering the synchronous vibration.
5. PC_1 and PC_2 which correspond to the planet *y* and *x* radial directions respectively are relatively higher for all the cases considered. This is due to the fact that the planet gears bear and share the load in the system and there may be larger deflection at the sun-planet and planet-ring mesh.

6.6 Conclusions

The individual extensive vibration measurements of the carrier, sun and planet gear has been presented for two different rotational speeds and loads. The benefit of such measurement is that there is no need to use any signal separation technique to identify the vibration of each component, which is the usual practice when accelerometers are mounted on the casing. This method is very good for fault diagnosis as all the responses at the resonance and mesh frequencies, responses associated with misalignment are measured. In this case, it is easier to identify a faulty component considering their vibrations in different directions within a short period. The severity of the faults can be measured and monitored for corrections to prevent damage of a planetary gear system.

The study on the effect of speed and load on the dynamic response reveals the following:

- In general, the response of the carrier and sun in the tangential direction is higher than the responses in the radial direction but the response of the planet gear is the highest.
- For a case of varying rotational speed and load, the tangential responses of the carrier and sun increase with increased speed and load. The response of the planet also increases as the speed and load increase. The radial and tangential response of the sun gear at a frequency associated with natural mode could be high when a light load is applied.
- For a case of constant load and varying speed, the tangential response of the carrier at the mesh frequency are the same except the response at the resonance frequency and the one close to it. The tangential response of the sun gear at mesh frequency increases as the speed increases. This is the same for the planet gear response at the mesh frequency. For the response at the frequencies relating to the natural mode, increased rotational speed does not show clearly if it affects the response of the carrier in both directions. The tangential response of the sun is high at low speed, while the response of the planet is high at a light load.
- For a constant speed and varying resistance load, the response of the carrier at the mesh frequency is high when the load is light. Either a light or heavy resistance load can lead to

damage of the teeth of the sun gear operating under a constant rotational speed. A light resistance load can damage the teeth of the planet gear under a constant speed.

- The study also shows that the tangential response of the carrier at the mesh frequency can be higher than the tangential response of the sun gear at the same frequency, if the stiffness of the planet bearing at the carrier-planet interface is less than that of the sun gear.
- A response level relating to misalignment of sun gear at low frequency is significant at the maximum rotational speed and resistance load. If the load is constant, the response level and the frequency are increasing with the increased rotational speed. Conversely, if the rotational speed is constant, the frequency and response level are increases as the load is decreases.

The study on vibration source identification shows the major source of synchronous vibration contributing to all the physical sources. For carrier-planet and sun-planet cases, the major source of vibration contributing to the planet (the third and fourth physical source) at the mesh frequency could not be established even when their rotational speeds were increased. The major source of vibration at the mesh frequency between carrier-planet and sun-planet is more noticeable when the resistance load was reduced from 100 Ohms to 47 Ohms.

Given the vibration that has been modelled and measured, this study will subsequently consider theoretically an active control approach known as pole placement. The theory of pole placement will be extended to include equation of motion of a planetary gear. The controller will be designed using both fixed and rotating frames of reference in order to control vibration of the system. Analysis with numerical examples will be presented in the next chapter.

Chapter 7 Active vibration control of planetary gears

Active vibration control involves changing the dynamics of a vibrating system by typically applying equal but opposite active forces to counter the effect of an excitation force. This chapter presents mainly the theory for pole placement applied to planetary gear using active vibration control method. The theory is an extension of that developed by Mottershead et al. and the dynamic model is an extended model developed by Parker [14]. Pole placement involves assigning the closed loop poles of a system at the desired locations in the complex *s*-plane for stability. The aim is to shift the natural frequencies of the system to avoid resonance which can cause failure of a system. This can be achieved for example by actively adding stiffness using displacement feedback as the control strategy. Likewise, damping can be actively added to the system using velocity feedback in the control strategy. It is also possible to combine the displacement and velocity feedback strategies (or output feedback) when controlling vibration of a system. In this case, the natural frequencies can be shifted and the response at resonance frequencies can be reduced simultaneously.

Vibration control of planetary gear is necessary to avoid any form of failure associated with vibration. These failures can cause breakdown of machines where planetary gears are used for torque transmission. It is believed that the poles of a planetary gear system can be shifted to avoid resonance, one method to achieve this for a linear system is by a receptance method. The control strategy to be implemented in this study is the output feedback and this will be done by pole placement. In some cases, the reverse method where the feedback gain is assigned will be demonstrated. According to Mottershead et al., collocated sensor-actuator arrangement is possible when using output feedback [15]. This implies that the sensors and the actuators are collocated at the same place. This is achievable if the characteristic nonlinear equation containing the gain terms is formulated. Closed loop poles will be assigned to the dynamic model of the planetary gear using pole placement by receptance method. The main purpose of doing this is to actively change the stiffness of the planetary gear system by displacement feedback, which results in a phenomenon called detuning. Detuning a system prevents resonance, which can cause failure associated with vibration. Another purpose is to reduce its response at resonance through velocity feedback which increases the damping of the system.

For simplicity, the application of displacement and velocity feedback will be demonstrated first numerically, using a three degree of freedom system in Figure 7.2. Subsequently, the displacement and velocity feedback will be considered simultaneously. It will be demonstrated that there is similarity between displacement and velocity feedback without pole placement and with pole placement.

However, for pole placement on the planetary gear, the theoretical and numerical studies cover the use of both fixed and rotating frames of reference as the coordinate systems. The controller design is such that the pole can be assigned considering the rotational speed of the reference frame. The pole placement method where the rotational speed of the reference frame is considered in the control law is rare in the literature. This is done to demonstrate that the control force required using a rotating frame of reference can be determined and transformed using a fixed frame of reference for practical implementation. Numerical examples will be demonstrated, first using a fixed frame of reference to determine the feedback gains after pole assignment. This feedback gain using a fixed frame of reference will be used to determine the equivalent poles using a rotating frame of reference. The next stage is to determine the feedback gain using a rotating frame of reference and take a further step to obtain the poles using a fixed frame of reference. Therefore, the procedure is in a cycle such that the equivalent control force using a rotating frame of reference can be determined using a fixed frame of reference.

The simulations in this study are for excitation due to transmission error between the sun and planet gear where equal but opposite forces are applied on them. This can give rise to a mesh excitation whose frequency is the product of the operating speed and the number of teeth on the stationary ring gear.

For the displacement and velocity feedback, two control forces will be used to assign poles on the vertical and the horizontal directions of the sun gear only. The same will be repeated on the carrier. Then, four actuators will be used to assign poles on the horizontal and vertical directions of the carrier and the sun gear simultaneously. The simulations will be done using both frames of reference. The *s*-plane will be presented to show how the poles have shifted after pole placement has been applied to the system.

7.1 Active stiffness and damping using both displacement and velocity feedback with numerical examples

For simplicity, the concept of feedback in active vibration control will be demonstrated first using displacement and velocity feedback in order to add active stiffness and damping to a dynamic system.

The general dynamic equation of motion for a dynamic system is given in the form of second order matrix equation in the Laplace domain as

$$(s^2\mathbf{M} + s\mathbf{C} + \mathbf{K})\mathbf{x}(s) = \mathbf{f}_p(s) + \mathbf{f}_s(s) \tag{7.1}$$

where, $\mathbf{M}$, $\mathbf{C}$, $\mathbf{K} \in \Re^{n\times n}$; $\mathbf{M} = \mathbf{M}^T$, $\mathbf{C} = \mathbf{C}^T$, $\mathbf{K} = \mathbf{K}^T$ are the mass, damping, stiffness matrices respectively. Also, where $\mathbf{f}_p(\mathrm{s}) \in \Re^{m\times 1}$, $\mathbf{f}_s(\mathrm{s}) \in \Re^{m\times 1}$ are the external disturbance and the control force respectively.

The control law is written as

$$\mathbf{F}_s(s) = -\mathbf{B}_s(\mathbf{G}_d + \mathbf{G}_v)\mathbf{y}(s) \tag{7.2}$$

where $\mathbf{B}_s \in \Re^{m\times n}$ is the control force distribution matrix, $\mathbf{B}_s^T = \mathbf{D}_s$ which is the sensor distribution matrix, $\mathbf{G_d}$ and $\mathbf{G_v}$ are the feedback gain matrices proportional to stiffness and damping respectively. The output equation is written as

$$\mathbf{y}(s) = \mathbf{D}_s\mathbf{x}(s) \tag{7.3}$$

For a collocated sensor and actuator arrangement $\mathbf{D}_s = \mathbf{B}_s^T$

$$\mathbf{F}_s(s) = -\mathbf{B}_s(\mathbf{G_d} + \mathbf{G_v})\mathbf{B}_s^T\mathbf{x}(s) \tag{7.4}$$

Equation 7.1 can now be written as

$$[s^2\mathbf{M} + s(\mathbf{C} + \mathbf{B}_s\mathbf{G}_v\mathbf{D}_s) + (\mathbf{K} + \mathbf{B}_s\mathbf{G}_d\mathbf{D}_s)]\mathbf{x}(\mathrm{s}) = \mathbf{F}_p(s) \tag{7.5}$$

7.1.1 Numerical example

A theoretical analysis and numerical example is given on a constrained three degree of freedom system shown in Figure 7-1 as follows.

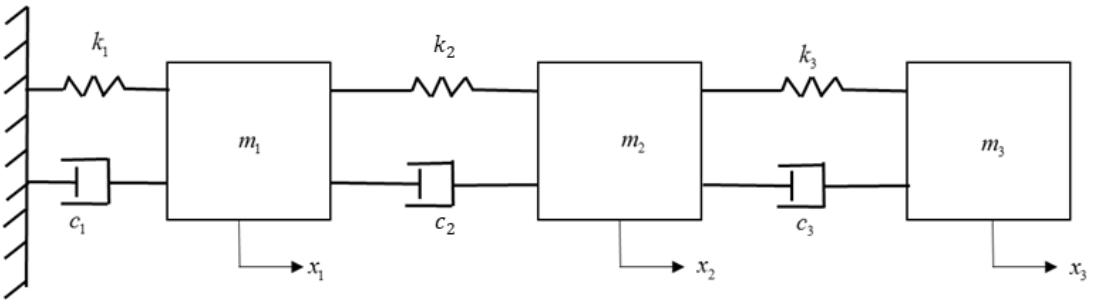

Figure 7-1 A constrained three degrees of freedom system.

The values of the parameters of the system in Figure 7-1 have been chosen as:

$m_1 = 1\ kg, m_2 = 2\ kg, m_3 = 4\ kg, C_1 = 0.4\ Ns/m, C_2 = 0.6\ Ns/m, C_3 = 0.8\ Ns/m,\ k_1 = 2\ N/m, k_2 = 4\ N/m, k_3 = 6\ N/m$. The mass **M**, damping **C** and stiffness **K** matrices are given by

$$\mathbf{M} = \begin{bmatrix} 1 & 0 & 0 \\ 0 & 2 & 0 \\ 0 & 0 & 4 \end{bmatrix} \text{kg}\ ,\ \mathbf{C} = \begin{bmatrix} 1.0 & -0.6 & 0 \\ -0.6 & 1.4 & -0.8 \\ 0 & -0.8 & 0.8 \end{bmatrix} \text{Ns/m}, \mathbf{K} = \begin{bmatrix} 6 & -4 & 0 \\ -4 & 10 & -6 \\ 0 & -6 & 6 \end{bmatrix} \text{N/m}$$

The initial poles of the system are as follows:

$$P_1 = -0.0171 \pm 0.4350i, P_2 = -0.2750 \pm 1.8949i, P_3 = -0.6579 \pm 2.8643i$$

In this analysis, both the displacement and velocity were fed back in order to achieve both active stiffness and damping simultaneously. Equation 7.5 shows that active stiffness and damping can be added to the system through feedback gains. Considering the first and the third masses, the following control gains were assigned considering equation (7.5).

$$\mathbf{G}_d = \begin{bmatrix} 0.5 & 0 \\ 0 & 0.7 \end{bmatrix}, \mathbf{G}_v = \begin{bmatrix} 0.7 & 0 \\ 0 & 0.4 \end{bmatrix}, \mathbf{D}_s = \begin{bmatrix} 1 & 0 & 0 \\ 0 & 0 & 1 \end{bmatrix}, \mathbf{B}_s = \mathbf{D}_s^T = \begin{bmatrix} 1 & 0 \\ 0 & 0 \\ 0 & 1 \end{bmatrix}$$

This changed the location of the initial poles of the system to other positions due to the change in the real and complex parts of the initial complex conjugate poles**.** The modified poles of the system after assigning feedback gains $\mathbf{G}_d$ and $\mathbf{G}_v$ are as follows:

$$\tilde{P}_1 = -0.0707 \pm 0.5777i, \tilde{P}_2 = -0.4248 \pm 1.9600i, \tilde{P}_3 = -0.8545 \pm 2.8143i$$

.

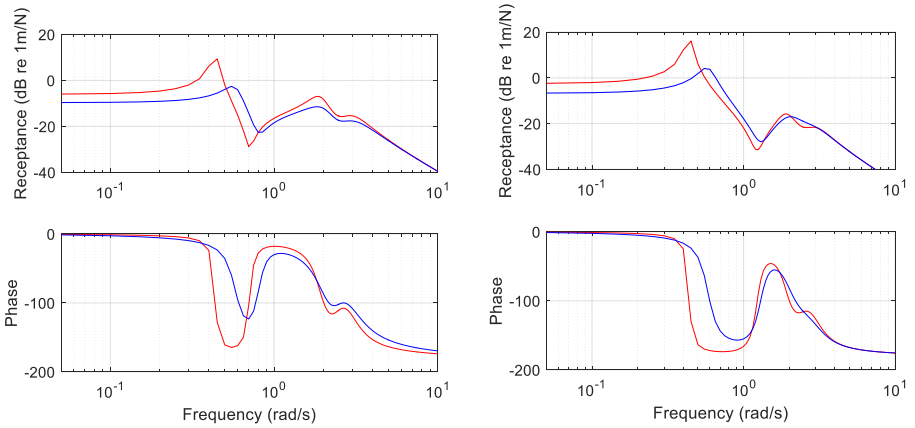

(a) First mass (b) Second mass

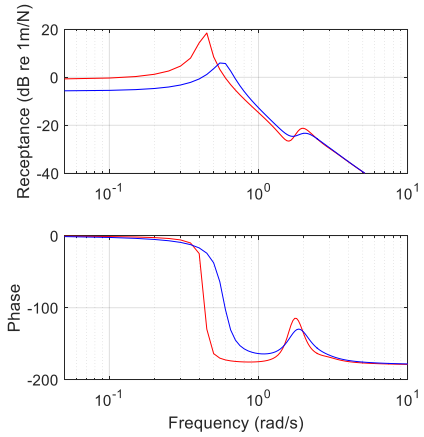

(c) Third mass

Figure 7-2 The response of the (a) first mass (b) second mass (c) third mass after assigning control gain using both displacement and velocity feedback. The initial and modified receptances are shown in red and blue respectively.

The pole of the first excited mode shown in Figure 7-2 (a) was shifted from -0.0171 ± 0.4350 to $-0.0707 \pm 0.5777i$ and a significant amount of damping was also added as the real part of the pole has increased. The same mode was shifted in the second and the third masses. The second mode as shown in both the Figures 7-2. (a) and (b), was shifted from $-0.2750 \pm 1.8949i$ to $-0.4248 \pm 1.9600i$. Although the control force is not applied on the second mass, it is evident in Figure 7-2 (b) that the frequency of the first mode has been shifted as in the second mass. This is because the first mass is statically coupled to the second mass while the second mass is statically coupled to the third mass where the control forces were applied. The active stiffness added has changed the damped natural frequencies of the system to prevent resonance if excited by external disturbance whose frequency matches the natural frequencies of the system. Active damping added to the system can increase the level of damping and therefore reduced the response at resonance frequency to prevent failure of the system.

7.2 Similarities between using displacement and velocity feedback by pole placement using receptance method

It will be demonstrated that displacement and velocity feedback by pole placement using receptance method gives the same result as the one demonstrated in sub-section 7.1.1. First and foremost the theory of pole placement by the receptance method will be analysed as follows.

From equation (7.5),

$$[s^2\mathbf{M} + s(\mathbf{C} + \mathbf{B}_s\mathbf{G}_v\mathbf{D}_s) + (\mathbf{K} + \mathbf{B}_s\mathbf{G}_d\mathbf{D}_s)]^{-1}\mathbf{F}_p(s) = \mathbf{x}(s) \tag{7.6}$$

where, $[s^2\mathbf{M} + s(\mathbf{C} + \mathbf{B}_s\mathbf{G}_v\mathbf{D}_s) + (\mathbf{K} + \mathbf{B}_s\mathbf{G}_d\mathbf{D}_s)]^{-1}$ is the closed loop receptance matrix. The open loop receptance matrix for the system in Figure 7.1 can be written as:

$$\mathbf{H}_d(s) = (s^2\mathbf{M} + s\mathbf{C} + \mathbf{K})^{-1} \tag{7.7}$$

If Equation (7.5) is pre-multiplied by Equation (7.7),

$\mathbf{H}_d(s)[s^2\mathbf{M} + s(\mathbf{C} + \mathbf{B}_s\mathbf{G}_v\mathbf{D}_s) + (\mathbf{K} + \mathbf{B}_s\mathbf{G}_d\mathbf{D}_s)]\mathbf{x}(s) = \mathbf{H}_d(s)\mathbf{F}_p(s)$, one obtains

$$[\mathbf{I} + \mathbf{H}(s)\mathbf{B}_s(\mathbf{G}_d + s\mathbf{G}_v)\mathbf{D}_s]\mathbf{x}(s) = \mathbf{H}_d(s)\mathbf{F}_p(s) \tag{7.8}$$

where, **I** is an identity matrix, then

$$\mathbf{x}(s) = [\mathbf{I} + \mathbf{H}_d(s)\mathbf{B}_s(\mathbf{G}_d + s\mathbf{G}_v)\mathbf{D}_s]^{-1}\mathbf{H}_d(s)\mathbf{F}_p(s) \tag{7.9}$$

$$\mathbf{x}(s) = \frac{\text{adj}[\mathbf{I} + \mathbf{H}_d(s)\mathbf{B}_s(\mathbf{G}_d + s\mathbf{G}_v)\mathbf{D}_s]}{\det[\mathbf{I} + \mathbf{H}_d(s)\mathbf{B}_s(\mathbf{G}_d + s\mathbf{G}_v)\mathbf{D}_s]}\mathbf{H}_d(s)\mathbf{F}(s) \tag{7.10}$$

The eigenvalues that make the denominator of Equation (7.10) equal to zero are known as poles. Likewise, the eigenvalues that makes the numerator equal to zero are called zeros. The closed loop poles may be assigned to the system to obtain feedback gains $\mathbf{g}_d$ and $\mathbf{g}_v$ such that the nonlinear equation $\det(\mathbf{I} + \mathbf{H}_d(\lambda_j)\mathbf{B}_s(\mathbf{G}_d + \lambda_j\mathbf{G}_v)\mathbf{D}_s) = \mathbf{0}$ can be satisfied.

7.2.1 Numerical example

The modified conjugate poles obtained after assigning feedback gains in Section 7.1.1 were assigned to the system in Figure 7.2. The poles are as follows:

$$\lambda_{1,2} = -0.0707 \pm 0.5777i, \lambda_{3,4} = -0.8545 \pm 2.8143i$$

There are four characteristic equations written as

$$\det[\mathbf{I}+\mathbf{H}_d(\lambda_j)\mathbf{B}_s(\mathbf{G}_d+\lambda_j\mathbf{G}_v)\mathbf{D}_s]=0 \qquad \lambda=1,....,4$$

while the open loop receptance matrix is written as

$$\mathbf{H}_d(\lambda_j)=(\lambda_j^2\mathbf{M}+\lambda_j\mathbf{C}+\mathbf{K})^{-1} \qquad \lambda=1,....,4$$

The numerical results for the feedback gains are:

$$\mathbf{G}_d=\begin{bmatrix}0.5 & 0\\ 0 & 0.6997\end{bmatrix}\text{Ns/m},\ \mathbf{G}_v=\begin{bmatrix}0.6999 & 0\\ 0 & 0.4000\end{bmatrix}\text{Ns/m}$$

The feedback gains are approximately equal to the ones assigned in subsection 7.1.1. This illustrates that the displacement and velocity feedback strategy without pole placement and by pole placement using the receptance method gives similar results in principle.

7.3 Active control of a planetary gear system by pole placement using a fixed frame of reference

The dynamic model for the pole assignment analysis is shown in Figure 7-3; this model has been described earlier in Chapter 3.

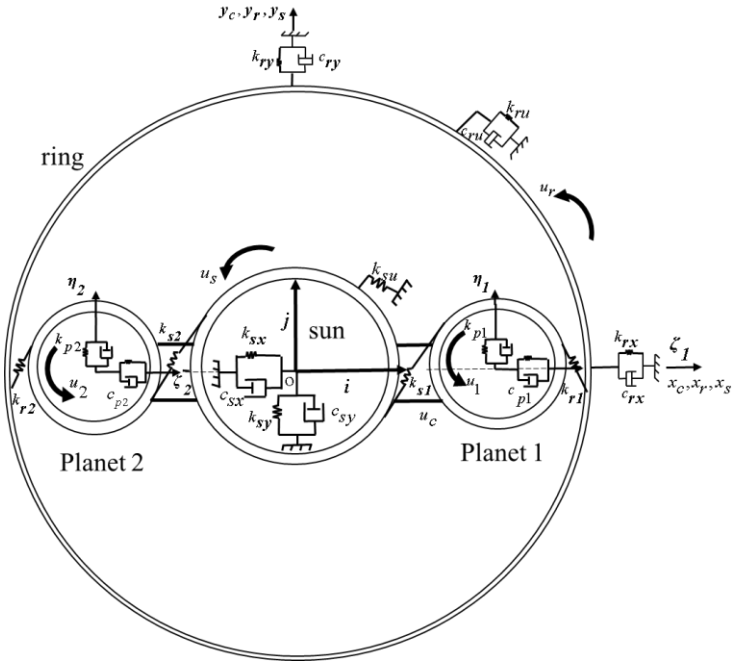

Figure 7-3 Lumped parameter model of a single stage planetary gear. It comprises a carrier, a ring, a sun and two planet gears.

For pole placement, the second order dynamic equation of motion for the planetary gear system using fixed frame of reference is formulated as follows

$$[\mathbf{s}^2\mathbf{M} + \mathbf{s}\mathbf{C}_b + (\mathbf{K}_b + \mathbf{K}_m)]\mathbf{q}(\mathbf{s}) = \mathbf{F}_{te}(\mathbf{s}) + \mathbf{B}\mathbf{U}(\mathbf{s}) \tag{7.11}$$

where,

$$\mathbf{F}_{te} = k_{sn} e_{sn} \begin{bmatrix} 0 & 0 & 0 & 0 & 0 & 0 & \sin\psi_{sn} & \cos\psi_{sn} & 1 & -\sin\alpha_s & -\cos\alpha_s & -1 & 0 & 0 & 0 \end{bmatrix}^T$$

$$\psi_{sn} = \psi_n - \alpha_s$$

and where, $\mathbf{M}, \mathbf{C}_b, \mathbf{K}_b, \mathbf{K}_m \in \Re^{n\times n}; \mathbf{M} = \mathbf{M}^T, \mathbf{C}_b = \mathbf{C}_b^T, \mathbf{K}_b = \mathbf{K}_b^T, \mathbf{K}_m = \mathbf{K}_m^T$ are the mass, damping, bearing and mesh stiffnesses respectively. $\mathbf{B} \in \Re^{m\times n}$ is the control force distribution matrix $\mathbf{u}(s) \in \Re^{m\times 1}$ and is the control force, while $\mathbf{F}_{te} \in \Re^{m\times 1}$ is the disturbance due to the transmission error in the sun-planet mesh. These are two opposing forces in the sun-planet mesh unlike the forces being applied in most dynamic systems. The pressure angle and planet positions are denoted by α_s and ψ_n.

The feedback control law can be expressed as:

$$\mathbf{U}(\mathrm{s}) = -(\mathbf{G} + \mathrm{s}\mathbf{F})\mathbf{q}_{op}(\mathrm{s}) \tag{7.12}$$

The matrices **G** and **F** give the feedback gains, which are directly proportional to active stiffness and damping respectively. Where, vector $\mathbf{q}_{op}(\mathrm{s})$ is the output. The output equation is written as

$$\mathbf{q}_{op}(\mathrm{s}) = \mathbf{D}\mathbf{q}(\mathrm{s}) \tag{7.13}$$

For collocated sensors and actuators, $\mathbf{B}^T = \mathbf{D} \in \Re^{m\times n}$, where **D** is the sensor distribution matrix. If **U(s)** is substituted into equation (7.11), then

$$[\mathbf{s}^2\mathbf{M} + \mathbf{s}\mathbf{C}_b + (\mathbf{K}_b + \mathbf{K}_m)]\mathbf{q}(\mathbf{s}) = \mathbf{F}_{te}(\mathbf{s}) + \mathbf{B}\left[-(\mathbf{G}+\mathrm{s}\mathbf{F})\mathbf{D}\mathbf{q}(\mathrm{s})\right] \tag{7.14}$$

Taking the second term on the right hand side to the left hand side,

$$[\mathbf{s}^2\mathbf{M} + \mathbf{s}(\mathbf{C}_b + \mathbf{BFD}) + (\mathbf{K}_b + \mathbf{K}_m + \mathbf{BGD})]\mathbf{q}(\mathbf{s}) = \mathbf{F}_{te}(\mathbf{s}) \tag{7.15}$$

$$\mathbf{q}(\mathbf{s}) = [\mathbf{s}^2\mathbf{M} + \mathbf{s}(\mathbf{C}_b + \mathbf{BFD}) + (\mathbf{K}_b + \mathbf{K}_m + \mathbf{BGD})]^{-1}\mathbf{F}_{te}(\mathbf{s}) \tag{7.16}$$

where, $[\mathbf{s}^2\mathbf{M} + \mathbf{s}(\mathbf{C}_b + \mathbf{BFD}) + (\mathbf{K}_b + \mathbf{K}_m + \mathbf{BGD})]^{-1}$ is the closed loop inverse dynamic stiffness matrix using the fixed frame of reference. The term $s(\mathbf{C}_b + \mathbf{BFD})$ provides active damping into the system while $(\mathbf{K}_b + \mathbf{K}_m + \mathbf{BGD})$ changes the natural frequencies of the system. The open loop inverse dynamic stiffness matrix is:

$$\mathbf{H(s)} = [s^2\mathbf{M} + s\mathbf{C}_b + (\mathbf{K}_b + \mathbf{K}_m)]^{-1}, \tag{7.17}$$

If equation (7.15 is pre-multiplied at both sides by the equation (7.17), we have,

$$[\mathbf{I} + \mathbf{H(s)B}(\mathbf{G} + s\mathbf{F})\mathbf{D}]\mathbf{q}(s) = \mathbf{H}(s)\mathbf{F}_{te}(s)$$

$$\mathbf{q}(s) = [\mathbf{I} + \mathbf{H(s)B}(\mathbf{G} + s\mathbf{F})\mathbf{D}]^{-1}\mathbf{H}(s)\mathbf{F}_{te}(s)$$

$$\mathbf{q}(s) = \frac{adj[\mathbf{I}+\mathbf{H(s)B}(\mathbf{G}+s\mathbf{F})\mathbf{D}]}{\det[\mathbf{I}+\mathbf{H(s)B}(\mathbf{G}+s\mathbf{F})\mathbf{D}]}\mathbf{H}(s)\mathbf{F}_{te}(s) \tag{7.18}$$

The eigenvalues μ_j that make the denominator equal to zero are known as poles and written as.

$$\det(\mathbf{I} + \mathbf{H}(\mu_j)\mathbf{B}(\mathbf{G} + \mu_j\mathbf{F})\mathbf{D}) = \mathbf{0} \tag{7.19}$$

The values of eigenvalues λ_i that make the numerator of equation (6.8) equal to zero are known as zeros and written as

$$\mathrm{adj}(\mathbf{I} + \mathbf{H}(\lambda_i)\mathbf{B}(\mathbf{G} + \lambda_i\mathbf{F})\mathbf{D})\mathbf{H}(\lambda_i)\mathbf{H}(\lambda_i) = \mathbf{0} \tag{7.20}$$

Where, **I** is an identity $n \times n$ matrix

Only the assignment of poles was considered in this analysis and numerical examples. The schematic diagram of the control system is shown in Figure 7-4, where the disturbance is applied at the input and the output is fed back to achieve stability in the system.

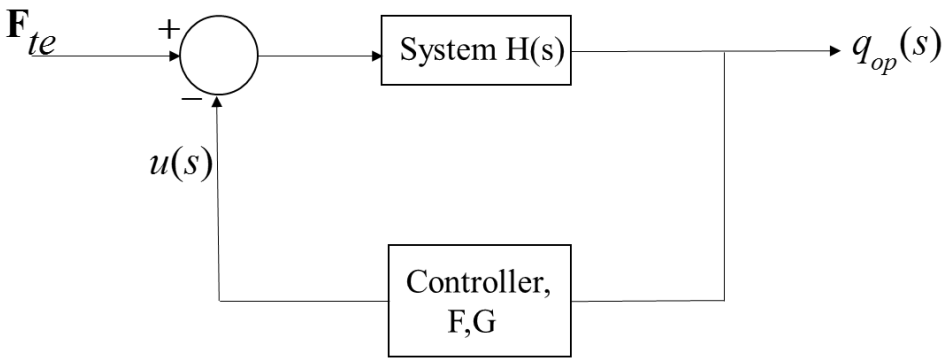

Figure 7-4 Schematic diagram of closed loop feedback control system.

7.4 Active control of by pole placement using a rotating frame of reference

The control algorithm in the rotating frame of reference can be obtained similarly. In this case, the **M**, **C** and **K** matrices are different as well as the coordinate system. This can be analysed using Figure 7-5, where the dynamics of the rigid bodies were modelled using a rotating frame of reference fixed to the carrier with origin **o**. The coordinate basis (i, j and k) rotates with a constant angular speed of the carrier Ω_c. It has been shown in chapter 3 how to transform from one frame of reference to another.

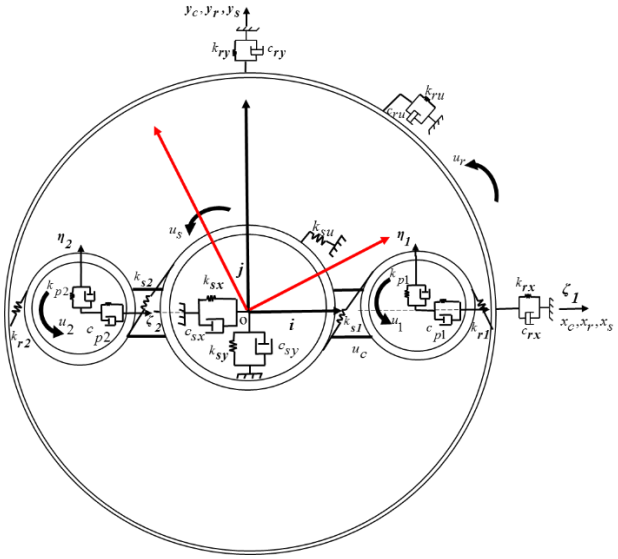

Figure 7-5 The planetary gear system showing the rotating frame of reference attached to the carrier at the centre.

For pole placement, the second order dynamic equation of motion for the planetary gear system using rotating frame of reference is written in the Laplace domain as:

$$[s^2\bar{\mathbf{M}} + s(\Omega_c \mathbf{G}_y + \bar{\mathbf{C}}) + (\bar{\mathbf{K}}_b + \mathbf{K}_m + \Omega_c \mathbf{K}_d - \Omega_c^2 \mathbf{K}_\Omega)]\bar{\mathbf{q}}(\mathbf{s}) = \mathbf{w}(\mathbf{s}) + \bar{\mathbf{B}}\bar{\mathbf{U}}(\mathbf{s}) \qquad (7.21)$$

where $\bar{\mathbf{M}}, \bar{\mathbf{C}}_b, \bar{\mathbf{K}}_b, \bar{\mathbf{K}}_m, \mathbf{G}_y \in \Re^{n\times n}$ are the mass, damping, bearing stiffness, mesh stiffness and Coriolis matrix respectively. $\bar{\mathbf{M}} = \bar{\mathbf{M}}^T, \mathbf{K}_b = \bar{\mathbf{K}}_b^T, \bar{\mathbf{K}}_m = \bar{\mathbf{K}}_m^T, \bar{\mathbf{K}}_\Omega = \bar{\mathbf{K}}_\Omega^T, \bar{\mathbf{C}}_b = \bar{\mathbf{C}}_b^T$ while the $\mathbf{G_y}$ and $\mathbf{K_d}$ matrices are skew-symmetric. $\bar{\mathbf{B}} \in \Re^{m\times n}$ is the control force distribution matrix and $\bar{\mathbf{U}}\mathbf{(s)} \in \Re^{m\times 1}$ is the control force, while $\mathbf{w} \in \Re^{m\times 1}$ is the disturbance due to the transmission error.

The output equation is written as:

$$\bar{\mathbf{q}}_{op}(\mathrm{s}) = \bar{\mathbf{D}}\bar{\mathbf{q}}(\mathrm{s}) \tag{7.22}$$

From Equation (7.12), the control force using a rotating frame of reference can be derived using the transformation matrix, **T**:

where

$$\mathbf{T} = \begin{bmatrix} \cos\Omega_c t & -\sin\Omega_c t & 0 \\ \sin\Omega_c t & \cos\Omega_c t & 0 \\ 0 & 0 & 1 \end{bmatrix} \tag{7.23}$$

The control force using a rotating frame of reference is written as

$$\bar{\mathbf{U}} = (\bar{\mathbf{G}} + \Omega_c\bar{\mathbf{F}}\mathbf{J} + s\bar{\mathbf{F}})\bar{\mathbf{D}}\bar{\mathbf{q}}(\mathrm{s}) \tag{7.24}$$

$$\mathbf{J}_h = \begin{bmatrix} 0 & -1 & 0 \\ 1 & 0 & 0 \\ 0 & 0 & 0 \end{bmatrix};\ h=c,\ s \tag{7.25}$$

where *c* and *s* are the carrier and sun gear because the control forces were applied to them. Substituting for $\bar{\mathbf{U}}$ in equation (7.21), one obtains,

$$[s^2\bar{\mathbf{M}} + s(\Omega_c\mathbf{G}_y + \bar{\mathbf{C}}) + (\bar{\mathbf{K}}_b + \bar{\mathbf{K}}_m + \Omega_c\mathbf{K}_d - \Omega_c^2\mathbf{K}_\Omega)]\bar{\mathbf{q}}(\mathbf{s}) = \mathbf{w}(\mathbf{s}) + \bar{\mathbf{B}}[-(\bar{\mathbf{G}} + \Omega_c\bar{\mathbf{F}}\mathbf{J} + s\bar{\mathbf{F}})]\bar{\mathbf{D}}\bar{\mathbf{q}}(\mathbf{s}) \tag{7.26}$$

$$[s^2\bar{\mathbf{M}} + s(\Omega_c\mathbf{G}_y + \bar{\mathbf{C}} + \bar{\mathbf{B}}\bar{\mathbf{F}}\bar{\mathbf{D}}) + (\bar{\mathbf{K}}_b + \bar{\mathbf{K}}_m + \Omega_c\mathbf{K}_d - \Omega_c^2\mathbf{K}_\Omega + \bar{\mathbf{B}}\bar{\mathbf{G}}\bar{\mathbf{D}} + \Omega_c\bar{\mathbf{B}}\bar{\mathbf{F}}\mathbf{J}\bar{\mathbf{D}})]\bar{\mathbf{q}}(\mathbf{s}) = \mathbf{w}(\mathbf{s}) \tag{7.27}$$

$$\bar{\mathbf{q}}(\mathbf{s}) = [s^2\bar{\mathbf{M}} + s(\Omega_c\mathbf{G}_y + \bar{\mathbf{C}} + \bar{\mathbf{B}}\bar{\mathbf{F}}\bar{\mathbf{D}}) + (\bar{\mathbf{K}}_b + \bar{\mathbf{K}}_m + \Omega_c\mathbf{K}_d - \Omega_c^2\mathbf{K}_\Omega + \bar{\mathbf{B}}\bar{\mathbf{G}}\bar{\mathbf{D}} + \Omega_c\bar{\mathbf{B}}\bar{\mathbf{F}}\mathbf{J}\bar{\mathbf{D}})]^{-1}\mathbf{w}(\mathbf{s}) \tag{7.28}$$

The closed loop inverse dynamic stiffness matrix is written as

$$[s^2\bar{\mathbf{M}} + s(\Omega_c\mathbf{G}_y + \bar{\mathbf{C}} + \bar{\mathbf{B}}\bar{\mathbf{F}}\bar{\mathbf{D}}) + (\bar{\mathbf{K}}_b + \bar{\mathbf{K}}_m + \Omega_c\mathbf{K}_d - \Omega_c^2\mathbf{K}_\Omega + \bar{\mathbf{B}}\bar{\mathbf{G}}\bar{\mathbf{D}} + \Omega_c\bar{\mathbf{B}}\bar{\mathbf{F}}\mathbf{J}\bar{\mathbf{D}})]^{-1} \tag{7.29}$$

The open loop inverse dynamic stiffness matrix is written as:

$$\bar{\mathbf{H}}(s) = [s^2\bar{\mathbf{M}} + s(\Omega_c \mathbf{G}_y + \bar{\mathbf{C}}) + (\bar{\mathbf{K}}_b + \bar{\mathbf{K}}_m + \Omega_c \mathbf{K}_d - \Omega_c^2 \mathbf{K}_\Omega)]^{-1} \tag{7.30}$$

Pre-multiplying equation (7.30) by equation (7.27)

$$[\mathbf{I} + \bar{\mathbf{H}}(s)\bar{\mathbf{B}}[(\bar{\mathbf{G}} + \Omega_c\bar{\mathbf{F}}\mathbf{J} + s\bar{\mathbf{F}})\bar{\mathbf{D}}]\bar{\mathbf{q}}(s) = \bar{\mathbf{H}}(s)\mathbf{w}(s)$$

$$\bar{\mathbf{q}}(s) = [\mathbf{I} + \bar{\mathbf{H}}(s)\bar{\mathbf{B}}[(\bar{\mathbf{G}} + \Omega_c\bar{\mathbf{F}}\mathbf{J} + s\bar{\mathbf{F}})\bar{\mathbf{D}}]^{-1}\bar{\mathbf{H}}(s)\mathbf{w}(s)$$

$$\bar{\mathbf{q}}(s) = \frac{adj[\mathbf{I}+\bar{\mathbf{H}}(s)\bar{\mathbf{B}}(\bar{\mathbf{G}}+\Omega_c\bar{\mathbf{F}}\mathbf{J}+s\bar{\mathbf{F}})\bar{\mathbf{D}}]}{\det[\mathbf{I}+\bar{\mathbf{H}}(s)\bar{\mathbf{B}}(\bar{\mathbf{G}}+\Omega_c\bar{\mathbf{F}}\mathbf{J}+s\bar{\mathbf{F}})\bar{\mathbf{D}}]}\bar{\mathbf{H}}(s)\mathbf{w}(s) \tag{7.31}$$

The corresponding eigenvalues μ_j are equal to poles given as solutions to $\det(\mathbf{I} + \bar{\mathbf{H}}(\mu_j)\bar{\mathbf{B}}(\bar{\mathbf{G}} + \Omega_c\bar{\mathbf{F}}\mathbf{J} + \mu_j\bar{\mathbf{F}})\bar{\mathbf{D}}) = \mathbf{0}$. The corresponding eigenvalues λ_i are equal to zeros given as solutions to $\text{adj}(\mathbf{I} + \bar{\mathbf{H}}(\lambda_i)\bar{\mathbf{B}}(\bar{\mathbf{G}} + \Omega_c\bar{\mathbf{F}}\mathbf{J} + \lambda_i\bar{\mathbf{F}})\mathbf{D})\bar{\mathbf{H}}(\lambda_i) = \mathbf{0}$.

7.5 Numerical examples of pole assignment using two control forces

The pole placement will be applied to the either sun gear or the carrier in both the vertical and horizontal directions simultaneously using a fixed and rotating frames of reference in each case. A transmission error of 1.05×10^{-3}m was assumed in this study and the subsequent ones.

7.5.1 Pole assignment to the sun gear using a fixed frame of reference

Two pairs of complex conjugate poles at $\lambda_{1,2} = -7 \pm 265i$ and $\lambda_{3,4} = -15.661 \pm 800i$ were assigned to the sun gear using two actuators supplying feedback control forces in the horizontal and vertical directions through the bearing as shown in Figure 7-6. The poles were chosen considering the open loop poles of the system.

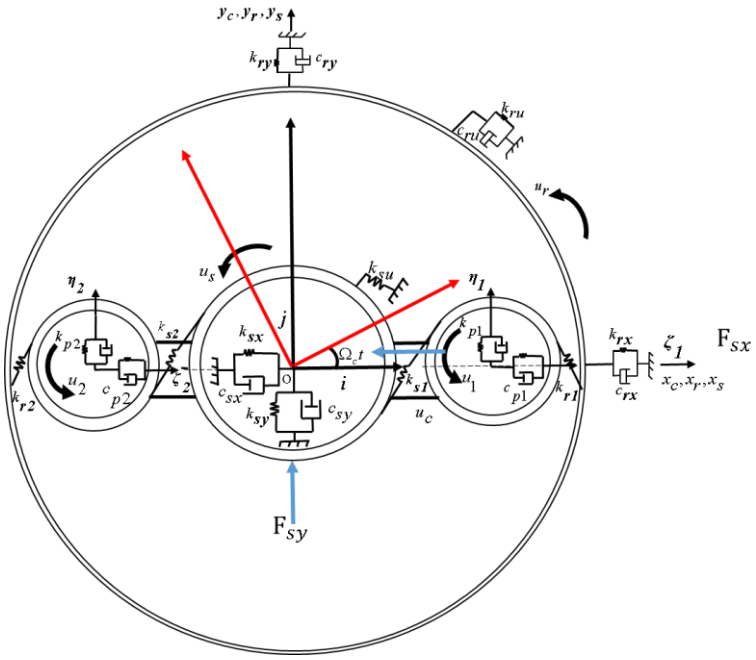

Figure 7-6 The control force being applied to the system in the x and y directions. They are denoted with blue arrows in both directions.

The mass, damping and stiffness matrices are as given in the Appendix E. The actuator distribution matrix $\mathbf{B} \in \Re^{15\times 2}$ and the sensor distribution matrix $\mathbf{D} \in \Re^{2\times 15}$ are then

$$\mathbf{D} = \mathbf{B}^{\mathrm{T}} = \begin{bmatrix} 0 & 0 & 0 & 0 & 0 & 0 & 1 & 0 & 0 & 0 & 0 & 0 & 0 & 0 & 0 \\ 0 & 0 & 0 & 0 & 0 & 0 & 0 & 1 & 0 & 0 & 0 & 0 & 0 & 0 & 0 \end{bmatrix}$$

In this case $q_{1op}(s) = \mathbf{D}x_s(s)$ and $q_{2op}(s) = \mathbf{D}y_s(s)$. The open-loop inverse dynamic stiffness matrices are written as

$$\mathbf{H}(\lambda_{cj}) = (\mathbf{M}\lambda_{cj}^2 + \mathbf{C}_b\lambda_{cj} + \mathbf{K}_b + \mathbf{K}_m)^{-1}, \quad j = 1,....,4$$

Four characteristic equations which are nonlinear in control gains **G** and **F** can be written as

$$\det(\mathbf{I} + \mathbf{H}(\lambda_j)\mathbf{B}(\mathbf{G} + \lambda_j\mathbf{F})\mathbf{B}^{\mathrm{T}}) = 0, \quad j = 1,....,4$$

The nonlinear equation was solved using the "fsolve" routine in MATLAB to obtain **G** and **F**. This was also used subsequently in the remaining numerical simulations. The numerical results for the control gains are:

$$\mathbf{G} = \begin{bmatrix} 0.28162 & 0 \\ 0 & -0.87076 \end{bmatrix} 10^6 \,\mathrm{N/m}\ ,\ \mathbf{F} = \begin{bmatrix} 34.9973 & 0 \\ 0 & 9.4773 \end{bmatrix} \mathrm{Ns/m}$$

The control gain, **G** is proportional to stiffness, this implies that stiffness is added to the sun gear in *x* direction and removed stiffness in y direction. The control gain, **F** is proportional to damping. It shows that damping is added to the sun gear in both *x* and *y* directions.

The result was validated using a state-space representation namely:

$$\mathbf{A} = \begin{bmatrix} \mathbf{0} & \mathbf{I} \\ \text{-}\mathbf{M}^{-1}(\mathbf{K}_b + \mathbf{K}_m + \mathbf{BGD}) & \text{-}\mathbf{M}^{-1}(\mathbf{C}_b + \mathbf{BFD}) \end{bmatrix} \tag{7.32}$$

which yields $s_{1,2} = -7 \pm 265i$ and $s_{3,4} = -15.662 \pm 800i$ which replicate the assigned poles.

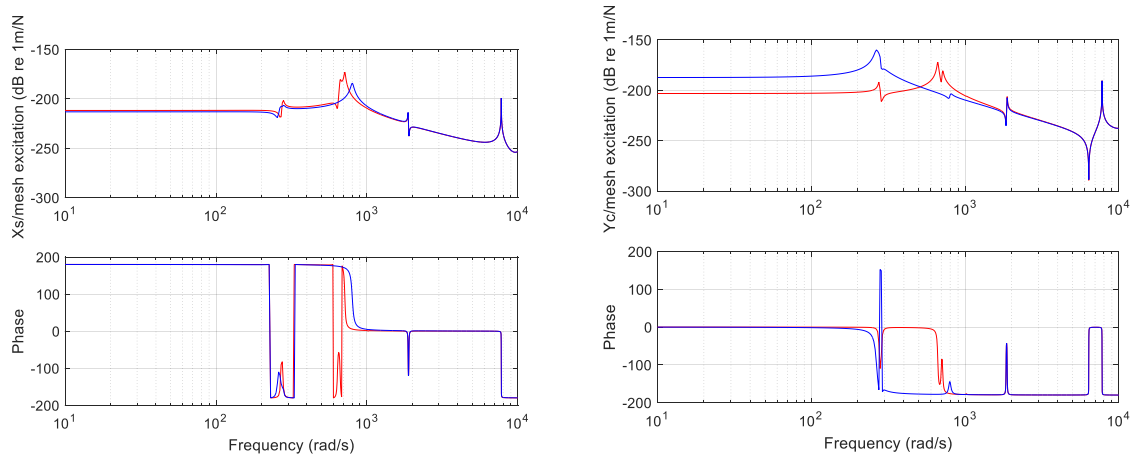

(a) **(b)**

Figure 7-7 Displacement per mesh excitation of the sun gear in the (a) *x* and (b) *y* direction with and without control due to mesh excitation. The initial and the modified displacement per mesh excitation are plotted in red and blue respectively.

The mesh excitation in this study is the product of the sun-planet mesh stiffness and the transmission error between the sun and planet gear which is 1.312×10^4N.

The result in Figure. 7-7 (a) which is the displacement of the sun gear in the horizontal direction, shows that a pole was shifted from $-2.8336 \pm 276.75i$ to $-7 \pm 265i$. Another pole was shifted from $-7.1425 \pm 714.11i$ to $-15.662 \pm 800i$ with significant damping added. This is a mode where only the sun gear is translating in both directions. Only the frequencies of translational modes were altered. Only the poles of translational mode have shifted the poles of the rotational mode remain unaltered. In Figure 7-7 (b), the pole at $-2.8336 \pm 276.75i$ to $-7 \pm 265i$ in the first excited mode while the second excited mode was shifted from $-7.1425 \pm 714.11i$ to $-15.662 \pm 800i$. There is a translational mode excited at 664 rad/s; this frequency was shifted to 280.5 rad/s but not excited after modification. The poles of higher modes remain unchanged, no damping was added. The stiffness has been reduced in the *y* direction which is why at low frequency the modified displacement per mesh excitation (i.e. the blue line) moved up (Figure 7-7 (b)).

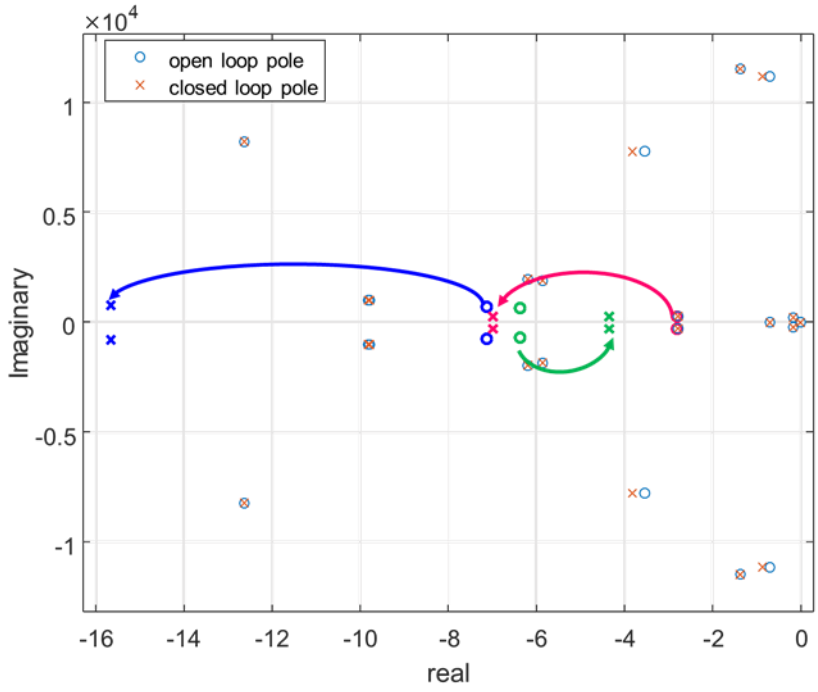

Figure 7-8 The s-plane plots showing the locations of the initial and the modified poles when the control forces were applied to the sun gear using a fixed frame of reference.

Figure 7-8 shows the three pairs of conjugate poles which were shifted. They are poles of the translational modes because the poles were assigned to the sun gear in the translational x and y directions. Five translational and 7 rotational modes remain unchanged. The magenta line shows the pole that shifted from $-2.8336 \pm 276.75i$ to $-7 \pm 265i$, the blue line shows the one from $-7.1425 \pm 714.11i$ to $-15.662 \pm 800i$ while the green line shows how a pole shifted from $-6.3894 \pm 664.34i$ to $-4.3504 \pm 280.5i$

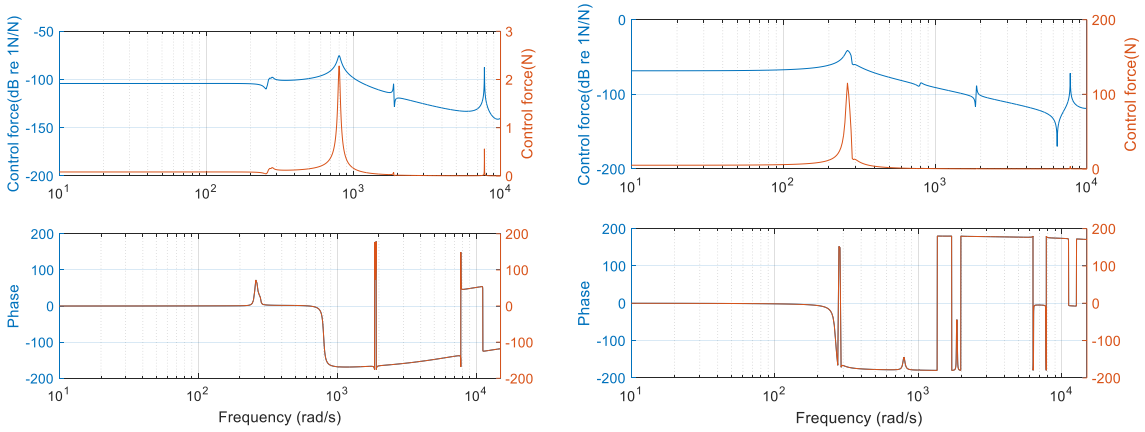

(a) **(b)**

Figure 7-9 Control forces applied on the sun gear in both the (a) x and (b) y directions using fixed frame of reference.

The normalised and absolute control forces are shown in Figure 7-9 in blue and orange line respectively. It depends on the control gains **G** and **F**, the closed-loop poles assigned and the amplitude of the excitation**.** Equation (7.12) shows the expression for the control force with the actuator distribution matrix **B**. The control forces in the *x* direction is less than the *y* direction. In Figure 7-9 (a), the absolute control forces are 0.2 N at 265 rad/s and 2.3 N at 800 rad/s. The absolute control forces required in *y* direction is 115.2 N at 265 rad/s Figure 7-9 (b)). Generally, the control forces in both directions are relatively low so actuators with low control force would be suitable for practical implementation.

The resistive and reactive power calculations and their interpretations, for both electrical and mechanical systems, are shown in Appendix E. The apparent control power or effort using a fixed frame of reference is determined by multiplying the control force by the Hermitian conjugate of the velocity in a Laplace domain. This is written as

$$\mathbf{P}_e = \frac{1}{2}[-(\mathbf{B}(\mathbf{G} + s\mathbf{F})\mathbf{Dq}(s))(conj(s\mathbf{Dq}(s))^T] \tag{7.33}$$

The active control power is determined by considering the real part of equation (7.33). Bobrovnitskii [73] gives the expressions for both the real and imaginary parts of the complex power flow. The real part of the complex power flow for this case study, which is also called the direct component, can be expressed as follows:

$$\mathbf{P}_a = \frac{1}{2}Re[-(\mathbf{B}(\mathbf{G} + s\mathbf{F})\mathbf{Dq}(s))(conj(s\mathbf{Dq}(s))^T] \tag{7.34}$$

Equation (7.34) is equivalent to time averaged active (resistive) power. The imaginary part of equation (7.33), known as the reactive power flow, can be expressed as follows

$$\mathbf{P}_r = \frac{1}{2}Im[-(\mathbf{B}(\mathbf{G} + s\mathbf{F})\mathbf{Dq}(s))(conj(s\mathbf{Dq}(s))^T] \tag{7.35}$$

Equation (7.35) is equivalent to the peak value of the periodic with zero time averaged mean (reactive) power flow. In addition, the time averaged mean square control force is also considered. This is given by

$$\mathbf{F}_c = \frac{1}{2}|[-\mathbf{B}(\mathbf{G} + s\mathbf{F})\mathbf{Dq}(s)]|^2 \tag{7.36}$$

For the sun gear, the control power required to shift the poles in *x* and *y* directions using a fixed frame of reference are shown in Figure 7.10 (a) and (b) respectively.

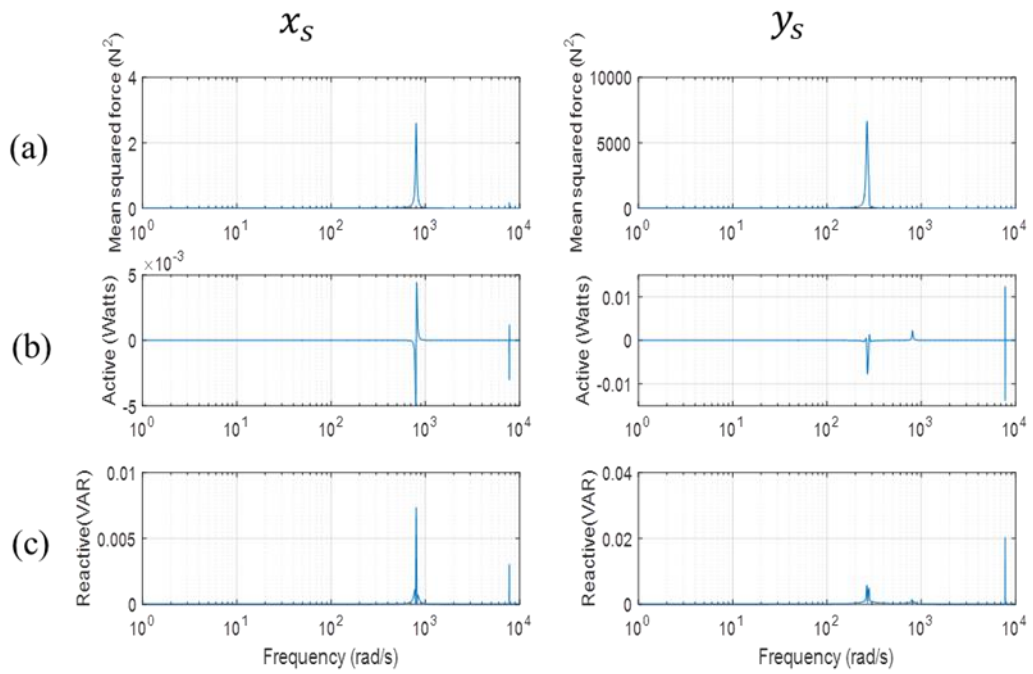

(a) **(b)**

Figure 7-10 (a) Mean square control force (b) Active control power (c) Peak reactive control power required by the sun gear in both the x and y directions respectively using a fixed frame of reference.

Figure 7-10 shows the active control power required by the sun gear in both the *x* and *y* directions. Very small magnitudes of active control power are required to shift the poles in both directions. As discussed earlier, the pole in *x* direction was shifted from $-7.1425 \pm 714.11i$ to $-15.662 \pm 800i$ while the pole in the *y* direction was shifted from $-2.8336 \pm 276.75i$ to $-7 \pm 265i$. The reactive control effort (or power) does no net work, as it flows from the source of the control power (i.e. the controller applying the force) to the PGT system and returns the same amount of power within each cycle of the corresponding frequency. This is analogous to the power flow into and then back in each cycle from the stiffness element in a single degree of freedom system when the stiffness supported mass is excited at a discrete frequency (see Appendix E).

7.5.2 Pole assignment to the sun gear using a rotating frame of reference

The closed-loop poles were determined using the state space at the carrier speed of 100 rpm. In this case, the control gains obtained using a fixed frame of reference were assigned using the state space equation (7.37) to obtain the poles. It is assumed that the control gains in both frames of reference are not changing with time.

$$\bar{\mathbf{A}} = \begin{bmatrix} \mathbf{0} & \mathbf{I} \\ -\bar{\mathbf{M}}^{-1}(\bar{\mathbf{K}}_b + \bar{\mathbf{K}}_m + \Omega_c \bar{\mathbf{K}}_d - \Omega_c^2 \bar{\mathbf{K}}_\Omega + \bar{\mathbf{B}}(\bar{\mathbf{G}} + \Omega_C \bar{\mathbf{F}}\mathbf{J})\bar{\mathbf{D}} & -\bar{\mathbf{M}}^{-1}(\Omega_C \mathbf{G}_y + \bar{\mathbf{C}}_b + \bar{\mathbf{B}}\bar{\mathbf{F}}\bar{\mathbf{D}}) \end{bmatrix} \tag{7.37}$$

The sensor and force distribution matrices as well as the gain matrices are the same as the ones using fixed frame of reference i.e. $\bar{\mathbf{B}} = \mathbf{B}$, $\bar{\mathbf{D}} = \mathbf{D}$, $\bar{\mathbf{G}} = \mathbf{G}$, $\bar{\mathbf{F}} = \mathbf{F}$. The closed-loop poles obtained from the state space at the carrier speed of 100 rpm are:

$\tilde{S}_{1,2} = -6.9108 \pm 264.18i$ and $\tilde{S}_{3,4} - 15.659 \pm 800.2i$

The open-loop inverse dynamic stiffness matrices are written as

$$\mathbf{H}(\lambda_{cj}) = (\mathbf{M}\lambda_{cj}^2 + (\Omega_c \mathbf{G}_y + \bar{\mathbf{C}}_b)\lambda_{cj} + (\bar{\mathbf{K}}_b + \mathbf{K}_m + \Omega_c \mathbf{K}_d - \Omega_c^2 \mathbf{K}_\Omega))^{-1} * \mathbf{F}_{te}, \ j = 1, ..., 4$$

while the four characteristic equations are written as

$$\det(\mathbf{I} + \bar{\mathbf{H}}(\lambda_j)\bar{\mathbf{B}}(\bar{\mathbf{G}} + \Omega_c \bar{\mathbf{F}}\mathbf{J} + \lambda_j \bar{\mathbf{F}})\bar{\mathbf{B}}^{\mathrm{T}}) = 0, \ j = 1, ..., 4$$

These poles obtained from the Equation (7.33) were assigned to the sun gear in the *x* and *y* directions. This yields the following control gains

$$\bar{\mathbf{G}} = \begin{bmatrix} 0.28161 & 0 \\ 0 & -0.87076 \end{bmatrix} 10^6 \text{ N/m}; \bar{\mathbf{F}} = \begin{bmatrix} 34.9977 & 0 \\ 0 & 9.4808 \end{bmatrix} \text{Ns/m}$$

The results was validated by state-space, Equation (7.37) and it yields the following poles:

$\tilde{S}_{1,2} = -6.9112 \pm 264.18i$ and $\tilde{S}_{3,4} = -15.659 \pm 800.2i$

The poles are almost the same as the closed loop poles assigned. The displacement per mesh excitation for both the horizontal and vertical directions are shown in Figure 7-11.

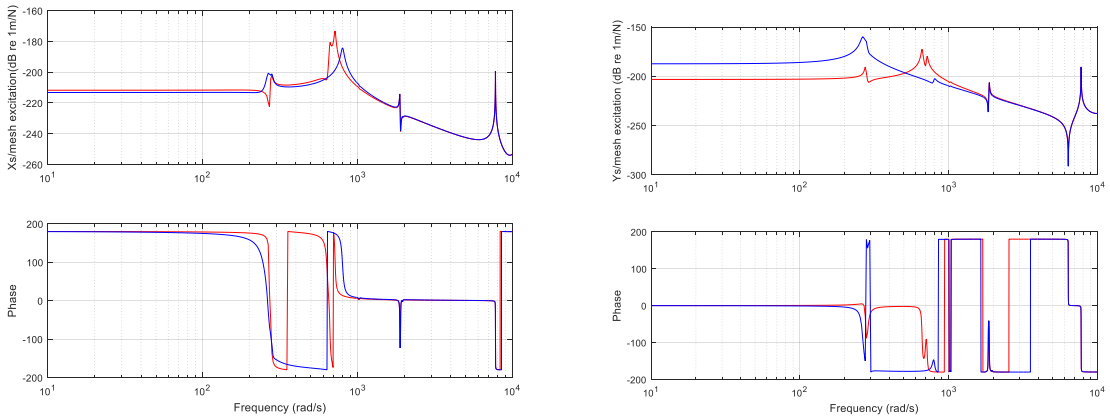

(a) **(b)**

Figure 7-11 Displacement per mesh excitation of the sun gear in the (a) *x* and (b) *y* directions with and without control due to mesh excitation using a rotating frame of reference at a carrier speed of 100 rpm. The initial and the modified displacement per mesh excitation are plotted in red and blue respectively.

The results in Figures 7-11 (a) and Figure 7-7 (a) are the same while the ones in Figures 7-11 (b) and 7-7 (b) are the same. The difference is the coordinate system used but at a low speed like 100 rpm of the rotating coordinate system attached to the centre of the carrier, the results are the same.

For a rotating frame of reference, the control force required for the sun gear in the *y* direction is higher than the *x* direction. The s-plane is shown in Figure E7.2 in Appendix E. The same number of poles are shifted in the *s*-plane as the ones shown in Figure 7-8. Approximately the same magnitude of control forces are needed using both frames of reference when control forces are applied on the sun gear in both the *x* and *y* directions for a low speed of the rotating coordinate. The control force in both the *x* and *y* direction when a rotating frame of reference was used is shown in Figure E7.3 in Appendix E.

The control power using a rotating frame of reference is determined by multiplying the control force by the Hermitian conjugate of velocity in a Laplace domain as written in equation (7.38). The active and apparent control power as well as the mean square control force are written respectively in equations (7.39), (7.40), and (7.41).

$$\mathbf{P}_e = \frac{1}{2}[-(\mathbf{B}(\mathbf{G} + \Omega_c\mathbf{FJ} + s\mathbf{F})\mathbf{Dq}(s))(conj(s\mathbf{Dq}(s))^T] \tag{7.38}$$

$$\mathbf{P}_a = \frac{1}{2}Re[-(\mathbf{B}(\mathbf{G} + \Omega_c\mathbf{FJ} + s\mathbf{F})\mathbf{Dq}(s))(conj(s\mathbf{Dq}(s))^T] \tag{7.39}$$

$$\mathbf{P}_r = \frac{1}{2}Im[-(\mathbf{B}(\mathbf{G} + \Omega_c\mathbf{FJ} + s\mathbf{F})\mathbf{Dq}(s))(conj(s\mathbf{Dq}(s))^T] \tag{7.40}$$

In addition, the mean square control force using a rotating coordinate is also considered. This is given by

$$\mathbf{F}_c = \frac{1}{2}|[-\mathbf{B}(\mathbf{G} + \Omega_c\mathbf{FJ} + s\mathbf{F})\mathbf{Dq}(s)]|^2 \tag{7.41}$$

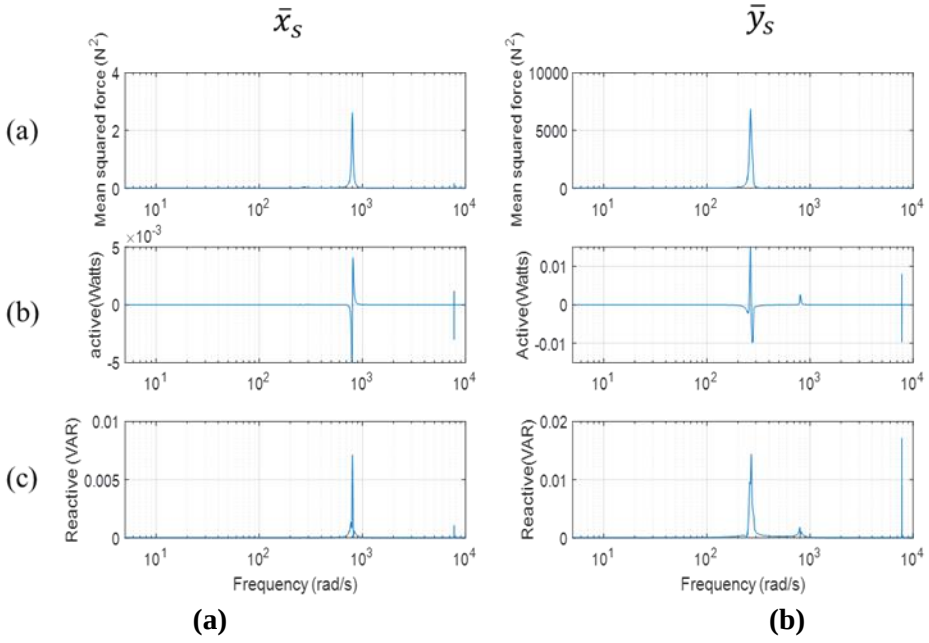

Figure 7-12 (a) Mean square control force (b) Active control power (c) Reactive control power required by the sun gear in both the x and y directions using a rotating frame of reference when the coordinate speed is 100 rpm.

For a relatively low rotational speed 100 rpm of the sun gear, the active control power required, is approximately the same as the effort required using a fixed frame of reference (Figures 7-10 (b) and 7-12 (b)).

7.5.3 Pole assignment to the carrier using both frames of reference

The method of pole placement was applied to the carrier only in the *x* and *y* directions simultaneously using both fixed and rotating frames of reference. The pole placement on the carrier will be compared to that of the sun gear in order to determine the best location to put the actuator in the system. Two conjugate poles $\lambda_{1,2} = -7 \pm 265i$ and $\lambda_{3,4} = -15.661 \pm 800i$ (which are the same assigned to the sun gear) were assigned to the carrier. This is done to compare the control effort required in both cases and determine the optimal place to apply control forces in a planetary gear system. The numerical results for the control gains are:

$$\mathbf{G} = \begin{bmatrix} -0.49326 & 0 \\ 0 & -0.40454 \end{bmatrix} 10^6 \text{ N/m} \; ; \; \mathbf{F} = \begin{bmatrix} 303.53 & 0 \\ 0 & 12.0127 \end{bmatrix} \text{Ns/m}$$

This result was validated and it yields $-7 \pm 265i$ and $-15.663 \pm 800i$.

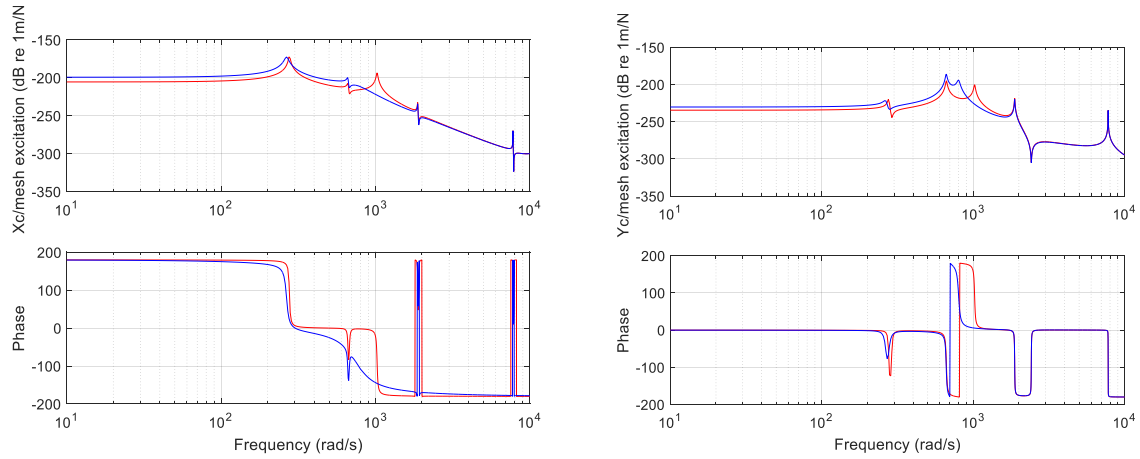

(a) **(b)**

Figure 7-13 Displacement per mesh excitation of the carrier in the (a) *x* and (b) *y* directions with and without control due to mesh excitation using a fixed frame of reference. The initial and the modified displacement per mesh excitation are plotted in red and blue respectively.

Figure 7-13 (a) shows the displacement per mesh excitation of the carrier in *x* direction where the pole of the first excited translational mode is shifted from $-2.8336 \pm 276.75i$ to $-7 + 265i$. Damping is added at 265 rad/s because the peak is not as sharp as the peak at 276.75 rad/s. Another pole of a translational mode moves slightly from $-6.3894 \pm 664.34i$ to $-6.6242 \pm 662.51i$. A pole was also shifted from -9.7772 ± 1023.7i to $-15.663 \pm 800i$ but the peak has vanished in the modified displacement per mesh excitation. In Figure 7-13 (b), the frequency of the first excited mode was shifted from 275 rad/s to 265 rad/s. The second mode was shifted from 664.34 to 662.51 rad/s while the third mode was shifted from 1023.7 to 800 rad/s. The peak of the assigned pole at 800 rad/s can be seen in *y* direction. The translational mode at 1876.6 rad/s was slightly damped while the last translational mode excited at 7773.2 rad/s remains unaltered.

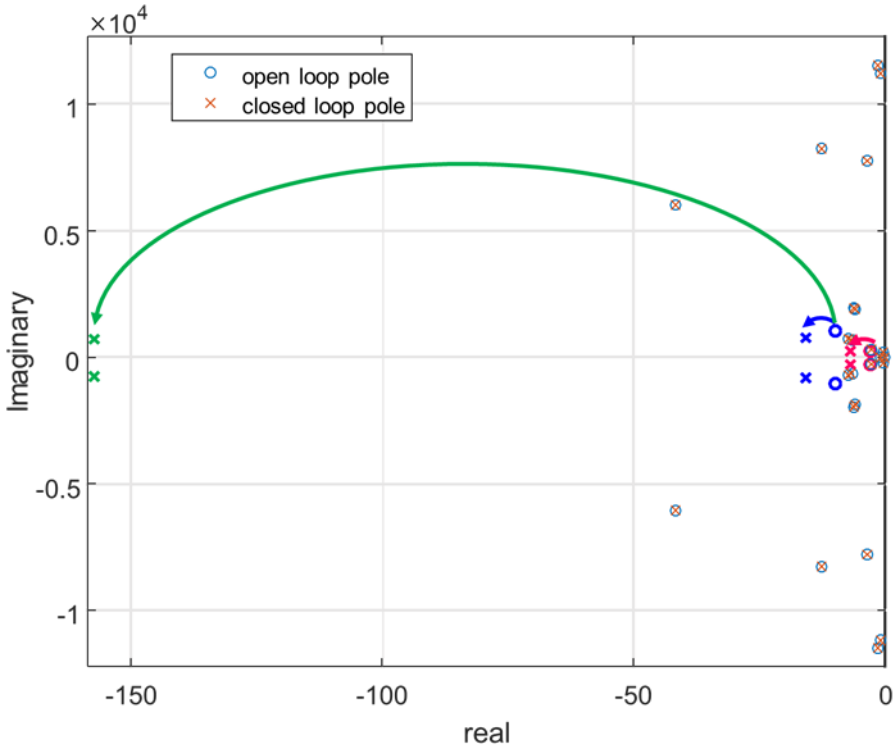

Figure 7-14 The s-plane showing the locations of the initial and modified poles when the control forces were applied to the carrier using a fixed frame of reference.

The conjugate poles shifted after pole placement are shown in Figure 7-14. The two assigned poles and other poles can be seen before and after modification. The real and imaginary part of the poles of the rotational modes remain unchanged. The magenta line shows the pole shifted from $-2.8336 \pm 276.75i$ to $-7 + 265i$ while the blue line shows the pole shifted from -9.7772 ± 1023.7i to $-15.663 \pm 800i$. The frequency of a closed-loop pole shown by a green line was shifted from 1020.9 to 730.55 rad/s with a significant level of damping added.

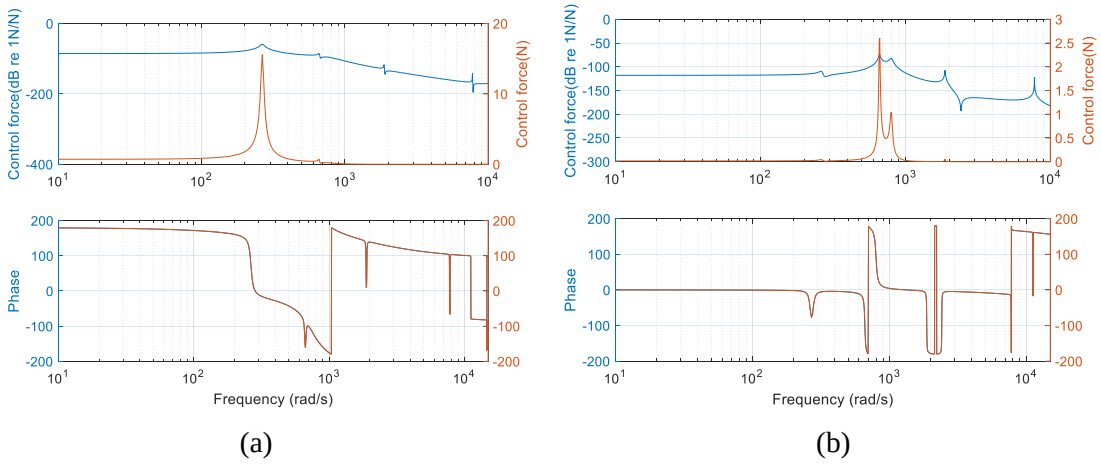

(a) (b)

Figure 7-15 Control forces applied on the carrier in both the (a) *x* and (b) *y* directions using a fixed frame of reference.

The normalized (blue line) and absolute (orange line) control forces are shown in Figures 7-15 (a) and (b). A force of 15.6 N is required in *x* direction to shift the pole from 276.75 to 265 rad/s while a force of 1.04 N is required to shift the pole from 1023.7 to 800 rad/s in *y* direction. The control forces vary and depend on the stiffness and damping added as well as the pole assigned.

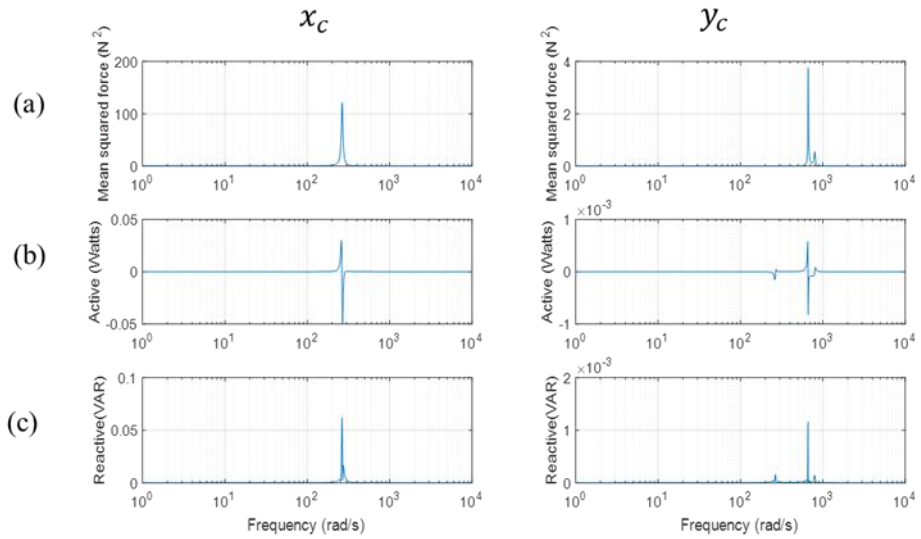

(a) **(b)**

Figure 7-16. (a) Mean square control force (b) Active control power (c) Reactive control power required by the carrier in both the x and y directions using a fixed frame of reference.

The active control power required by the carrier is relatively higher than that required by the sun gear in both the *x* and *y* directions (comparing Figures 7-10 (b) and 7-16 (b)). It can be seen from both the figures aforementioned, that the active control power required by the carrier to shift a pole of $-2.8336 \pm 276.75i$ to $-7 \pm 265i$ in the *x* direction is higher than that required by the sun gear in the *y* direction. The control effort required by the carrier to shift a pole from $-7.1425 \pm 714.11i$ to $-15.662 \pm 800i$ in the *y* direction is less than that required by the sun gear in the *x* direction. There is no significant difference in the active control effort required by the carrier using either frames of reference (Figure 7-16 (b) and Figure E 7.3 (b) in Appendix E).

For a high margin between the open and closed loop poles, the control effort required by the sun gear is higher because it has higher support stiffness. This is not the case for the low margin between the open and closed loop poles where the control effort required by the carrier is higher. Therefore, the optimal place to apply control in the planetary gear system considering the control effort required depends on the initial location of the poles and the desired final shifted pole location in the s-plane for stability. Another factor to be considered is the bearing stiffness of the carrier and the sun gear. For high bearing stiffness, more control effort will be required to shift the pole from a particular location to another especially for the case where the margin between the open and closed loop is high.

For the carrier when a rotating frame of reference was used, the poles obtained at a rotational speed of 100 rpm using equation (7.33) are $-7.0025 \pm 264.78i$ and $-16.271 \pm 800.31i$. The poles were assigned and yield the following gains:

$$\mathbf{G} = \begin{bmatrix} -0.49335 & 0 \\ 0 & -0.40455 \end{bmatrix} \times 10^6 \text{ N/m} \ , \ \mathbf{F} = \begin{bmatrix} 303.41 & 0 \\ 0 & 12.0221 \end{bmatrix} \text{Ns/m}$$

The results were validated by state-space equation as written in equation (7.33), and this yields $-7.0024 \pm 264.78i$ and $-16.275 \pm 800.3i$. The closed-loop poles obtained are the same with the ones assigned.

The displacement per mesh excitation and the control efforts of the carrier using a rotating frame of reference is shown in Figures E7.3 and E7.4 in Appendix E. They are the same with the ones when a fixed frame of reference was used at a carrier speed of 100 rpm except for a peak which appeared at 715.9 rad/s in *y* direction. In this case the control forces and efforts in both directions are the same as using a fixed frame of reference.

It has been shown by numerical examples that the poles can be assigned in a fixed frame of reference and the equivalent control force and effort can be obtained using a fixed frame of reference. Conversely, this can also be done using a rotating frame of reference. This means a pole can be assigned using a rotating frame of reference where the accelerometers are rotating with the system at a particular carrier speed, the equivalent pole can be obtained using fixed frame of reference where the accelerometers are fixed. However, since the actuators cannot rotate with the system, so the control force and effort required to shift the pole using a rotating frame of reference can be transformed using a fixed frame of reference for practical implementation. The conjugate closed-loop poles and control gains for the sun gear and carrier at higher carrier speeds of 500 and 1000 rpm are determined and shown in the table 7-1. This is achievable because the controller was design such that the poles can be obtained at any rotational speed of the rotating coordinate.

Table 7-1 The conjugate closed loop poles and control gains at higher carrier speeds.

	Sun gear	**Carrier**
Poles obtained at the carrier speed of 500 rpm	$-6.3618 \pm 249.18i$ $-15.579 \pm 804.89i$	$-7.0617 \pm 259.58i$ $-30.819 \pm 809.75i$
Control gains at the carrier speed of 500 rpm	$\mathbf{G} = diag(2.8163, -8.7077) \times 10^5$ $\mathbf{F} = diag(35.0022, 9.4758)$	$\mathbf{G} = diag(-4.9322, -4.0468) \times 10^5$ $\mathbf{F} = diag(303.51, 12.0025)$
Poles obtained at the carrier speed of 1000 rpm	$-6.2341 \pm 219i$ $-15.35 \pm 819i$	$-7.2383 \pm 242.82i$ $-58.474 \pm 853.38i$
Control gains at the carrier speed of 1000 rpm	$\mathbf{G} = diag(2.8163, -8.7075) \times 10^5$ $\mathbf{F} = diag(34.9992, 9.4797)$	$\mathbf{G} = diag(-4.9332, -4.0455) \times 10^5$ $\mathbf{F} = diag(303.46, 12.0327)$

It shows from table 7-1 that the equivalent closed-loop poles at different rotational speeds of the rotating coordinate system can be obtained. For simplicity, the procedure for pole placement using both fixed and rotating frames of reference is shown in Figure 7-17.

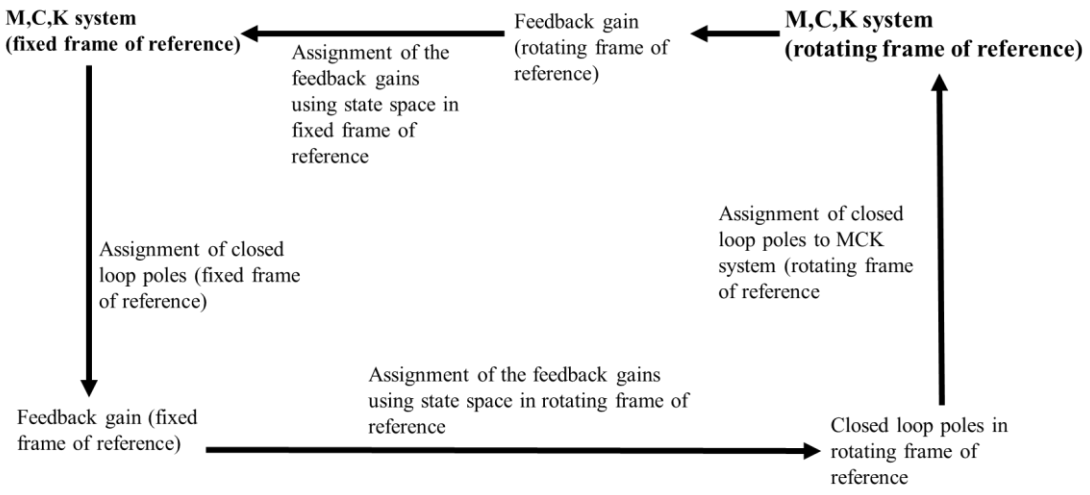

Figure 7-17 Procedure for pole assignment using both the fixed and rotating frame of reference.

In this study, the theory of pole placement extend to the vibration control of planetary gear is such that the required control force can be determined considering the rotational speed of the reference frame

and the control gains. The equivalent control force needed for instance at 500 and 1000 rpm can be determined using a fixed frame of reference for implementation.

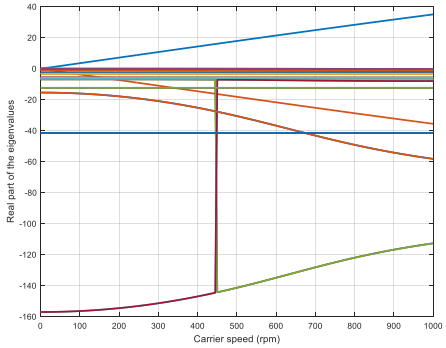

(a) Real part of the poles

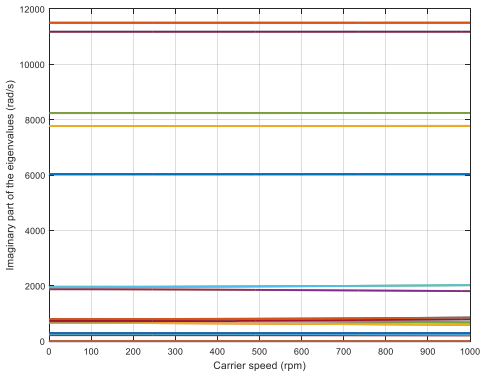

(b) Imaginary part of the poles

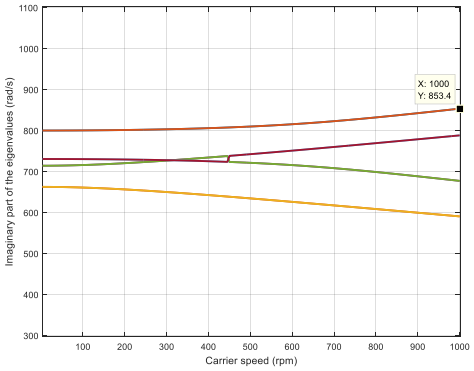

(c) Zoomed view of the imaginary part.

Figure 7-18 Effect of the carrier speed on the closed-loop poles for constant feedback gains at 100 rpm when the poles were placed on the carrier.

The effect of the varying carrier speed on the closed loop poles is studied when the feedback gains are constant. The feedback gain used is that of the carrier at 1000 rpm shown in Table 7-1. It shows that the real part of some poles are not constant over a wide range of carrier speed but the real part of the poles at high frequencies (from tenth to fifteenth mode) are constant. They are not affected by the carrier speed (Figure 7-18 (a)). For the imaginary part (shown in Figure 7-18 (a)), which represents the damped natural frequencies, some frequencies of translational modes are changing as the carrier speed is increasing. For instance the frequency of the eighth mode changed from 800 rad/s at low speed of the carrier to 853 rad/s at 1000 rpm. The damped natural frequencies of the higher modes remain unaltered.

7.6 Numerical examples of poles assignment using four control forces

In this section, the method of pole placement will be simultaneously applied to the carrier and sun gear in the vertical and horizontal directions using the fixed and rotating frames of reference in each case. There are eight characteristic nonlinear equations to be solved in this case because four complex conjugate closed-loop poles will be assigned.

7.6.1 Pole assignment to the carrier and sun gear using a fixed frame of reference

In this case, four conjugate poles were assigned and the feedback gains were determined. The following poles were assigned to the carrier and sun gear both in the *x* and *y* directions.

$\lambda_{1,2} = -2.9588 \pm 278.11i$

$\lambda_{3,4} = -23.326 \pm 705.97i$

$\lambda_{5,6} = -27.170 \pm 762.17i$

$\lambda_{7,8} = 34.651 \pm 1081.7i$

The open loop inverse dynamic stiffness matrix is then:

$$\mathbf{H}(\lambda_{cj}) = (\mathbf{M}\lambda_{cj}^2 + \mathbf{C}_b\lambda_{cj} + \mathbf{K}_b + \mathbf{K}_m)^{-1},\ j = 1,...,8,$$

and the characteristic equations are

$$\det(\mathbf{I} + \mathbf{H}(\lambda_j)\mathbf{B}(\mathbf{G} + \lambda_j\mathbf{F})\mathbf{B}^{\mathrm{T}}) = 0,\ j = 1,...,8.$$

The sensor and actuator distribution matrices are then:

$$\mathbf{D} = \mathbf{B}^T = \begin{bmatrix} 1 & 0 & 0 & 0 & 0 & 0 & 0 & 0 & 0 & 0 & 0 & 0 & 0 & 0 & 0 \\ 0 & 1 & 0 & 0 & 0 & 0 & 0 & 0 & 0 & 0 & 0 & 0 & 0 & 0 & 0 \\ 0 & 0 & 0 & 0 & 0 & 0 & 1 & 0 & 0 & 0 & 0 & 0 & 0 & 0 & 0 \\ 0 & 0 & 0 & 0 & 0 & 0 & 0 & 1 & 0 & 0 & 0 & 0 & 0 & 0 & 0 \end{bmatrix}$$

In this case $q_{1op}(s) = \mathbf{D}x_c(s)$, $q_{2op}(s) = \mathbf{D}y_c(s)$, $q_{3op}(s) = \mathbf{D}x_s(s)$ and $q_{4op}(s) = \mathbf{D}y_s(s)$

The numerical results for the control gains are:

$$\mathbf{G} = \begin{bmatrix} 0.12366 & & & \\ & 0.12871 & & \\ & & 0.01549 & \\ & & & 0.28533 \end{bmatrix} 10^6 \text{ N / m}$$

$$\mathbf{F} = \begin{bmatrix} 49.8991 & & & \\ & 49.8148 & & \\ & & 68.0236 & \\ & & & 93.6318 \end{bmatrix} \text{Ns / m}$$

This result was validated and the following closed-loop poles were obtained:

$\lambda_{1,2} = -2.9588 \pm 278.11i$

$\lambda_{3,4} = -23.326 \pm 705.97i$

$\lambda_{5,6} = -27.171 \pm 762.17i$

$\lambda_{7,8} = 34.672 \pm 1081.7i$

The returned closed-loop poles are the same with the assigned closed loop poles

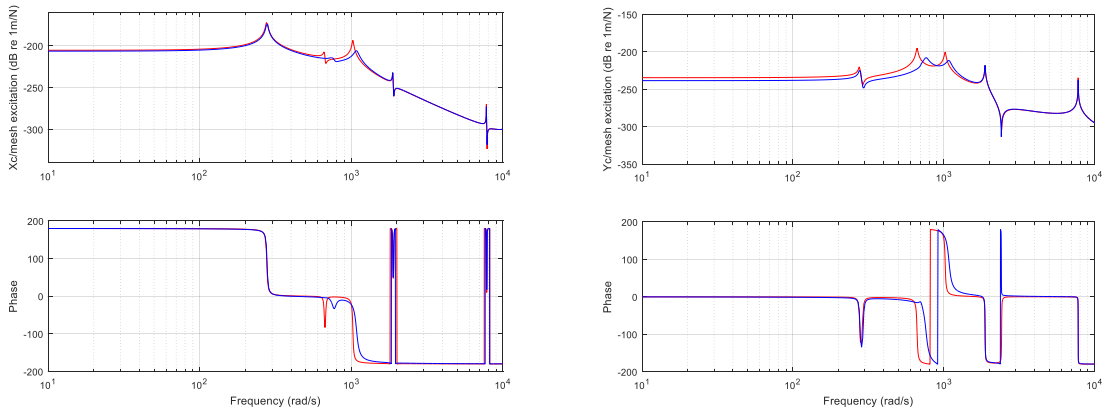

(a) **(b)**

Figure 7-19 Displacement of the carrier per mesh excitation in both the (a) *x* and (b) *y* directions using fixed frame of reference. The initial and the modified displacement per mesh excitation are plotted in red and blue respectively.

Figure 7-19 (a) shows an open loop of the first excited mode was slightly shifted from $-2.8336 \pm 276.75i$ to $-2.9588 \pm 278.11i$. Another pole was shifted from $-9.7772 \pm 1023.7i$ to $-34.672 \pm 1081.7i$ with significant damping added. The damped natural frequency at 1876.6 remain unchanged while the one at 7773.2 rad/s is unaltered but little damping was added because it changed from $-3.5370 \pm 7773.2i$ to $-5.6809 \pm 7774.0i$.

In Figure 7-19 (b), the open-loop pole at $-2.8336 \pm 276.75i$ was shifted to $-2.9588 \pm 278.11i$ while the one at $-6.3894 \pm 664.34i$ was shifted to $-27.171 \pm 762.17i$. The pole of the third excited mode was shifted from $-9.7772 \pm 1023.7i$ to $-34.672 \pm 1081.71i$. Significant amount of damping were added in the modified poles of the second and third modes.

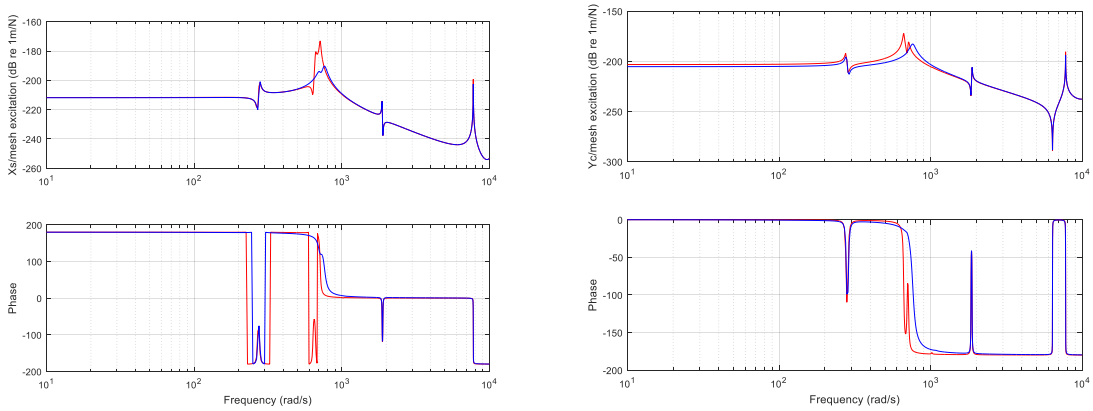

(a) **(b)**

Figure 7-20 Displacement of the sun gear per mesh excitation in both the (a) *x* and (b) *y* directions using fixed frame of reference. The initial and the modified displacement per mesh excitation are plotted in red and blue respectively.

In the horizontal and vertical directions of the sun gear as shown in Figure. 7-20 (a) and (b), the open-loop pole of the first excited mode was shifted from $-7.1425 \pm 714.11i$ to $-27.7171 \pm 762.17i$. There is a peak at 664.34 rad/s in the y direction of the sun gear which disappeared in the modified response probably because of significant amount of damping added in the y direction of the sun gear as shown in the gain matrix **F** (row 4, column 4).

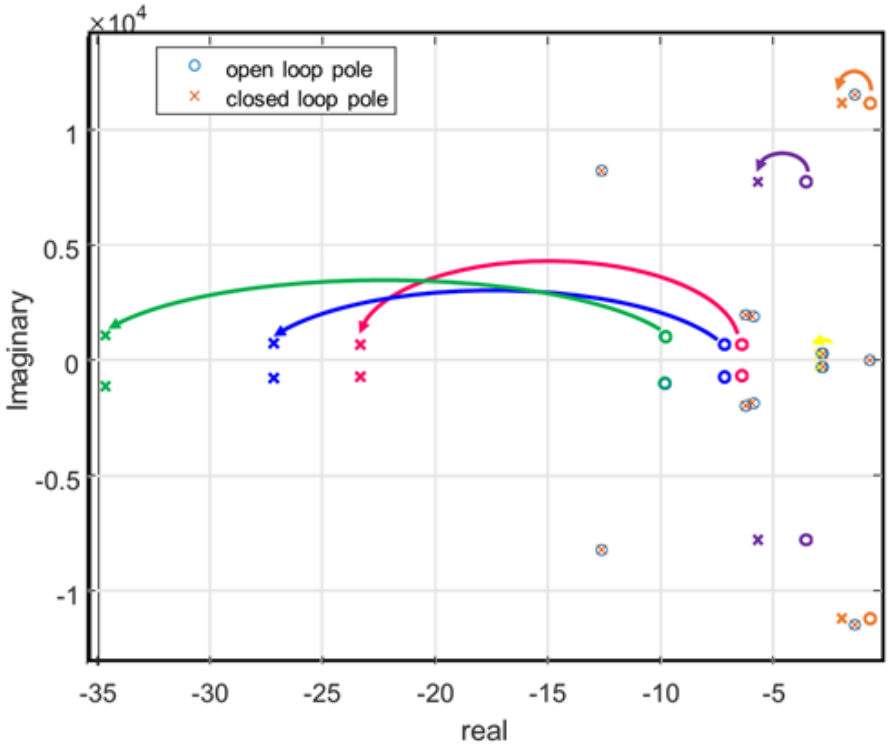

Figure 7-21 The s-plane plane showing the locations of the initial and modified poles when the control forces were applied to the carrier and sun gear using a fixed frame of reference.

Figure 7-21 shows more poles are shifted from their original location when using four actuators. This can be compared to Figures 7-8 and 7-14 where only two control forces were applied on either the carrier or sun gear in both the horizontal and vertical directions. Three poles were effectively shifted using two control forces on either the carrier or the sun gear. In this case, where four control forces were applied on the carrier and the sun gear simultaneously, six poles of the translational modes were altered. There are two poles among the six poles where only the real parts were slightly altered. In general, only the poles of translational modes are altered, the poles of the rotational modes remain unchanged.

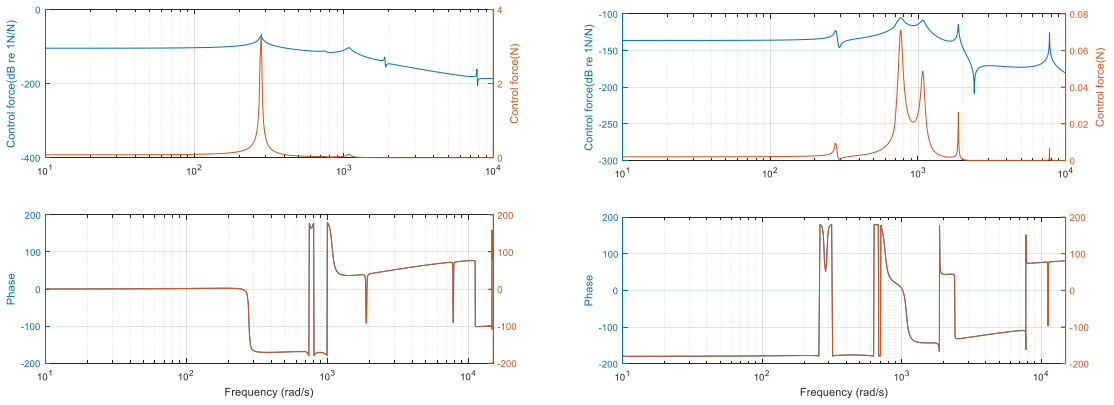

(a) **(b)**

Figure 7-22 Normalised and absolute control forces to the carrier in both the (a) *x* and (b) *y* directions using a fixed frame of reference.

The control forces applied on the carrier in the *x* and *y* directions at different excited frequencies are shown in Figures 7-22 (a) and (b) respectively. They are not as high as shown in the Figures 7-19 where two actuators were applied on the carrier only.

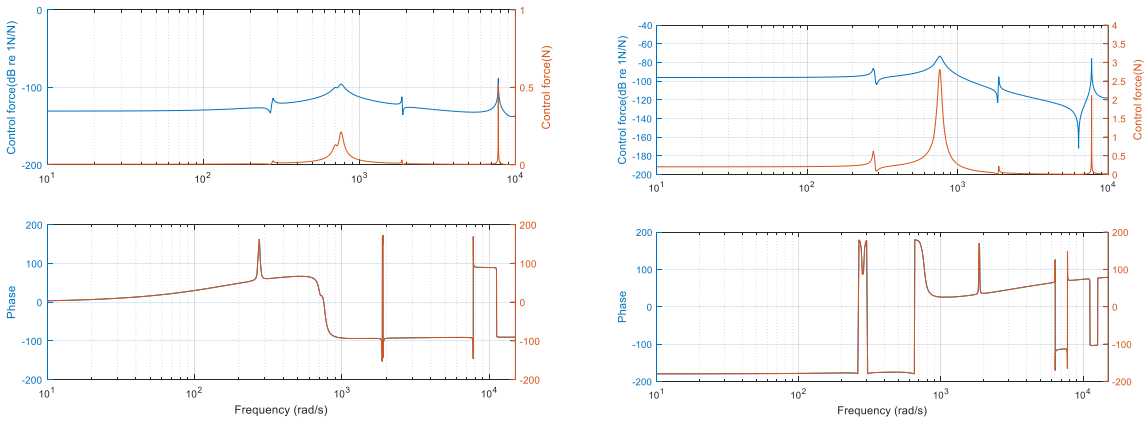

(a) **(b)**

Figure 7-23 Normalised and absolute control forces to the sun gear in both the (a) *x* and (b) *y* directions using a fixed frame of reference.

Likewise, Figure 7-23 (a) and (b) shows the control forces applied on the sun gear in both *x* and *y* directions. This can be compared with the control forces applied to sun gear with two actuators shown in Figure 7-10 which are higher. Less control force are required if more actuators are used but this may be expensive. In general, actuators that can deliver relatively low displacement and low force should be suitable for the control experiment. For the control experiment, the control force will be

applied through a bearing fitted in an adapter. This bearing will be mounted on either the carrier or sun gear shaft

7.7 Discussion

This study has numerically demonstrated how a pole placement method can be used to actively control the vibration of a planetary gear system. The controller was designed such that the closed-loop poles can be assigned using both fixed and rotating frames of reference. The control gain can be determined at any rotational speed using a rotating frame of reference. The control force and effort required can then be determined at each frequency, therefore the kind of actuator required for the control experiment can be known. The numerical predictions show that the assigned poles of lower frequencies corresponding to translational modes are shifted to avoid resonance with the addition of damping to reduce the response. The control forces required for the method are relatively small, therefore actuators with low control force are suitable for practical implementation. The control experiment on pole placement method in controlling vibration of planetary gear is recommended to know if the numerical result closely approximate the dynamic of the system after pole placement. The control experiment should be such that the rotational displacement can be measured over a wide range of frequency and the poles of the excited rotational modes can be shifted. For this method, the transmission error and the mesh stiffness must be known unlike the one demonstrated by Mottershead et al which makes use of measured receptance.

There is a feedforward method used by Montague et al. [42] to control mesh vibration of parallel axis gear, this can also be applied to planetary gear for mesh vibration reduction. The piezoelectric actuators were mounted 20^{o} to the common tangent to the pitch circles such that they are collinear with the line of contact or pressure line.

7.8 Conclusions

The theory of pole placement in active vibration control has been extended to control the vibration of planetary gear in this study. The new contribution is that a controller was designed such that the closed-loop poles can be assigned using both fixed and rotating frames of reference. The feedback gains can be obtained at any rotational speed of the rotating coordinate. This pole placement method considers output feedback and this was presented and numerically implemented using both fixed and rotating reference frames. First and foremost, the same poles were assigned to the sun gear only and subsequently the carrier in the x and y (translational) directions using both frames of reference. Three open-loop poles corresponding to translational modes out of eight were shifted with two control forces applied either on the carrier or sun gear. This shows that the method is suitable to actively

control the mesh vibration of a planetary gear system but requires that the mesh excitation should be known.

It was shown that the control force determined using a rotating frame of reference can be transformed to the fixed frame of reference for practical implementation. This is because with current technology, actuators cannot easily rotate with the planetary gear in practice to control the vibration. Also, the control forces required by the actuators are not high, hence actuators with low control forces and displacement will be suitable for practical implementation.

The optimal place to apply control force when two actuators are used to apply control force on either the carrier or the sun gear was determined using the control effort required. For comparison, the control effort required by the sun gear to achieve stability is more because the stiffness of its bearing is higher. So the optimal place to apply control force depends on the stiffnesses of the bearings. The lesser the stiffness of the bearing the less the control effort required. In this study, the optimal place to apply control force is the carrier.

Furthermore, the number of control forces was increased from two to four and they were simultaneously applied to the carrier and sun gear in x and y directions. The simultaneous assignment of poles to both the carrier and sun gear shows a better vibration controllability than assigning the poles to one of them. Five poles corresponding to translational modes were shifted and damped with four control forces. The poles of the six rotational modes remain unchanged with two and four control forces applied. This is because the closed-loop poles were applied in both the x and y directions of the carrier and sun gear which are translating. In general, the translational modes of vibration (i.e. transverse vibration) which are the largest in high speed machinery can be controlled effectively by pole placement.

Chapter 8 General conclusions and future work

This study focuses mainly on the vibration measurement and control of planetary gear. Dynamic modelling and analysis was considered first to predict the natural frequencies and the mode shapes of vibration using a fixed and rotating frame of reference. The results using both frames of reference were compared. A customized planetary gear test rig was designed and constructed such that the independent vibration of the carrier, sun and planet gears can be measured when they are rotating. This was achieved by considering a sufficient space on the components where MEMS accelerometers can be mounted. Some of the parameters needed to predict vibrations were calculated analytically while some were measured and compared to the values of the existing formula. For instance modal analysis was used to determine the bearing stiffnesses of the carrier, sun and planet gears and the results were compared to the existing formula in the literature. Also, modal analysis was carried out in order to compare the predicted vibration results with the experimental results. The spinning test was carried out where the MEMS accelerometers were rotating with the components in order to measure the true vibrations of the components. Vibration source identification was carried out to determine the major source of vibration within a particular frequency range. Finally some poles of the system were shifted to another location to avoid resonance which can lead to damage and breakdown of a planetary gear system.

8.1 General conclusions

8.1.1 Dynamic modelling using fixed and rotating frame of reference

The dynamic modelling and analysis was done using both the fixed and rotating frames of reference. It was discovered that the natural frequencies are the same when using both frames of reference provided that the rotational speed of the rotating coordinate is low. It shows that there is the possibility of having a mode where only the sun or ring gear is translating in a planetary gear system with two planet gears unlike system with higher number of planets.

8.1.2 Test rig design and construction

A suitable vibration test rig of planetary gear was designed and developed such that individual vibration response of each component in the system can be measured while rotating. The parts of the test rig can be easily dismantled for modification because temporary fasteners were used to couple them together. Furthermore, the test rig is designed such that there are spaces where wireless accelerometers can be mounted on the rotating components. The test rig was used for measuring the bearing stiffnesses of the components. The ratio of bearing stiffnesses estimated in the horizontal and

vertical directions were determined and compared to the ones presented in literature. It shows that the difference is not significant. The mesh stiffness was also estimated using the result of the modal testing conducted on the test rig with the predicted results. The vertical stiffness of the ring gear could not be estimated correctly because it was bolted to the base of the test in the vertical direction.

8.1.3 Comparison between predictions and measurement

The sun-planet and ring-planet mesh stiffnesses were determined with the measured and predicted natural frequencies using error function. The predicted and measured responses shows a certain degree of agreement but not fully agreed especially the planet and ring gears. In general, the analytical model seems to show the behaviour of the planetary gear system.

8.1.4 Spinning test and vibration source identification

It has been presented in this study that vibration of individual components of a planetary gear system can be measured when rotating. There is no need to use signal separation techniques to isolate signals in order to identify faulty components. The effect of load and rotational speed on the response at the natural and mesh frequencies are studied and presented. The study shows that a light load can cause a significant response on the gears which can damage the teeth as well as a heavy load under a constant speed. The response associated with unbalance on the sun gear and their side bands were also measured at a low frequency range. The effect of rotational speeds and loads on this response was presented.

8.1.5 Vibration Source identification

The virtual source of vibration in a planetary gear has been identified using PCA technique. The method shows the virtual source over a low frequency range which includes the frequency of synchronous vibration of each component. For a high frequency range which includes the mesh frequency, the virtual sources could not be identified on the sun and planet at a load 100 ohms. However the virtual sources become easier to identify at a lighter load of 47 ohms. It is highly recommended that this study should be carried out with a seeded fault on the teeth of sun or planet gear.

8.1.6 Pole placement

The vibration of a planetary gear system using an active control by a pole placement has been presented. It has been predicted that the method is effective in controlling the vibration of the system by shifting the some poles to avoid resonance which may damage the system using two control forces

on either the sun gear or the carrier. However, it shows that the control effort required depends on the bearing stiffness of the component where the control force is being applied. The optimal place to put the control force is on the component with lesser stiffness of the bearing. The controllability of the system increases with increase in the number of points where control force is added, but the challenge is the cost of getting more actuators. This predictions need to be validated with a controlled experiments where the control forces can be applied by connecting the actuators to the bearings fitted in adapters. These bearings can be mounted on either the carrier or sun gear shafts.

8.2 Suggestions for future work

- Modification of the test rig such that the meshing teeth can be lubricated evenly during operation.
- The coulomb damping (dry friction) between the meshing teeth should be estimated.
- The dynamic range of MEMS accelerometers should be increased and the size of the accelerometers can be reduced in order to measure vibrations at higher rotational speeds
- The tangential response of the planet gears should be measured and compared to the tangential response of the planet gears to know which response is higher. The size of the planet gears can be increased in order to provide a space to mount the accelerometers tangentially.
- Experimental validation of pole placement predictions should be done using both fixed and rotating frames of reference. This may be achievable with the advancement in vibration measurement and control technology.
- Creation of a seeded fault by breaking a tooth on the sun gear and take the measurement. The PCA method should be done again and comparison should be done with the result presented in this thesis. This will clarify the reason why there is no correlation at the mesh frequency in some of the results. A light load can also be considered.

Appendices

Appendix A

Equation of motion for the sun gear in matrix form using a fixed frame of reference

$$\begin{bmatrix} m_s & 0 & 0 \\ 0 & m_s & 0 \\ 0 & 0 & I_s / r_s^2 \end{bmatrix} \begin{Bmatrix} \ddot{x}_s \\ \ddot{y}_s \\ \ddot{u}_s \end{Bmatrix} + \begin{bmatrix} c_{sx} & 0 & 0 \\ 0 & c_{sy} & 0 \\ 0 & 0 & 0 \end{bmatrix} \begin{Bmatrix} \dot{x}_s \\ \dot{y}_s \\ \dot{u}_s \end{Bmatrix} + \begin{bmatrix} k_{sx} & 0 & 0 \\ 0 & k_{sy} & 0 \\ 0 & 0 & 0 \end{bmatrix} \begin{Bmatrix} x_s \\ y_s \\ u_s \end{Bmatrix} +$$
$$k_{sn} \begin{bmatrix} \sin^2 \psi_{sn} & -\cos\psi_{sn} \sin\psi_{sn} & -\sin\psi_{sn} \\ -\cos\psi_{sn} \sin\psi_{sn} & \cos^2 \psi_{sn} & \cos\psi_{sn} \\ -\sin\psi_{sn} & \cos\psi_{sn} & 1 \end{bmatrix} \begin{Bmatrix} x_s \\ y_s \\ u_s \end{Bmatrix} + k_{sn} \begin{bmatrix} \sin\alpha_s \sin\psi_{sn} & \cos\alpha_s \sin\psi_{sn} & -\sin\psi_{sn} \\ -\sin\alpha_s \cos\psi_{sn} & -\cos\alpha_s \cos\psi_{sn} & \cos\psi_{sn} \\ -\sin\alpha_s & \cos\alpha_s & 1 \end{bmatrix} \begin{Bmatrix} x_s \\ y_s \\ u_s \end{Bmatrix}$$

(A3.1)

Equation of motion for the ring gear in matrix form using a fixed frame of reference

$$\begin{bmatrix} m_r & 0 & 0 \\ 0 & m_r & 0 \\ 0 & 0 & I_r / r_r^2 \end{bmatrix} \begin{Bmatrix} \ddot{x}_r \\ \ddot{y}_r \\ \ddot{u}_r \end{Bmatrix} + \begin{bmatrix} c_{rx} & 0 & 0 \\ 0 & c_{ry} & 0 \\ 0 & 0 & 0 \end{bmatrix} \begin{Bmatrix} \dot{x}_r \\ \dot{y}_r \\ \dot{u}_r \end{Bmatrix} + \begin{bmatrix} k_{rx} & 0 & 0 \\ 0 & k_{ry} & 0 \\ 0 & 0 & 0 \end{bmatrix} \begin{Bmatrix} x_r \\ y_r \\ u_r \end{Bmatrix} +$$
$$k_{rn} \begin{bmatrix} \sin^2 \psi_{rn} & -\cos\psi_{rn} \sin\psi_{rn} & -\sin\psi_{rn} \\ -\cos\psi_{rn} \sin\psi_{rn} & \cos^2 \psi_{rn} & \cos\psi_{rn} \\ -\sin\psi_{rn} & \cos\psi_{rn} & 1 \end{bmatrix} \begin{Bmatrix} x_r \\ y_r \\ u_r \end{Bmatrix} + k_{rn} \begin{bmatrix} -\sin\alpha_s \sin\psi_{rn} & \cos\alpha_r \sin\psi_{rn} & \sin\psi_{rn} \\ \sin\alpha_r \cos\psi_{rn} & -\cos\alpha_r \cos\psi_{rn} & -\cos\psi_{rn} \\ \sin\alpha_r & -\cos\alpha_r & -1 \end{bmatrix} \begin{Bmatrix} x_r \\ y_r \\ u_r \end{Bmatrix}$$

(A3.2)

Equation of motion for the carrier in matrix form using a fixed frame of reference

$$\begin{bmatrix} m_c & 0 & 0 \\ 0 & m_c & 0 \\ 0 & 0 & I_c / r_c^2 \end{bmatrix} \begin{Bmatrix} \ddot{x}_c \\ \ddot{y}_c \\ \ddot{u}_c \end{Bmatrix} + \begin{bmatrix} c_c & 0 & 0 \\ 0 & c_c & 0 \\ 0 & 0 & 0 \end{bmatrix} \begin{Bmatrix} \dot{x}_c \\ \dot{y}_c \\ \dot{u}_c \end{Bmatrix} + \begin{bmatrix} k_c & 0 & 0 \\ 0 & k_c & 0 \\ 0 & 0 & 0 \end{bmatrix} \begin{Bmatrix} x_c \\ y_c \\ u_c \end{Bmatrix} + k_p \begin{bmatrix} 1 & 0 & \sin\psi_n \\ 0 & 1 & \cos\psi_n \\ \sin\psi_n & \cos\psi_n & 1 \end{bmatrix} \begin{Bmatrix} \overline{x}_c \\ \overline{y}_c \\ \overline{u}_c \end{Bmatrix} +$$
$$k_p \begin{bmatrix} -\cos\psi_n & -\sin\psi_n & 0 \\ \sin\psi_n & -\cos\psi_n & 0 \\ 0 & -1 & 0 \end{bmatrix} \begin{Bmatrix} \zeta_n \\ \eta_n \\ u_n \end{Bmatrix}$$

(A3.3)

Equation of motion for the planet gear in matrix form using a fixed frame of reference

$$\begin{bmatrix} m_p & 0 & 0 \\ 0 & m_p & 0 \\ 0 & 0 & I_p / r_p^2 \end{bmatrix} \begin{Bmatrix} \ddot{\zeta}_n \\ \ddot{\eta}_n \\ \ddot{u}_n \end{Bmatrix} + \begin{bmatrix} c_p & 0 & 0 \\ 0 & c_p & 0 \\ 0 & 0 & 0 \end{bmatrix} \begin{Bmatrix} \dot{\zeta}_n \\ \dot{\eta}_n \\ \dot{u}_n \end{Bmatrix} + \begin{bmatrix} k_p & 0 & 0 \\ 0 & k_p & 0 \\ 0 & 0 & 0 \end{bmatrix} \begin{Bmatrix} \zeta_n \\ \eta_n \\ u_n \end{Bmatrix} + k_p \begin{bmatrix} -\cos\psi_n & \sin\psi_n & 0 \\ -\sin\psi_n & -\cos\psi_n & -1 \\ 0 & 0 & 0 \end{bmatrix} \begin{Bmatrix} \overline{x}_c \\ \overline{y}_c \\ \overline{u}_c \end{Bmatrix} +$$

$$k_{sn} \begin{bmatrix} \sin\alpha_s \sin\psi_{sn} & -\sin\alpha_s \cos\psi_{sn} & -\sin\alpha_s \\ \cos\alpha_s \sin\psi_{sn} & -\cos\alpha_s \cos\psi_{sn} & -\cos\alpha_s \\ -\sin\psi_{sn} & \cos\psi_{sn} & 1 \end{bmatrix} \begin{Bmatrix} x_s \\ y_s \\ u_s \end{Bmatrix} + k_{sn} \begin{bmatrix} \sin^2\alpha_s & \cos\alpha_s \sin\alpha_s & -\sin\alpha_s \\ \cos\alpha_s \sin\alpha_s & \cos^2\alpha_s & -\cos\alpha_s \\ -\sin\alpha_s & -\cos\alpha_s & 1 \end{bmatrix} \begin{Bmatrix} \zeta_n \\ \eta_n \\ u_n \end{Bmatrix}$$

$$+k_{rn} \begin{bmatrix} -\sin\alpha_r \sin\psi_{rn} & \sin\alpha_r \cos\psi_{rn} & \sin\alpha_r \\ \cos\alpha_r \sin\psi_{rn} & -\cos\alpha_r \cos\psi_{rn} & -\cos\alpha_r \\ \sin\psi_{rn} & -\cos\alpha_r & -1 \end{bmatrix} \begin{Bmatrix} x_r \\ y_r \\ u_r \end{Bmatrix} + k_{rn} \begin{bmatrix} \sin^2\alpha_r & \cos\alpha_r \sin\alpha_r & -\sin\alpha_r \\ -\cos\alpha_r \sin\alpha_r & \cos^2\alpha_r & \cos\alpha_s \\ -\sin\alpha_r & \cos\alpha_s & 1 \end{bmatrix} \begin{Bmatrix} \zeta_n \\ \eta_n \\ u_n \end{Bmatrix}$$

(A3.4)

Equations of motion using a rotating frame of reference

Equation of motion for the sun gear in matrix form using a rotating frame of reference

$$\begin{bmatrix} \overline{m}_s & 0 & 0 \\ 0 & \overline{m}_s & 0 \\ 0 & 0 & I_s / r_s^2 \end{bmatrix} \begin{Bmatrix} \ddot{\overline{x}}_s \\ \ddot{\overline{y}}_s \\ \ddot{\overline{u}}_s \end{Bmatrix} + \Omega_c \begin{bmatrix} 0 & -2\overline{m}_s & 0 \\ -2\overline{m}_s & 0 & 0 \\ 0 & 0 & 0 \end{bmatrix} \begin{Bmatrix} \dot{\overline{x}}_s \\ \dot{\overline{y}}_s \\ \dot{\overline{u}}_s \end{Bmatrix} + \begin{bmatrix} \overline{c}_{sx} & 0 & 0 \\ 0 & \overline{c}_{sy} & 0 \\ 0 & 0 & 0 \end{bmatrix} \begin{Bmatrix} \dot{\overline{x}}_s \\ \dot{\overline{y}}_s \\ \dot{\overline{u}}_s \end{Bmatrix} + \begin{bmatrix} \overline{k}_{sx} & 0 & 0 \\ 0 & \overline{k}_{sy} & 0 \\ 0 & 0 & 0 \end{bmatrix} \begin{Bmatrix} \overline{x}_s \\ \overline{y}_s \\ \overline{u}_s \end{Bmatrix} +$$

$$k_{sn} \begin{bmatrix} \sin^2\psi_{sn} & -\cos\psi_{sn} \sin\psi_{sn} & -\sin\psi_{sn} \\ -\cos\psi_{sn} \sin\psi_{sn} & \cos^2\psi_{sn} & \cos\psi_{sn} \\ -\sin\psi_{sn} & \cos\psi_{sn} & 1 \end{bmatrix} \begin{Bmatrix} \overline{x}_s \\ \overline{y}_s \\ \overline{u}_s \end{Bmatrix} + k_{sn} \begin{bmatrix} \sin\alpha_s \sin\psi_{sn} & \cos\alpha_s \sin\psi_{sn} & -\sin\psi_{sn} \\ -\sin\alpha_s \cos\psi_{sn} & -\cos\alpha_s \cos\psi_{sn} & \cos\psi_{sn} \\ -\sin\alpha_s & \cos\alpha_s & 1 \end{bmatrix} \begin{Bmatrix} \overline{x}_s \\ \overline{y}_s \\ \overline{u}_s \end{Bmatrix}$$

$$-\Omega_c^2 \begin{bmatrix} m_s & 0 & 0 \\ 0 & m_s & 0 \\ 0 & 0 & 0 \end{bmatrix} \begin{Bmatrix} \overline{x}_s \\ \overline{y}_s \\ \overline{u}_s \end{Bmatrix}$$

(A3.5)

Equation of motion for the ring gear in matrix form using a rotating frame of reference

$$\begin{bmatrix} \bar{m}_r & 0 & 0 \\ 0 & \bar{m}_r & 0 \\ 0 & 0 & I_r / r_r^2 \end{bmatrix} \begin{Bmatrix} \ddot{\bar{x}}_r \\ \ddot{\bar{y}}_r \\ \ddot{\bar{u}}_r \end{Bmatrix} + \Omega_c \begin{bmatrix} 0 & -2m_r & 0 \\ -2m_r & 0 & 0 \\ 0 & 0 & 0 \end{bmatrix} \begin{Bmatrix} \dot{\bar{x}}_r \\ \dot{\bar{y}}_r \\ \dot{\bar{u}}_r \end{Bmatrix} + \begin{bmatrix} c_{rx} & 0 & 0 \\ 0 & c_{ry} & 0 \\ 0 & 0 & 0 \end{bmatrix} \begin{Bmatrix} \dot{\bar{x}}_r \\ \dot{\bar{y}}_r \\ \dot{\bar{u}}_r \end{Bmatrix} + \begin{bmatrix} \bar{k}_{rx} & 0 & 0 \\ 0 & \bar{k}_{ry} & 0 \\ 0 & 0 & 0 \end{bmatrix} \begin{Bmatrix} \bar{x}_r \\ \bar{y}_r \\ \bar{u}_r \end{Bmatrix} +$$

$$k_{rn} \begin{bmatrix} \sin^2 \psi_{rn} & -\cos\psi_{rn} \sin\psi_{rn} & -\sin\psi_{rn} \\ -\cos\psi_{rn} \sin\psi_{rn} & \cos^2 \psi_{rn} & \cos\psi_{rn} \\ -\sin\psi_{rn} & \cos\psi_{rn} & 1 \end{bmatrix} \begin{Bmatrix} \bar{x}_r \\ \bar{y}_r \\ \bar{u}_r \end{Bmatrix} + k_{rn} \begin{bmatrix} -\sin\alpha_s \sin\psi_{rn} & \cos\alpha_r \sin\psi_{rn} & \sin\psi_{rn} \\ \sin\alpha_r \cos\psi_{rn} & -\cos\alpha_r \cos\psi_{rn} & -\cos\psi_{rn} \\ \sin\alpha_r & -\cos\alpha_r & -1 \end{bmatrix} \begin{Bmatrix} \bar{x}_r \\ \bar{y}_r \\ \bar{u}_r \end{Bmatrix}$$

$$-\Omega_c^2 \begin{bmatrix} \bar{m}_r & 0 & 0 \\ 0 & \bar{m}_r & 0 \\ 0 & 0 & 0 \end{bmatrix} \begin{Bmatrix} \bar{x}_r \\ \bar{y}_r \\ \bar{u}_r \end{Bmatrix}$$

(A3.6)

Equation of motion for the carrier in matrix form using a rotating frame of reference

$$\begin{bmatrix} \bar{m}_c & 0 & 0 \\ 0 & \bar{m}_c & 0 \\ 0 & 0 & I_c / r_c^2 \end{bmatrix} \begin{Bmatrix} \ddot{x}_c \\ \ddot{y}_c \\ \ddot{u}_c \end{Bmatrix} + \Omega_c \begin{bmatrix} 0 & -2\bar{m}_c & 0 \\ -2\bar{m}_c & 0 & 0 \\ 0 & 0 & 0 \end{bmatrix} \begin{Bmatrix} \dot{x}_r \\ \dot{y}_r \\ \dot{u}_r \end{Bmatrix} + \begin{bmatrix} c_p & 0 & 0 \\ 0 & c_p & 0 \\ 0 & 0 & 0 \end{bmatrix} \begin{Bmatrix} \dot{x}_c \\ \dot{y}_c \\ \dot{u}_c \end{Bmatrix} + \begin{bmatrix} \bar{k}_c & 0 & 0 \\ 0 & \bar{k}_c & 0 \\ 0 & 0 & 0 \end{bmatrix} \begin{Bmatrix} x_c \\ y_c \\ u_c \end{Bmatrix} +$$

$$k_p \begin{bmatrix} 1 & 0 & -\sin\psi_n \\ 0 & 1 & \cos\psi_n \\ -\sin\psi_n & \cos\psi_n & 1 \end{bmatrix} \begin{Bmatrix} \bar{x}_c \\ \bar{y}_c \\ \bar{u}_c \end{Bmatrix} + k_p \begin{bmatrix} -\cos\psi_n & \sin\psi_n & 0 \\ -\sin\psi_n & -\cos\psi_n & 0 \\ 0 & -1 & 0 \end{bmatrix} \begin{Bmatrix} \zeta_n \\ \eta_n \\ u_n \end{Bmatrix} - \Omega_c^2 \begin{bmatrix} \bar{m}_c & 0 & 0 \\ 0 & \bar{m}_c & 0 \\ 0 & 0 & 0 \end{bmatrix} \begin{Bmatrix} x_c \\ y_c \\ u_c \end{Bmatrix}$$

(A3.7)

Equation of motion for the planet gear in matrix form using a rotating frame of reference

$$\begin{bmatrix} \bar{m}_p & 0 & 0 \\ 0 & \bar{m}_p & 0 \\ 0 & 0 & I_p / r_p^2 \end{bmatrix} \begin{Bmatrix} \ddot{\bar{\zeta}}_n \\ \ddot{\bar{\eta}}_n \\ \ddot{\bar{u}}_n \end{Bmatrix} + \Omega_c \begin{bmatrix} 0 & -2\bar{m}_p & 0 \\ -2\bar{m}_p & 0 & 0 \\ 0 & 0 & 0 \end{bmatrix} \begin{Bmatrix} \dot{\bar{\zeta}}_n \\ \dot{\bar{\eta}}_n \\ \dot{\bar{u}}_n \end{Bmatrix} + \begin{bmatrix} \bar{c}_p & 0 & 0 \\ 0 & \bar{c}_p & 0 \\ 0 & 0 & 0 \end{bmatrix} \begin{Bmatrix} \dot{\bar{\zeta}}_n \\ \dot{\bar{\eta}}_n \\ \dot{\bar{u}}_n \end{Bmatrix} + \begin{bmatrix} \bar{k}_p & 0 & 0 \\ 0 & \bar{k}_p & 0 \\ 0 & 0 & 0 \end{bmatrix} \begin{Bmatrix} \bar{\zeta}_n \\ \bar{\eta}_n \\ \bar{u}_n \end{Bmatrix} +$$

$$k_p \begin{bmatrix} -\cos\psi_n & \sin\psi_n & 0 \\ -\sin\psi_n & -\cos\psi_n & -1 \\ 0 & 0 & 0 \end{bmatrix} \begin{Bmatrix} \bar{x}_c \\ \bar{y}_c \\ \bar{u}_c \end{Bmatrix} + k_{sn} \begin{bmatrix} \sin\alpha_s \sin\psi_{sn} & -\sin\alpha_s \cos\psi_{sn} & -\sin\alpha_s \\ \cos\alpha_s \sin\psi_{sn} & -\cos\alpha_s \cos\psi_{sn} & -\cos\alpha_s \\ -\sin\psi_{sn} & \cos\psi_{sn} & 1 \end{bmatrix} \begin{Bmatrix} \bar{x}_s \\ \bar{y}_s \\ \bar{u}_s \end{Bmatrix} + k_{sn}$$

$$\begin{bmatrix} \sin^2 \alpha_s & \cos\alpha_s \sin\alpha_s & -\sin\alpha_s \\ \cos\alpha_s \sin\alpha_s & \cos^2 \alpha_s & -\cos\alpha_s \\ -\sin\alpha_s & -\cos\alpha_s & 1 \end{bmatrix} \begin{Bmatrix} \bar{\zeta}_n \\ \bar{\eta}_n \\ \bar{u}_n \end{Bmatrix} + k_{rn} \begin{bmatrix} -\sin\alpha_r \sin\psi_{rn} & \sin\alpha_r \cos\psi_{rn} & \sin\alpha_r \\ \cos\alpha_r \sin\psi_{rn} & -\cos\alpha_r \cos\psi_{rn} & -\cos\alpha_r \\ \sin\psi_{rn} & -\cos\alpha_r & -1 \end{bmatrix} \begin{Bmatrix} \bar{x}_r \\ \bar{y}_r \\ \bar{u}_r \end{Bmatrix} +$$

$$k_{rn} \begin{bmatrix} \sin^2 \alpha_r & \cos\alpha_r \sin\alpha_r & -\sin\alpha_r \\ -\cos\alpha_r \sin\alpha_r & \cos^2 \alpha_r & \cos\alpha_s \\ -\sin\alpha_r & \cos\alpha_s & 1 \end{bmatrix} \begin{Bmatrix} \bar{\zeta}_n \\ \bar{\eta}_n \\ \bar{u}_n \end{Bmatrix} - \Omega_c^2 \begin{bmatrix} m_p & 0 & 0 \\ 0 & m_p & 0 \\ 0 & 0 & 0 \end{bmatrix} \begin{Bmatrix} \bar{\zeta}_n \\ \bar{\eta}_n \\ \bar{u}_n \end{Bmatrix}$$

(A3.8)

$$\begin{bmatrix} \mathbf{I} & \mathbf{0} \\ \mathbf{0} & \bar{\mathbf{M}} \end{bmatrix} \begin{Bmatrix} \dot{\bar{\mathbf{q}}} \\ \ddot{\bar{\mathbf{q}}} \end{Bmatrix} + \begin{bmatrix} \mathbf{0} & -\mathbf{I} \\ \bar{\mathbf{K}}_b + \bar{\mathbf{K}}_m - \Omega_c^2 \mathbf{K}_\Omega & \Omega_c \mathbf{G}_y \end{bmatrix} \begin{Bmatrix} \bar{\mathbf{q}} \\ \dot{\bar{\mathbf{q}}} \end{Bmatrix} = \begin{Bmatrix} \mathbf{0} \\ \mathbf{0} \end{Bmatrix} \tag{A3.9}$$

Contact stiffness matrix for two-planet model

$$\mathbf{K}_m = \begin{bmatrix} \Sigma \mathbf{K}_{c1}^n & \mathbf{0} & \mathbf{0} & \mathbf{K}_{c2}^1 & \mathbf{K}_{c2}^2 \\ \mathbf{0} & \Sigma \mathbf{K}_{r1}^n & \mathbf{0} & \mathbf{K}_{r2}^1 & \mathbf{K}_{r2}^2 \\ \mathbf{0} & \mathbf{0} & \Sigma \mathbf{K}_{s1}^n & \mathbf{K}_{s2}^1 & \mathbf{K}_{s2}^2 \\ \mathbf{K}_{c2}^{1^{\mathrm{T}}} & \mathbf{K}_{r2}^{1^{\mathrm{T}}} & \mathbf{K}_{s2}^{1^{\mathrm{T}}} & \mathbf{K}_{pp}^1 & \mathbf{0} \\ \mathbf{K}_{c2}^{2^{\mathrm{T}}} & \mathbf{K}_{r2}^{2^{\mathrm{T}}} & \mathbf{K}_{s2}^{2^{\mathrm{T}}} & \mathbf{0} & \mathbf{K}_{pp}^2 \end{bmatrix} \tag{A3.10}$$

The $\mathbf{K}_{\mathrm{m}}$ matrix can be decomposed into three matrices such that the sun-planet and planet-ring mesh stiffness can be varied.

$$\mathbf{K}_m = \begin{bmatrix} \Sigma \mathbf{K}_{c1}^n & \mathbf{0} & \mathbf{0} & \mathbf{K}_{c2}^1 & \mathbf{K}_{c2}^2 \\ \mathbf{0} & \mathbf{0} & \mathbf{0} & \mathbf{0} & \mathbf{0} \\ \mathbf{0} & \mathbf{0} & \mathbf{0} & \mathbf{0} & \mathbf{0} \\ \mathbf{K}_{c2}^{1^{\mathrm{T}}} & \mathbf{0} & \mathbf{0} & \mathbf{K}_{c3}^1 & \mathbf{0} \\ \mathbf{K}_{c2}^{2^{\mathrm{T}}} & \mathbf{0} & \mathbf{0} & \mathbf{0} & \mathbf{K}_{c3}^2 \end{bmatrix} + \mathbf{K}_{rn} \begin{bmatrix} \mathbf{0} & \mathbf{0} & \mathbf{0} & \mathbf{0} & \mathbf{0} \\ \mathbf{0} & \Sigma \mathbf{K}_{r1}^n & \mathbf{0} & \mathbf{K}_{r2}^1 & \mathbf{K}_{r2}^2 \\ \mathbf{0} & \mathbf{0} & \mathbf{0} & \mathbf{0} & \mathbf{0} \\ \mathbf{0} & \mathbf{K}_{r2}^{1^{\mathrm{T}}} & \mathbf{0} & \mathbf{K}_{r3}^1 & \mathbf{0} \\ \mathbf{0} & \mathbf{K}_{r2}^{2^{\mathrm{T}}} & \mathbf{0} & \mathbf{0} & \mathbf{K}_{r3}^2 \end{bmatrix} + \mathbf{K}_{sn} \begin{bmatrix} \mathbf{0} & \mathbf{0} & \mathbf{0} & \mathbf{0} & \mathbf{0} \\ \mathbf{0} & \mathbf{0} & \mathbf{0} & \mathbf{0} & \mathbf{0} \\ \mathbf{0} & \mathbf{0} & \Sigma \mathbf{K}_{s1}^n & \mathbf{K}_{s2}^1 & \mathbf{K}_{s2}^2 \\ \mathbf{0} & \mathbf{0} & \mathbf{K}_{s2}^{1^{\mathrm{T}}} & \mathbf{K}_{s3}^1 & \mathbf{0} \\ \mathbf{0} & \mathbf{0} & \mathbf{K}_{s2}^{2^{\mathrm{T}}} & \mathbf{0} & \mathbf{K}_{s3}^2 \end{bmatrix}$$

(A3.11)

For a fixed frame of reference,

$$\mathbf{K}_{c1}^n = k_p \begin{bmatrix} 1 & 0 & \sin\psi_n \\ 0 & 1 & \cos\psi_n \\ \sin\psi_n & \cos\psi_n & 1 \end{bmatrix}; \mathbf{K}_{c2}^n = k_p \begin{bmatrix} -\cos\psi_n & -\sin\psi_n & 0 \\ \sin\psi_n & -\cos\psi_n & 0 \\ 0 & -1 & 0 \end{bmatrix} \tag{A3.12}$$

For a rotating frame of reference

$$\bar{\mathbf{K}}_{c1}^n = k_p \begin{bmatrix} 1 & 0 & -\sin\psi_n \\ 0 & 1 & \cos\psi_n \\ -\sin\psi_n & \cos\psi_n & 1 \end{bmatrix}; \bar{\mathbf{K}}_{c2}^n = k_p \begin{bmatrix} -\cos\psi_n & \sin\psi_n & 0 \\ -\sin\psi_n & -\cos\psi_n & 0 \\ 0 & -1 & 0 \end{bmatrix} \tag{A3.13}$$

Other contact matrices are as follows

$$\mathbf{K}_{c3}=\begin{bmatrix} k_p & 0 & 0 \\ 0 & k_p & 0 \\ 0 & 0 & 0 \end{bmatrix};\ \mathbf{K}_{r1}^{n}=k_{rn}\begin{bmatrix} \sin^2\psi_{rn} & -\cos\psi_{rn}\sin\psi_{rn} & -\sin\psi_{rn} \\ -\cos\psi_{rn}\sin\psi_{rn} & \cos^2\psi_{rn} & \cos\psi_{rn} \\ -\sin\psi_{rn} & \cos\psi_{rn} & 1 \end{bmatrix} \quad \text{(A3.14)}$$

$$\mathbf{K}_{r2}^{n}=k_{rn}\begin{bmatrix} -\sin\alpha_s\sin\psi_{rn} & \cos\alpha_r\sin\psi_{rn} & \sin\psi_{rn} \\ \sin\alpha_r\cos\psi_{rn} & -\cos\alpha_r\cos\psi_{rn} & -\cos\psi_{rn} \\ \sin\alpha_r & -\cos\alpha_r & -1 \end{bmatrix}; \quad \text{(A3.15)}$$

$$\mathbf{K}_{r3}=k_{rn}\begin{bmatrix} \sin^2\alpha_r & \cos\alpha_r\sin\alpha_r & -\sin\alpha_r \\ -\cos\alpha_r\sin\alpha_r & \cos^2\alpha_r & \cos\alpha_s \\ -\sin\alpha_r & \cos\alpha_s & 1 \end{bmatrix}; \quad \text{(A3.16)}$$

$$\mathbf{K}_{s1}=k_{sn}\begin{bmatrix} \sin^2\psi_{sn} & -\cos\psi_{sn}\sin\psi_{sn} & -\sin\psi_{sn} \\ -\cos\psi_{sn}\sin\psi_{sn} & \cos^2\psi_{sn} & \cos\psi_{sn} \\ -\sin\psi_{sn} & \cos\psi_{sn} & 1 \end{bmatrix} \quad \text{(A3.17)}$$

$$\mathbf{K}_{s2}=k_{sn}\begin{bmatrix} \sin\alpha_s\sin\psi_{sn} & \cos\alpha_s\sin\psi_{sn} & -\sin\psi_{sn} \\ -\sin\alpha_s\cos\psi_{sn} & -\cos\alpha_s\cos\psi_{sn} & \cos\psi_{sn} \\ -\sin\alpha_s & \cos\alpha_s & 1 \end{bmatrix} \quad \text{(A3.18)}$$

$$\mathbf{K}_{s3}=k_{sn}\begin{bmatrix} \sin^2\alpha_s & \cos\alpha_s\sin\alpha_s & -\sin\alpha_s \\ \cos\alpha_s\sin\alpha_s & \cos^2\alpha_s & -\cos\alpha_s \\ -\sin\alpha_s & -\cos\alpha_s & 1 \end{bmatrix} \quad \text{(A3.19)}$$

Appendix B

Table B1. Natural frequencies used in minimising the difference in the sum of the predicted and estimated natural frequencies for determination of sun-planet mesh stiffness..

S/N	Estimated from experiment (Hz)	Prediction (Hz)
1	62.5	50
2	85.7	92
3	134	122
4	1097	1397

Table B2. Natural frequencies used in minimising the difference in the sum of the predicted and estimated natural frequencies for determination of planet-ring mesh stiffness.

S/N	Estimated from experiment (Hz)	Prediction (Hz)
1	47.5	47
2	90.66	98
3	515	519
4	1117	712

Procedures for calculating the mass moment of inertia of the components

1. Carrier

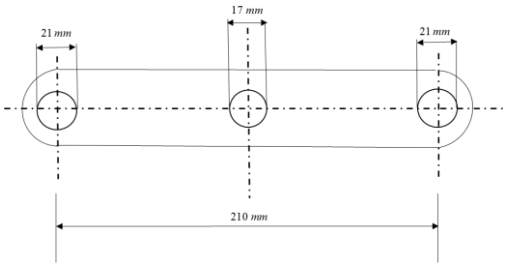

Figure B4.1

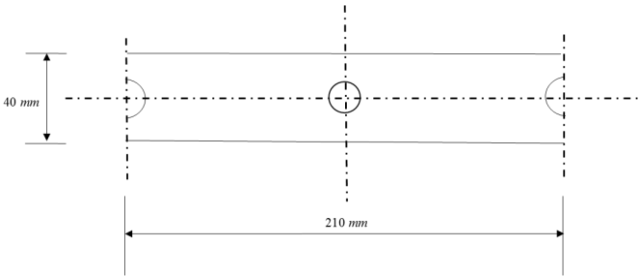

Figure B4.2

The mass moment of inertia of the rectangular part and the two semi-circles is

$$I_1 = \frac{\rho t A_r (a^2 + b^2)}{12} - \frac{\rho t A_{c1} (r^2)}{2}; \qquad \text{(B4.1)}$$

The mass moment of inertia of the centre circle in the rectangle

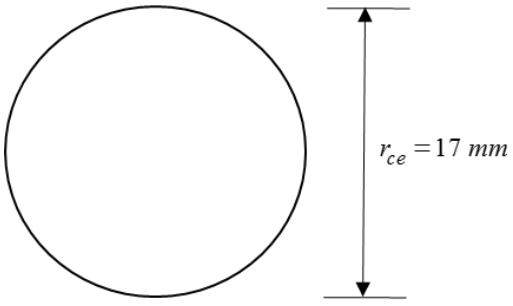

Figure B4.3

$$I_{ce} = \frac{\rho t A_{ce}(r_{ce}{}^2)}{2} \tag{B4.2}$$

The mass moment of inertia of the two concentric semi-circles at the end

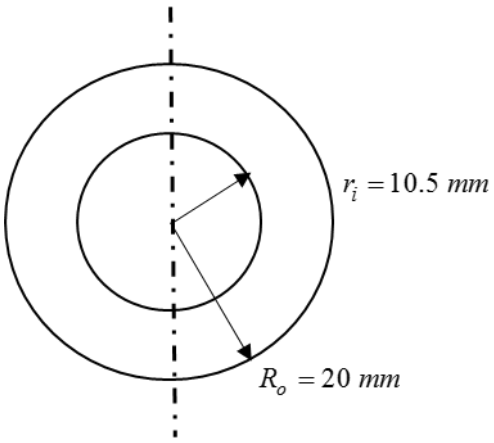

Figure B4.4

$$I_2 = \frac{\rho t A_o (R_o{}^2)}{2} - \frac{\rho t A_i (r_i^2)}{2} \tag{B4.3}$$

The total mass moment of the carrier

$$I_c = (I_1 - I_{ce}) + I_2 \tag{B4.4}$$

2. Ring gear

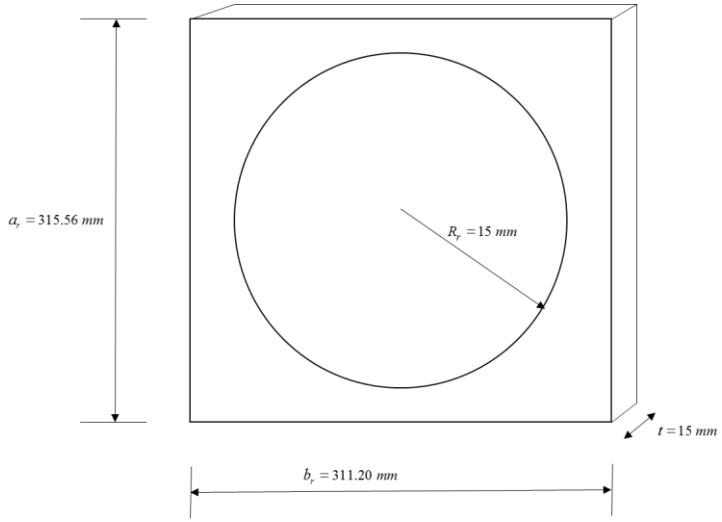

Figure B4.5

$$I_r = \frac{\rho t A_r (a_r{}^2 + b_r{}^2)}{12} - \frac{\rho t A_{cy} (R_r{}^2)}{2} \tag{B4.5}$$

3. Sun gear

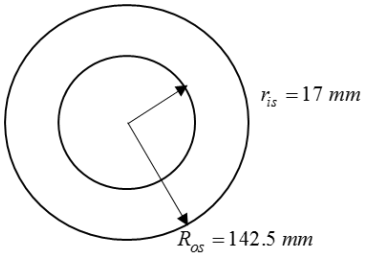

Figure B4.6

$$I_s = \frac{\rho t A_{os} (R_{os}{}^2)}{2} - \frac{\rho t A_{is} (r_{is}{}^2)}{2} \tag{B4.6}$$

4. Planet gear

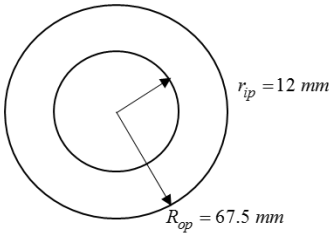

Figure B4.7

$$I_p = \frac{\rho t A_{op}(R_{op}{}^2)}{2} - \frac{\rho t A_{ip}(r_{ip}{}^2)}{2} \qquad \text{(B4.7)}$$

5. Torsional stiffness of the ring gear

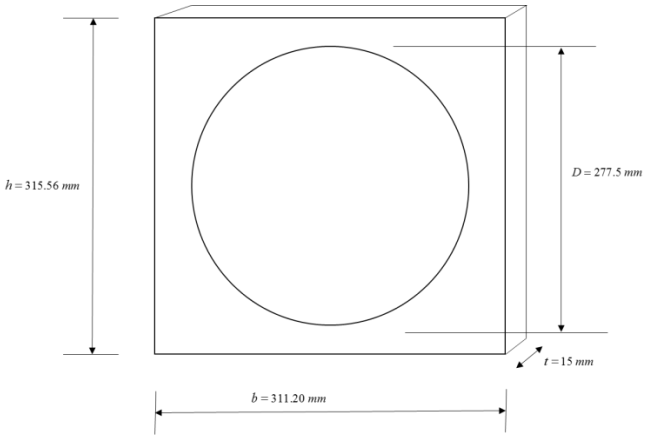

Figure B4.8

$K_{tr} = \frac{GJ_r}{L}$ **;** where G is the modulus of rigidity of steel which is $80\,\mathrm{GN/m}$, J_r is the polar moment of inertia of the ring geometry while *L* is the length of the whole body which is *h*.

The polar moment of inertia of a rectangular section about its axis

$$J_{rs} = \frac{bh(b^2 + h^2)}{12} = 0.00164\,m^4$$

The polar moment of inertia of a circular section axial direction

$$J_{cs} = \frac{\pi D^4}{32} = 5.823 \times 10^{-4} m^4$$

$$J_r = J_{rs} - J_{cs} = 0.0010 m^4$$

Therefore, the torsional stiffness of the ring gear, K_{tr} is 2.54×10^8 Nm/rad.

Bearing stiffness estimation

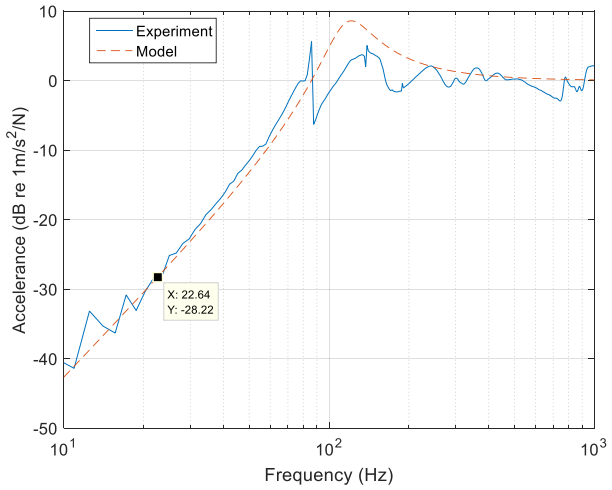

Figure B4.9. The accelerance of the carrier in the horizontal direction compared to a single degree of freedom system showing the stiffness line is 40 dB/decade slope. Coherence is good from 22.4 Hz.

Appendix C

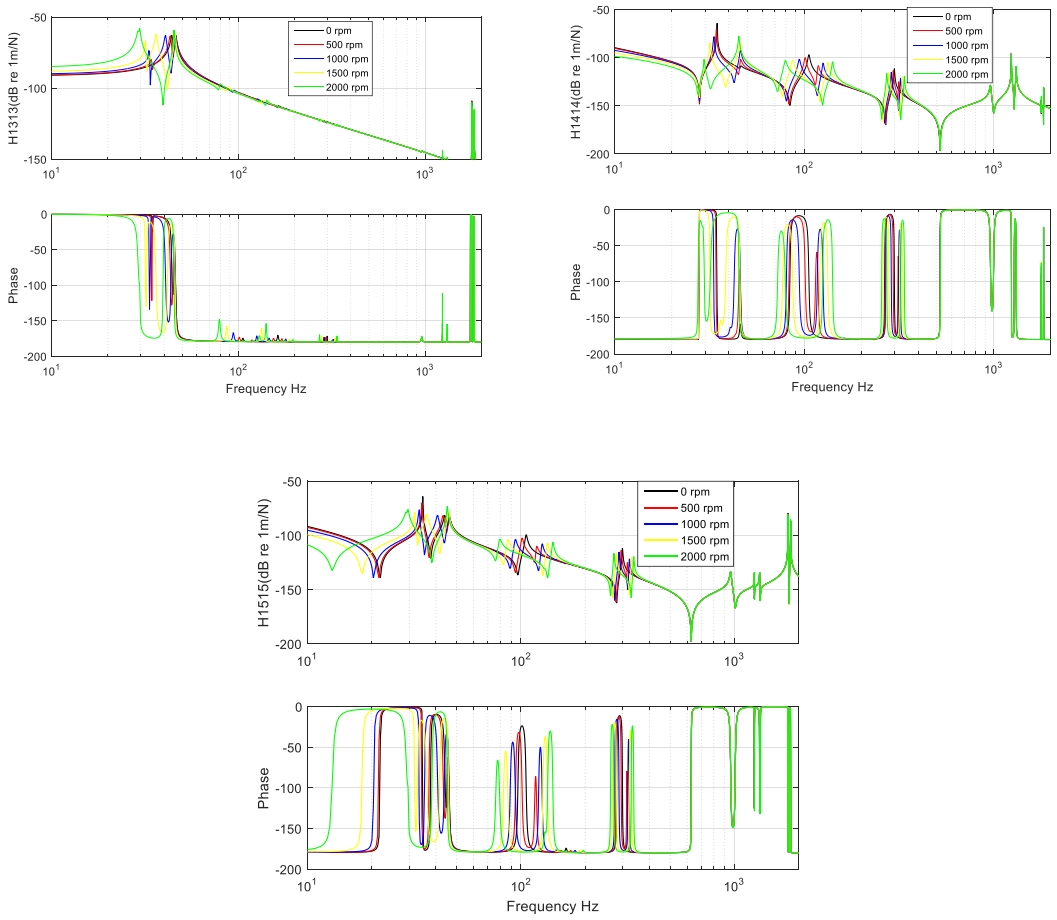

Figure C5.1

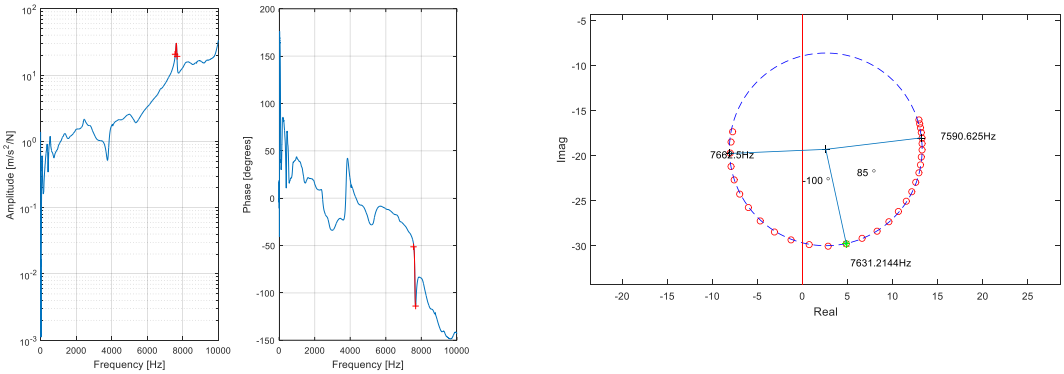

Figure C5.2. Carrier in x direction.

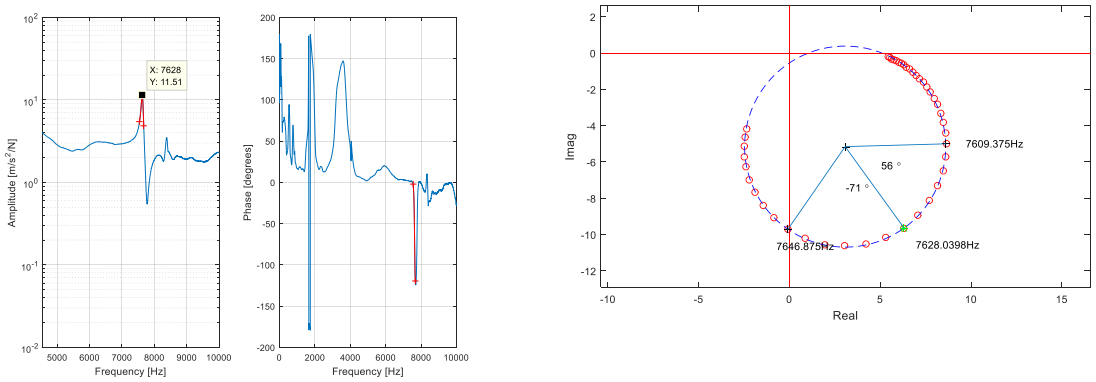

Figure C5.3. Carrier in y direction.

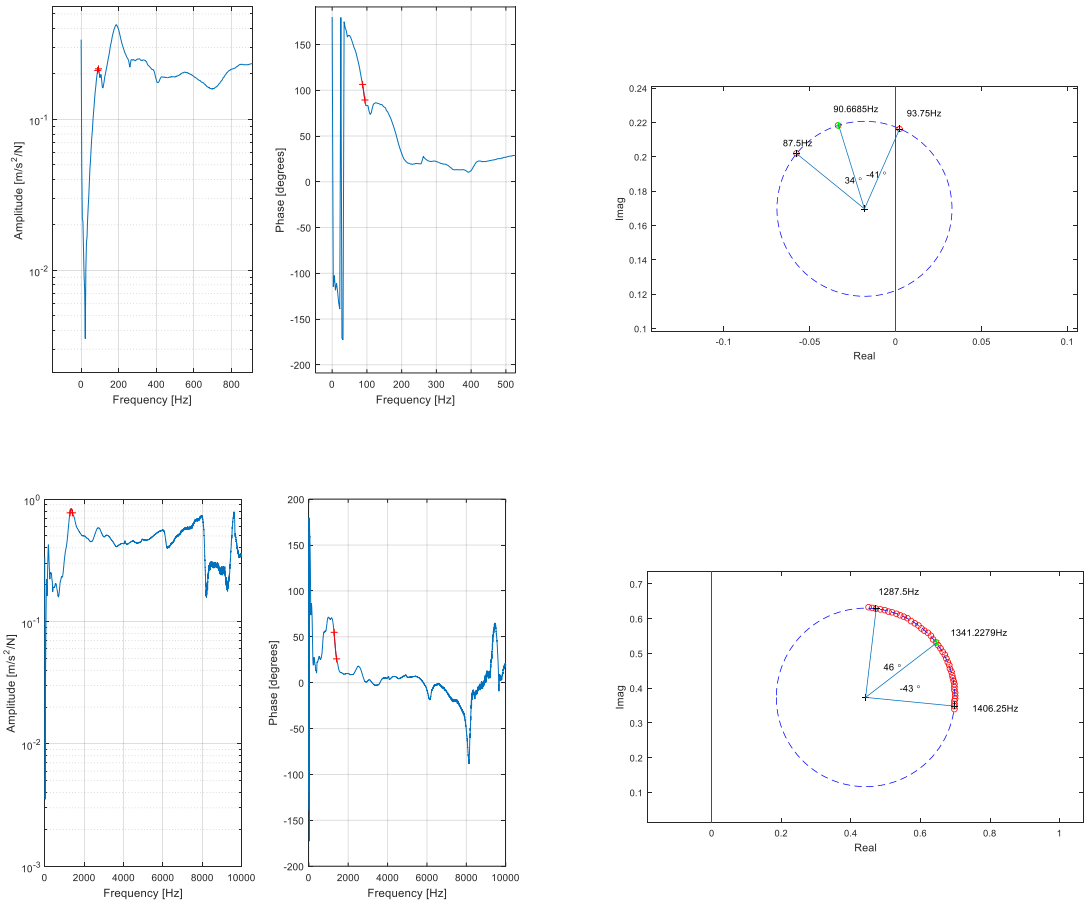

Figure C5.4. Sun gear in x direction.

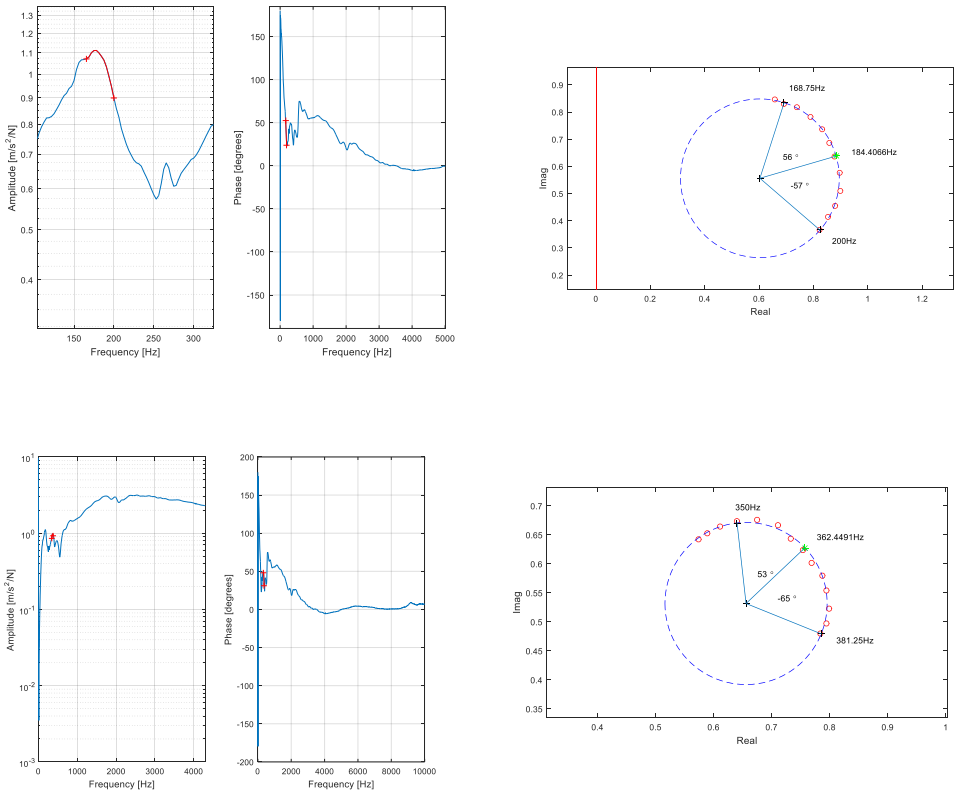

Figure C5.5. Planet gear in x direction.

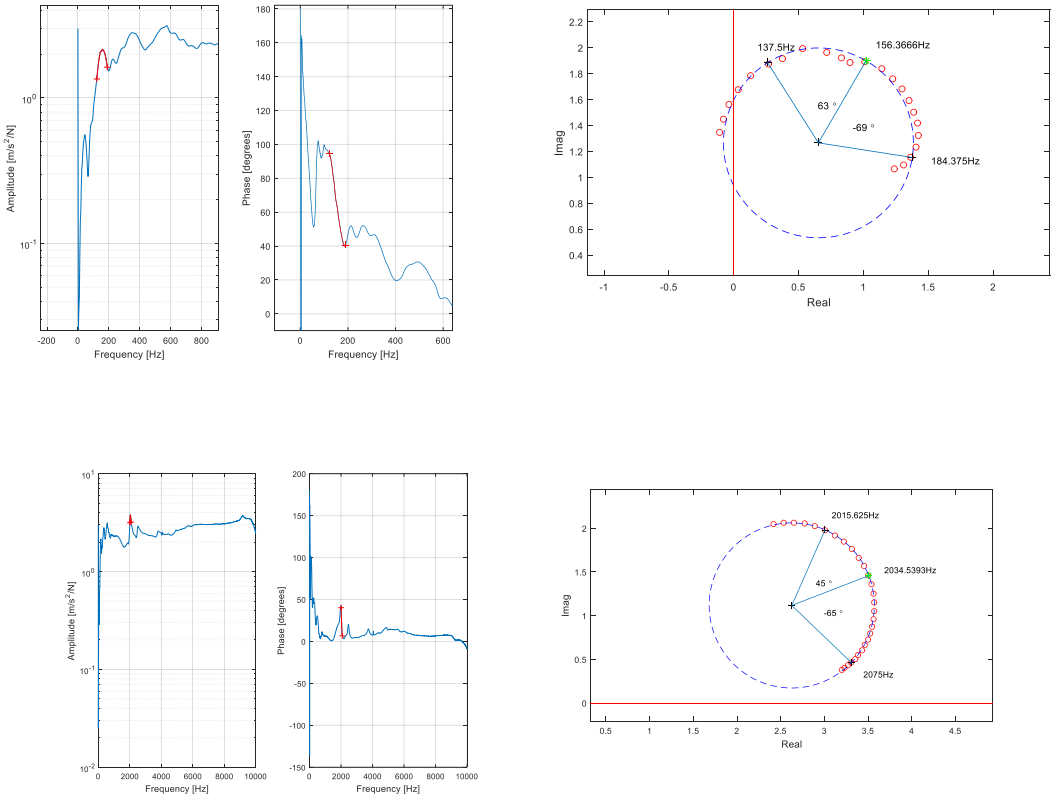

Figure C5.6. Planet gear in y direction

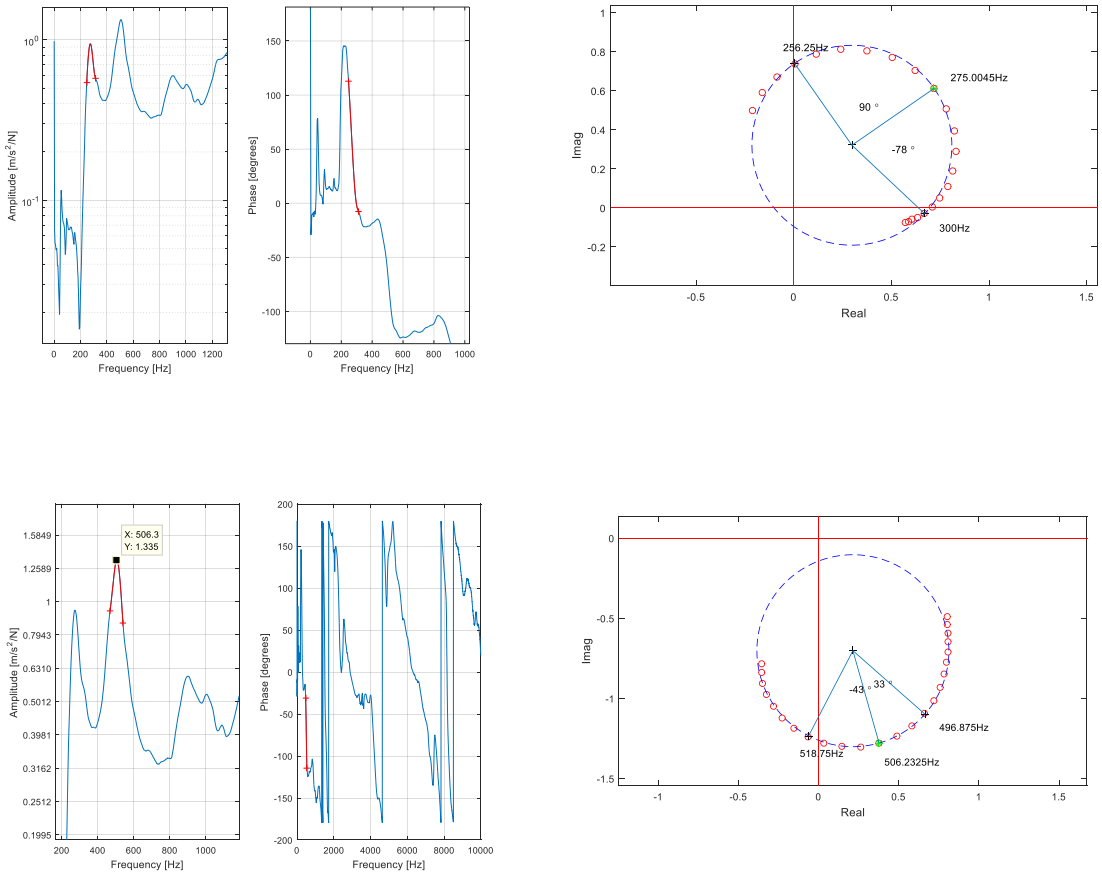

Figure C5.7. Ring gear in x direction.

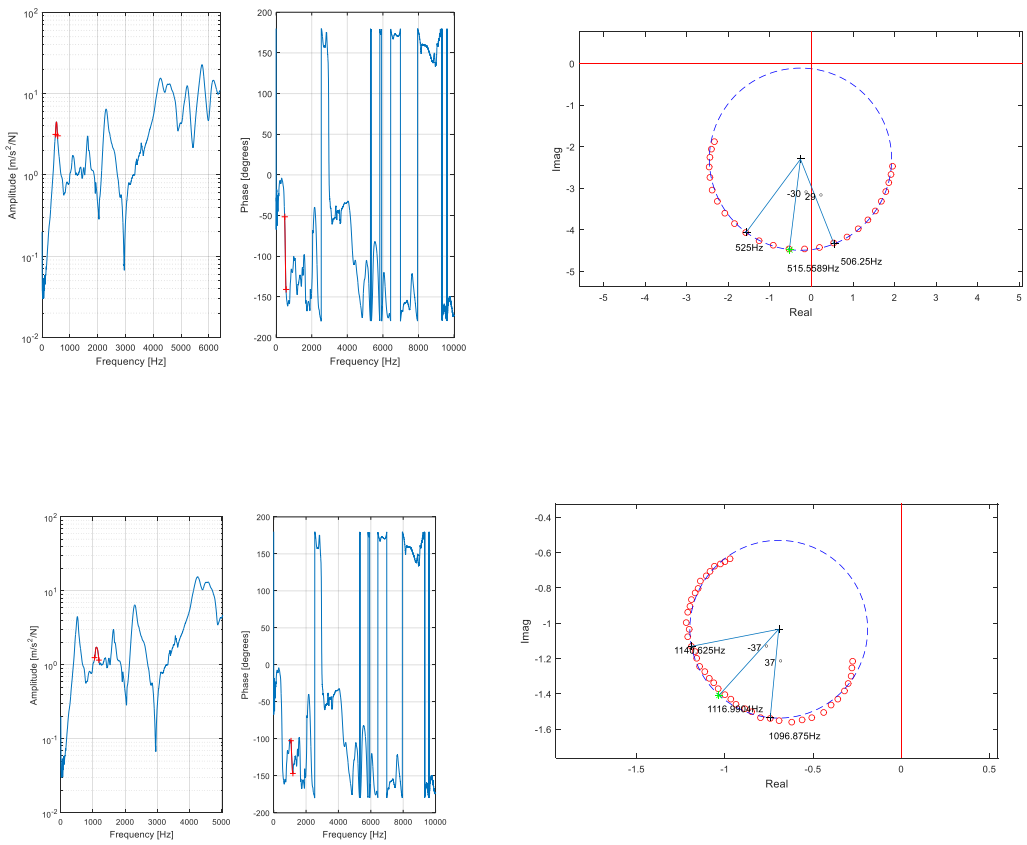

Figure C5.8. Ring gear in y direction.

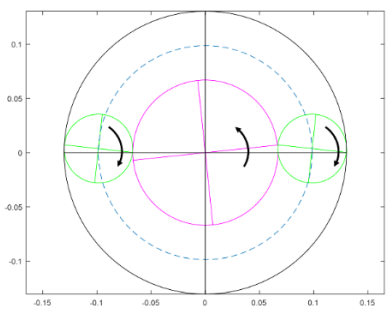

(a) Rotational mode at 0 Hz.

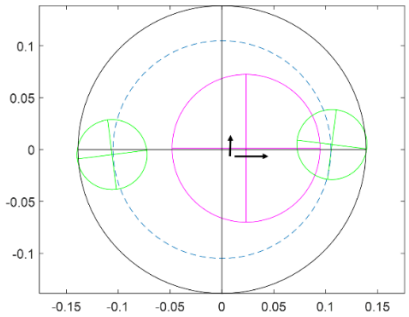

(b) Translational mode at 92 Hz.

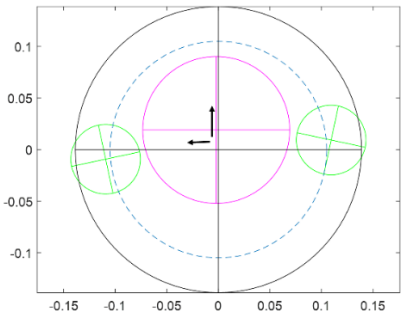

(c) Translational mode at 122.9 Hz.

Figure C5.9. Typical modes of vibration (a) rigid body mode (b) Translational mode at 92 Hz (c) The two horizontal and vertical including the dashed lines are the equilibrium positions.

Appendix D

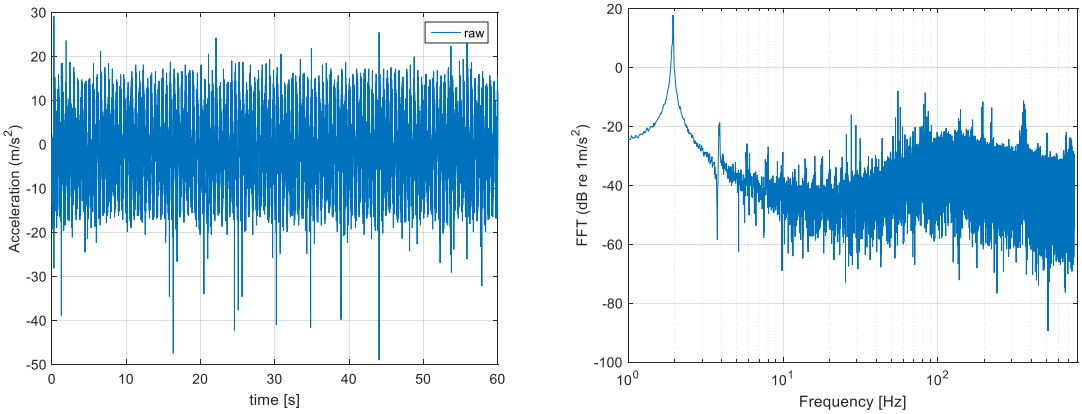

Figure D6.1 (a**).** Time history of the unloaded carrier acceleration in the tangential direction (b) The frequency content when the carrier speed is 117 rpm (the corresponding values in Hz is 1.95 Hz).

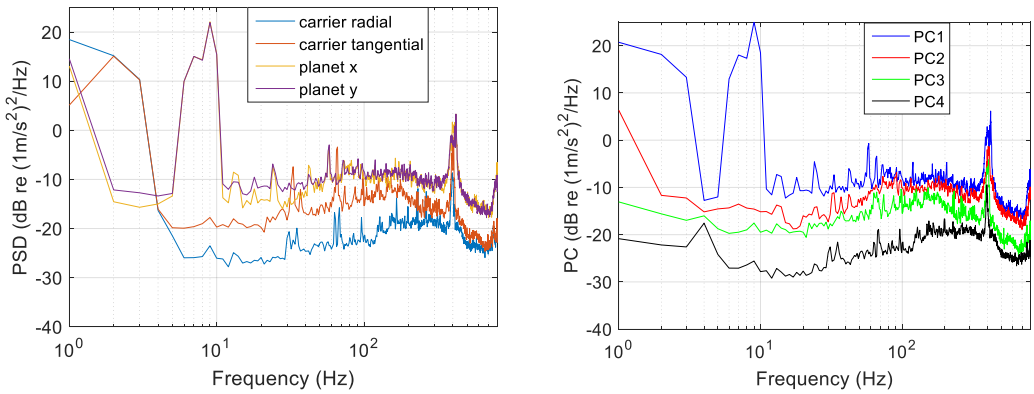

Figure D6.2 (a) The power spectral density of the carrier and planet gear accelerations at a higher speed. (b) The eigenvalues of the principal components PC_1, PC_2, PC_3 and PC_4.

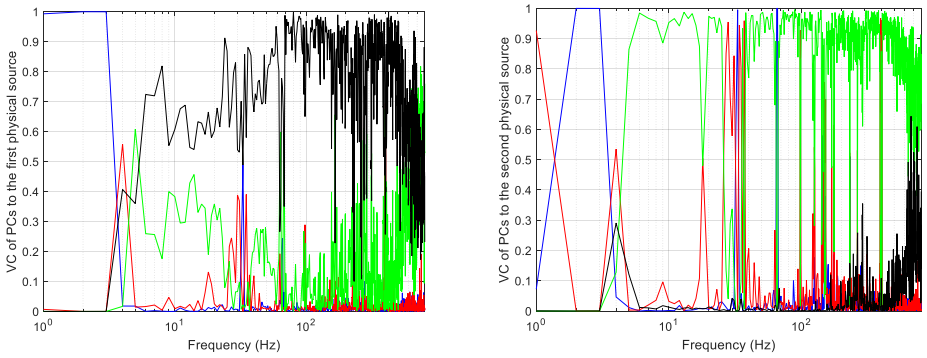

Figure D6.3. Virtual coherence of the PC_1, PC_2, PC_3 and PC_4 of Carrier-planet at a higher speed to the (a) first physical source (radial direction of the carrier) and (b) second physical source (tangential direction of the carrier). The blue, red, green and black lines denotes PC1, PC2, PC3 and PC4 respectively

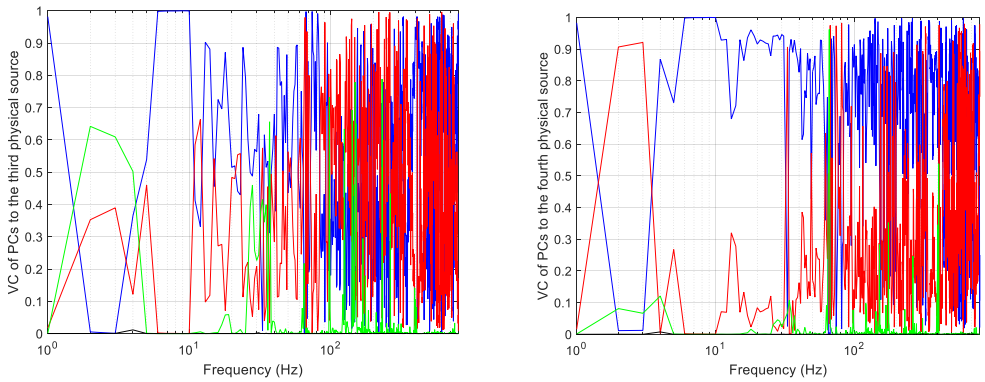

Figure D6.4. Virtual coherence of the PC_1, PC_2, PC_3 and PC_4 of Carrier-planet at a higher speed to the (c) third physical source (horizontal radial direction of the planet gear) and (d) fourth physical source (vertical radial direction of the planet gear). The blue, red, green and black lines denotes PC1, PC2, PC3 and PC4 respectively

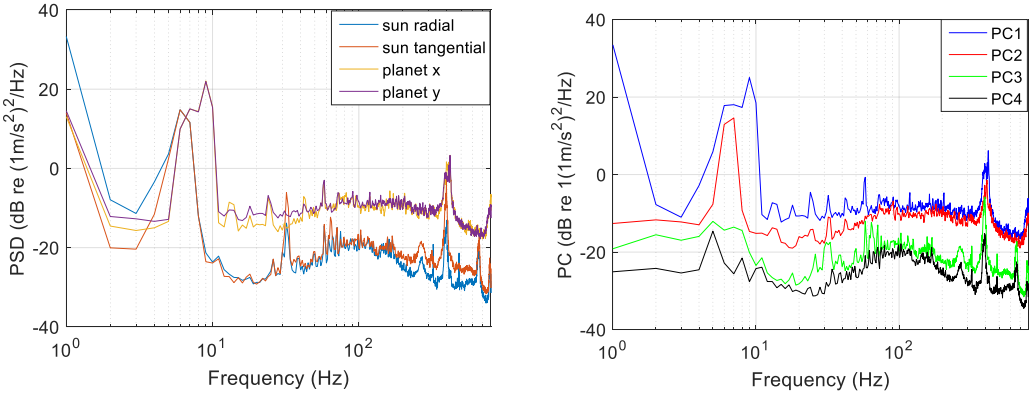

Figure D6.5 (a) The power spectral density of the sun and planet gear accelerations at a higher speed. (b) The eigenvalues of the principal components PC_1, PC_2, PC_3 and PC_4.

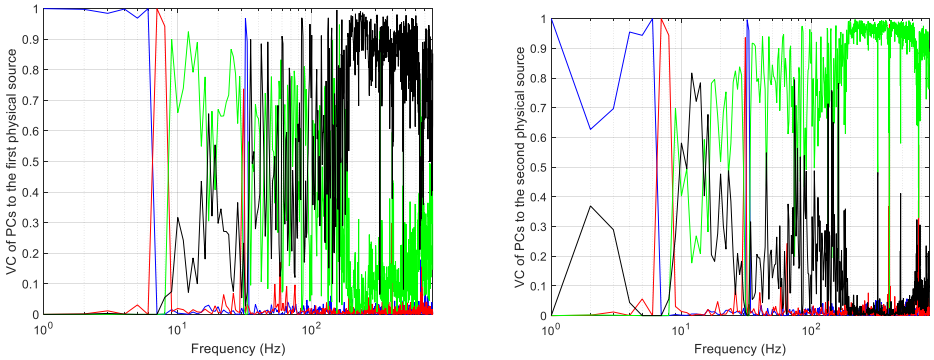

Figure D6.6 Virtual coherence of the PC_1, PC_2, PC_3 and PC_4 of sun-planet at a higher speed to the (a) first physical source (radial direction of the sun) and (b) second physical source (tangential direction of the sun). The blue, red, green and black lines denotes PC1, PC2, PC3 and PC4 respectively

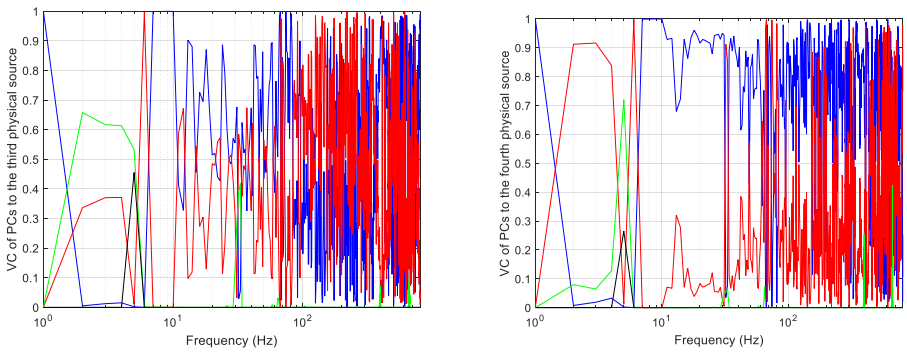

Figure D6.7 Virtual coherence of the PC_1, PC_2, PC_3 and PC_4 of sun-planet at a higher speed to the (a) third physical source (*x* direction of the planet) and (b) fourth physical source (*y* direction of the planet). The blue, red, green and black lines denotes PC1, PC2, PC3 and PC4 respectively

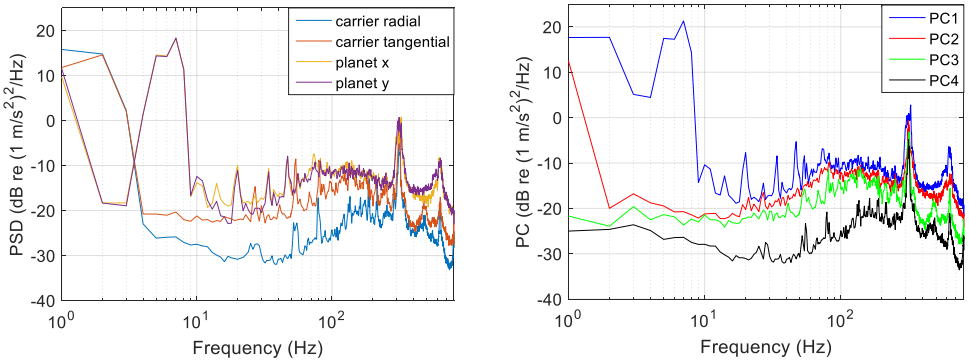

Figure D6.8. (a) The power spectral density of the carrier and planet gear accelerations. (b) The eigenvalues of the principal components PC1, PC2, PC3 and PC4 at 47 ohms.

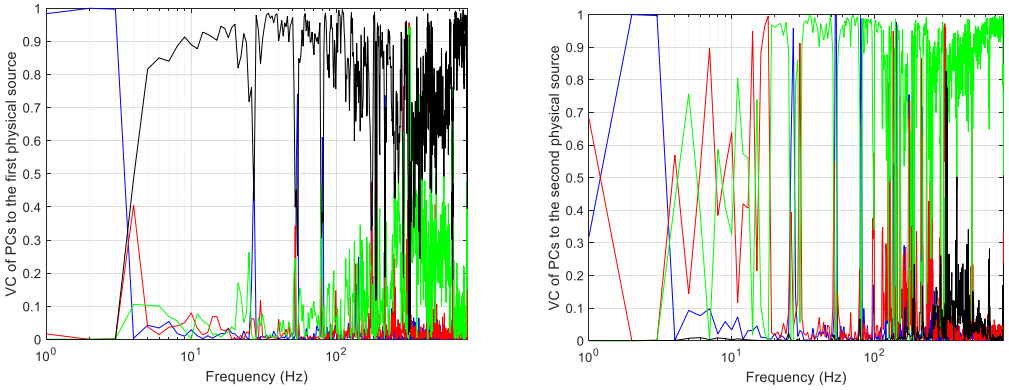

Figure D6.9. Carrier-planet virtual coherence of the PC1, PC2, PC3 and PC4 showing their contributions to the (a) first physical source (radial direction of the carrier) and (b) second physical source (tangential direction of the carrier). The blue, red, green and black lines denotes PC1, PC2, PC3 and PC4 respectively at 47 ohms.

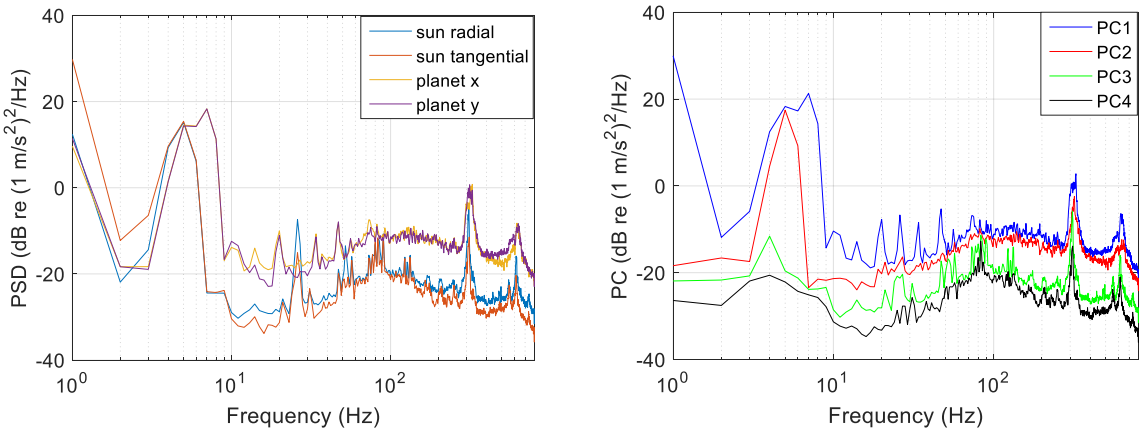

Figure D6.10. (a) The power spectral density of the sun and planet gear accelerations. (b) The eigenvalues of the principal components PC1, PC2, PC3 and PC4 at 47 ohms.

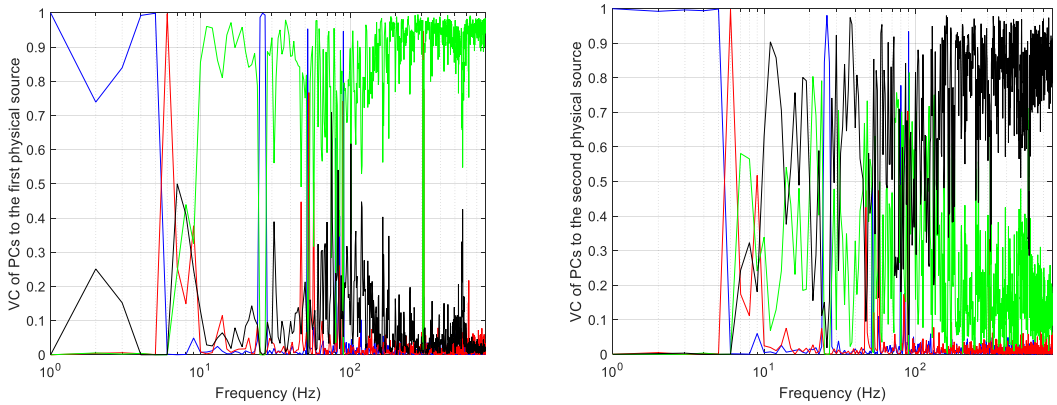

Figure D6.11. Sun-planet virtual coherence of the PC1, PC2, PC3 and PC4 showing their contributions to the (a) first physical source (radial direction of the sun) and (b) second physical source (tangential direction of the sun). The blue, red, green and black lines denotes PC1, PC2, PC3 and PC4 respectively at 47 ohms.

Appendix E

Complex power flow – electrical and structural analogies

E7.1 Instantaneous and time averaged power quantities in electrical circuits.

The following analysis is a short reduction of the analysis presented by Auld [74]. He considers the instantaneous power flow in a circuit as the product of the real positive voltage and current terms, i.e.

$$P(t) = V(t)I(t) \qquad \textbf{(E7.1)}$$

This is applicable to arbitrary waveforms, including harmonic. To simplify the analysis one can replace the terms in the above by their complex representation, i.e.

$$V(t) = |V_0|\cos(\omega t + \phi_v) = \frac{V_0 e^{j\omega t} + V_0^* e^{-j\omega t}}{2} = \Re e V_0 e^{j\omega t}$$

$$I(t) = |I_0|\cos(\omega t + \phi_I) = \frac{I_0 e^{j\omega t} + I_0^* e^{-j\omega t}}{2} = \Re e I_0 e^{j\omega t}$$

where the complex numbers

$$V_0 = |V_0| e^{j\psi_v}$$

$$I_0 = |I_0| e^{j\psi_I}$$

Substituting these expressions using the complex formulation into equation (E7.1) and taking an arbitrary reference time such that $\phi_v = 0$, then $V_o = V_0^*$ is real. Hence from the substitution and equation (E7.1), one has the **instantaneous** power given by

$$P(t) = \frac{\Re e V_0 (I_0)^*}{2} + \frac{V_0 I_0 e^{j2\omega t} + V_0 (I_0)^* e^{-j2\omega t}}{4}$$

$$= \frac{\Re e V_0 (I_0)^*}{2}(1 + cos2\omega t) + \frac{\Im m V_0 (I_0)^*}{2}\sin 2\omega t \qquad \textbf{(E.72)}$$

The first term in equation (xx.1) represents a periodic, always positive or zero, unidirectional power flow

$$\Re e \frac{V_0 (I_0)^*}{2}(1 + \cos 2\omega t)$$

This term supplies resistive losses (dissipation and resistance components) and has a time averaged value equal to

$$P_{AV} = \Re e \frac{V_0 (I_0)^*}{2};$$

The second term $\frac{\Im m V_0 (I_0)^*}{2} \sin 2\omega t$ is a periodic (reactive) power flow, with a time averaged value equal to zero. It corresponds to the power flow which is flowing into and then out of any coils (inductance) and capacitors within the circuit. Its time averaged value is zero and it has a peak value given by

$$P_x = \frac{\Im m V_0 (I_0)^*}{2}$$

Figure E7.1 illustrates, for a harmonic voltage and current, the resistive and reactive powers for this scenario.

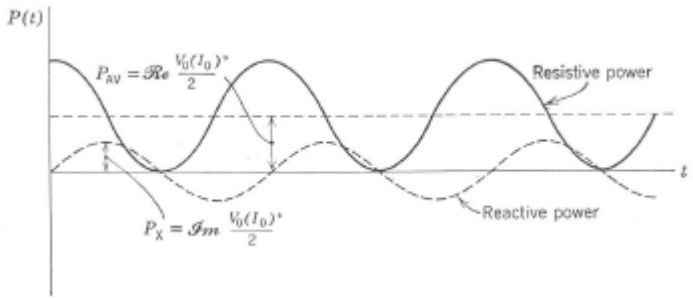

Figure E7.1. The time varying resistive and reactive powers and their time averaged quantities.

The real and imaginary parts of the complex power flow *P*, are related to time averaged resistive power and the peak reactive power by

$$P = \frac{V_0 (I_0)^*}{2} = P_{AV} + jP_x$$

This has been used in Chapter 7 for the Active Pole Placement and the corresponding evaluated power quantities and their interpretation.

E7.2 Instantaneous and time averaged power quantities in a SDOF mechanical system

Without any loss of generality one can analyse a single degree of freedom mass-spring-viscous damper system responding to a harmonic force applied to the mass. In complex notation, for a force $Fe^{j\omega t}$ one has the following differential equation of motion for the complex displacement $x(t)$,

$$m\ddot{x} + c\dot{x} + kx = Fe^{j\omega t}$$

The corresponding real force and response velocity *v* are then given by, assuming *F* is real without any loss of generality,

$$v(t) = Re\left[\frac{j\omega F e^{j\omega t}}{k - \omega^2 m + j\omega c}\right] = \frac{F}{\left|k - \omega^2 m + j\omega c\right|^2} Re\left[j\omega e^{j\omega t}\left(k - \omega^2 m - j\omega c\right)\right]$$

After further manipulation and taking the real parts, one has

$$v(t) = \frac{F}{\left|k - \omega^2 m + j\omega c\right|^2}\left[\omega^2 c\cos\omega t - \omega\left(k - \omega^2 m\right)\sin\omega t\right]$$

and $$Re\left[Fe^{j\omega t}\right] = F\cos\omega t$$

The instantaneous power *P* is then

$$P(t) = v(t)F\cos\omega t = \frac{F^2\cos\omega t}{\left|k - \omega^2 m + j\omega c\right|^2}\left[\omega^2 c\cos\omega t - \omega\left(k - \omega^2 m\right)\sin\omega t\right]$$

i.e.

$$P(t) = \frac{F^2\omega^2 c\left(1 + \cos 2\omega t\right)}{2\left|k - \omega^2 m + j\omega c\right|^2} - \frac{\omega\left(k - \omega^2 m\right)F^2\sin 2\omega t}{2\left|k - \omega^2 m + j\omega c\right|^2}$$

Which is exactly analogous to the two power quantities given in equation (E7.2), i.e. the pulsating unidirectional resistive power flow, due to dissipation in the viscous damper, and the periodic, with zero time average reactive power flow, due to the instantaneous power flow to the spring and mass.

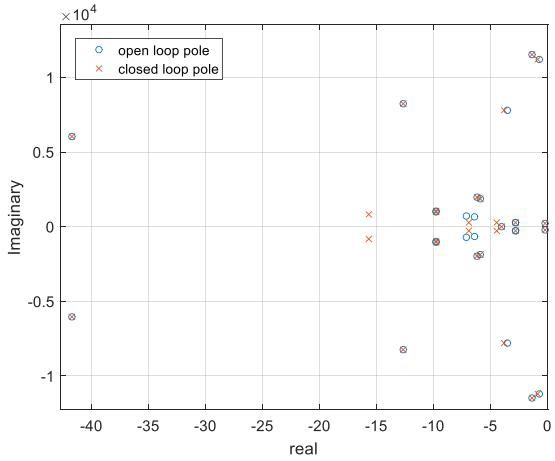

Figure E7.2. The *s*-plane plots showing the locations of the initial and the modified poles when the control forces were applied on the sun gear using a rotating frame of reference at the carrier speed of 100 rpm. The movement of the poles are the same as they are moving using the fixed frame of reference.

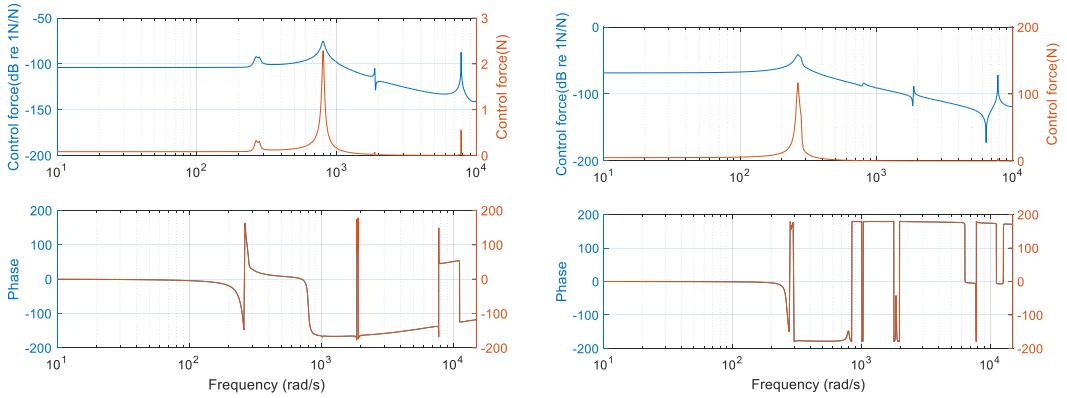

Figure E7.3. Control forces applied on the sun gear in both the (a) *x* and (b) *y* directions using rotating frame of reference at the carrier speed of 100 rpm.

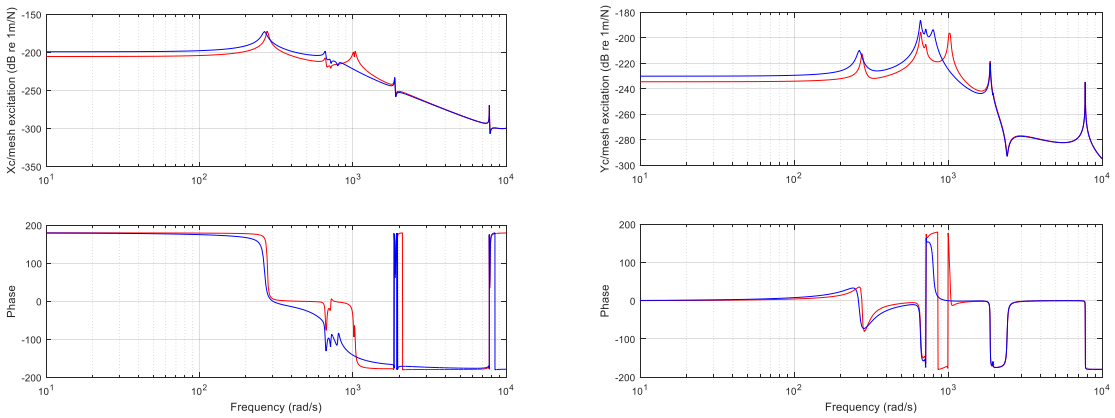

(a) (b)

Figure E7.4. Displacement per mesh excitation of the carrier in (a) x and (b) y direction using a rotating frame of reference at 100 rpm.

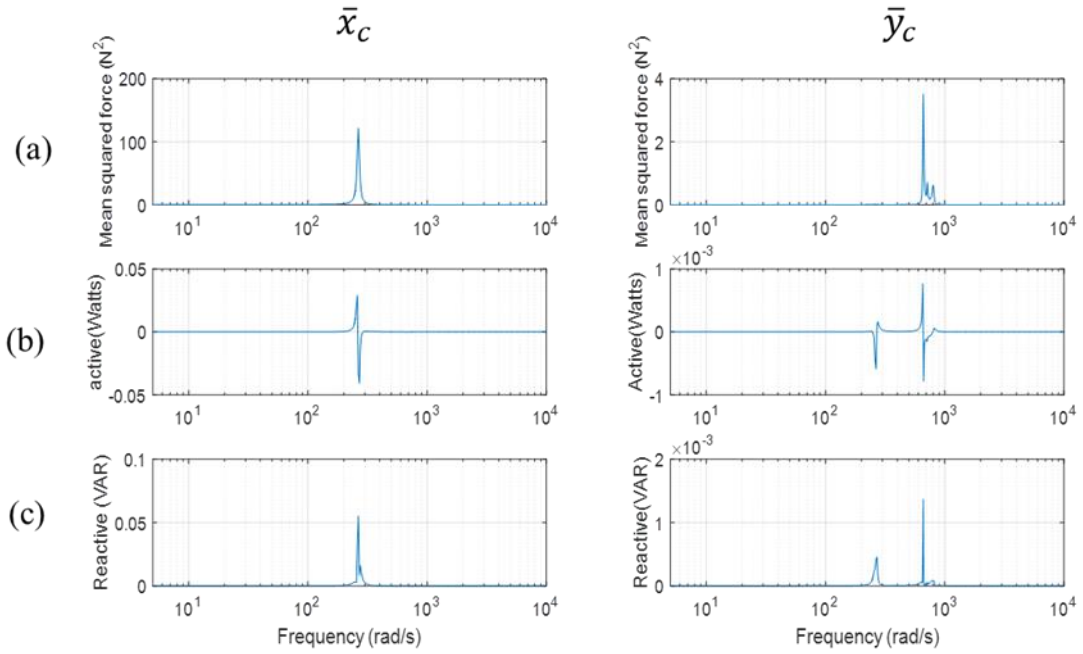

(a) (b)

Figure E7.5. Control power required by the carrier in *x* and *y* directions respectively using a rotating frame of reference when two control forces were applied in sub-section 7.5.3 of the thesis.

References

1. Kahraman, A., *Free Torsional Vibration Characteristics of Compound Planetary Gear Sets.* Mechanism and Machine Theory, 2001. **36**: p. 953-971.

2. Guo, Y., J. Keller, and R. Parker. *Dynamic analysis of wind turbine planetary gears using an extended harmonic balance approach*. in *International Conference on Noise and Vibration Engineering, Leuven, Belgium*. 2012.

3. Dresig, H. and U. Schreiber, *Vibration analysis for planetary gears. Modeling and multibody simulation.* Proceedings of ICMEM2005, 2005. **1**: p. 24-28.

4. Gawande, S. and S. Shaikh, *Experimental Investigations of Noise Control in Planetary Gear Set by Phasing.* Journal of Engineering, 2014.

5. Saxena, A., B. Wu, and G. Vachtsevanos. *A methodology for analyzing vibration data from planetary gear systems using complex Morlet wavelets*. in *Proceedings of the 2005, American Control Conference, 2005*. IEEE.

6. Ha, J.M., et al., *Autocorrelation-based time synchronous averaging for condition monitoring of planetary gearboxes in wind turbines.* Mechanical Systems and Signal Processing, 2016. **70**: p. 161-175.

7. Smith, J.D., *Gears and their vibration: a basic approach to understanding gear noise.* Marcel Dekker, Inc, 270 Madison Ave, New York, N. Y. 10016, 1983. 170.

8. Welbourn, D., *Fundamental knowledge of gear noise: a survey*. 1979.

9. Akerblom, M., *Gear Noise and Vibration - A Literature Survey*. Volvo Construction Equipments Components AB, Sweden.

10. Bahk, C.-J. and R.G. Parker, *Analytical investigation of tooth profile modification effects on planetary gear dynamics.* Mechanism and Machine Theory, 2013. **70**: p. 298-319.

11. Parker, R.G., *A physical explanation for the effectiveness of planet phasing to suppress planetary gear vibration.* Journal of Sound and Vibration, 2000. **236**(4): p. 561-573.

12. Fuller, C.R. and A.H.V. Flowtow, *Active Control of Sound and Vibration.* IEEE Control Systems, 1995: p. 9 - 19.

13. Zhou, S. and J. Shi, *Active balancing and vibration control of rotating machinery: a survey.* Shock and Vibration Digest, 2001. **33**(5): p. 361-371.

14. Parker, R.G., *Analytical Characterization of Unique Properties of Planetary Gear Free Vibration.* Transactions of ASME, 1999. **121**(July 1999): p. 316 - 321.

15. Mottershead, J.E., et al., *Active vibration suppression by pole-zero placement using measured receptances.* Journal of Sound and Vibration, 2008. **311**(3): p. 1391-1408.

16. Özgüven, H.N. and D.R. Houser, *Mathematical models used in gear dynamics—a review.* Journal of sound and vibration, 1988. **121**(3): p. 383-411.

17. Kahraman, A., *Natural modes of planetary gear trains.* Journal of Sound Vibration, 1994. **173**: p. 125-130.

18. Kahraman, A., *Planetary gear train dynamics.* Journal of Mechanical design, 1994. **116**(3): p. 713-720.

19. Lin, J. and R. Parker, *Structured vibration characteristics of planetary gears with unequally spaced planets.* Journal of Sound and Vibration, 2000. **233**(5): p. 921-928.

20. Kiracofe, D.R. and R.G. Parker, *Structured vibration modes of general compound planetary gear systems.* Journal of Vibration and Acoustics, 2007. **129**(1): p. 1-16.

21. Lin, J. and R. Parker, *Planetary gear parametric instability caused by mesh stiffness variation.* Journal of Sound and vibration, 2002. **249**(1): p. 129-145.

22. Lin, J. and R. Parker, *Sensitivity of planetary gear natural frequencies and vibration modes to model parameters.* Journal of Sound and Vibration, 1999. **228**(1): p. 109-128.

23. Chaari, F., et al., *Analysis of planetary gear transmission in non-stationary operations.* Frontiers of Mechanical Engineering, 2013. **8**(1): p. 88-94.

24. Howard, I., S. Jia, and J. Wang, *The dynamic modelling of a spur gear in mesh including friction and a crack.* Mechanical systems and signal processing, 2001. **15**(5): p. 831-853.

25. Inalpolat, M., M. Handschuh, and A. Kahraman, *Impact of indexing errors on spur gear dynamics.* Gear Technology, 2015.

26. Guo, Y. and R.G. Parker, *Dynamic modeling and analysis of a spur planetary gear involving tooth wedging and bearing clearance nonlinearity.* European Journal of Mechanics-A/Solids, 2010. **29**(6): p. 1022-1033.

27. Guo, Y. and R.G. Parker, *Dynamic analysis of planetary gears with bearing clearance.* Journal of Computational and Nonlinear Dynamics, 2012. **7**(4): p. 041002.

28. Farshad S.A., M.M., Farhad S.S., and Mohammed A.H., *Vibration behaviour optimization of planetary gear sets.* Propulsion and Power Research, 2014. **3(4)**(2014): p. 197 - 206.

29. Bahk, C.-J. and R.G. Parker, *Analytical solution for the nonlinear dynamics of planetary gears.* Journal of Computational and Nonlinear Dynamics, 2011. **6**(2): p. 021007.

30. Kahraman, A., *Load Sharing Characteristics of Planetary Transmissions.* Elsevier Science, 1994. **29**: p. 1151 - 1165.

31. He Zhaoxia, L.Q., Chang Lehao, Wu Jinsong, *Transverse-Torsional Vibrations of High-Speed Planetary Gear Transmission.* The Open Mechanical Engineering Journal, 2014. **8**: p. 396 - 401.

32. Parker, R., S. Vijayakar, and T. Imajo, *Non-linear dynamic response of a spur gear pair: modelling and experimental comparisons.* Journal of sound and vibration, 2000. **237**(3): p. 435-455.

33. Cheon, G.-J. and R.G. Parker, *Influence of manufacturing errors on the dynamic characteristics of planetary gear systems.* KSME international journal, 2004. **18**(4): p. 606-621.

34. Mosher, M. *Understanding vibration spectra of planetary gear systems for fault detection*. in *ASME 2003 International Design Engineering Technical Conferences and Computers and Information in Engineering Conference*. 2003. American Society of Mechanical Engineers.

35. Inalpolat, M. and A. Kahraman, *A theoretical and experimental investigation of modulation sidebands of planetary gear sets.* Journal of Sound and Vibration, 2009. **323**(3-5): p. 677-696.

36. McFadden, P. and J. Smith, *An explanation for the asymmetry of the modulation sidebands about the tooth meshing frequency in epicyclic gear vibration.* Proceedings of the Institution of Mechanical Engineers, Part C: Journal of Mechanical Engineering Science, 1985. **199**(1): p. 65-70.

37. Cooley, C.G. and R.G. Parker, *The geometry and frequency content of planetary gear single-mode vibration.* Mechanical Systems and Signal Processing, 2013. **40**(1): p. 91-104.

38. Mbarek, A., et al., *Effect of load and meshing stiffness variation on modal properties of planetary gear.* Applied Acoustics, 2017.

39. Seager, D.L., *Conditions for the Neutralization of Excitation bt the Teeth in Epicyclic Gearing.* Mechanical Engineering Science, I Mech E, 1975. **5**: p. 293 - 299.

40. Richards, D. and D.J. Pines, *Passive reduction of gear mesh vibration using a periodic drive shaft.* Journal of Sound and Vibration, 2003. **264**(2): p. 317-342.

41. Tharmakulasingam, R., G. Alfano, and M. Atherton, *Reduction of gear pair transmission error with tooth profile modification.* 2008.

42. Montague, G.T., et al., *Feedforward control of gear mesh vibration using piezoelectric actuators.* Shock and Vibration, 1994. **1**(5): p. 473-484.

43. Rebbechi, B., C. Howard, and C. Hansen. *Active control of gearbox vibration*. in *INTER-NOISE and NOISE-CON Congress and Conference Proceedings*. 1999. Institute of Noise Control Engineering.

44. Derouiche, A., N. Hamzaoui, and T. Boukharouba, *Vibroacoustic Sources Identification of Gear Mechanism Transmission*, in *Damage and Fracture Mechanics*. 2009, Springer. p. 143-152.

45. Zimroz, R. and A. Bartkowiak. *Investigation on spectral structure of gearbox vibration signals by principal component analysis for condition monitoring purposes*. in *Journal of Physics: Conference Series*. 2011. IOP Publishing.

46. He, Q., et al., *Machine condition monitoring using principal component representations.* Mechanical Systems and Signal Processing, 2009. **23**(2): p. 446-466.

47. Parker, R.G., J. Lin, and T.L. Krantz, *Modeling, modal properties, and mesh stiffness variation instabilities of planetary gears.* 2001.

48. Friswell, M.I., et al., *Dynamics of rotating machines*. 2010: Cambridge University Press.

49. Ondrives, *Precision Gear Manufacturing Catalogue*. 2014. p. 148.

50. Khurmi, R. and J. Gupta, *Theory of machines*. 2005: Eurasia publishing house New Delhi.

51. Krämer, E., *Dynamics of rotors and foundations*. 2013: Springer Science & Business Media.

52. Ericson, T. and R. Parker, *Design and conduct of precision planetary gear vibration experiments*. 2009, SAE Technical Paper.

53. Baskar, N., *Bearing Stiffness measurement test setup.* Unpublished work of Controlled Power Technologies.

54. Raghuwanshi, N.K. and A. Parey, *Mesh stiffness measurement of cracked spur gear by photoelasticity technique.* Measurement, 2015. **73**: p. 439-452.

55. Ian Howard, S.J.a.J.W., *The Dynamic Modelling of a Spur Gear in Mesh Including Friction and a Crack.* Mechanical Systems and Signal Processing, 2001. **15(5)**: p. 831 - 853.

56. Wadkar, S. and D.S. Kajale. *Theoretical evaluation of effect of gear parameters on mesh stiffness variations*. in *Proceedings of 14th International Conference on Mechanical Engineering in Knowledge Age at Delhi College of Engineering, India (December 2005)*. 2005.

57. Chang, L., G. Liu, and L. Wu, *A robust model for determining the mesh stiffness of cylindrical gears.* Mechanism and Machine Theory, 2015. **87**: p. 93-114.

58. Kiekbusch, T., et al., *Calculation of the Combined Torsional Mesh Stiffness of Spur Gears with Two-and Three-Dimensional Parametrical FE Models.* Strojniski Vestnik/Journal of Mechanical Engineering, 2011. **57**(11).

59. Sánchez, M.B., M. Pleguezuelos, and J.I. Pedrero, *Approximate equations for the meshing stiffness and the load sharing ratio of spur gears including hertzian effects.* Mechanism and Machine Theory, 2017. **109**: p. 231-249.

60. Miao, Q. and Q. Zhou, *Planetary gearbox vibration signal characteristics analysis and fault diagnosis.* Shock and Vibration, 2015. **2015**.

61. Järvinen, V. *Correlation between fixed and rotating frame measurements*. in *In: Rao, RBKN et al.(eds). Profit through innovation & proactive management, Proceedings of the 17th International Congress on Condition Monitoring and Diagnostic Engineering Management, COMADEM 2004*. 2004.

62. Smith, W., et al., *Gear diagnostics in a planetary gearbox: a study using internal and external vibration signals.* International Journal of Condition Monitoring, 2013. **3**(2): p. 36-41.

63. Ericson, T.M. and R.G. Parker, *Planetary gear modal vibration experiments and correlation against lumped-parameter and finite element models.* Journal of Sound and Vibration, 2013. **332**(9): p. 2350-2375.

64. De Smidt, M.R., *Internal vibration monitoring of a planetary gearbox*. 2008, University of Pretoria.

65. Jan Biloš, A.B., *Vibration Diagnostics.* VSB-TU,Technical University of Ostrava, 2012.

66. Sawalhi, N., *Vibration sideband modulations and harmonics separation of a planetary helicopter gearbox with two different configurations.* Advances in Acoustics and Vibration, 2016. **2016**.

67. Ericson, T., *Vibration of a Helicopter Planetary Gear: Experiments and Analytical Simulation.* 2011.

68. Li, Z., et al. *A Study of Vibration Characteristics of Planetary Gear Trains*. in *Proceedings of the 21st International Congress of Sound and Vibration, Beijing, July*. 2014.

69. Gupta, J. and R. Khurmi, *A Textbook of Machine Design.* SI Edition, 2005.

70. Abdalla, G., et al., *Misalignment diagnosis of a planetary gearbox based on vibration analysis*. 2014.

71. Huang, Y. and N. Ferguson. *Principal component analysis and virtual coherence of the cross-axis apparent mass in whole-body vibration*. in *The 47th United Kingdom Conference on Human Responses to Vibration*. 2012.

72. Bellino, A., et al., *PCA-based detection of damage in time-varying systems*. Mechanical Systems and Signal Processing, 2010. **24**(7): p. 2250-2260.

73. Bobrovnitskii, Y.I. *Some energy relations for mechanical systems*. in *IUTAM Symposium on Statistical Energy Analysis*. 1999. Springer.

74. Auld, B.A., *Acoustic fields and waves in solids*. 1973: Рипол Классик.